Large eddy simulation of supersonic combustion in cavity-based scramjets

Jiangheng Loïc Ruan

▶ To cite this version:

Jiangheng Loïc Ruan. Large eddy simulation of supersonic combustion in cavity-based scramjets. Fluids mechanics [physics.class-ph]. Normandie Université, 2019. English. NNT : 2019NORMIR14 . tel-02924025

HAL Id: tel-02924025
https://theses.hal.science/tel-02924025

Submitted on 27 Aug 2020

Normandie Université

THÈSE

Pour obtenir le diplôme de doctorat

Spécialité Mécanique des Fluides

Préparée à l'INSA de Rouen

Large Eddy Simulation of Supersonic Combustion in Cavity-based Scramjets

présentée et soutenue par

Jiangheng, Loïc RUAN

Thèse soutenue publiquement le 11 juillet 2019 devant le jury composé de		
N. Darabiha	Professeur CentraleSupélec, CNRS-EM2C	Rapporteur
V. Robin	Maître de Conférences ISAE-ENSMA, CNRS-PPRIME	Rapporteur
N. Chaumeix	Directrice de Recherche ICARE - CNRS Orléans	Examinateur
B. Cuenot	Chef de projet CERFACS	Examinateur
P. Domingo	Directrice de Recherche CNRS-CORIA	Dir. de thèse
G. Ribert	Maître de Conférences INSA de Rouen Normandie, CNRS-CORIA	Codir. de thèse

Thèse dirigée par Pascale DOMINGO et Guillaume RIBERT, laboratoire CORIA (UMR 6614 CNRS)

INSA INSTITUT NATIONAL DES SCIENCES APPLIQUÉES ROUEN NORMANDIE

ED PSIME

CORIA UMR 6614

Remerciements

Je tiens tout d'abord à remercier la Direction Générale de l'Armement (DGA) d'avoir entièrement financé cette thèse et le CNRS de Normandie pour la gestion de celle-ci. Ces travaux se sont déroulés au laboratoire CORIA, je remercie donc tout naturellement ses directeurs successifs, Mourad Boukhalfa et Armelle Cessou, ainsi que Valérie Thieury et Isabelle Lebon pour m'avoir permis d'effectuer la thèse dans les meilleures conditions possibles.

Je tiens également à remercier tous les membres de mon jury, à commencer par Nasser Darabiha et Vincent Robin, pour avoir consacré du temps et de l'attention à la revue de l'intégralité du manuscrit, puis à Nabiha Chaumeix et Bénédicte Cuenot pour avoir montré de l'intérêt pour mes travaux, en y apportant leurs expertises.

Je souhaite maintenant remercier mes encadrants de thèse, Pascale Domingo et Guillaume Ribert, de m'avoir encadré, soutenu et fait confiance durant ces trois ans et demi. Je n'aurais jamais pu finir cette thèse sans vos conseils et soutiens. Et c'est en discutant avec des doctorants d'autres laboratoires que j'ai compris à quel point j'avais de la chance d'avoir des encadrants comme vous, des encadrants qui se rendaient disponibles pratiquement tous les jours pour aider leur doctorant à avancer. En dehors des discussions scientifiques, j'ai aussi beaucoup apprécié les conversations avec Pascale sur la ville de Rouen, les coins sympathiques à visiter en Normandie ou alors les restaurants sur Rouen ou Paris. J'ai également beaucoup apprécié les barbecues annuels chez Guillaume où j'ai très bien mangé et bu :).

Ma thèse n'aurait pu aboutir sans l'aide du CRIANN, en particulier Béatrice Charton et Patrick Bousquet-Melou qui m'ont aidé lorsque j'ai eu besoin et qui m'ont permis de réaliser une quinzaine de millions d'heures de calcul sur MYRIA.

Le début de ma thèse aurait pu être pénible sans l'aide de Bastien, alias babadu95, qui m'a enseigné une grande partie de son savoir sur SiTComB et surtout, comment le compiler sur les supercalculateurs. Je remercie en particulier mon voisin de bureau, mon acolyte, Umut, alias kurdoBG, qui a toujours été là pour moi, aussi bien professionel que privé. Je me rappelle encore des petites anecdotes que tu nous racontais pendant la pause café, ou alors de toutes les bêtises qu'on a pu faire en Floride (à éviter de les sortir à chaque fois que t'as bu) et au Café Pop'. Il y a eu beaucoup de va-et-viens dans le bureau MaBR115 et je sais que parfois c'est dur de me supporter :). Merci donc à Kévin ou kekedu76 si affinité pour les 3 ans de bons moments au bureau et aux bars, à Geogeo pour avoir mis du Lorie tous les vendredi, à Alex pour sa gentillesse et surtout ses caipis. Je félicite Andréa d'avoir survécu à 5 garçons lourds, voire très lourds (je ne parle pas que du poids bien sûr) et d'avoir amené un peu de féminité au bureau. Heureusement qu'il y a maintenant tes petits padawans, Camille et Huu-Tri pour te soutenir. Je tiens aussi à remercier Luc Vervisch, Ghislain Lartigue, Vincent Moureau et Pierre Bénard, les anciens Nicolas, Dorian, Jean-Baptiste, les doctorants de l'équipe YALES2.

J'ai eu la chance de faire partie du bureau de l'A2DoC pendant 2 ans où j'ai rencontré plein de personnes formidables. Nathalie, Petra, Florestan, Benjamin, Patricia et d'autres personnes, je tiens à vous remercier également pour ces deux merveilleuses années où on a organisé de nombreux événements pour le laboratoire.

Je remercie la Rouen family, Anne, Alyssa et Henry qui ont été là quand la solitude commençait à avoir raison de moi. Henry, qui, d'ailleurs est devenu mon coloc pendant 2 ans. Merci pour tes croque-monsieurs et tes salades. Je remercie aussi les amis que j'ai rencontré à l'AJCF avec qui j'ai passé des moments inoubliables, voyage en Floride, organisation de la Faguo Event, CFW etc... Je tiens également à remercier mes "vieux" amis David et Antoine d'être venus assister à ma soutenance de thèse et d'avoir été là pour moi quand j'en ai eu besoin.

Enfin, je souhaite remercier mes parents et ma soeur qui m'ont soutenu de près et de loin. Merci de m'avoir laissé poursuivre mes études, de m'avoir fait confiance, de m'avoir apporté votre soutien. C'est à ma famille et mes proches que je dédie cette thèse.

Résumé

Les dernières décennies ont été marquées par de grands progrès dans les technologies hypersoniques. La course aux avions plus rapides devient d'autant plus importante que l'innovation technologique progresse. Les appareils hypersoniques existent de nos jours, mais seulement avec des moteurs-fusées. Le vol le plus célèbre a été effectué en 1967 par un appareil nord-américain, X-15, propulsé par un moteur-fusée, qui a atteint Mach 6.7 et reste le record du monde de la vitesse la plus élevée jamais atteinte avec un avion piloté. Toutefois, les aéronefs équipés de moteurs-fusées ne peuvent pas être utilisés pour les transports civils, car leurs performances dépendent fortement de la masse transportée. Plus l'avion est lourd, plus on doit transporter de carburant et de comburant, ce qui augmente d'autant plus son poids, et ainsi de suite. C'est le cercle vicieux bien connu de la technologie des moteurs-fusées. Par exemple, le SpaceX Falcon-9 avait besoin de 549 tonnes de poids brut pour lever 23 tonnes de charge utile en orbite terrestre basse et environ 65% du poids brut provenait du comburant.

En revanche, les moteurs aérobies, qui utilisent l'air présent dans l'atmosphère pour la combustion, sont réputés fiables pour les vols subsoniques ou supersoniques. Mais seuls des prototypes sont disponibles aujourd'hui pour atteindre des vitesses hypersoniques. Le principe de propulsion de ces moteurs est basé sur le processus de compression-combustion-détente. L'air entrant dans le moteur est d'abord comprimé, puis réagit avec le combustible dans la chambre de combustion. Enfin, les gaz chauds issus de la combustion sont détendus et éjectés par la tuyère pour atteindre la vitesse de croisière souhaitée. La technologie des moteurs aérobies, étant plus efficace que la technologie des fusées (pas besoin de transporter un comburant), peut conduire à des véhicules hypersoniques pouvant être utilisés pour des transports civils ou des missiles à longue portée à frappe rapide. Les moteurs aérobies peuvent également être utilisés en tant qu'auxiliaire d'un moteur-fusée pour le transport spatial jusqu'à la sortie de l'atmosphère. Le rêve de voyager un jour dans un avion hypersonique a conduit à plusieurs programmes de recherche hypersonique qui ont été présentés dans les travaux de Ferri [53], Curran et al. [31] et Urzay [165].

Parmi les différents types de moteurs aérobies, le turboréacteur à double flux (turbofan, voir Fig. 2), qui fonctionne avec des parties mobiles (compresseur et turbine), est très efficace pour les vols à “faibles” nombres de Mach (< 3). Cependant, au-dessus de Mach 3, le turboréacteur devient obsolète car les parties mobiles ne peuvent plus supporter l'augmentation de température provoquée par une compression plus intense de l'air entrant dans le système. En revanche, le statoréacteur (voir Fig. 2), qui a la particularité de ne pas avoir de partie mobile, convient à ce type d'écoulement. Le flux est comprimé puis ralenti à une vitesse subsonique par un système de chocs avant d'entrer dans la chambre de combustion. Le compresseur peut donc être retiré, ainsi que la turbine car sa fonction principale est d'alimenter le compresseur. Le phénomène de choc entraîne la création d'entropie, ce qui correspond à une perte d'énergie. Le taux de compression (P_2/P_1) et la variation d'entropie (ΔS) peuvent être liés au nombre de Mach de l'écoulement à l'aide des relations à travers

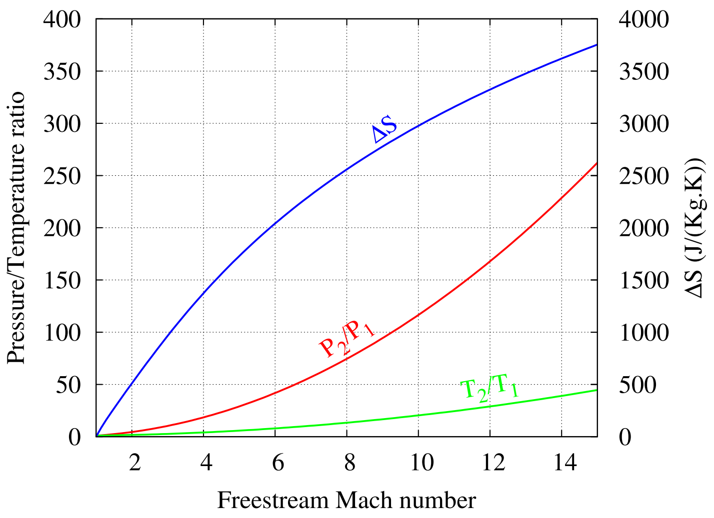

Figure 1: Propriétés de l'air à travers un choc sur une large gamme de nombres de Mach.

un choc :

$$\frac{P_2}{P_1} = 1 + \frac{2\gamma}{\gamma+1}\left(M_1^2 - 1\right)$$

$$\frac{T_2}{T_1} = \left[1 + \frac{2\gamma}{\gamma+1}\left(M_1^2 - 1\right)\right]\frac{2+(\gamma-1)M_1^2}{(\gamma+1)M_1^2}$$

$$\Delta S = C_p \ln\frac{T_2}{T_1} - R\ln\frac{P_2}{P_1}$$

Ces équations sont tracées sur la Fig. 1 dans le cas d'un gaz parfait avec $\gamma = 1.4$. Un meilleur taux de compression ferait adhérer plus d'air dans le circuit qui améliorerait la performance du moteur. Cependant, la perte d'énergie est beaucoup plus sensible à l'augmentation du nombre de Mach que le taux de compression, à tel point qu'au-dessus de Mach 5, l'utilisation d'un statoréacteur deviendrait impertinent. Le statoréacteur doit être modifié pour éviter une telle perte de performances et l'idée d'un statoréacteur à combustion supersonique (superstatoréacteur, voir Fig. 2) est ainsi apparue. Dans cette nouvelle configuration, le flux d'air est moins comprimé et ralenti, ce qui entraîne une perte d'énergie moindre pour une meilleure performance, mais également une vitesse supérieure à celle d'un statoréacteur. Le flux dans la chambre de combustion devient donc supersonique, ce qui aboutit à de nouveaux problèmes, car le temps disponible pour l'injection, le mélange et la combustion devient très court, de l'ordre de 1 ms. La stabilisation de la flamme est par conséquent un réel défi pour la conception du superstatoréacteur. L'ajout d'une cavité dans les superstatoréacteurs pourrait palier à ce problème grâce aux zones de recirculation de la cavité qui emprisonnent les gaz brûlés, et permettent ainsi de rallumer continuellement le combustible. Cependant, la littérature existante sur ce sujet est encore très restreinte, d'autant plus que la recherche sur les superstatoréacteurs est généralement liée au domaine militaire et est traditionnellement classée confidentielle.

Afin de comparer les performances des moteurs à réaction, l'impulsion spécifique, qui mesure la force exercée par l'appareil en fonction de la quantité de carburant consommé par unité de temps, est montrée sur la Fig. 3. Le superstatoréacteur présente des performances très limitées, mais représente le seul moteur aérobie capable d'atteindre des vitesses hypersoniques. Les (super)statoréacteurs ont un défaut considérable, ils ne peuvent pas assurer la propulsion à vitesse nulle et ne peuvent donc pas être utilisés à l'arrêt. Des vitesses supersoniques sont nécessaires pour produire de fortes ondes de choc afin de comprimer le flux d'air. Les statoréacteurs et les superstatoréacteurs peuvent donc

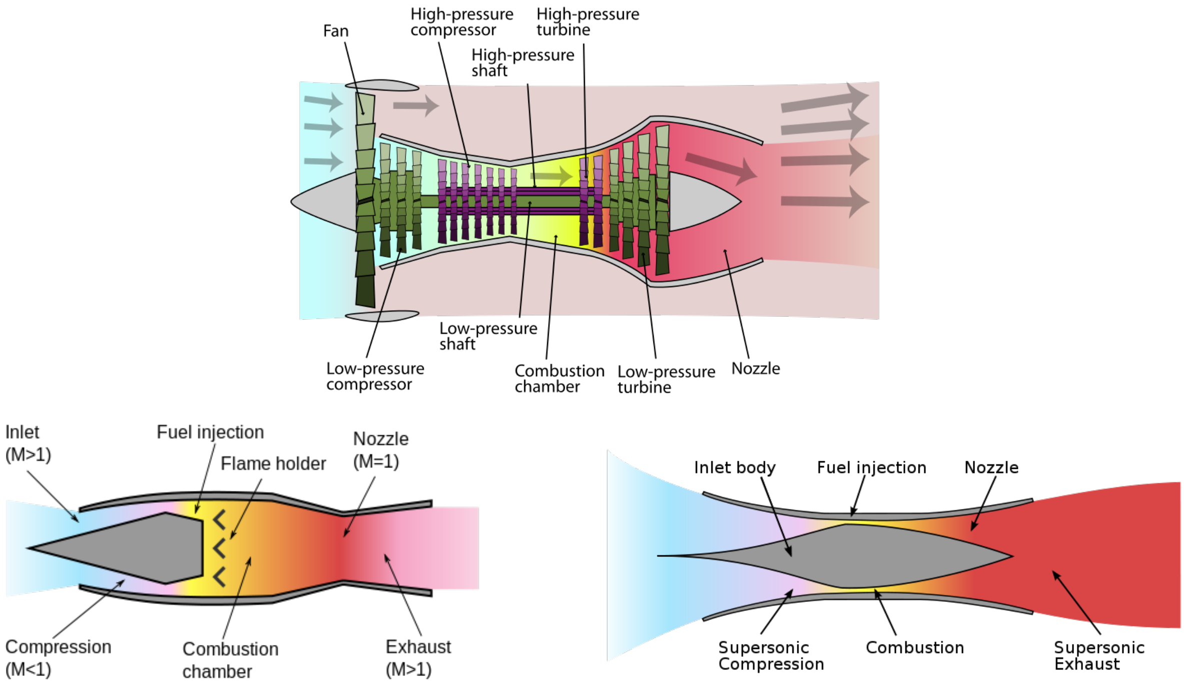

Figure 2: Schémas de turboréacteur à double flux (haut), du statoréacteur (gauche) et du superstatoréacteur (droite) [27].

fonctionner respectivement à partir de Mach 1 et 5. Pour cette raison, les appareils équipés de la technologie de statoréacteur sont généralement propulsés par un lanceur pour atteindre Mach 1. Les superstatoréacteurs peuvent ensuite être combinés à des statoréacteurs pour un moteur à double mode de fonctionnement.

Une revue sur les recherches expérimentales et numériques dans les superstatoréacteurs à cavité a été réalisée au cours de cette thèse. Les cavités permettent de maintenir la flamme grâce aux zones de recirculation qui sont induites par la différence de vitesses entre l'écoulement principal (supersonique) et l'écoulement dans la cavité (subsonique). La performance d'un superstatoréacteur dépend grandement du choix du combustible, de la géométrie de la cavité, ainsi que de la zone d'injection (Fig. 4).

Dû au temps très court passé dans le moteur, le délai d'inflammation du carburant doit être faible pour permettre la combustion. L'hydrogène (H_2) est connu pour brûler très facilement et rapidement, en raison de sa densité d'énergie élevée et de sa petite structure moléculaire. Mais les hydrocarbures sont plus attrayants d'un point de vue logistique que l'hydrogène, car ils nécessitent moins d'espace (densité plus élevée) et moins de mesures de sécurité. Certains hydrocarbures présentent également l'avantage d'être liquides à température ambiante, ce qui facilite leur stockage.

Le kérosène ($C_{10}H_{22}$) est communément utilisé pour les moteurs à combustion subsonique (turboréacteur et statoréacteur), mais ne convient pas à la combustion supersonique, car son temps d'allumage est trop important. . Rasmussen et al. ont étudié la stabilité des flammes d'éthylène et de méthane dans [137]. Les flammes d'éthylène semblent avoir un domaine de stabilité plus large que le méthane, car le délai d'auto-allumage de l'éthylène est plus court et sa vitesse de flamme plus élevée.

L'éthylène est généralement utilisé comme substitut des hydrocarbures lourds lors des essais au sol, car il s'agit d'un produit intermédiaire dans la combustion de la plupart des hydrocarbures

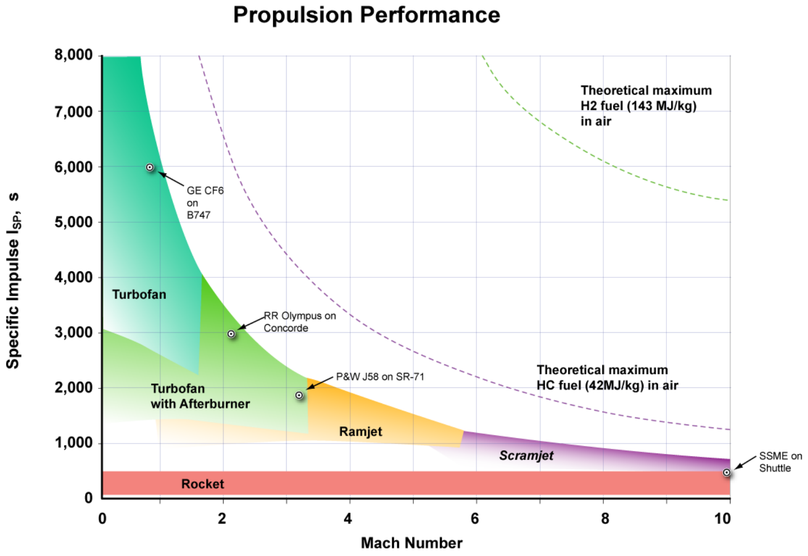

Figure 3: Performance des moteurs à réaction [27].

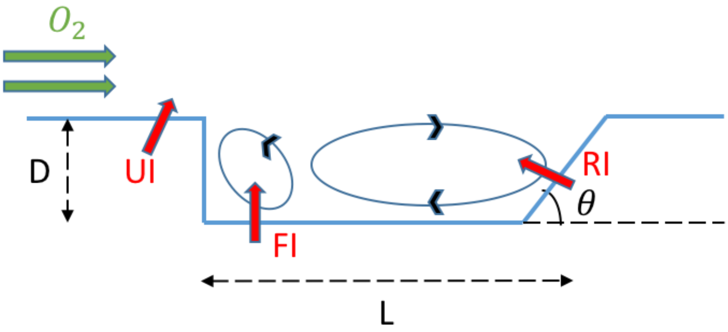

Figure 4: Schéma d'une cavité inclinée à l'arrière avec 3 zones d'injection : en amont de la cavité (UI), par le bas de la cavité (FI) et sur la rampe de la cavité (RI).

lourds et constitue l'hydrocarbure le plus rapide à brûler [26]. Cependant, on peut difficilement obtenir une auto-allumage de combustibles hydrocarbonés dans une chambre de combustion d'un superstatoréacteur. Une bougie ou une flamme pilote (hydrogène) peut être utilisée pour pallier à ce problème.

La géométrie de la cavité est déterminée par son rapport longueur sur hauteur L/D et son angle d'inclinaison à l'arrière θ. Le premier paramètre est responsable de la forme de la couche de cisaillement et du temps de séjour de la cavité, tandis que le second contrôle les oscillations à l'intérieur de la cavité.

En fonction de la valeur du rapport L/D, l'écoulement peut être divisé en deux régimes [5, 64] : écoulement de cavité ouvert ou fermé (Fig. 5). Le premier régime se produit lorsque le rapport $L/D < 10$, caractérisé par la couche de cisaillement supérieure se rattachant à l'arrière de la cavité. Cependant, lorsque le rapport est trop faible (< 3), des oscillations transversales peuvent perturber le flux principal [181]. Dans le cas où $3 < L/D < 10$, on assiste à des oscillations longitudinales. Le flux de la cavité est considéré comme fermé pour $L/D > 10$, lorsque la couche de cisaillement touche la paroi inférieure de la cavité. Mais les pertes de traînée sont amplifiées en raison de la forte différence de pression impliquée dans ce cas. Par conséquent, le rapport L/D doit rester entre 3 et 10 pour éviter tout phénomène non-désiré.

Les oscillations longitudinales sont causées par l'écoulement pénétrant dans la cavité depuis la paroi arrière. La pression dans la cavité augmente alors et crée une onde acoustique qui se propage en amont à la vitesse du son locale et induit de petits tourbillons. Ce phénomène peut être évité en utilisant des techniques de stabilisation des oscillations [5] illustrées à la figure 6. La première méthode (a) consiste à incliner la paroi arrière de la cavité d'un certain angle θ, ce qui évite la génération de chocs dus à l'impact de la couche de cisaillement sur la cavité. Les ondes de pression ne sont donc pas réfléchies vers l'amont [182]. Ben-Yakar et Hanson [5] suggèrent qu'il pourrait exister un angle d'inclinaison critique entre 16 et 45°, pour lequel les pénalités de traînée sont minimes. La deuxième méthode (b) consiste à ajouter une petite perturbation en amont pour améliorer le taux de croissance de la couche de cisaillement, ce qui peut également atténuer les oscillations dans la cavité [71, 125]. Les méthodes précédentes sont dites passives car elles interviennent directement dans la géométrie de la configuration. Plusieurs autres méthodes, dites actives, ont aussi été étudiées ailleurs [88, 146, 166], mais ne sont pas discutées ici. Les méthodes passives sont très efficaces et simples à mettre en œuvre, mais peuvent altérer les performances de la cavité.

La zone d'injection joue un rôle crucial dans les performances d'un superstatoréacteur à cavité. Que le carburant soit injecté en amont, depuis la paroi inférieure ou depuis la rampe (Fig. 4), le mélange et la combustion dans la zone de recirculation diffèrent.

Gruber et al. [65] ont étudié de manière expérimentale les injections dans la cavité en utilisant la fluorescence plane induite par laser d'oxyde nitrique (NO-PLIF) et du radical hydroxyle (OH-PLIF). L'injection en amont semble être attrayante puisqu'elle alimente à la fois l'écoulement principal et la cavité. Mais dans la pratique, le carburant reste au-dessus de la couche de cisaillement, seule une petite partie entre dans la cavité. Par rapport à l'injection en amont, l'injection depuis la paroi inférieure améliore le remplissage de la cavité mais conduit à une distribution non uniforme du carburant en raison de la petite zone de recirculation en avant de la cavité. L'injection en rampe fournit quant à elle, du carburant directement dans la grande zone de recirculation et établit une distribution uniforme du carburant dans la cavité.

En prenant en compte tous les critères de performance cités au-dessus, la configuration expérimentale du laboratoire de recherche de US Air Force a été retenue pour réaliser la simulation aux grandes échelles.

Dans cette configuration, l'écoulement d'air est accéléré pour atteindre la vitesse supersonique et pénètre dans l'isolateur à une valeur nominale de Mach 2, avec respectivement une température

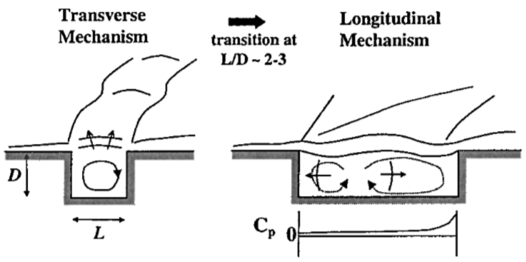

a) Open cavity flow for L/D < 7–10

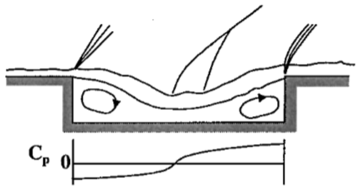

b) Closed cavity flow for L/D >10–13

Figure 5: Schéma des cavités avec de différents rapports L/D dans un écoulement supersonique [5].

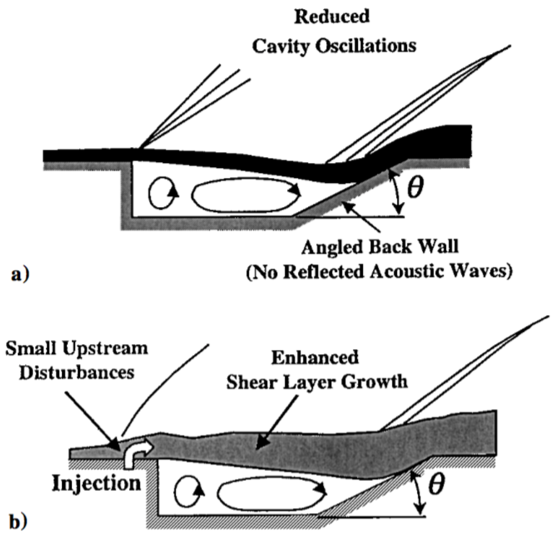

Figure 6: Techniques de stabilisation des oscillations dans la cavité : a) cavité inclinée sur la paroi arrière, b) perturbation à l'amont de la cavité [5].

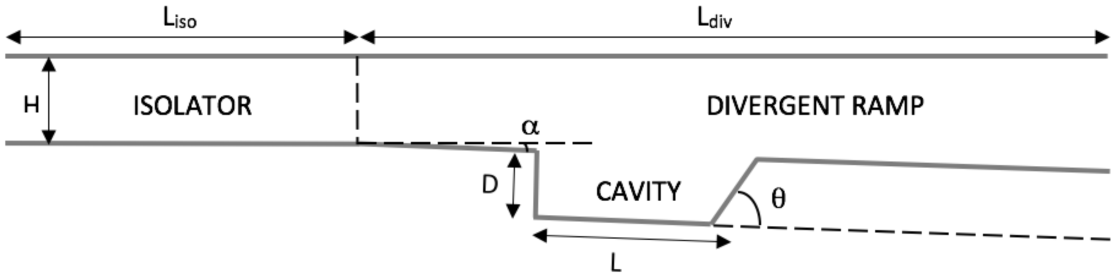

Figure 7: Schéma du canal supersonique de l'AFRL.

et une pression totales de 589 K et de 483 kPa. Le domaine de simulation dans cette thèse ne commencera qu'à partir l'isolateur. Le canal supersonique est donc modélisée comme un simple conduit rectangulaire avec une cavité inclinée à l'arrière (voir Fig. 7). L'écoulement d'air rencontre l'éthylène (C_2H_4) dans la cavité où a lieu la combustion. L'éthylène est injecté à 310 K, ce qui empêche l'auto-allumage de se produire. Des bougies d'allumage sont installées au fond de la cavité pour faciliter l'allumage. L'isolateur couvre 177.8 mm (L_{iso}) du canal et a une section constante $H \times W$ de 50.8×152.4 mm^2. A la sortie de l'isolateur, la paroi inférieure du conduit est divergente d'un angle α de 2.5°. La cavité est située à 76.2 mm de l'isolateur. Sa longueur et sa hauteur sont respectivement de 66 et 16.5 mm, ce qui donne un rapport L/D de 4, correspondant à un régime d'écoulement à cavité ouverte. La paroi arrière de la cavité est inclinée de 22.5° afin d'éviter les oscillations des ondes acoustiques à l'intérieur de la cavité [5]. Un réseau de 11 orifices d'injection de carburant de diamètre $d = 1.6$ mm est réparti sur la paroi arrière inclinée de la cavité. Tous ces paramètres géométriques sont résumés dans le tableau 1.

Tuttle et al. [164] ont réalisé cinq expériences en faisant varier le débit massique de carburant (Tab. 2). La température totale, la pression totale et la vitesse de l'écoulement d'air sont les mêmes pour tous les cas. La méthode de vélocimétrie par images de particules (PIV) a été utilisée pour déterminer la vitesse à l'intérieur de la cavité dans des conditions non-réactives et réactives. Les profils de vitesses horizontale (U) et transverse (V) sont mesurés à 8 emplacements dans la cavité

Nom	Symbole	Valeur
Longueur de la cavité	L	66 mm
Hauteur de la cavité	D	16.5 mm
Angle d'inclinaison de la cavité	θ	22.5°
Largeur du domaine	W	152.4 mm
Longueur de l'isolateur	L_{iso}	177.8 mm
Hauteur de l'isolateur	H	50.8 mm
Longueur du divergent	L_{div}	740 mm
Angle d'inclinaison du divergent	α	2.5°
Diamètre des injecteurs	d	1.6 mm

Table 1: Dimensions de la configuration expérimentale de l'AFRL.

Cas	1	2	3	4	5
T_0 [K]	589	589	589	589	589
P_0 [kPa]	483	483	483	483	483
Mach	2	2	2	2	2
U_∞ [m/s]	727	727	727	727	727
Débit carburant [SLPM]	0	56	99	39 → 36	110

Table 2: Conditions des expériences réalisées par Tuttle et al. [164].

situés respectivement à 2, 11, 20, 30, 39, 48, 57 et 66 mm du bord d'attaque de la cavité.

Les expériences de superstatoréacteur sont en réalité très difficiles à réaliser en raison du coût et des difficultés liées à la sécurité. De plus, même lorsqu'une expérience est possible, il est difficile d'effectuer des mesures dans des écoulements réactifs supersoniques et de comprendre toute la physique qui en découle. Les techniques existantes sont très limitées, la plupart des données expérimentales fournies sont des pressions pariétales ou des informations sur la stabilité de la combustion, l'accès à d'autres grandeurs physiques telles que les champs de vitesse ou de température n'est pas simple.

Afin de mieux comprendre les phénomènes physiques impliqués, il est nécessaire de développer des outils prédictifs capables de reproduire la complexité de cet écoulement, combinant des écoulements turbulents hautement compressibles avec de la chimie. Les connaissances acquises durant ce travail aideront au développement de futurs scramjets. Cependant, comme indiqué précédemment, la littérature existante est très restreinte, et la grande majorité des simulations dans les superstatoréacteurs à cavité ont été réalisées en RANS, reposant alors fortement sur des modèles. Grâce à l'essor de l'informatique, la simulation aux grandes échelles (LES) d'un telle configuration devient possible de nos jours.

Les objectifs de la thèse sont dans un premier temps d'évaluer la capacité d'une simulation aux grandes échelles à prédire des écoulements compressibles réactifs, et dans un second temps, de comprendre les phénomènes propres aux superstatoréacteurs à cavité.

Pour répondre aux objectifs, la thèse est organisée comme suit :

Chapitre 2 - Équations de l'aérothermochimie
Les bases de la thermodynamique ainsi que les équations de Navier-Stokes réactifs sont explicitées dans cette partie.

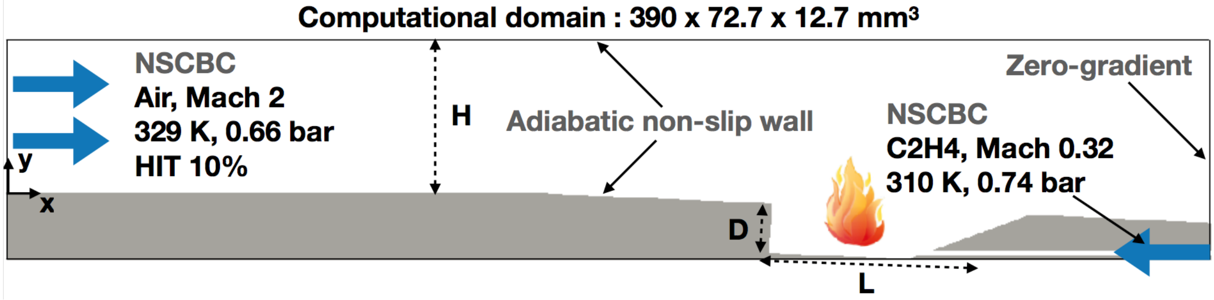

Figure 8: Schéma du domaine de simulation. La partie en gris correspond au domaine solide, coupé par la méthode des frontières immergées. $L = 66$ mm, $D = 16.5$ mm, $H = 50.8$ mm.

Cas	Maillage	Largeur (mm)	THI	Modèle paroi	Heures CPU
NRC1	Grossier	12.7	×	×	40 000
NRF1	Fin	12.7	×	×	150 000
NRC2	Grossier	25.4	×	×	80 000
NRC1H	Grossier	12.7	√	×	40 000
NRC1W	Grossier	12.7	×	√	40 000
NRC1HW	Grossier	12.7	√	√	40 000

Table 3: Cas de simulations d'écoulement à froid. Les heures CPU sont basées sur des simulations sur le supercalculateur MYRIA du CRIANN [29] qui est équippé de coeurs de calcul Xeon de 403 Tflops.

Chapitre 3 - Équations filtrées et modèles

Ce chapitre traite des équations de Navier-Stokes filtrées pour la simulation aux grandes échelles, ainsi que des modèles pour fermer ce système d'équations. Une brève description du code utilisé, SiTCom-B, est donnée dans cette partie, avec une attention particulière sur la méthode des frontières immergées (IBM).

Chapitre 4 - Simulation aux grandes échelles de l'écoulement à froid

Cette partie est dédiée aux écoulements à froid de la configuration expérimentale de l'AFRL. La partie du dispositif expérimental simulée est indiquée sur la figure 8. Le domaine de calcul comprend l'insolateur complet (177.8 mm), suivi d'une petite partie du divergent (212.2 mm) où se trouve la cavité.

Plusieurs cas de simulations à froid ont été effectués en faisant varier le maillage (grossier ou fin), la taille du domaine (1 ou 2 injecteurs simulés) ou alors en activant ou désactivant l'injection de la turbulence homogène isotrope (THI) et le modèle de paroi. Un récapitulatif de ces cas est présenté sur le tableau 3.

Dans un premier temps, une étude sur les maillages a été effectuée. Les profils de vitesses moyennes ont été comparés pour les maillages grossier et fin (Fig. 9). Les résultats sont très proches pour ces deux maillages et on remarque que les simulations parviennent à prédire la vitesse horizontale, mais des différences peuvent être observées sur la vitesse transverse.

Les lignes de courant moyennées de l'écoulement non réactif sont illustrées sur la Fig. 10 pour le maillage fin. La différence de vitesse entre l'écoulement d'air supersonique et celui à l'intérieur de la cavité crée une grande zone de recirculation dans le sens horaire, responsable de l'échange de masse au niveau de la couche de mélange. Cette zone de recirculation est la principale caractéristique de la stabilisation de la flamme par une cavité, car elle est destinée à piéger les produits de combustion chauds afin de maintenir la cavité à haute température, assurant ainsi le préchauffage et l'allumage des réactifs frais. La vitesse dans cette grande zone de recirculation est très élevée, de l'ordre de Mach 0.5. Une zone de recirculation secondaire beaucoup plus petite dans le sens anti-horaire se trouve à l'avant de la cavité, à très basse vitesse. La forme des zones de recirculation est similaire à celle des travaux de Baurle [4], et la vitesse de la zone de recirculation primaire est très proche des données expérimentales fournies par Tuttle et al. [164].

La Fig. 11 présente de diverses propriétés moyennées de l'écoulement non réactif. Les maillages grossier et fin montrent les mêmes caractéristiques d'écoulement. Comme indiqué précédemment, le nombre de Mach à l'intérieur de la cavité est très faible, se rapprochant de 0 à l'avant de la cavité et inférieur à 0.5 dans la grande zone de recirculation. La vitesse dans toute la cavité est subsonique. Un système de chocs de réattachement où la pression environne les 90 kPa est identifié depuis la paroi arrière de la cavité jusqu'à la sortie du domaine de calcul. Ce système de chocs est également présent à la même position dans le RANS/LES réalisé par Baurle [4]. Ce système de chocs est en fait responsable de l'augmentation de la température à l'intérieur de la cavité : l'impact du choc sur la paroi arrière de la cavité réchauffe l'écoulement environnant qui est ensuite amené à l'avant et au milieu de la cavité par les recirculations. Il y a aussi un petit préchauffage dû aux frictions avec la paroi en amont de la cavité. Tous ces échauffements conduisent à une température moyenne de 450 K dans la cavité, soit 120 K de plus que l'écoulement d'air. Enfin, la pression à l'intérieur de la cavité est hétérogène, variant de 40 à 90 kPa.

Ensuite, une comparaison a été effectuée entre le cas à un injecteur (NRC1) et le cas à deux injecteurs (NRC2) sur des maillages grossiers. Aucune différence notable n'a été observée sur ces deux cas. Enfin, l'étude sur l'ajout de la THI et/ou de la loi de paroi a montré que la THI permettrait d'obtenir une turbulence plus développée à l'approche de la cavité, qui favoriserait le mélange éthylène-air dans la couche de cisaillement. En revanche, l'activation ou non de la loi de paroi n'apporte aucune différence quand il y a injection de la THI.

Chapitre 5 - Simulation aux grandes échelles de l'écoulement réactif
Ce chapitre est dédié aux écoulements réactifs. Le carburant, l'éthylène, et ses schémas réactionnels réduits sont d'abord présentés. Ensuite, les simulations d'écoulements réactifs ont été effectuées pour un, deux et onze injecteurs avec un débit massique de carburant permettant une combustion stable à l'intérieur de la cavité (99 SLPM). Le cas à un injecteur a également été étudié pour deux autres débits de carburant: un cas pauvre (36 SLPM) qui donne une combustion instable pour comprendre le phénomène d'extinction de flamme dans ce cas, et un cas moyen (56 SLPM) pour comparer le processus de stabilisation de la flamme avec le cas stable précédent. Le tableau 4 récapitule tous les cas réactifs étudiés dans cette partie. Cependant, seul le cas RFA1 sera traité dans ce résumé. Le lecteur est invité à lire la partie en anglais pour les autres cas.

De diverses propriétés de l'écoulement dans le plan de l'injecteur et dans le plan entre deux injecteurs sont montrées sur la Fig. 12 pour le cas réactif en utilisant le schéma réduit à 22 espèces (S22) et avec un maillage fin (RFA1). Ces résultats ont permis d'identifier quatre zones de combustion : (I) la couche de mélange au-dessus de la petite zone de recirculation où la réaction est faible, (II) la couche de mélange au-dessus de la grande zone de recirculation avec une forte réaction au milieu de la cavité et une intensité plus faible vers l'arrière de la cavité, (III) le région entre les

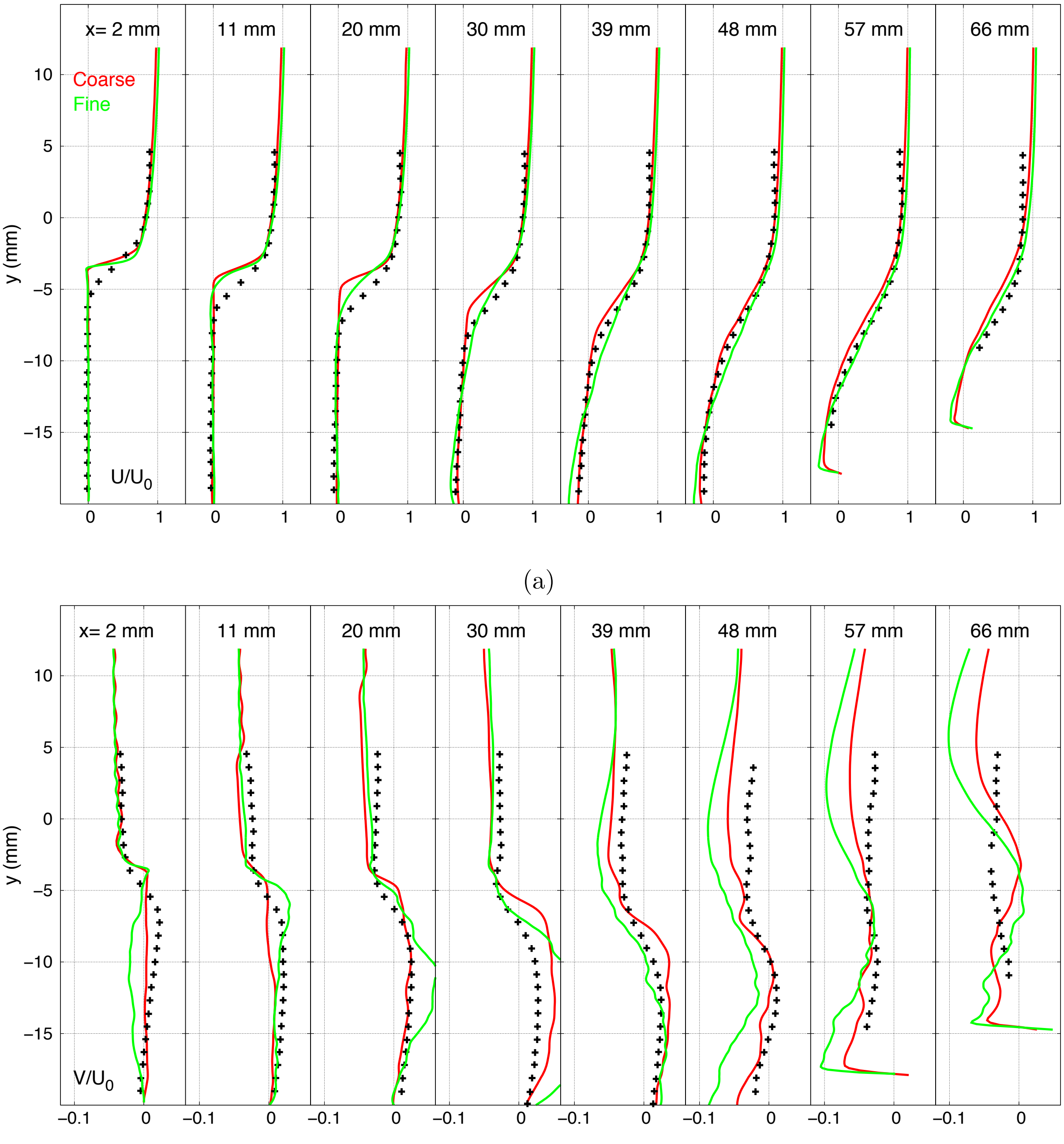

(a)

(b)

Figure 9: Comparaison des profils de vitesses avec l'expérience de Tuttle et al. [164] pour les maillages fin et grossier : (a) vitesse horizontale moyenne et (b) vitesse transverse moyenne.

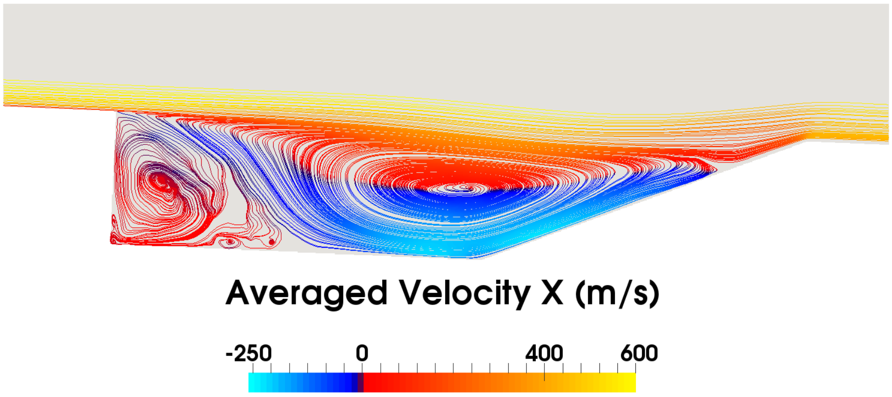

Figure 10: Lignes de courant moyennées, coloriées par la vitesse horizontale, maillage fin.

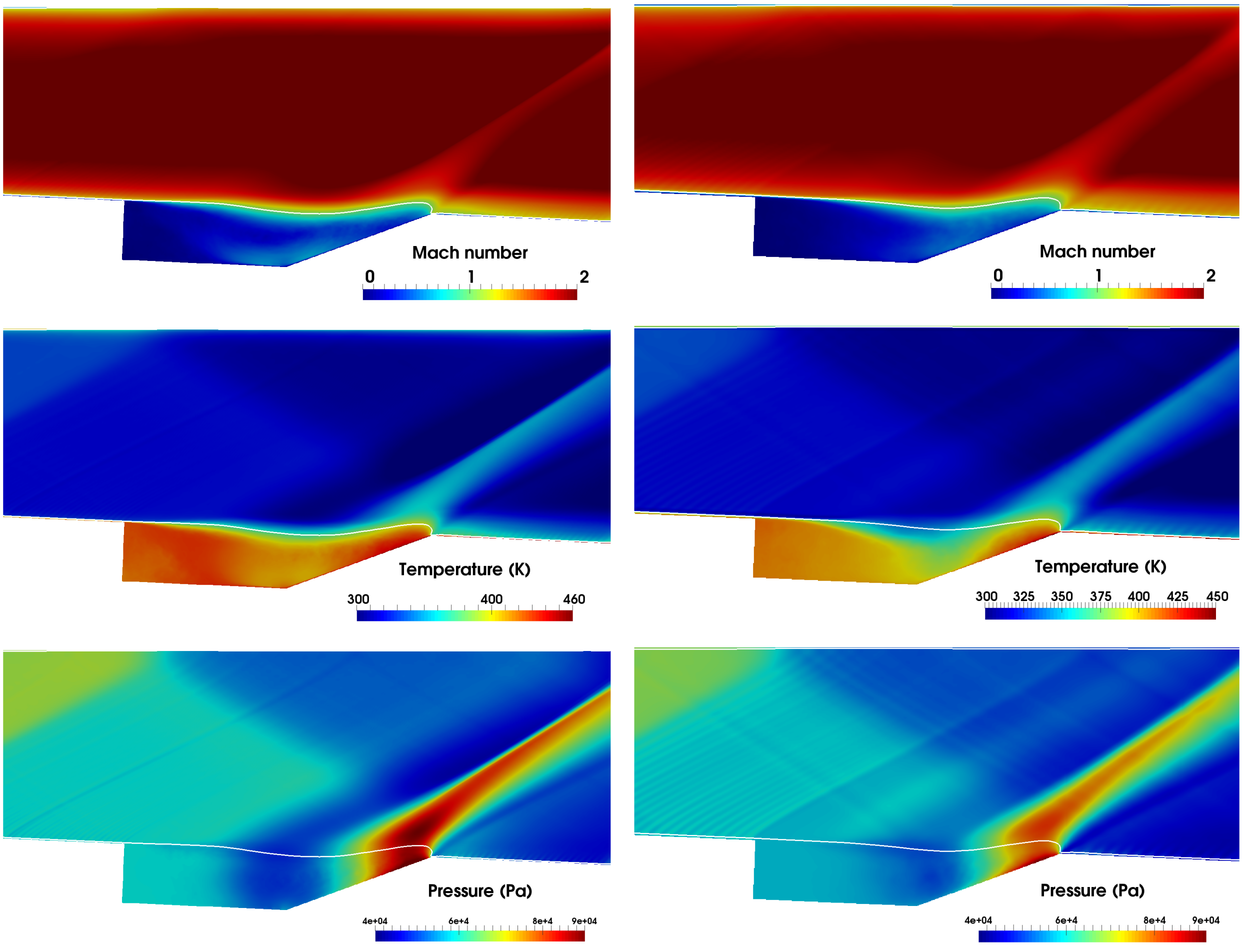

Figure 11: Diverses propriétés de l'écoulement pour les maillages fin (gauche) et grossier (droite) : nombre de Mach (haut), température (milieu) et pression (bas). L'iso-contour Mach = 1 est montré en blanc.

Cas	Dimension	Injecteurs	Chimie	Paroi	Maillage	Points (M)
R2D	2D	-	S22	Adiabatique	Fin	3
NRCS22	3D	1	-	Adiabatique	Grossier	45
RCS10	3D	1	S10	Adiabatique	Grossier	45
RCA1	3D	1	S22	Adiabatique	Grossier	45
RCA1L	3D	1	S22	Adiabatique	Grossier	45
RCA1M	3D	1	S22	Adiabatique	Grossier	45
RFA1	3D	1	S22	Adiabatique	Fin	300
RCI1	3D	1	S22	Isotherme	Grossier	45
RFI1	3D	1	S22	Isotherme	Fin	300
RCA2	3D	2	S22	Adiabatique	Grossier	90
RCA11	3D	11	S22	Adiabatique	Grossier	542

Table 4: Simulations étudiées dans ce chapitre. Le débit massique du carburant est de 99 SLPM pour tous les cas, sauf RCA1L and RCA1M qui ont respectivement des débits de 36 et 56 SLPM.

deux zones de recirculation où l'intensité de la combustion est moyenne, et enfin (IV) à la sortie de l'injecteur avec une forte intensité de combustion. Les résultats du cas RFA1 ont aussi permis de comprendre le processus de stabilisation de la flamme dans ce cas 13 :

- La carburant issu des injecteurs réagit immédiatement avec l'oxygène qui est entré par la rampe. La combustion est possible car l'oxygène est préchauffé par les gaz brûlés présents dans la grande zone de recirculation.
- Les gaz brûlés issus de la combustion réchauffent la cavité.
- Le carburant présent dans la petite zone de recirculation est préchauffé, puis réagit en contact de l'air venant de l'écoulement principal au niveau de la couche de mélange.
- La combustion provoque le préchauffage de l'air qui va entrer dans la cavité par la rampe.

Des comparaisons entre les résultats numériques et expérimentales [164] dans le cas d'un écoulement réactif sont présentées sur la Fig. 14 pour la pression et sur la Fig. 15 pour les profils de vitesses à x = 2, 11, 20, 30, 39, 48, 57, 66 mm du coin à l'avant de la cavité. La pression pariétale est très proche des données expérimentales pour les deux maillages, sauf pour le dernier point au niveau de la rampe de la cavité. Ce point n'est certainement pas très bien capturé en raison du système de chocs de réattachement présent dans cette région. La comparaison des profils de vitesse ne montre qu'une faible différence entre l'expérience et les données numériques pour la vitesse horizontale. Mais là encore, de grandes disparités peuvent exister pour la vitesse transverse.

Chapitre 6 - Analyse de la structure de flamme

Cette dernière partie est consacrée à l'analyse de la structure de la flamme dans les superstatoréacteurs. Cette étude est réalisée sur le maillage fin (RFA1) en prenant en compte seulement les points qui ont une valeur de dégagement de chaleur signifiante, c'est à dire : $|\dot{\omega}_E| > 0.01\dot{\omega}_{E,max}$. Le

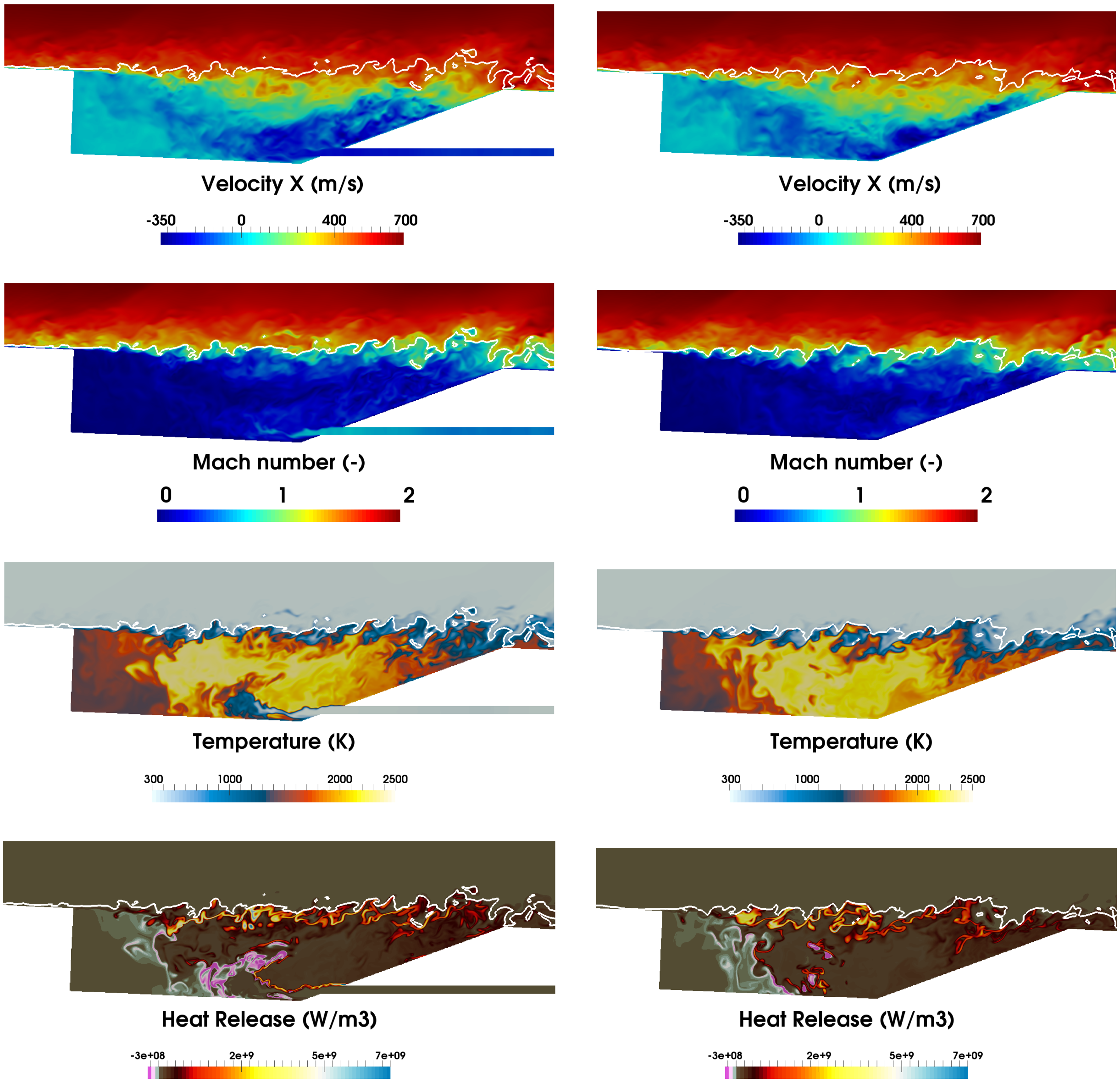

Figure 12: Champs instantanés de vitesse horizontale, du nombre de Mach, de la température et du dégagement de chaleur dans le plan central de l'injecteur (gauche) et dans le plan central aux deux injecteurs (droite). L'iso-contour Mach = 1 est montré en blanc. Cas RFA1.

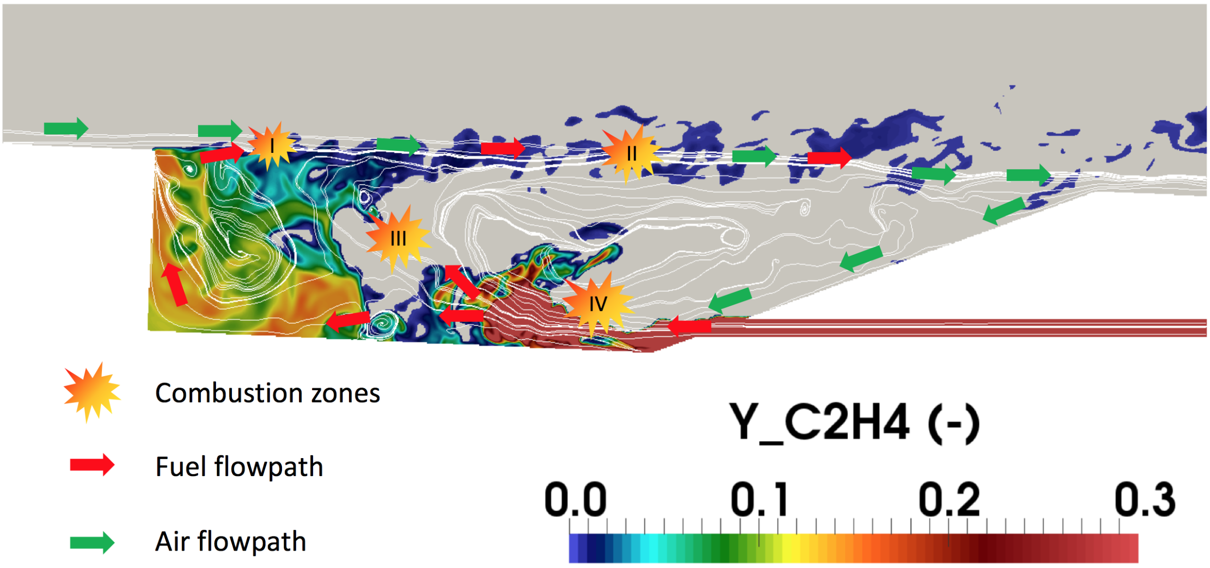

Figure 13: Schéma de la stabilisation de la flamme par cavité.

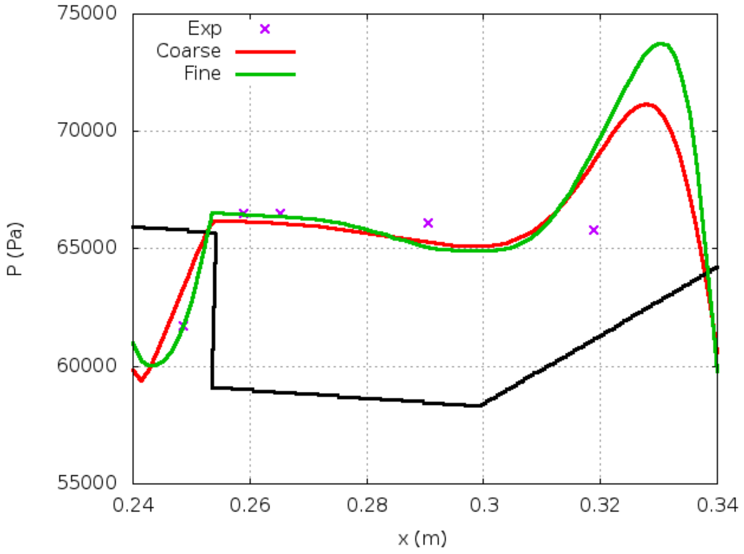

Figure 14: Comparaison entre l'expérience et la simulation pour la pression pariétale moyennée dans le plan central aux deux injecteurs pour le cas RFA1.

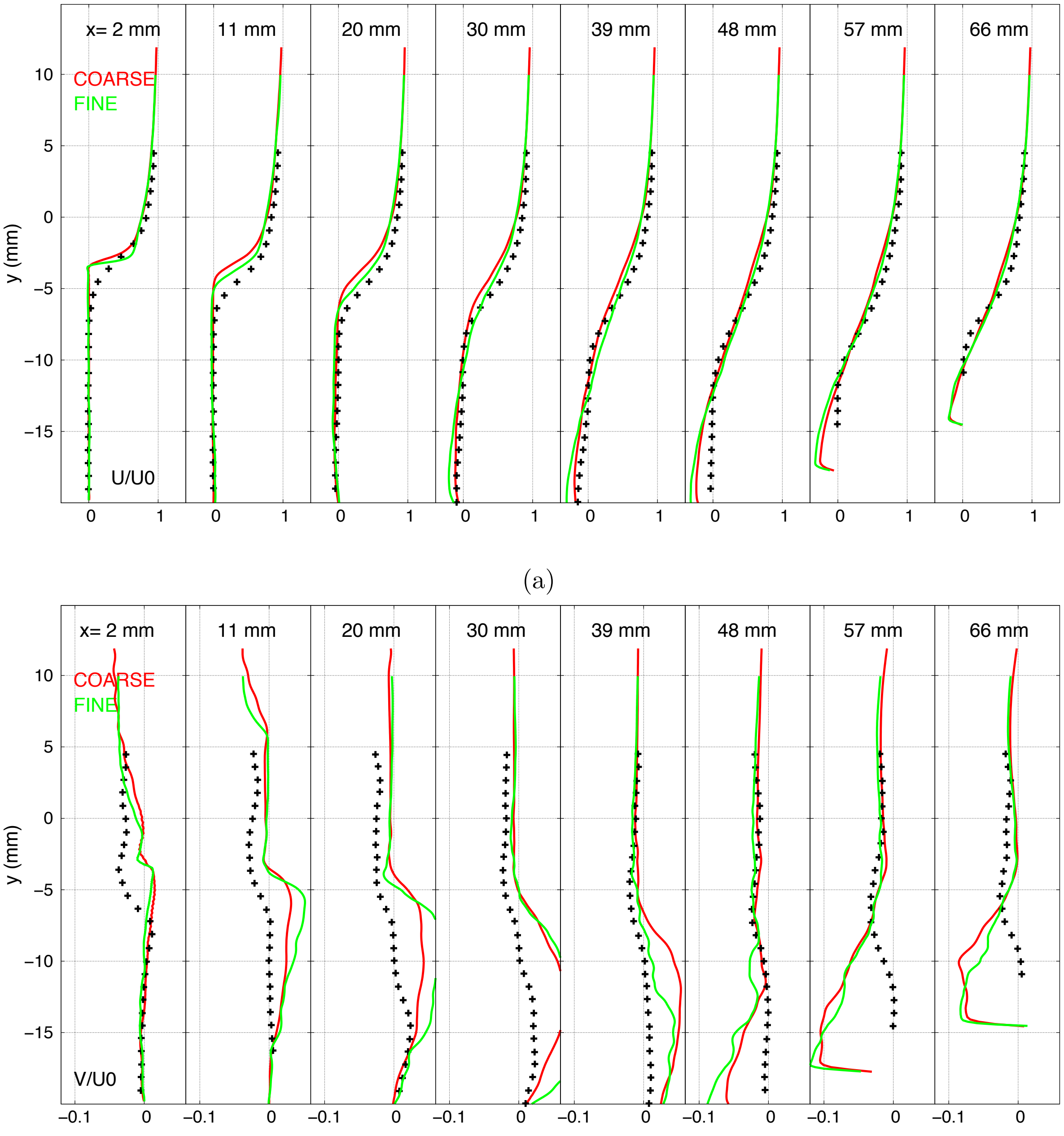

(a)

(b)

Figure 15: Comparaison entre l'expérience et la simulation pour les profils de vitesses moyennées dans le plan central aux deux injecteurs pour les cas RCA1 et RFA1.

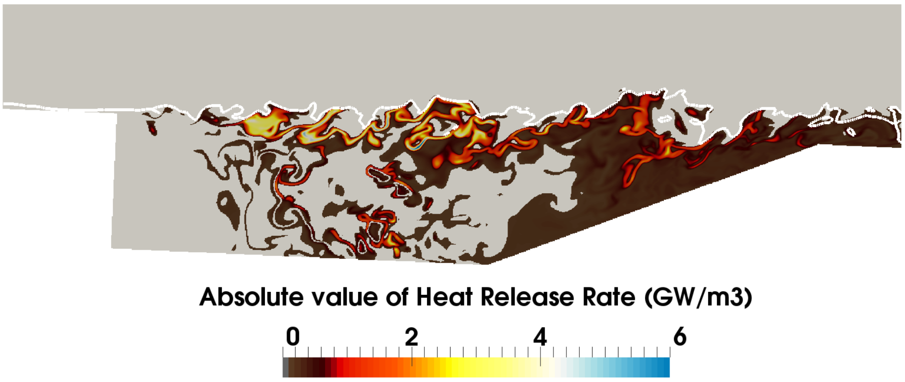

Figure 16: Champ instantané du dégagement de chaleur pour le cas RFA1. Seulement les points avec un dégagement de chaleur supérieur à 1% de la valeur maximale du dégagement de chaleur sont représentés. L'iso-contour Mach = 1 est montré en blanc.

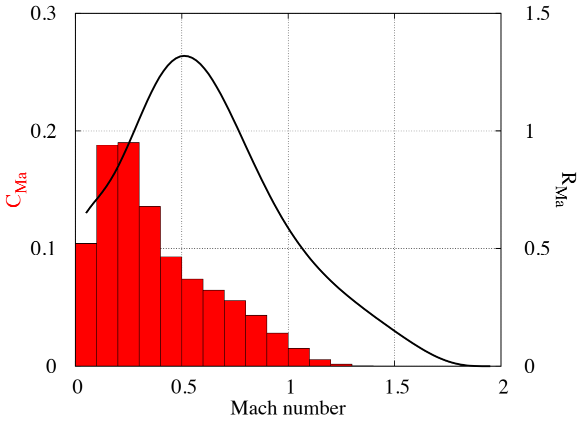

Figure 17: Dimensionless conditional mean of the heat release on Mach number R_{Ma} (curve), and percentage of cells contributing to the statistics in each interval (0.1) of Mach number C_{Ma} (histogram): fine mesh (left) and coarse mesh (right).

champ correspondant est montré sur la Fig. 16.

Une étude sur la moyenne conditionnée du dégagement de chaleur par le nombre de Mach a été effectuée pour connaître la vitesse des zones de combustion. La Fig. 17 montre en histogramme rouge le pourcentage de cellules dans chaque intervalle de nombre de Mach et en courbe noire la moyenne conditionnée du dégagement de chaleur par le nombre de Mach adimensionnée. On observe que la combustion a essentiellement lieu en régime subsonique (> 95%). Et on remarque aussi que la zone avec la plus grande activité chimique se trouve aux alentours de Mach 0.5.

L'indice de flamme, initialement introduit par Yamashita et al. [178], sert à distinguer les flammes prémélangées des flammes de diffusion. Cet indice a été modifié par Lock et al. [101] en ajoutant une pondération qui permet de distinguer le régime riche du pauvre. La formulation de l'indice de flamme utilisée dans cette thèse est donc la suivante :

$$F.I. = \frac{1}{2}\frac{Z - Z_{st}}{|Z - Z_{st}|} \times \left(1 + \frac{\nabla Y_F . \nabla Y_{O_2}}{|\nabla Y_F . \nabla Y_{O_2}|}\right)$$

où Z est la fraction de mélange de Bilger et al. [8] et Z_{st} sa valeur à la stoechiométrie. La flamme

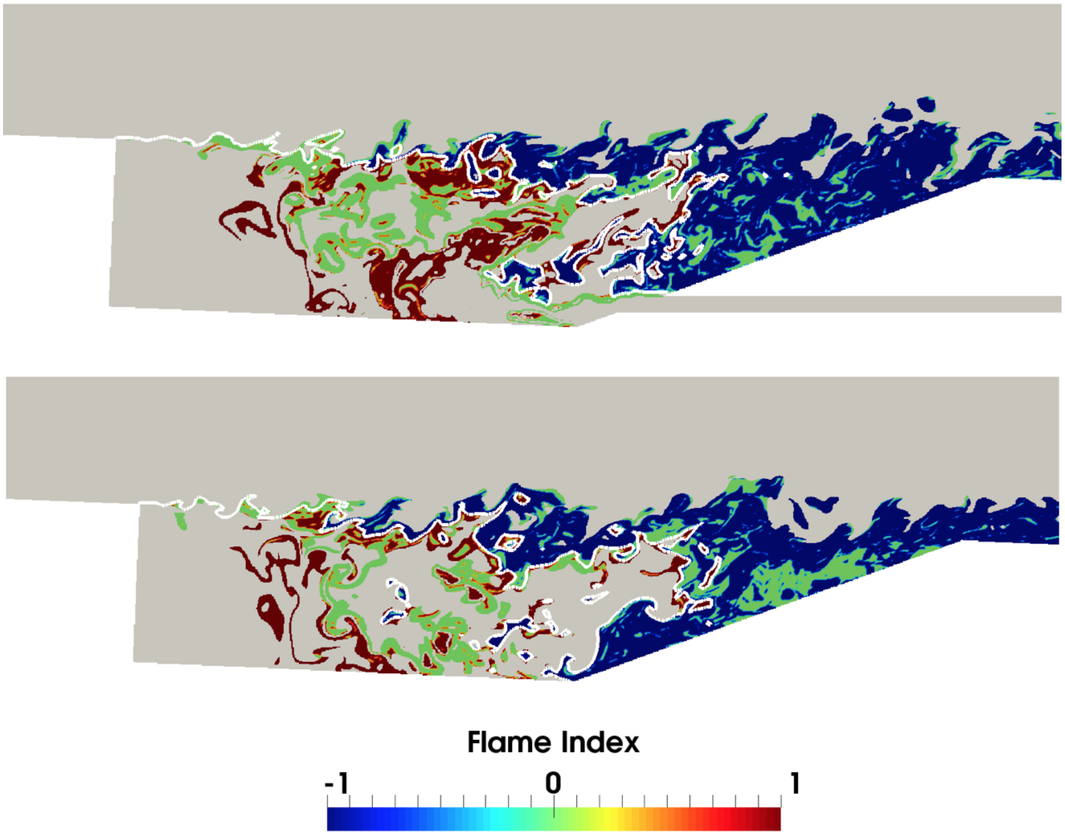

Figure 18: Distribution de l'indice de flamme dans la cavité dans le plan central de l'injecteur (haut) et dans le plan central aux deux injecteurs (bas). -1: prémélangée pauvre, 0: diffusion, 1: prémélangée riche. La ligne stoechiométrique $Z = Z_{st}$ est représentée en blanc. Cas RFA1.

est prémélangée riche si $F.I. = 1$, prémélangée pauvre si $F.I. = -1$ et de diffusion si $F.I. = 0$. Le champ de l'indice de flamme est montré sur la Fig. 18 dans le plan central de l'injecteur et dans le plan central aux deux injecteurs. On observe que les trois régimes sont présents dans la cavité, avec des flammes de prémélange riche et de diffusion au milieu de la cavité et des flammes de prémélange pauvre à l'arrière de la cavité. Le régime de combustion des quatre zones de réaction trouvées précédemment peut être déterminé à l'aide de l'indice de flamme. La couche de mélange au-dessus de la petite zone de recirculation (I), l'interface entre les deux zones de recirculation (III) et la sortie de l'injecteur (IV) sont principalement contrôlées par des flammes de diffusion, tandis que des flammes de prémélange riche et pauvre sont essentiellement présentes dans la couche de mélange au-dessus de la grande zone de recirculation.

Le temps de résidence a été codé au cours de cette thèse en se basant sur l'équation de transport fournie par Enjalbert et al. [49] :

$$\frac{\partial \overline{\rho}\widetilde{\tau}_r}{\partial t} + \frac{\partial}{\partial x_i}(\overline{\rho}\widetilde{u}_i\widetilde{\tau}_r) = \frac{\partial}{\partial x_i}\left[\overline{\rho}(\nu + \nu_t)\frac{\partial \widetilde{\tau}_r}{\partial x_i}\right] + \overline{\rho}S_{\widetilde{Z}}$$

où le facteur $S_{\widetilde{Z}}$ n'est égal à 1 seulement dans les zones de mélanges ($\widetilde{Z} \in [\epsilon, 1-\epsilon]$ avec $\epsilon = 10^{-4}$) et 0 ailleurs. Cette implémentation permet d'incrémenter le temps de résidence de δt à chaque pas de temps uniquement dans les zones d'intérêts. Les champs moyens du temps de résidence sont montrés sur la Fig. 19 pour le cas RCA1. On observe que le temps de résidence dans la grande zone de recirculation est faible, de 0.8 ms à 1.2 ms, tandis qu'il est plus élevé dans la petite zone de recirculation en raison de la vitesse locale plus basse. Le temps de résidence de la grande zone de

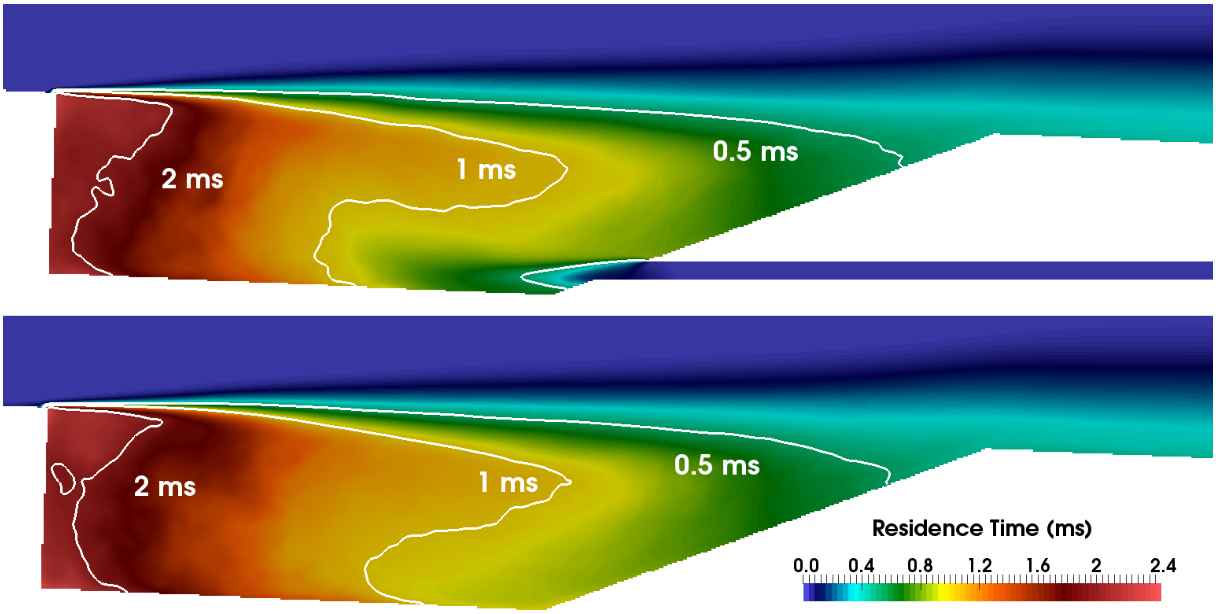

Figure 19: Champ moyen du temps de résidence dans le plan central de l'injecteur (haut) et dans le plan central aux deux injecteurs (bas). Cas RCA1. Les iso-contours sont montrés en blanc.

recirculation est caractérisque du temps de séjour de la cavité puisque la grande majorité du transfert de masse s'effectue à ce niveau. Et cette valeur du temps de résidence est cohérente avec la loi empirique de Davis et Bowersox [35, 36], mais aussi avec la littérature où ce temps est d'environ 1 ms dans tous les travaux sur les superstatoréacteurs.

Plusieurs librairies de flammes de prémélange ont été construites sur des richesses allant de 0.4 à 19.5 (prolongation linéaire au-delà de ces limites) pour une comparaison avec la LES. Les paramètres de contrôle de la table sont la fraction de mélange qui est basée sur la formule de Bilger et al. [8] et une variable de progrès définie comme suit : $Y_c = Y_{CO_2} + Y_{CO} + Y_{H_2O}$. Une comparaison entre les valeurs extraites de la LES et les valeurs reconstruites en fonction de la fraction de mélange locale et de la variable de progrès est montrée sur la Fig. 20 pour la température et la fraction massique de H_2O. Les résultats sont très encourageants pour ces deux grandeurs. Cependant, dans la zone de recirculation secondaire où un temps de résidence très long est attendu, certaines espèces telles que le CO et le CO_2 ne sont pas bien capturées par l'approche flammelette prémélangée (Fig. 21). Une approche hybride dans laquelle la table serait construite à partir des flammelettes prémélangées et de diffusion permettrait probablement d'améliorer les résultats pour ces espèces.

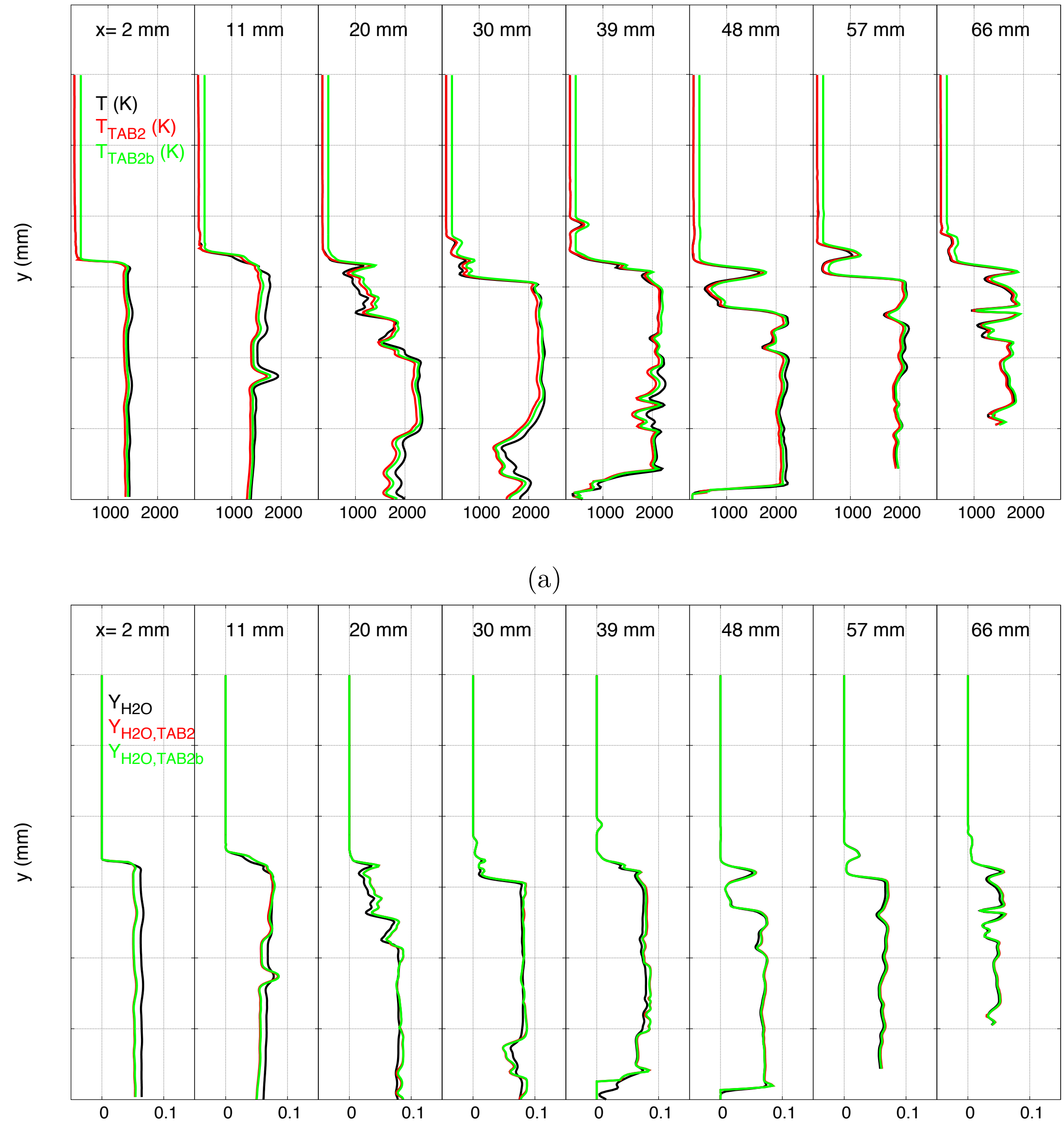

(a)

(b)

Figure 20: Profils instantanés de (a) température et (b) fraction massique de H_2O dans le plan central de l'injecteur : comparaison entre la LES et la tabulation.

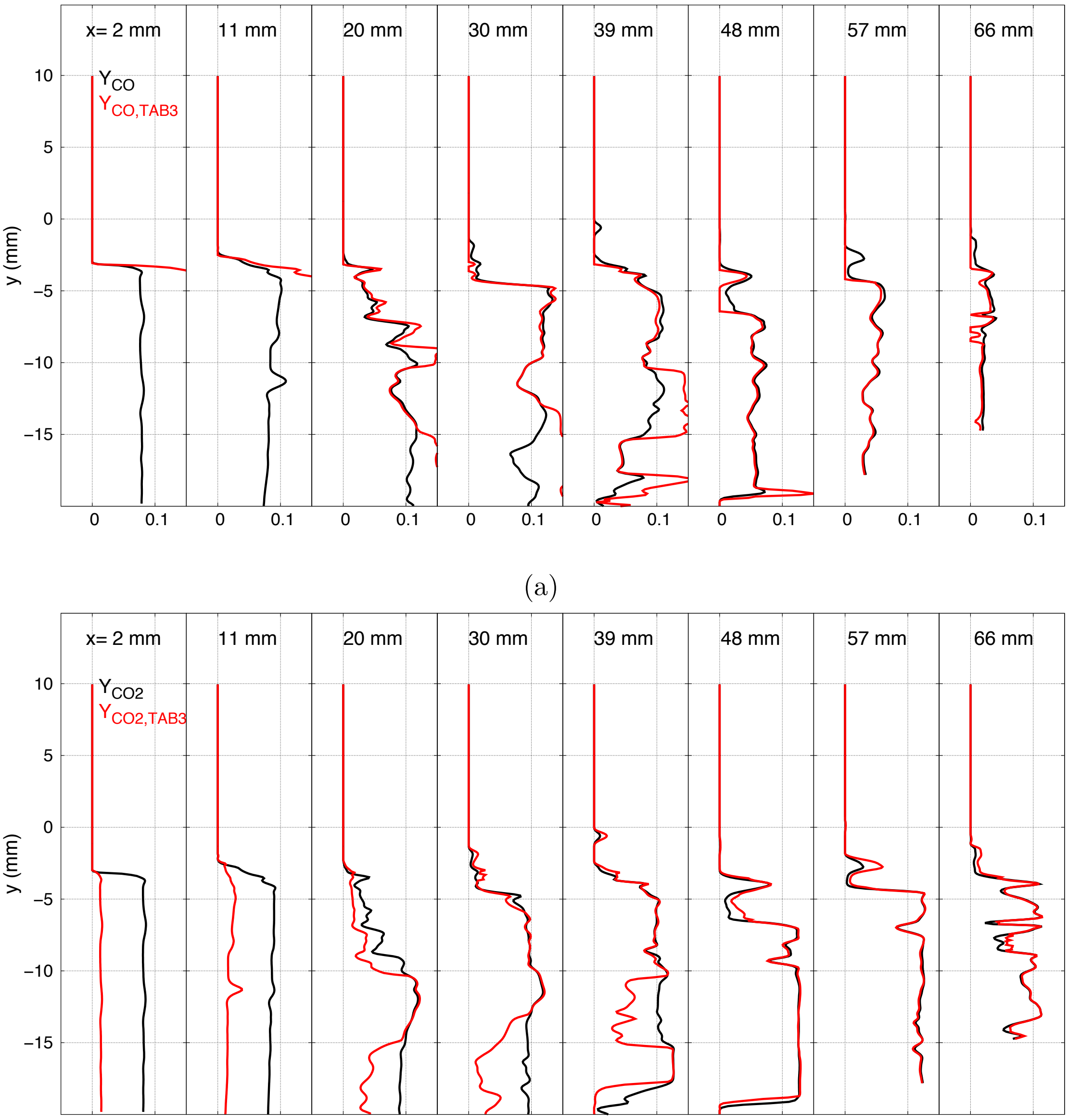

(a)

(b)

Figure 21: IProfils instantanés de fraction massique de (a) CO et (b) H_2O dans le plan central de l'injecteur : comparaison entre la LES et la tabulation.

Contents

Nomenclature

Acronyms

AFRL	Air Force Research Laboratory
AHSTF	Arc-Heated Scramjet Test Facility
DSTO	Defence Science and Technology Organisation
EDC	Eddy Dissipation Concept
HDRC	HIFiRE Direct-Connect Rig
HF2	HIFiRE Flight 2
HTV	Hydroxyl-Tagging Velocimetry
HIFiRE	Hypersonic International Flight Research and Experimentation
IBM	Immersed Boundary Method
LES	Large Eddy Simulation
LIBS	Laser-Induced Breakdown Spectroscopy
NASA	National Aeronautics and Space Administration
PaSR	Partially Stirred Reactor
PIV	Particle Image Velocimetry
PSR	Perfectly Stirred Reactor
RANS	Reynolds-Averaged Navier-Stokes
SiTCom-B	Simulating Turbulent Combustion of Billions of points
SLPM	Standard Liters Per Minute
TFM	Thickened Flame Model
VULCAN	Viscous Upwind Algorithm for Complex Flow Analysis
WALE	Wall Adapting Local Eddy Viscosity

Dimensionless number

Da	Damköhler number
Ka	Karlovitz number

Le	Lewis number
M	Mach number
Pr	Prandtl number
Re	Reynolds number
Sc	Schmidt number

Greek Symbols

θ	Cavity aft ramp angle
τ	Cavity residence time (s)
η_c	Combustion efficiency
ρ	Density (kg/m^3)
α	Divergent ramp angle
μ	Dynamic viscosity (Pa.s)
ϕ	Equivalence ratio
ϕ_g	Global equivalence ratio
ν	Kinematic viscosity (m^2/s)
Δ	LES filter size (m)
η_m	Mixing efficiency
η_p	Pressure loss
γ	Specific heat ratio

Roman Symbols

D	Depth (m)
C_p	Heat capacity at constant pressure (J.kg^{-1}.K^{-1})
C_v	Heat capacity at constant volume (J.kg^{-1}.K^{-1})
L	Length (m)
m	Mass (kg)
$\dot{m}$	Mass flow rate (kg/s)
Y_k	Mass fraction of species k
Z	Mixture fraction
$[X_k]$	Molar concentration of species k (mol/m^3)
X_k	Molar fraction of species k
W_k	Molar mass of species k (kg/mol)

W	Molar mass of the mixture (kg/mol)
P	Pressure (Pa)
T	Temperature (K)
N_{sp}	Total number of species
U	Velocity (m/s)
V	Volume (m^3)
W	Width (m)

Subscripts

cav	Cavity
div	Divergent
∞	Freestream parameters
F	Fuel
0	Initial conditions
iso	Isolator
O	Oxidizer
st	Stoichiometric
sgs	Subgrid scale
t	Turbulent

Chapter 1

Introduction

Contents

1.1 Context and motivations

The last decades have been marked by a large progress in hypersonic technologies. The race for faster aircraft becomes all the more important as the innovation in technology advances. Hypersonic speed aircrafts are available nowadays, but only when they are powered by rocket engines. The most famous flight has been performed in 1967 by the rocket-powered North American X-15 which reached Mach 6.7, and still remains the world record for the highest speed ever reached with a manned aircraft. However, aircraft powered by rocket engines cannot be used for civil transport, since the performance of such vehicles is highly dependent of its weight. The heavier the aircraft becomes, the more fuel and oxidizer the aircraft needs to carry, which increases all the more its weight, and so on. That is the well-known vicious circle of the rocket engine technology. As an example, the SpaceX Falcon-9 required 549 tons of gross weight to lift 23 tons of payload to low Earth orbit, and about 65 % of the gross weight are from the oxidizer.

On the other hand, airbreathing jet engines, which use the oxidizer present in the atmosphere for combustion, are known to be reliable for supersonic flights, but only prototypes are available for hypersonic speeds. The propulsion of these engines is performed with a process of compression-combustion-expansion. Hot gases from the combustion chamber are then ejected through the rear nozzle to reach the desired cruise speed. The airbreathing engine technology, being more efficient than the rocket technology (no need to carry oxidizer), can lead to hypersonic vehicles that could be used for civil transport or long-range fast strike missiles. The airbreathing engines can also be used as the first stage of a rocket-powered vehicle to help space transportation of payloads until the exit of the atmosphere. The ambition of travelling in hypersonic aircraft one day has led to several hypersonic research programs that have been well presented in the reviews of Ferri [53], Curran et

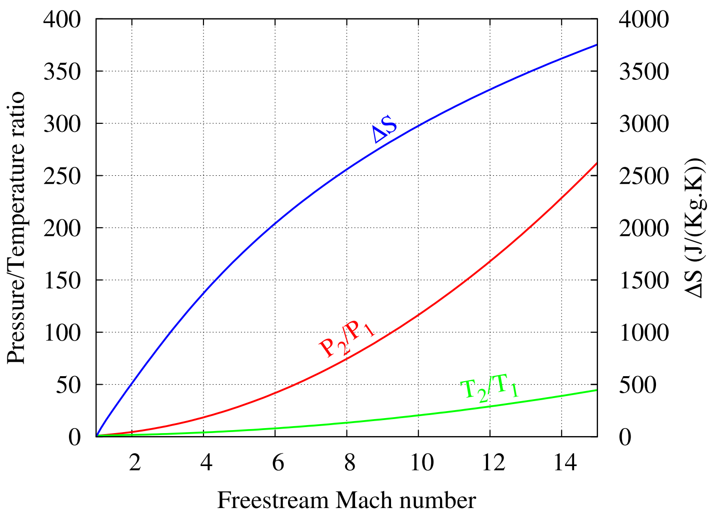

Figure 1.1: Shock jump properties for air over a range of Mach numbers.

al. [31] and Urzay [165].

Among the different airbreathing jet engines, the turbofan (see Fig. 1.2), which works with rotary mechanical parts (compressor and turbine), is very efficient for low to mid Mach numbers. However, above Mach 3, the turbofan becomes obsolete because the rotary parts cannot hold the temperature increase caused by a more intense compression of air entering the system. The ramjet (see Fig. 1.2), which has the particularity of having no rotary part, fits well this range of Mach number. The flow is compressed and then slowed down to subsonic speed through a system of shocks, before entering the combustion chamber. The compressor can therefore be removed, and also the turbine since its main function is to feed the compressor. The phenomenon of shock results in creation of entropy, which corresponds to the loss of energy. The compression rate and the entropy can be linked to the freestream Mach number through the shock jump equations 1.1.1:

$$\begin{aligned}
\frac{P_2}{P_1} &= 1 + \frac{2\gamma}{\gamma+1}\left(M_1^2 - 1\right) \\
\frac{T_2}{T_1} &= \left[1 + \frac{2\gamma}{\gamma+1}\left(M_1^2 - 1\right)\right]\frac{2+(\gamma-1)M_1^2}{(\gamma+1)M_1^2} \\
\Delta S &= C_p \ln\frac{T_2}{T_1} - R\ln\frac{P_2}{P_1}
\end{aligned} \tag{1.1.1}$$

These equations are plotted in Fig. 1.1 in the case of an ideal gas with $\gamma = 1.4$. If the compression rate is kept unchanged, the loss in energy is strongly increasing with the freestream Mach number, to such an extend that above Mach 5, the use of a ramjet becomes irrelevant. The ramjet needs to be modified to avoid such a loss in performance and the idea of a supersonic combustion ramjet (scramjet, see Fig. 1.2) has thus emerged. In the configuration of a scramjet, the airflow is less compressed and slown down, resulting in a lower energy loss for a better performance, but also in a higher speed compared to a ramjet. The flow in the combustion chamber therefore becomes supersonic which creates some new issues as the time available for injection, mixing and combustion becomes very short, in the order of 1 ms. The flame stabilization is consequently a real challenge for the scramjet design, and cavities have recently been considered as a promising flameholding device. They are able to retain hot burnt gases which helps auto-ignition and stabilizes combustion. However, the existing literature on this subject is still very poor, all the more since the research on scramjets is generally linked to military domain and is traditionally shielded behind classification.

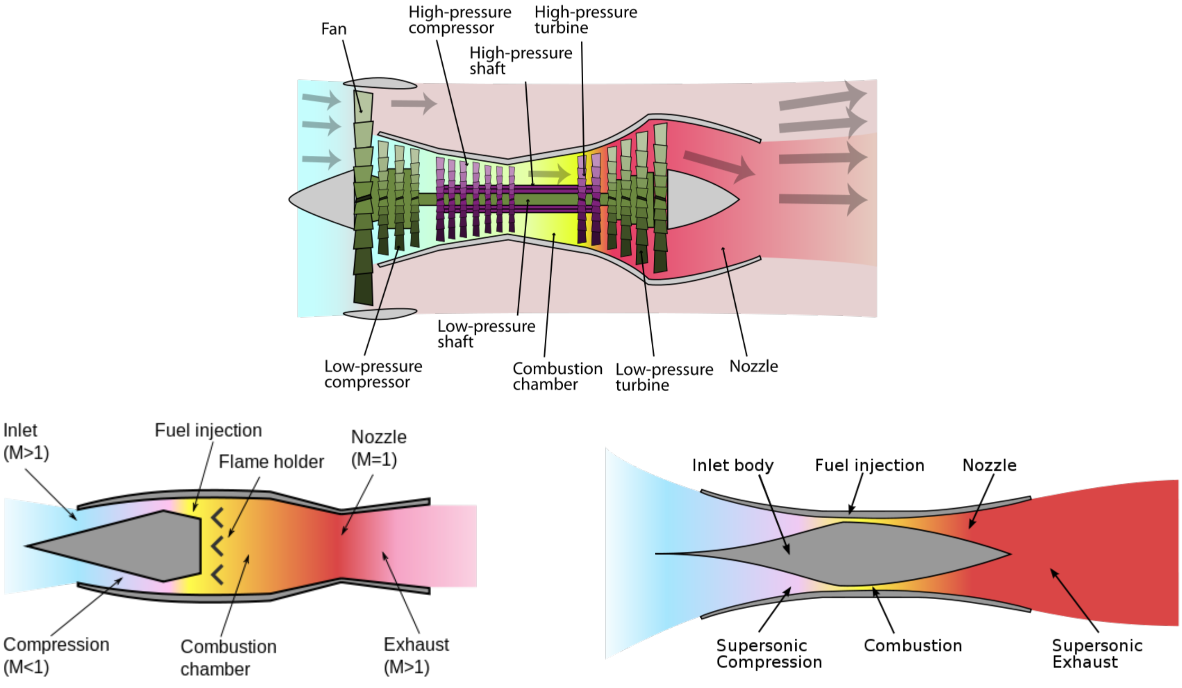

Figure 1.2: Schematics of turbofan (top), ramjet (left) and scramjet (right) [27].

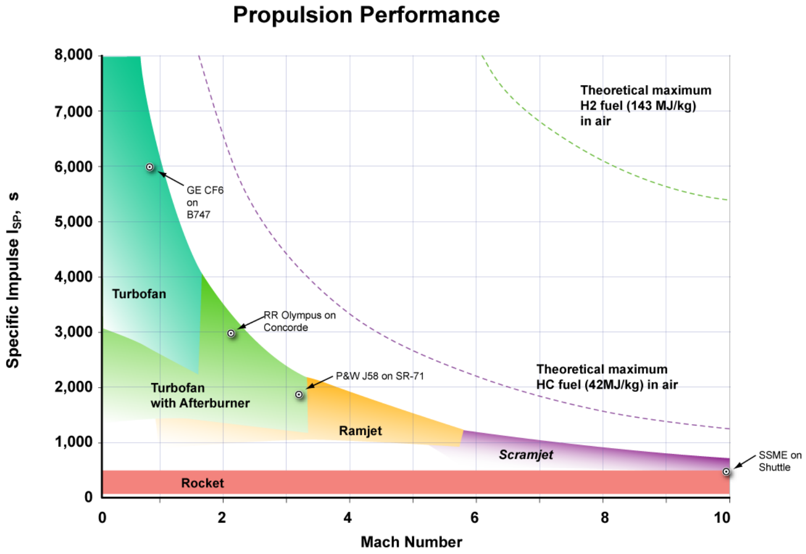

Figure 1.3: Propulsion performance of different jet engines [27].

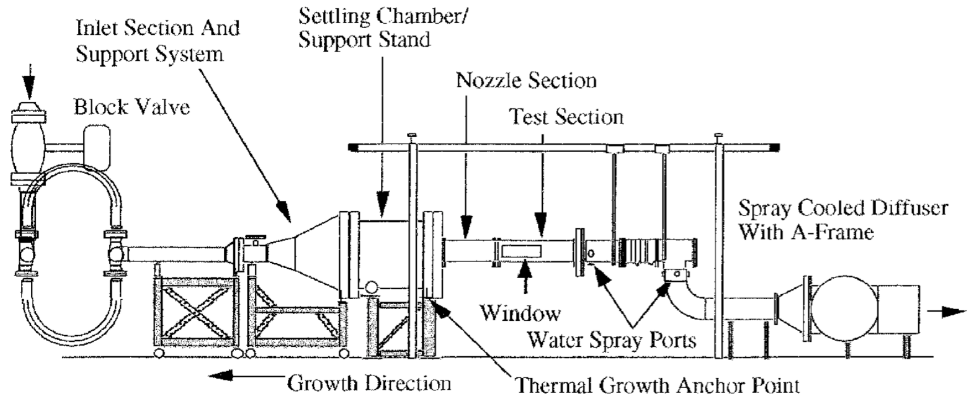

Figure 1.4: AFRL facility schematic [66].

In order to compare the performance of jet engines, the specific impulse, which is the ratio of thrust over the propellant flow rate, is shown in Fig. 1.3. The scramjet presents a very limited performance, but is the only airbreathing jet engine to reach hypersonic speeds. The (sc)ramjets have a considerable defect, they cannot produce thrust at zero airspeed, thus cannot be used from a standstill. Supersonic speeds are required to produce strong shockwaves to compress the airflow. Ramjets and scramjets can therefore be operated respectively at least at Mach 1 and Mach 5. For that reason, prototypes are generally propulsed by a launcher to reach Mach 1, and scramjets combined to ramjets for a dual operating mode engine.

1.2 Experimental review

The following section is a review of experimental research efforts focused on combustion in cavity-based scramjets. Those without cavity-stabilization are not in the scope of the present work. Experiments are very expensive and hard to carry out, therefore the number of laboratories working on supersonic combustion experiments is very limited.

1.2.1 US AFRL experimental facility

The US Air Force Research Laboratory (AFRL) is located at the Wright-Patterson Air Force Base, in the state of Ohio. Supersonic flow experiments were conducted at the propulsion department of this laboratory [66]. The flow facility (see Fig. 1.4) allows studies of the basic fluid dynamic mechanisms that govern fuel-air mixing in supersonic combustors. A continuous source of clean compressed air is available to provide stagnation conditions up to 922 K and 5.27 MPa and a total flow rate of 15.4 kg/s. Multiple experiments were carried out with this facility and a non exhaustive list is provided below.

Gruber et al. [64] performed some non reactive experiments in 2001 to investigate the impact of cavity aspect ratio L/D_u, offset ratio D_u/D_d and ramp rangle θ (see Fig. 1.5 for definitions) on the dynamic of the flow. The oxidizer, air, is flowing into the system at Mach 3, at a stagnation pressure of 690 kPa and a stagnation temperature of 300 K for all the cavity models. Wall static pressure was measured, and some Schlieren and shadowgraph flow visualizations are available in [64].

The first successful ignition and sustained combustion of ethylene with the AFRL facility was performed by Mathur et al. [110]. Air was injected through two separate facility nozzles (Mach 1.8 and 2.2) to simulate flight Mach numbers between 4 and 6, at a flight dynamic pressure of 47.9 kPa. Ethylene was injected upstream of the cavity and from its floor (see Fig. 1.6). The cavity

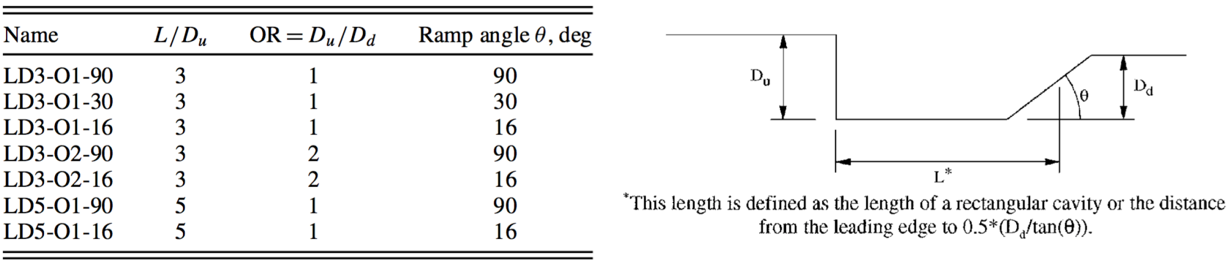

Name	L/D_u	$\mathrm{OR} = D_u/D_d$	Ramp angle θ, deg
LD3-O1-90	3	1	90
LD3-O1-30	3	1	30
LD3-O1-16	3	1	16
LD3-O2-90	3	2	90
LD3-O2-16	3	2	16
LD5-O1-90	5	1	90
LD5-O1-16	5	1	16

*This length is defined as the length of a rectangular cavity or the distance from the leading edge to $0.5^*(D_d/\tan(\theta))$.

Figure 1.5: Non reactive cavity cases [64].

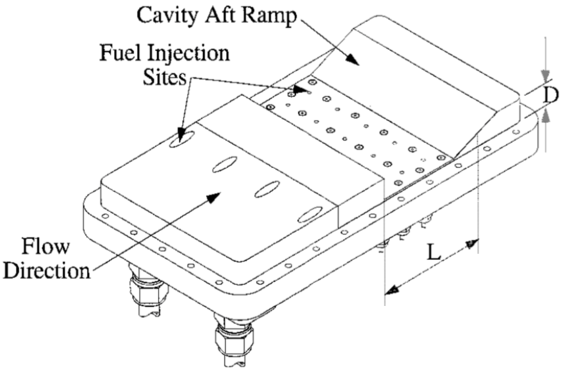

Figure 1.6: Schematic of the cavity with the injection sites [110].

dimensions were optimized from the non reactive case, its aspect ratio and ramp angle were respectively 4.8 and 22.5°. Few years later, Neely et al. [120] used the same set-up to investigate the consequence of hydrocarbon and hydrogen fuel equivalence ratios on the cavity-based flameholder.

After the previous experiments, an optimal configuration for the test section has emerged. Most reactive experiments carried out at the AFRL from 2004 are using the same test section, composed of an isolator directly connected to the Mach 2 facility nozzle and a divergent ramp, where the cavity is mounted (see Fig. 1.7). The dimensions are given in Tab. 1.1. The experiments were performed with a stagnation temperature of 589 K and a stagnation pressure of 483 kPa. Ethylene was used for the combustion and could be injected from multiple locations. Besides, spark plugs were installed in the cavity base to ensure the ignition of ethylene.

Using this facility, Gruber et al. [65] investigated the effect of fuel injection locations on mixing and combustion in a supersonic flow. Rasmussen et al. [137] examined the stability and the blowout limits of hydrocarbon-fueled flames with several injector locations. Hsu et al. [71] studied the impact

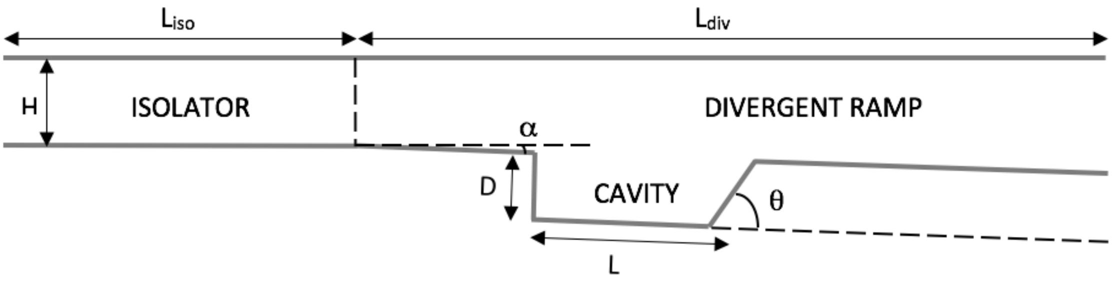

Figure 1.7: Schematic of AFRL supersonic wind tunnel.

Name	Symbol	Value
Cavity length	L	66 mm
Cavity depth	D	16.5 mm
Cavity angle	θ	22.5°
Tunnel width	W	152.4 mm
Isolator length	L_{iso}	177.8 mm
Isolator height	H	50.8 mm
Divergent length	L_{div}	740 mm
Divergent angle	α	2.5°

Table 1.1: AFRL supersonic wind tunnel dimensions.

of strut injectors near the cavity leading edge to investigate flame propagation and ignition of fuel in the combustor. Lin et al. [94] explored thermoacoustic instabilities inside an ethylene fueled scramjet. Grady et al. [62] performed non-reactive experiments using hydroxyl-tagging velocimetry (HTV) to measure the velocity inside the cavity, and to investigate the effect of a strut on the cavity recirculation. Tuttle et al. [164] used particle image velocimetry (PIV) to measure velocity and vorticity fields for non reactive and reactive cavities with different fuel flow rates. Later, Do et al. [38] continued with the case 2 of the experiments performed by Tuttle et al. [164] by using laser-induced breakdown spectroscopy (LIBS) to measure species concentrations and gas density.

1.2.2 Other experimental facilities

Nakaya et al. [119] performed supersonic combustion experiments in a cavity flameholder to investigate the behavior of both liquid and gaseous ethanol at Mach 2 and stagnation temperature between 1800 and 2400 K. The experiments were conducted using the installations of the University of Tokyo (see Fig. 1.8). The fuel was injected upstream and the cavity dimensions are shown in Fig. 1.9. Gaseous ethanol requires lower stagnation temperature for ignition than in liquid form. Besides, gaseous ethanol seems to be more reactive than ethane, bus less than ethylene. Nakaya et al. [119] concluded that cavities with upstream injections cannot hold flame since the fuel is not entering the cavity in that case, making it ineffective. They also provide instantaneous images of CH chemiluminescence for liquid ethanol at stagnation temperature of 2200 K and pressure distribution on the upper wall of their combustor.

Wang et al. [175] studied pressure and flame oscillations in cavity-based scramjets at the National University of Defense Technology based in Changsha, China. The experiments involved multiple cavities with aspect ratio $L/D = 4$ or 7 and ramp angle $\theta = 22.5°$, 45° or 90°. Hydrogen was injected upstream of the cavity leading edge and air was admitted through a Mach 2.5 nozzle. Considering these conditions, flame can be stabilized with longer cavities in the case of upstream injection. Higher ramp angle tends to display more intense flame oscillations but also shorter ignition distance, which suggests that moderate oscillations may be beneficial both to ignition and combustion.

Micka and Driscoll [115] conducted scramjet experiments at the University of Michigan to investigate ignition and combustion stabilization by the cavity flameholder (see Fig. 1.10). This cavity had an aspect ratio L/D of 4 and was not slanted at the back ($\theta = 90°$). Hydrogen was injected upstream of the cavity leading edge at several mass flow rates and air was admitted through a Mach 2.2 or 2.5 nozzle.

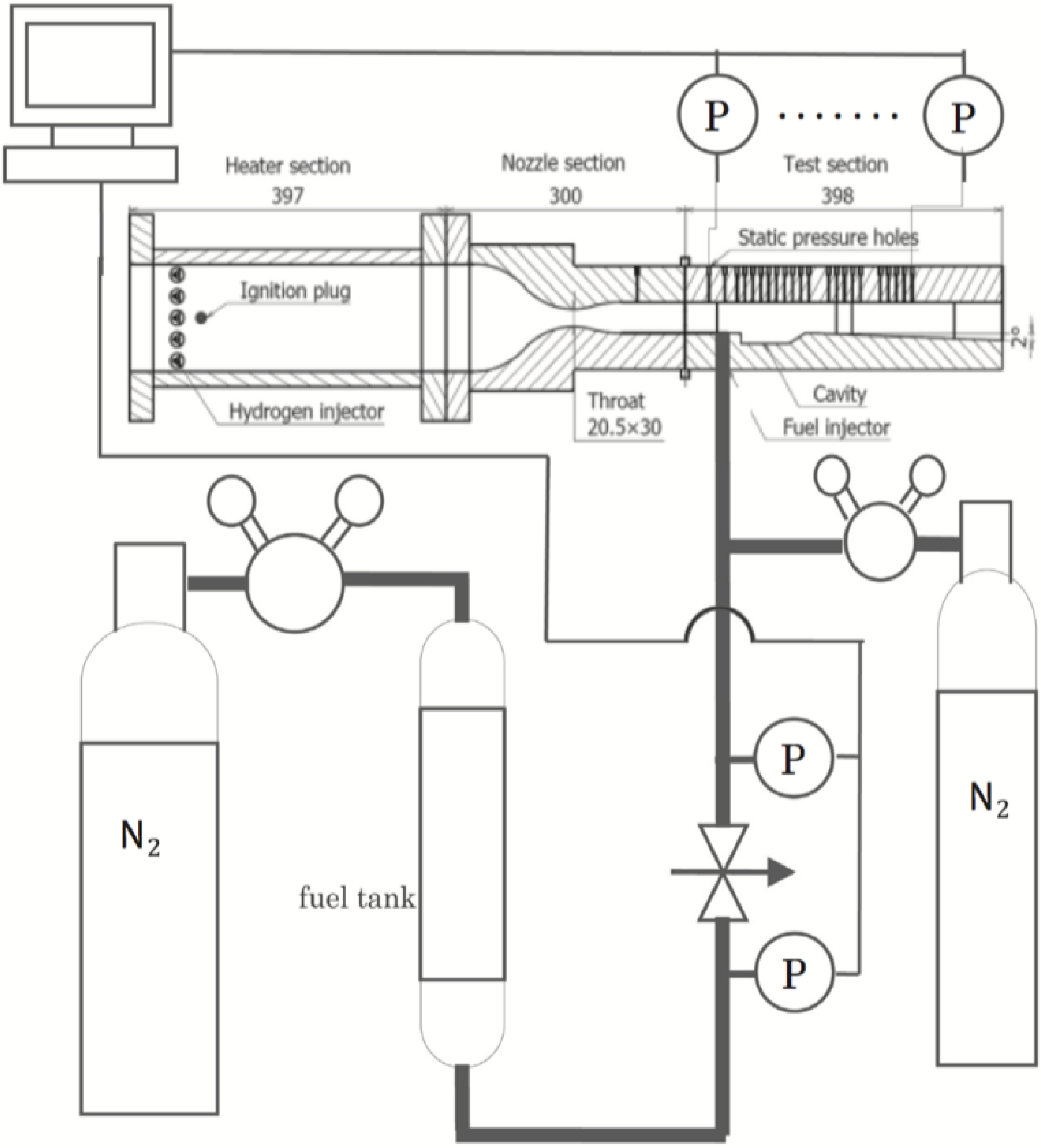

Figure 1.8: Supersonic wind tunnel of the University of Tokyo [119].

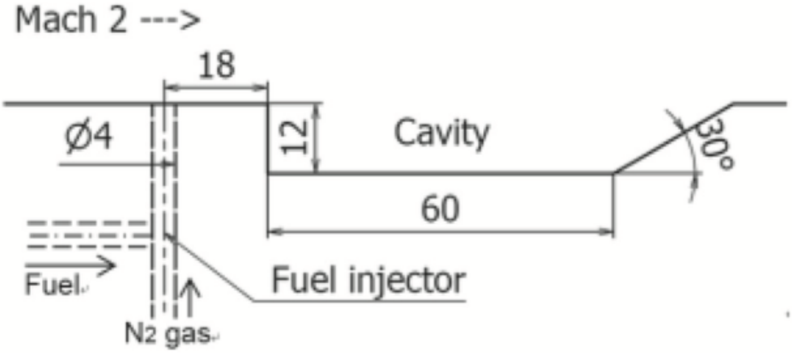

Figure 1.9: Schematic of the cavity used for experiments in [119].

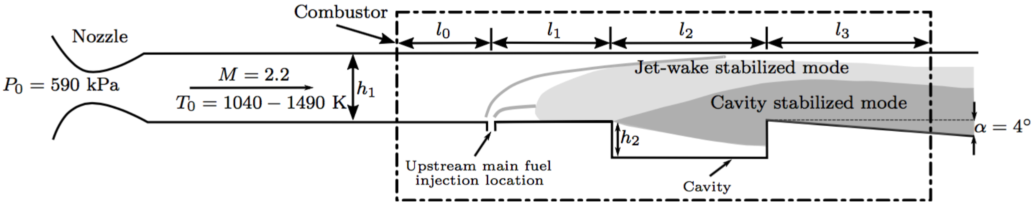

Figure 1.10: Schematic of the supersonic combustor of the University of Michigan [115].

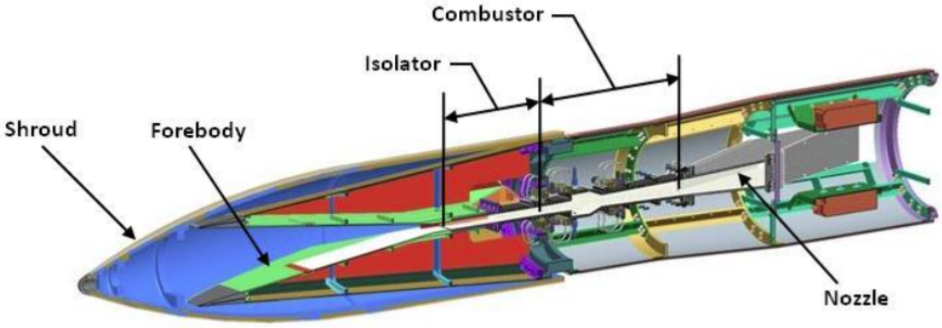

Figure 1.11: Schematic of HIFiRE Flight 2 [17].

1.2.3 The HIFiRE Program

The Hypersonic International Flight Research and Experimentation (HIFiRE) program was developed during 2005-2006 to draw up and resolve hypersonic flight issues. The HIFiRE program gathered the United States Air Force Research Lab (AFRL), the National Aeronautics and Space Administration (NASA) and the Australian Defence Science and Technology Organisation (DSTO). HIFiRE was intented to be a multiple-flight and economically efficient program, which accepts high technical risk to facilitate the collection of critical scientific data to help the development of future programs [147]. Among the several flights, the HIFiRE Flight 2 (HF2), which main role was to collect data of ramjet to scramjet transition using hydrocarbon fuel, was mounted with cavities as flameholder (Fig. 1.11).

The HIFiRE flowpath is similar to the AFRL configuration described in the previous section. Prior to the flight test, ground test was performed at the NASA Langley Arc-Heated Scramject Test Facility (AHSTF) with a direct-connect test rig (HDCR), which is nearly an exact copy of the HF2 [17]. The goals of the ground test were to verify the engine performance and operability through a ram to scram mode transition and to provide data to support analytical tools verification. Numerical simulations were also used to examine the validity of a one-dimensional combustor performance analysis tool and to provide input data for use in sensitivity and uncertainty analysis [63]. The HF2 was launched in 2012 and an overview of this program is shown in [74]. Wall pressure measurements are provided in the literature [17].

1.3 Numerical review

The following section is a review of numerical simulations focused on combustion in cavity-based scramjets. Those without cavity-stabilization are not in the scope of the present work. Due to the complexity of phenomena involved in the domain of supersonic combustion, few simulations exist in the literature, most of them are carried out using RANS approach.

The first cavity-based scramjet simulations were performed in 2001 by Gruber et al. [64] with the VULCAN (Viscous Upwind Algorithm for Complex Flow Analysis) solver [156] of NASA Langley Research Center, in the configuration of AFRL experimental facility. RANS approach was used along with the Wilcox $k - \omega$ model for turbulence. These simulations were non-reactive and had for objectives to investigate the impact of cavity geometry on the flow. Consequently, five cases by varying the cavity length-to-depth ratio L/D (3 and 5) and the cavity ramp angle (16, 30 and 90°) were carried out. Wall pressure of each case was compared to their own experiment, and results are displayed on Fig. 1.12. The previous study helped to find out the optimal cavity geometry that Gruber et al. [65] used for the reactive experiment performed in 2004.

Kim et al. [80] reproduced numerically the experiment performed by Gruber et al. [64] in 2004. After validating the non reactive case with the experimental data using RANS with an eddy viscosity model from Baldwin-Lomax [3], they simulated several reactive cases with various cavity aft angle (0, 15 30 and 60°) by injecting hydrogen (H_2), which chemical mechanism is taken from Evans and Schexnayder [50] (7 species and 8 reactions). Isocontours of some flow properties (Mach, pressure, temperature and mass fractions of H_2, OH and H_2O) are displayed and compared for cases with and without cavity. They computed three quantities to assess the performance of the combustor: combustion efficiency, mixing efficiency and pressure loss. They are respectively defined as:

$$\eta_c = \frac{\dot{m}_{f,0} - \dot{m}_f}{\dot{m}_{f,0}} \quad , \quad \eta_m = \frac{\int Y_R \rho U dA}{\int Y_F \rho U dA} \quad , \quad \eta_p = 1 - \frac{\int P \rho U dA}{\int P_0 \rho U dA} \tag{1.3.1}$$

where $\dot{m}_{f,0}$ is the mass flow rate of the fuel at the injector, $\dot{m}_f$ is the local mass flow rate of the fuel, P_0 is a reference pressure, Y_F is the fuel mass fraction and Y_R is defined as:

$$Y_R = \begin{cases} Y_F & \text{if} \quad Y_F \leq Y_{F,st} \\ Y_F \left(\dfrac{1 - Y_F}{1 - Y_{F,st}} \right) & \text{else} \end{cases} \tag{1.3.2}$$

with $Y_{F,st}$ the mass fraction of the fuel at stoichiometry. These quantites are displayed in Fig. 1.13. It is shown that the total pressure loss is higher in presence of cavity, and even higher when the cavity aft angle increases, but combustion and mixing are more efficient with cavity.

Liu et al. [99] performed in 2006 RANS simulations of the AFRL configuration with the VULCAN [156] code using ethylene as fuel. The cavity geometry is identical to the one in Gruber et al. 2004 [65] with the length-to-depth ratio $L/D = 4$ and the cavity aft angle $\theta = 22.5°$. The goal of the study was to highlight the importance of using an accurate chemical mechanism for the simulations. Three chemical kinetics were used: a 3-step global mechanism developed by researchers at AFRL [48], a 10-step quasi-global mechanism from Singh and Jachimowski [152] and a 15-step reduced kinetic mechanism from the author. The 3 and 10 step mechanisms failed to predict the flame stability since they were designed to match only the ignition time within a certain range of initial conditions. An investigation on the extinction residence time shows that this time is two orders of magnitude higher for the global and quasi-global mechanisms (see Fig. 1.14), going over the cavity residence time which is approximately 1 ms. The extinction residence time is defined as the minimum residence time to get strong flames [90, 149]. Stable combustion can then hardly be obtained with those mechanisms. On the other hand, using the 15-step mechanism could lead to a stable flame.

Lin et al. [95] investigated in 2009 experimentally and numerically the lean and rich blowout limits of the AFRL scramjet configuration with various cavity length-to-depth ratios (L/D = 4, 5 and 6). The simulations were still done with the VULCAN code [156] using the 19 species and 15 steps reduced kinetic scheme developed by Liu et al. [99]. It is observed that higher L/D leads to

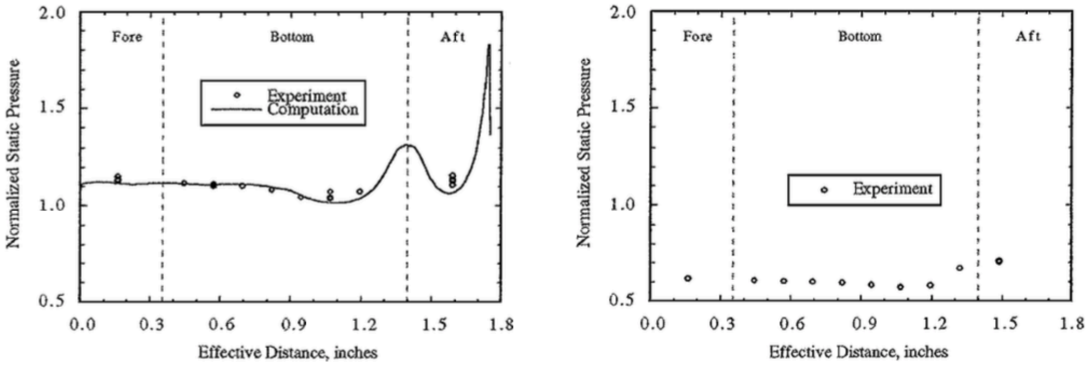

a) LD3-O1-90 **d) LD3-O2-90**

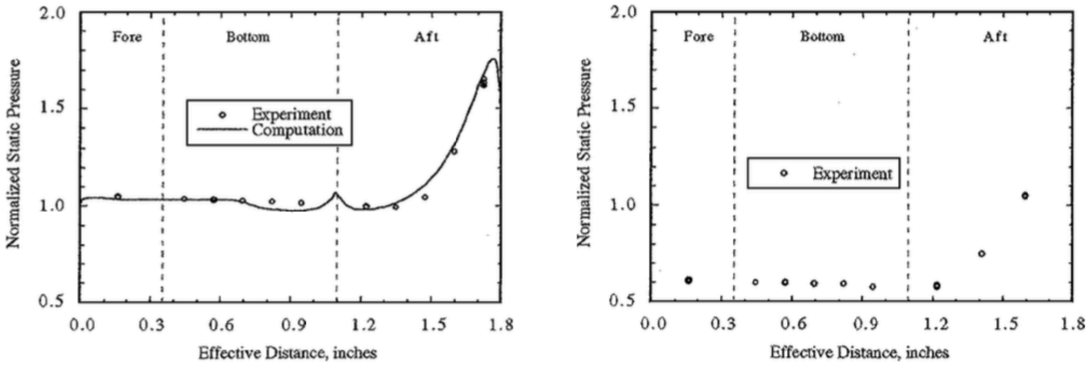

b) LD3-O1-30 **e) LD3-O2-16**

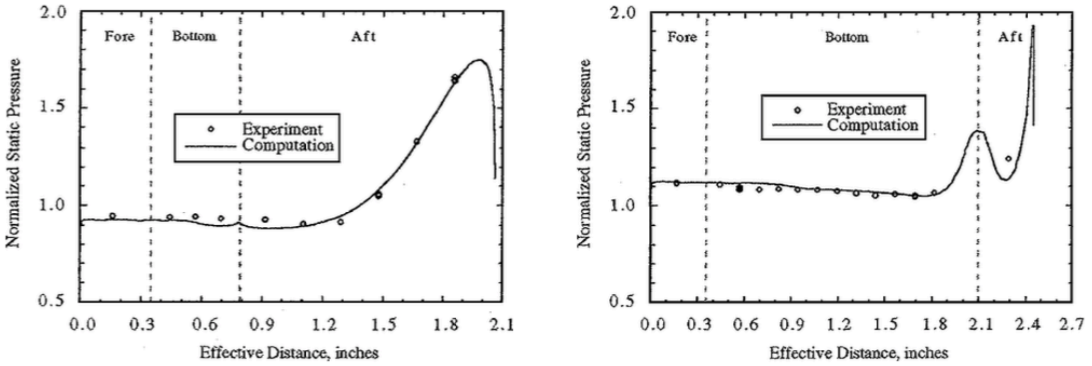

c) LD3-O1-16 **f) LD5-O1-90**

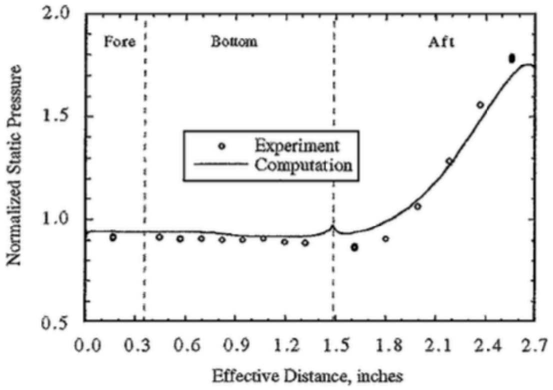

g) LD5-O1-16

Figure 1.12: Experimental and numerical wall static pressure distributions from [64]. LD is the cavity length-to-depth ratio, O stands for the offset which is defined as the ratio between the cavity front and rear depths and the last number is the cavity ramp angle.

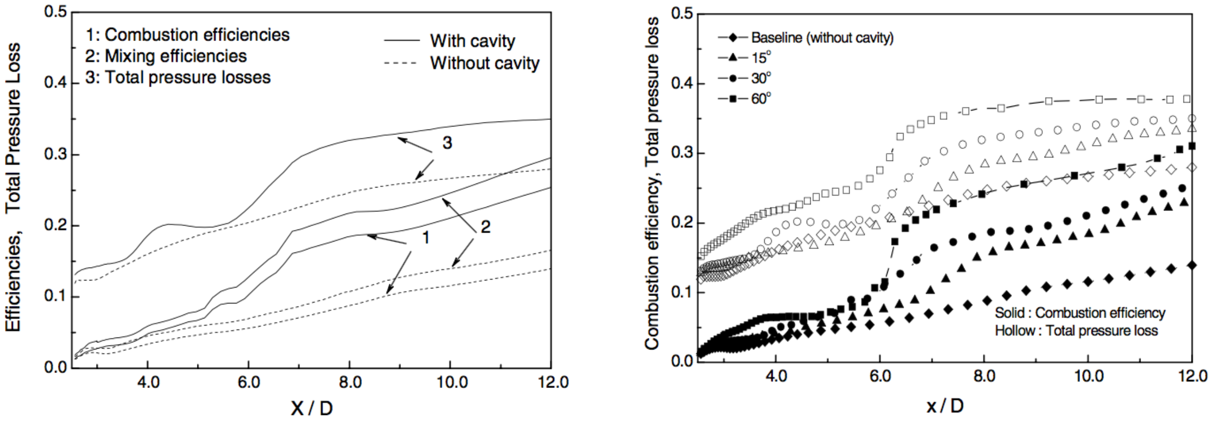

Figure 1.13: Combustion and mixing efficiencies and total pressure losses for the combustor with and without cavity (left). Combustion efficiency and total pressure loss for various cavity aft angles [80].

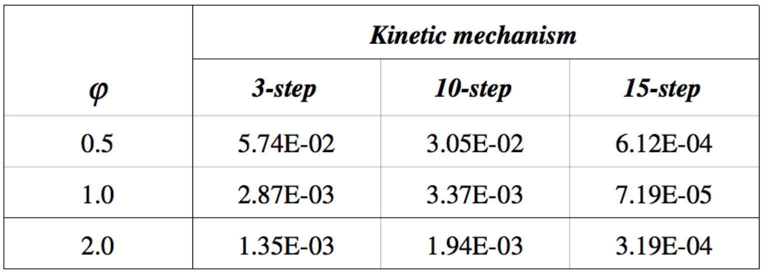

	Kinetic mechanism		
φ	3-step	10-step	15-step
0.5	5.74E-02	3.05E-02	6.12E-04
1.0	2.87E-03	3.37E-03	7.19E-05
2.0	1.35E-03	1.94E-03	3.19E-04

Figure 1.14: Comparison of extinction residence time (in seconds) for three kinetic mechanisms [99].

lower lean blowout limits but higher rich blowout limits, probably due to difference in cavity volume.

Grady et al. [62] performed in 2015 experimentally and numerically the AFRL scramjet configuration to investigate the presence of strut near the cavity leading on the flow. It was found that the installing of a strut could shift the shear layer impingement higher on the cavity ramp and increase the cavity recirculation.

Wang et al. [176] performed in 2015 simulations of the scramjet configuration of the Chinese National University of Defense Technology (CNUDT) [174] using hybrid RANS/LES approach. The fuel, hydrogen, is injected upstream of the cavity which dimensions are L/D = 7 and $\theta = 45°$. Turbulence and combustion are respectively modelled by a one-equation Spalart-Allmaras model [158] and an assumed PDF closure [174]. Hydrogen-air combustion is modelled by a 9 species and 19 steps detailed mechanism from Jachimowski [72]. Simulation is found to reproduce with fidelity the experiment.

During the same year, the HIFiRE direct-connect rig [17] has been reproduced numerically in LES by Saghafian et al. [144] using a compressible flamelet/progress variable approach to model turbulent combustion. The fuel is a JP-7 surrogate composed of 64% of ethylene and 36% of methane. The HIFiRE configuration has two sets of injectors, the primary injectors are located upstream of the cavity where 40% of the fuel is injected and 60% for the secondary injectors located downstream of the cavity. The compressible flamelet progress variable model is found to perform better than the existing flamelet models, generally designed for incompressible flows. A modified wall model taking into account viscous heating was compared to a case with traditional wall model and to a case without wall model (Fig. 1.15). Significant discrepancies were observed due to viscous heating increasing the wall temperature, thus enhancing combustion in that region.
The HIFiRE direct connect rig has also been simulated by Lacaze et al. [87] in 2017 using the RAPTOR code [123] to investigate the turbulence and mixing characteristics of supersonic flow with LES, and the combustion regimes involved in this configuration with the Takeno flame index [178].

Baurle [4] performed in 2017 non-reactive and reactive simulations with the VULCAN [156] code of the experiments carried out by Tuttle et al. [164] at AFRL. The non-reactive computation was done with a hybrid RANS/LES approach, while the reactive case was performed with RANS, due to the computational cost being too important. The fuel, ethylene, was modelled by a 22-species reduced kinetic scheme from [105]. The simulations were compared to the experiments for velocity profiles inside the cavity at four positions (Fig. 1.16). The streamwise velocity is well predicted, while important discrepancies is observed for transverse velocity.

Ribeiro et al. [139] performed in 2018 LES of the experiments conducted at the University of Michigan by Micka and Driscoll [115] with the solver CREAMS [109]. The eddy viscosity was expressed with the WALE model [43]. Immersed boundary method (IBM) was used to model the supersonic combustor. Hydrogen was modelled with a detailed mechanism of O'Conaire et al. [122] (9 species and 21 reactions). The simulations were found to be able to retrieve the two different stabilization modes dependent of the inlet air temperature that were observed in the experiments.

Recently, Hassan et al. [68] performed RANS/LES on the case 2 of the experiments carried out by Tuttle et al. [164]. Three different numerical approaches were used: dynamic hybrid RANS/LES (DHRL), steady and unsteady improved delayed detached eddy simulations (IDDLES and UIDDLES respectively) [151]. Ethylene was modelled with a 6 species 3 step mechanism. The simulations were compared to the experiment of Tuttle et al. [164] for velocity measurements inside the cavity (Fig. 1.17) and to the experiment of Do et al. [38] for species concentrations. DHRL and

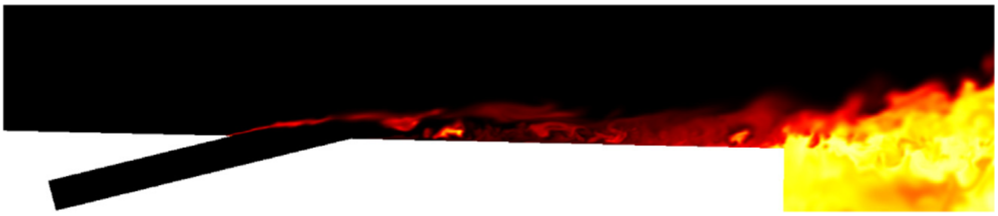

(a) with source term correction, with wall model

(b) without source term correction, with wall model

(c) with source term correction, without wall model

Figure 1.15: Contours of the progress variable from C = 0 (black) to C = 0.3 (white) [144]. (a) wall model with viscous heating, (b) wall model without viscous heating, and (c) no wall model.

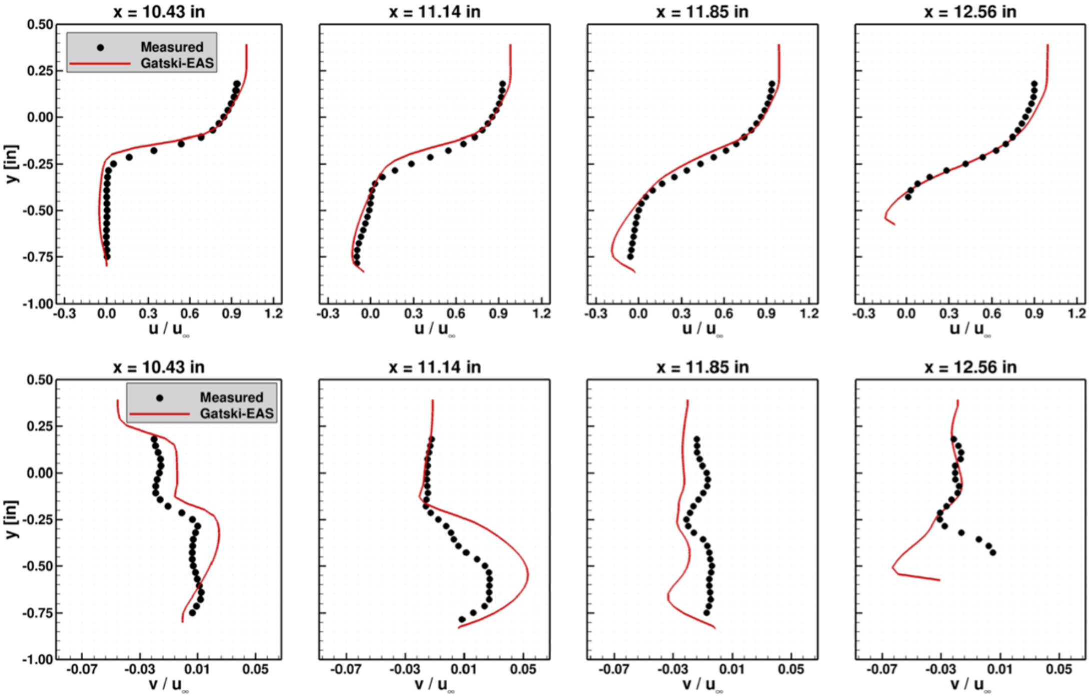

Figure 1.16: Comparison of averaged streamwise and transverse velocities between the reactive RANS performed by Baurle [4] and the experiments of Tuttle et al. [164] for the case 3 (fuel mass flow rate of 99 SLPM).

UIDDLES were found to have better performance than IDDLES. The streamwise velocity profiles show that there are some discrepancies between the simulation and the experiment at the mixing layer for the first profiles and near the bottom wall of the cavity for the last profiles, regardless of the numerical approach. Furthermore, the simulations are overpredicting the transverse velocity in the cavity.

All the numerical simulations presented above are gathered in table 1.2.

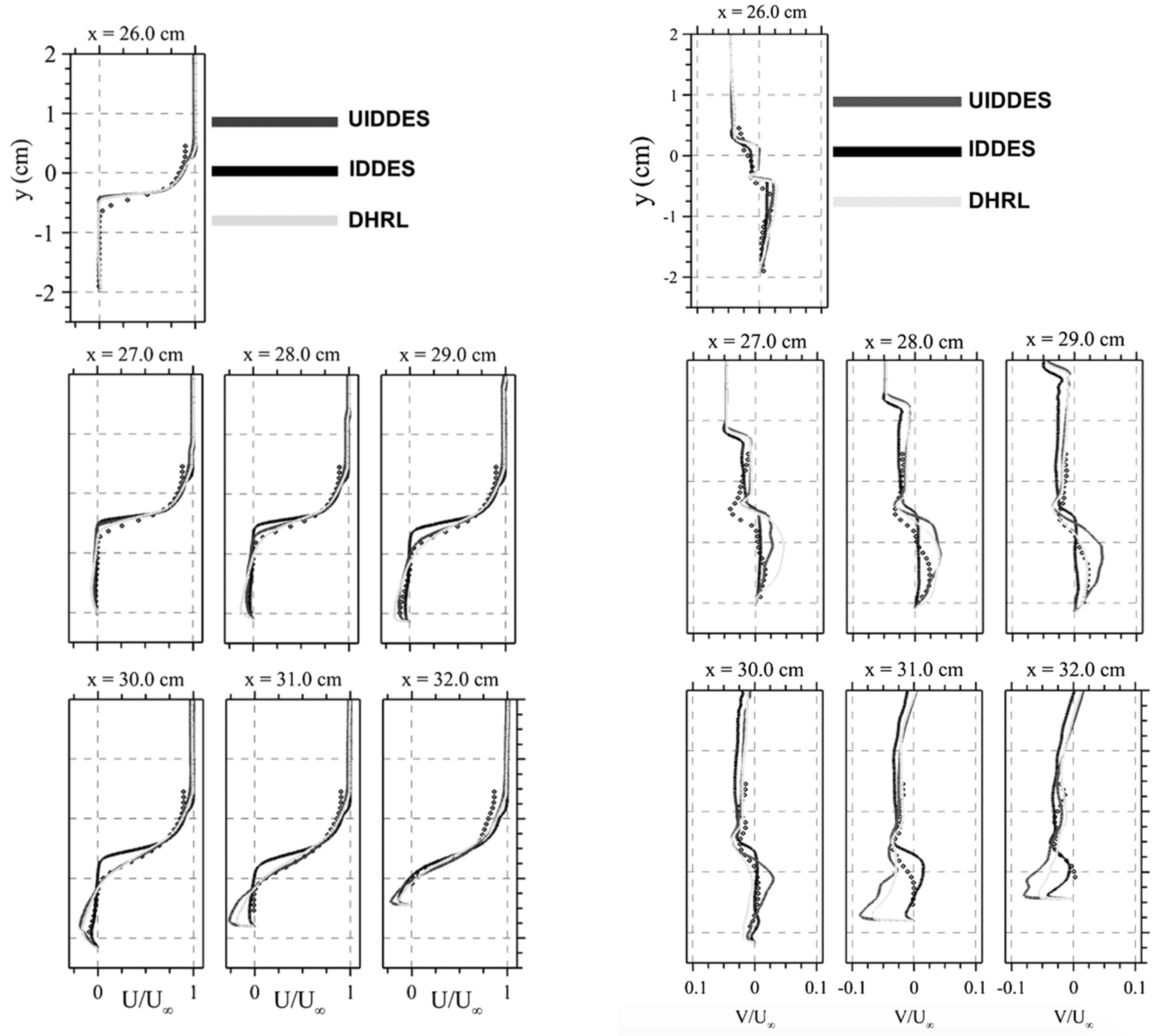

Figure 1.17: Comparison of averaged streamwise and transverse velocities between the reactive RANS/LES performed by Hassan et al. [68] and the experiments of Tuttle et al. [164] for the case 2 (fuel mass flow rate of 56 SLPM). The numerical approaches are dynamic hybrid RANS/LES (DHRL), steady and unsteady improved delayed detached eddy simulations (IDDLES and UIDDLES respectively).

Author	Fuel	Cavity	Approach	Configuration
Gruber et al. [64] 2001	Non reactive	L/D : 3, 5 $\theta : 16, 30, 90°$	RANS	AFRL
Kim et al. [80] 2004	Hydrogen, 7 species 8 reactions	L/D : 3, 5 $\theta : 30°$	RANS	AFRL
Liu et al. [99] 2006	Ethylene, 19 species 15 reactions	L/D : 4 $\theta : 22.5°$	RANS	AFRL
Lin et al. [95] 2009	Ethylene, 19 species 15 reactions	L/D : 4, 5, 6	RANS	AFRL
Grady et al. [62] 2012	Non reactive	L/D : 4 $\theta : 22.5°$	LES	AFRL
Wang et al. [176] 2015	Hydrogen, 9 species 19 reactions	L/D : 7 $\theta : 45°$	RANS/LES	CNUDT
Saghafian et al. [144] 2015	JP-7 surrogate (0.64 Ethylene, 0.36 Methane)		LES	HIFiRE
Lacaze et al. [87] 2017	JP-7 surrogate (0.64 Ethylene, 0.36 Methane)		LES	HIFiRE
Baurle [4] 2017	Ethylene, 22 species 206 reactions	L/D : 4 $\theta : 22.5°$	RANS	AFRL
Ribeiro et al. [139] 2018	Hydrogen, 9 species 21 reactions	L/D : 4 $\theta : 90°$	LES	Michigan
Hassan et al. [68] 2019	Ethylene, 22 species 206 reactions	L/D : 4 $\theta : 22.5°$	RANS/LES	AFRL

Table 1.2: Review of numerical simulations featuring cavity-based scramjets.

1.4 Objectives and outline

1.4.1 Objectives

Experiments of scramjet are actually very difficult to carry out because of the difficulties related to safety and the cost of doing such an experiment. Moreover, even when an experiment is possible, it is challenging to perform measurements in supersonic reacting flows and understand all the physics behind. The existing techniques are very limited, most experimental data provided are wall pressures or information about combustion stability, the access to other physical quantities such as velocity or temperature fields is not straightforward.

In order to have a better understanding of the involved physical phenomena, it is necessary to develop predictive tools capable of reproducing the complexity of this flow, which combines highly compressible turbulent flows with finite rate chemistry effects. The acquired knowledge will help in the development of future scramjets. However, as shown previously, the existing literature is scarce or restricted, and the vast majority of computational work in cavity-based scramjet was performed in Reynolds- averaged Navier-Stokes (RANS) framework then relying heavily on modeling assumptions. Due to the increase in high performance computing, the use of Large-Eddy Simulation (LES)

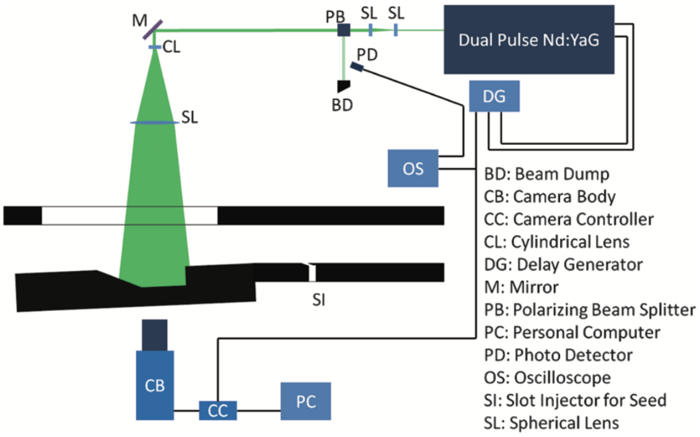

Figure 1.18: Diagram of the optical setup used in the experiments performed by Tuttle et al. [164].

for supersonic combustion is now becoming relevant, as was very recently achieved in [144, 87] for the HIFiRE test-bench.

The objectives of the present study are twofold: first, contribute to the evaluation of the LES framework to predict compressible multi-species reacting flows; and second, provide some fundamental insights of cavity-based scramjet physics, such as mixing and combustion stabilization. Experiments conducted at the US Air Force Research Laboratory (AFRL) by Tuttle et al. [164] will support this goal, since they provide, additionally to the wall pressure, velocity measurements inside the cavity. This experimental facility has already been reproduced numerically in hybrid RANS/LES for non-reactive flow and RANS for reactive flow by Baurle [4] using the code VULCAN of the NASA Langley Research Center [156]. Large eddy simulations in this thesis are performed with the CORIA inhouse code SiTCom-B that is presented in chapter 3.

1.4.2 Outline

The current work is organized as follow:

Chapter 2 - Equations of aerothermochemistry
Some basic thermodynamic properties and Navier-Stokes equations for reacting flows are presented in this chapter. Turbulent combustion is also briefly introducted.

Chapter 3 - LES: filtered equations and model descriptions as resolved in LES
The filtered Navier-Stokes equations, as well as the unclosed terms modelling are displayed. Particular attention is paid to the modelisation of turbulent combustion, followed by a quick presentation of wall-layer model for LES. Finally, a description of the code SiTCom-B is given, with a focus on the immersed boundary method (IBM).

Chapter 4 - Large eddy simulation of supersonic airflow
The design of cavity-based scramjet is first discussed in this chapter, followed by the description of experimental and numerical set-ups. After studying the impact of the grids, results of non reacting flows are presented for one and two injectors cases. The impact of HIT and wall modeling is also investigated.

Chapter 5 - Large eddy simulation of supersonic combustion
This chapter displays reacting flow results. The fuel, ethylene, and its chemical mechanisms are first

presented. The reacting flow simulations have been performed with one, two and eleven injectors for a fuel mass flow rate that leads to stable combustion inside the cavity. The one injector case has also been investigated for two other fuel mass rates: a lean fuel loading that gives unstable combustion to understand the flame blowoff phenomenon in that case, and a medium fuel loading to compare the flame stabilization process with the previous stable case.

Chapter 6 - Analysis of flame structures
The validity of quasi-laminar model employed in this thesis for the reactive simulations is first discussed. The flame topology is then extracted. The velocity found in the reactive areas (supersonic or subsonic) is studied, followed by the identification of flame regimes with the Takeno flame index. A detailed study on the cavity residence time is done in this chapter to have a better understanding on the mixing and combustion in such a configuration. The last section of this chapter is dedicated to a priori comparisons with a tabulated chemistry approach based on one dimensional premixed flamelets.

Chapter 7 - Conclusions and perspectives

Chapter 2

Equations of aerothermochemistry

Contents

This chapter is dedicated to the governing equations for reacting flows, which differ from the usual Navier-Stokes equations by the number of species involved. While the latter requires only one equation of mass conservation, the multiple species need as many equations as the number of species involved. Therefore, the multi-species approach has to be defined before presenting the equations.

2.1 Description of the mixture

2.1.1 Composition of a mixture

A mixture of N_{sp} species is caracterized by its total density ρ defined as the ratio between its mass m and the volume that the mixture occupies V:

$$\rho = \frac{m}{V} \tag{2.1.1}$$

A partial density ρ_k, weighted by the contribution of the species k to the total density, can be defined for each species composing the mixture:

$$\rho_k = \rho Y_k \tag{2.1.2}$$

where Y_k is the mass fraction of the species k defined as follow:

$$Y_k = \frac{m_k}{m} \tag{2.1.3}$$

One will naturally get:

$$\sum_{k=1}^{N_{sp}} Y_k = 1 \quad \text{and} \quad \sum_{k=1}^{N_{sp}} \rho_k = \rho \tag{2.1.4}$$

Other variables exist to describe a mixture, such as the mole fraction X_k or the molar concentration $[X_k]$. The mole fraction is the ratio between the number of moles n_k of the species k and the total number of moles n of the mixture contained in the volume V:

$$X_k = \frac{n_k}{n} \tag{2.1.5}$$

On the other hand, the molar concentration of the species k is the number of moles of the species in the volume V:

$$[X_k] = \frac{n_k}{V} \tag{2.1.6}$$

The previous molar quantities can easily be linked to the mass fraction:

$$\begin{cases} X_k = \dfrac{W}{W_k} Y_k \\ [X_k] = \rho \dfrac{Y_k}{W_k} \end{cases} \tag{2.1.7}$$

where W_k and W are respectively the molar mass of the species k and the molar mass of the mixture defined as:

$$W = \sum_{k=1}^{N_{sp}} X_k W_k \tag{2.1.8}$$

or in terms of mass fraction:

$$\frac{1}{W} = \sum_{k=1}^{N_{sp}} \frac{Y_k}{W_k} \tag{2.1.9}$$

2.1.2 Stoichiometry of a mixture

During a combustion process, the equivalence ratio ϕ is used to identify whether a fuel-oxidizer mixture is rich, stoichiometric or lean. In the context of premixed flames, ϕ is defined as:

$$\phi = s \frac{Y_F}{Y_O} \tag{2.1.10}$$

where Y_F and Y_O are respectively the mass fraction of the fuel and the oxidizer, and s is the stoichiometric ratio defined for Y_F and Y_O at stoichiometry:

$$s = \left(\frac{Y_O}{Y_F} \right)_{st} \tag{2.1.11}$$

One gets $\phi = 1$ for the stoichiometric mixture, and the combustion regime is called rich when the ratio fuel/oxidizer is higher than the stoichiometry ratio, which means $\phi > 1$, and lean otherwise ($\phi < 1$).

While the equivalence ratio can be easily defined in premixed flames where fresh and burnt gas are clearly separated, it is not true in diffusion flames or in reaction or past reaction zones. For a diffusion flame with two or more inlets, a global equivalence ratio ϕ_g is introduced to describe the regime:

$$\phi_g = s\frac{\dot{m}_F^1}{\dot{m}_O^2} \tag{2.1.12}$$

where $\dot{m}_F^1$ and $\dot{m}_O^2$ are respectively the mass flow rates of fuel in the first inlet and oxidant in the second inlet.

The mixture fraction Z is a passive scalar which changes only because of convection and diffusion, independently of combustion. Z can be computed locally using the mass fraction of species. In diffusion flames with two separate inlets, the mixture fraction can be expressed as:

$$Z = \frac{sY_F - Y_O + Y_{O,2}}{sY_{F,1} + Y_{O,2}} \tag{2.1.13}$$

where Y_F and Y_O are the mass fractions of fuel and oxidizer, and the subscripts 1 and 2 respectively refer to pure fuel and oxidizer injection streams. The stoichiometric mixture fraction Z_{st} is obtained when all the fuel and oxidizer are consumed $Y_F = Y_O = 0$, which leads to:

$$Z_{st} = \frac{Y_{O,2}}{sY_{F,1} + Y_{O,2}} = \frac{1}{1 + s\dfrac{Y_{F,1}}{Y_{O,2}}} \tag{2.1.14}$$

However, Eq. 2.1.13 is badly fitted for detailed chemistry approach. The definition proposed by Bilger et al. [8], which involves all species, is then used in this work:

$$Z = \frac{2(Y_C - Y_{C,2})/W_C + (Y_H - Y_{H,2})/(2W_H) - (Y_O - Y_{O,2})/W_O}{2(Y_{C,1} - Y_{C,2})/W_C + (Y_{H,1} - Y_{H,2})/(2W_H) - (Y_{O,1} - Y_{O,2})/W_O} \tag{2.1.15}$$

where W_X and Y_X are the molar mass and the mass fraction of the chemical element $X \in \{C, H, O\}$ respectively, and Y_X is defined as:

$$Y_X = \sum_{k=1}^{N_{sp}} \frac{n_{X,k} W_X}{W_k} Y_k \tag{2.1.16}$$

with $n_{X,k}$ the number of atoms of element X in the species k, W_k the molar mass of the species k and Y_k the mass fraction of the species k. The subscripts 1 and 2 correspond to the fuel and oxidizer streams respectively. The stoichiometric value Z_{st} is defined as:

$$Z_{st} = \frac{Y_{O,2}/W_O}{2(Y_{C,1} - Y_{C,2})/W_C + (Y_{H,1} - Y_{H,2})/(2W_H) - (Y_{O,1} - Y_{O,2})/W_O} \tag{2.1.17}$$

Eq. 2.1.17 is equivalent to Eq. 2.1.14 when the fuel and oxizider streams are not diluted. The local equivalence ratio can be linked to the mixture fraction according to:

$$\phi = \frac{Z}{1-Z}\frac{1-Z_{st}}{Z_{st}} \tag{2.1.18}$$

2.1.3 Thermodynamics of a mixture

The heat capacities at constant pressure, C_p, or constant volume, C_v, of a mixture can be constructed from the partial heat capacities of each species just as the total density:

$$C_p = \sum_{k=1}^{N_{sp}} C_{pk} Y_k \quad \text{and} \quad C_v = \sum_{k=1}^{N_{sp}} C_{vk} Y_k \quad , \tag{2.1.19}$$

where C_{pk} and C_{vk} are the heat capacities of species k at a given temperature. Their values are tabulated using polynomial functions of temperature [79]. The ratio of C_p into C_v gives the isentropic expansion factor γ:

$$\gamma = \frac{C_p}{C_v} \tag{2.1.20}$$

The energy e and the enthalpy h of the mixture can be defined in the same way:

$$e = \sum_{k=1}^{N_{sp}} e_k Y_k \quad , \quad h = \sum_{k=1}^{N_{sp}} h_k Y_k \tag{2.1.21}$$

where e_k and h_k are the energy and enthalpy of the species k, and can be decomposed into a sensible term (e_{sk} and h_{sk}) and a chemical term (formation enthalpies $\Delta h^0_{f,k}$):

$$\begin{cases} e_k = e_{sk} + \Delta h^0_{f,k} = \displaystyle\int_{T_0}^{T} C_{vk} dT - \frac{R T_0}{W_k} + \Delta h^0_{f,k} \\ h_k = h_{sk} + \Delta h^0_{f,k} = \displaystyle\int_{T_0}^{T} C_{pk} dT + \Delta h^0_{f,k} \end{cases} \tag{2.1.22}$$

The superscrit or subscript 0 refers to the standard reference state used for tabulation, and corresponds here to a temperature $T_0 = 298.15$ K.
Combining Eqs. 2.1.21 and 2.1.22 and reversing the sum and the integral ($\sum \int = \int \sum$), one gets:

$$\begin{cases} e = \displaystyle\int_{T_0}^{T} C_v dT - \frac{R T_0}{W} + \sum_{k=1}^{N_{sp}} \Delta h^0_{f,k} Y_k \\ h = \displaystyle\int_{T_0}^{T} C_p dT + \sum_{k=1}^{N_{sp}} \Delta h^0_{f,k} Y_k \end{cases} \tag{2.1.23}$$

The total energy e_t and enthalpy h_t are obtained by adding the kinetic energy $e_c = \frac{1}{2} u_i u_i$ to e or h:

$$\begin{cases} e_t = e + e_c \\ h_t = h + e_c \end{cases} \tag{2.1.24}$$

2.1.4 Definition of reaction rate

Considering a system of N_{sp} species and N_R elementary reactions:

$$\sum_{k=1}^{N_{sp}} \nu'_{kj} \mathcal{M}_k \rightleftharpoons \sum_{k=1}^{N_{sp}} \nu''_{kj} \mathcal{M}_k \quad \text{for } j = 1, N_R \tag{2.1.25}$$

where $\mathcal{M}_k$ is the species k, ν'_{kj} and ν''_{kj} are the molar stoichiometric coefficients of species k in reaction j. Defining $\nu_{kj} = \nu''_{kj} - \nu'_{kj}$, mass conservation implies:

$$\forall j \in [\![1, N_R]\!] \quad \sum_{k=1}^{N_{sp}} \nu_{kj} W_k = 0 \tag{2.1.26}$$

For each species k, a partial reaction rate $\dot{\omega}_{kj}$ can be defined for each reaction j, and the sum of $\dot{\omega}_{kj}$ on all reactions gives the reaction rate $\dot{\omega}_k$ of the species k:

$$\dot{\omega}_k = \sum_{j=1}^{N_R} \dot{\omega}_{kj} = W_k \sum_{j=1}^{N_R} \nu_{kj} \mathcal{Q}_j \tag{2.1.27}$$

where $\mathcal{Q}_j$ is the progress rate of reaction j defined as:

$$\mathcal{Q}_j = K_{fj} \prod_{k=1}^{N_{sp}} [X_k]^{\nu'_{kj}} - K_{rj} \prod_{k=1}^{N_{sp}} [X_k]^{\nu''_{kj}} \tag{2.1.28}$$

with K_{fj} and K_{rj} respectively the forward and reverse rates of reaction j. They are usually modeled using the Arrhenius law:

$$K_{fj} = A_{fj} T^{\beta_j} \exp\left(-\frac{T_{aj}}{T}\right) \tag{2.1.29}$$

where A_{fj} is the preexponential constant, β_j the temperature exponent and T_{aj} the activation temperature of reaction j. The reverse constant K_{rj} can be computed from K_{fj} [135].

2.1.5 Equation of state

In the present work, fluids are assumed to be perfect gases, thus following the perfect gas equation of state (EoS):

$$p = \rho r T \tag{2.1.30}$$

where p and T are the pressure and the temperature of the gas, and r the specific perfect gas constant defined as:

$$r = \frac{R}{W} \tag{2.1.31}$$

with $R = 8.3144621$ J.K^{-1}.mol^{-1} the universal perfect gas constant.

2.2 Navier-Stokes equations

2.2.1 Conservation of momentum

The equation of momentum in the direction j is:

$$\frac{\partial}{\partial t}\rho u_j + \frac{\partial}{\partial x_i}\rho u_i u_j = \frac{\partial \sigma_{ij}}{\partial x_i} + \rho \sum_{k=1}^{N_{sp}} Y_k f_{k,j} \tag{2.2.1}$$

where σ_{ij} is the stress tensor, defined as:

$$\sigma_{ij} = \tau_{ij} - p\delta_{ij} \tag{2.2.2}$$

with δ_{ij} the Kronecker symbol ($\delta_{ij} = 1$ if $i = j$ and 0 otherwise), and τ_{ij} the viscous tensor defined as follow :

$$\tau_{ij} = 2\mu \left[S_{ij} - \frac{1}{3} S_{kk} \delta_{ij}\right] \tag{2.2.3}$$

where μ is the dynamic viscosity of the fluid and S_{ij} and S_{kk} are respectively the strain tensor and its trace ($S_{kk} = Tr(S_{ij})$):

$$S_{ij} = \frac{1}{2}\left(\frac{\partial u_i}{\partial x_j} + \frac{\partial u_j}{\partial x_i}\right) \tag{2.2.4}$$

$f_{k,j}$ is the volume force acting on species k in direction j. Thereafter, no volumic force is assumed to act on the flows, thus $f_{k,j} = 0$ for any species k in any direction j. Considering all the assumptions, Eq. 2.2.1 can be recast as :

$$\begin{aligned} \frac{\partial}{\partial t}\rho u_j + \frac{\partial}{\partial x_i}\rho u_i u_j &= -\frac{\partial p}{\partial x_j} + \frac{\partial \tau_{ij}}{\partial x_i} \\ &= -\frac{\partial p}{\partial x_j} + \frac{\partial}{\partial x_i}\left[\mu\left(\frac{\partial u_i}{\partial x_j} + \frac{\partial u_j}{\partial x_i} - \frac{2}{3}\frac{\partial u_k}{\partial x_k}\delta_{ij}\right)\right] \end{aligned} \tag{2.2.5}$$

2.2.2 Conservation of mass and species

The total mass conservation equation is:

$$\frac{\partial \rho}{\partial t} + \frac{\partial \rho u_i}{\partial x_i} = 0 \tag{2.2.6}$$

The mass of each species k is conserved during a chemical reaction, and follows:

$$\frac{\partial \rho Y_k}{\partial t} + \frac{\partial}{\partial x_i}\left[\rho\left(u_i + V_{k,i}\right)Y_k\right] = \dot{\omega}_k \tag{2.2.7}$$

where $V_{k,i}$ is the diffusion velocity V_k of the species k in the direction i and $\dot{\omega}_k$ is the reaction rate of species k, due to production or consumption of this species. $V_{k,i}$ and $\dot{\omega}_k$ must verify the following equations to recover the mass balance equation:

$$\sum_{k=1}^{N_{sp}} V_{k,i}Y_k = 0 \quad , \quad \sum_{k=1}^{N_{sp}} \dot{\omega}_k = 0 \quad . \tag{2.2.8}$$

The diffusion velocity is due to mass fraction gradient, temperature gradient (Soret effect) and pressure gradient (baro-diffusive effect). In the present work, only mass fraction gradient is retained to model the diffusion velocity. For multicomponent gas mixtures, V_k is usually modelled by Hirschfelder and Curtiss approximation [70]:

$$V_k X_k = -D_k \nabla X_k \quad \text{with} \quad D_k = \frac{1 - Y_k}{\sum_{j\neq k}\dfrac{X_j}{D_{j,k}}} \tag{2.2.9}$$

where D_k is an equivalent diffusion coefficient of species k into the mixture, defined with all the binary diffusion coefficients D_{kj} of species k to the rest of the species j. The diffusion velocity in the balance equation is therefore :

$$V_{k,i}Y_k = V_{k,i}X_k\frac{W_k}{W} = -D_k\frac{W_k}{W}\frac{\partial X_k}{\partial x_i} \tag{2.2.10}$$

and Eq. 2.2.7 becomes :

$$\frac{\partial \rho Y_k}{\partial t} + \frac{\partial}{\partial x_i}\left(\rho u_i Y_k\right) = \frac{\partial}{\partial x_i}\left(\rho D_k\frac{W_k}{W}\frac{\partial X_k}{\partial x_i}\right) + \dot{\omega}_k \tag{2.2.11}$$

Summing Eq. 2.2.11 on k, one gets:

$$\frac{\partial \rho}{\partial t} + \frac{\partial \rho u_i}{\partial x_i} = \frac{\partial}{\partial x_i}\left(\rho \sum_{k=1}^{N_{sp}} D_k \frac{W_k}{W}\frac{\partial X_k}{\partial x_i}\right) \tag{2.2.12}$$

The rhs term is a priori not equal to 0, the mass is thus not conserved with this approximation. A correction velocity $V_{c,i}$ is added to ensure mass balance [135]:

$$V_{k,i}X_k = -D_k\frac{\partial X_k}{\partial x_i} + V_{c,i}X_k \quad \text{with} \quad V_{c,i} = \sum_{k=1}^{N_{sp}} D_k \frac{W_k}{W}\frac{\partial X_k}{\partial x_i} \tag{2.2.13}$$

The species balance equation becomes:

$$\frac{\partial \rho Y_k}{\partial t} + \frac{\partial}{\partial x_i}\left(\rho u_i Y_k\right) = \frac{\partial}{\partial x_i}\left(\rho D_k \frac{W_k}{W}\frac{\partial X_k}{\partial x_i} - \rho V_{c,i} Y_k\right) + \dot{\omega}_k \tag{2.2.14}$$

In the special case where all the species diffusion coefficients are equal to D, the Hirschfelder and Curtiss approximation along with velocity correction leads to Fick's law:

$$V_k Y_k = -D\nabla Y_k \tag{2.2.15}$$

The species balance equation can be simplified into:

$$\frac{\partial \rho Y_k}{\partial t} + \frac{\partial}{\partial x_i}\left(\rho u_i Y_k\right) = \frac{\partial}{\partial x_i}\left(\rho D \frac{\partial Y_k}{\partial x_i}\right) + \dot{\omega}_k \tag{2.2.16}$$

2.2.3 Conservation of energy

The conservation equation for the total energy e_t is:

$$\frac{\partial \rho e_t}{\partial t} + \frac{\partial}{\partial x_i}\left(\rho u_i e_t\right) = -\frac{\partial q_i}{\partial x_i} + \frac{\partial}{\partial x_j}\left(\sigma_{ij} u_i\right) + \dot{\mathcal{Q}} + \rho \sum_{k=1}^{N_{sp}} Y_k f_{k,i}(u_i + V_{k,i}) \tag{2.2.17}$$

where q_i is the energy flux in the i-th direction, neglecting heat flux due to species mass fraction gradients (Dufour effect), the energy flux is formed by a heat diffusion term from the Fourier's law with thermal conductivity λ and a species diffusion term:

$$q_i = -\lambda \frac{\partial T}{\partial x_i} + \rho \sum_{k=1}^{N_{sp}} h_k Y_k V_{k,i} \tag{2.2.18}$$

$\dot{\mathcal{Q}}$ is the heat source term due to external effets (sparks, laser) or radiative flux, and is neglected in the current study. As for the conservation of momentum, volumic forces $f_{k,i}$ are neglected. The total energy equation thus becomes:

$$\frac{\partial \rho e_t}{\partial t} + \frac{\partial}{\partial x_i}\left(\rho u_i e_t\right) = \frac{\partial}{\partial x_i}\left(\lambda \frac{\partial T}{\partial x_i}\right) - \frac{\partial}{\partial x_i}\left(\rho \sum_{k=1}^{N_{sp}} h_k Y_k V_{k,i}\right) + \frac{\partial}{\partial x_j}\left(\sigma_{ij} u_i\right) \tag{2.2.19}$$

The chemical reactions are contained implicitly in the expression of the total energy, therefore the heat release term is not present in the conservation equation. The total non chemical energy E is defined to separate the chemistry from e_t:

$$E = e_t - \sum_{k=1}^{N_{sp}} \Delta h^0_{f,k} Y_k \tag{2.2.20}$$

The total non chemical energy conservation equation is:

$$\frac{\partial \rho E}{\partial t} + \frac{\partial}{\partial x_i}\left(\rho u_i E\right) = \frac{\partial}{\partial x_i}\left(\lambda \frac{\partial T}{\partial x_i}\right) - \frac{\partial}{\partial x_i}\left(\rho \sum_{k=1}^{N_{sp}} h_{s,k} Y_k V_{k,i}\right) + \frac{\partial}{\partial x_j}\left(\sigma_{ij} u_i\right) + \dot{\omega}_T \tag{2.2.21}$$

where the additional term $\dot{\omega}_T$ is the heat release due to combustion:

$$\dot{\omega}_T = -\sum_{k=1}^{N_{sp}} \Delta h^0_{f,k} \dot{\omega}_k \tag{2.2.22}$$

The energy balance equation can also be expressed in terms of total non chemical enthalpy $H = E + p/\rho$:

$$\frac{\partial \rho H}{\partial t} + \frac{\partial}{\partial x_i}\left(\rho u_i H\right) = \frac{\partial p}{\partial t} + \frac{\partial}{\partial x_i}\left(\lambda \frac{\partial T}{\partial x_i}\right) - \frac{\partial}{\partial x_i}\left(\rho \sum_{k=1}^{N_{sp}} h_{s,k} Y_k V_{k,i}\right) + \frac{\partial}{\partial x_j}\left(\tau_{ij} u_i\right) + \dot{\omega}_T \tag{2.2.23}$$

2.3 Comparison of transport phenomena

Transport phenomena are compared through dimensionless numbers. The Lewis number Le_k compares thermal diffusion to molecular diffusion of species k:

$$Le_k = \frac{D_{th}}{D_k} \tag{2.3.1}$$

where D_{th} is the thermal diffusivity, defined as:

$$D_{th} = \frac{\lambda}{\rho C_p} \tag{2.3.2}$$

The Prandtl number Pr is the ratio of momentum diffusivity to thermal diffusivity:

$$Pr = \frac{\nu}{D_{th}} \tag{2.3.3}$$

And finally, the Schmidt number Sc_k compares momentum and molecular diffusion of species k:

$$Sc_k = \frac{\nu}{D_k} \tag{2.3.4}$$

The Schmidt number can be linked to the Prandtl and Lewis numbers by the relation:

$$Sc_k = Pr Le_k \tag{2.3.5}$$

2.4 Introduction to turbulent combustion

2.4.1 Description of turbulence

The phenomenon of turbulence is very complex as it is chaotic, unstable, tridimensional. It is present in the vast majority of flows that people encounter in their everyday life or in industries. Turbulence can be distinguished easily in the nature by observing instable mechanisms, such as the Kelvin-Helmholtz instability (Fig. 2.1), due to the velocity difference across the interface between two fluids and characterized by the appearance of vortices in the shear layer; or the Rayleigh-Taylor instability (Fig. 2.2), due to the mass difference between the fluids, and characterized by a “mushroom cap”.

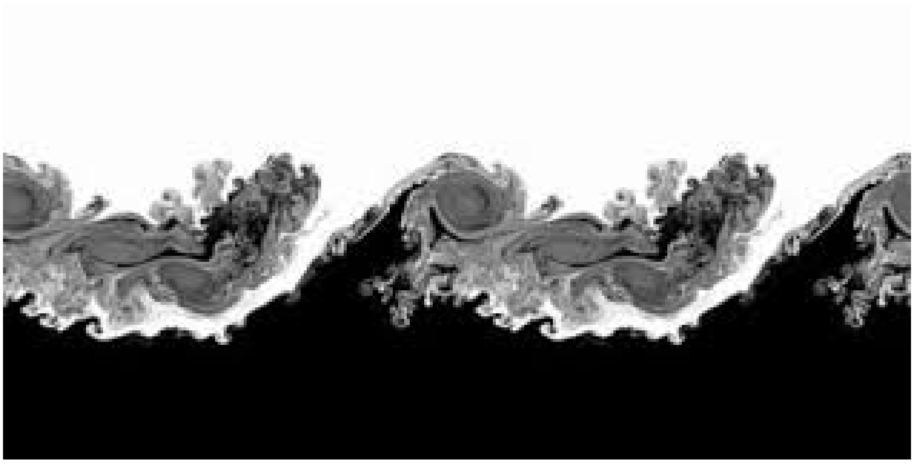

Figure 2.1: Kelvin-Helmholtz instability [27].

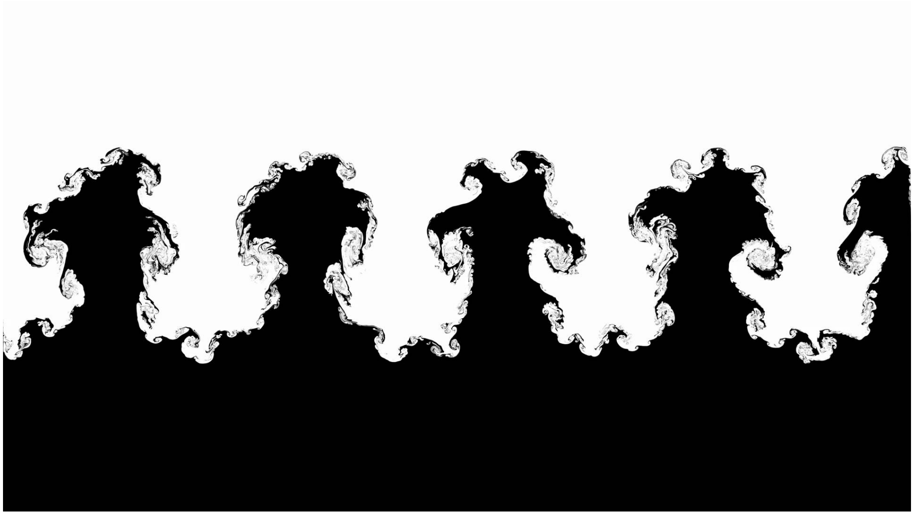

Figure 2.2: Rayleigh-Taylor instability [27].

Turbulence is usually identified by computing the Reynolds number Re defined as the ratio of inertial forces to viscous forces:

$$Re = \frac{\rho u L}{\mu} = \frac{uL}{\nu} \tag{2.4.1}$$

where u is the velocity of the flow, L a characteristic length and ν the kinematic viscosity. A laminar flow corresponds to low Reynolds numbers where viscous effect are dominant, while turbulent flow occurs at high Reynolds numbers. As turbulence causes fluctuations of any property ϕ, the latter can be decomposed into a mean value $\overline{\phi}$ and a fluctuating value ϕ':

$$\phi = \overline{\phi} + \phi' \tag{2.4.2}$$

The turbulence intensity I can then be defined as the ratio of root mean square of ϕ' into $\overline{\phi}$:

$$I = \frac{\sqrt{\overline{\phi'^2}}}{\overline{\phi}} \tag{2.4.3}$$

A Reynolds number can be constructed from the fluctuation velocity u' and the length scales of the fluctuations, from integral scale l_t to Kolmogorov scale η_k. The integral length scale is due to large anisotropic structures, which transport almost the totality of turbulent kinetic energy. The turbulent Reynolds number Re_t is therefore defined using this length scale:

$$Re_t = \frac{u'_t l_t}{\nu} \tag{2.4.4}$$

where u'_t is the characteristic velocity of the fluctuations. On the other hand, the Kolmogorov length scale is associated to smallest structures which are isotropic and ensure the residual energy dissipation. The Reynolds number of these structures of velocity u'_k is Re_k:

$$Re_k = \frac{u'_k \eta_k}{\nu} \approx 1 \tag{2.4.5}$$

Between these two scales comes the Taylor scale which is responsible of turbulent energy transfer from integral to Kolmogorov scale. Figure 2.3 shows the energy cascade introduced by Richardson [140] and Kolmogorov [82], which displays the evolution of the energy $E(k)$ versus the wave number k. Turbulent energy is produced by large structures at low wave numbers, then transferred to the inertial region, and finally dissipated in the small scales.

In the case of homogeneous and isotropic turbulence, the local dissipation rate of turbulent kinetic energy can be computed from the fluctuation velocity $u'(r)$ and the size of the eddy r, varying from the Kolmogorov scale η_k and the integral scale l_t:

$$\epsilon = \frac{u'(r)^3}{r} \tag{2.4.6}$$

A turbulent time can be defined for any eddy of size r:

$$\tau_m(r) = \frac{r}{u'(r)} = \frac{r^{2/3}}{\epsilon^{1/3}} \tag{2.4.7}$$

A smaller structure will clearly have a smaller turbulent time : $\tau_m(\eta_k) < \tau_m(l_t)$.

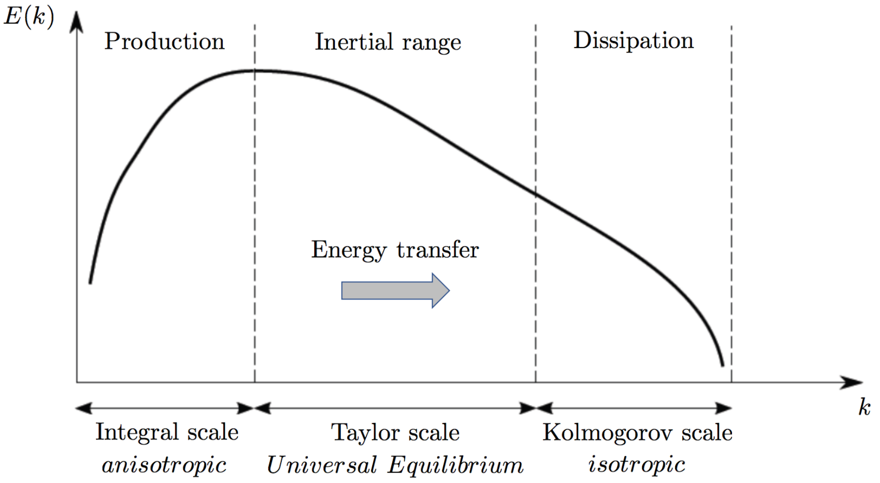

Figure 2.3: Energy cascade of Kolmogorov from [113].

2.4.2 Interaction between turbulence and combustion

Turbulence and combustion are two complex phenomena in fluid mechanics. And the combination of both leads to an even more difficult task to deal with. Indeed, a turbulent flow can modify combustion either by increasing the reaction rate, due to a better mixing of reactants, or in the case of an extremely strong turbulence, by quenching the flame. On the other hand, heat release from combustion can lead to strong flow accelerations, and also increase kinematic viscosity by heating the flow, thus modifying the turbulence.

In the case of premixed combustion, two dimensionless numbers are introduced to classify the combustion regimes:

- The Damköhler number Da, defined for large eddies, is the ratio of the integral time scale $\tau_t = \tau_m(l_t)$ into the chemical time scale τ_c:

  $$Da = \frac{\tau_t}{\tau_c} \tag{2.4.8}$$

  In the case of large Damköhler numbers ($Da \gg 1$), the chemical time is very small compared to the time of large structures, which means that combustion finishes before turbulence modifies the process. This case is close to a laminar flame wrinkled by turbulence, called the flamelet regime. At low Damköhler numbers ($Da \ll 1$), chemical time is higher than turbulent time, which allows turbulence to mix the reactants before they burn, this regime is called the perfectly stirred reactor (PSR).

- The Karlovitz number K_a, defined for small eddies, is the ratio of the chemical time scale into the Kolmogorov time scale $\tau_k = \tau_m(\eta_k)$:

  $$Ka = \frac{\tau_c}{\tau_k} \tag{2.4.9}$$

  The case $Ka < 1$ ($\tau_c < \tau_k < \tau_t$) is found when the chemical time scale is smaller than the turbulent time, and corresponds to the flamelet regime. This regime can be divided into two sub-regimes based on the ratio between the fluctuation velocity u' and the laminar flame speed s_L^0 : wrinkled flamelet ($u' < s_L^0$) or corrugated flamelet ($u' > s_L^0$). The case $Ka > 1$ and $Da > 1$ ($\tau_k < \tau_c < \tau_t$) corresponds to a chemical time scale shorter than the integral time but larger than the Kolmogorov time, known as the thickened flame regime where the inner

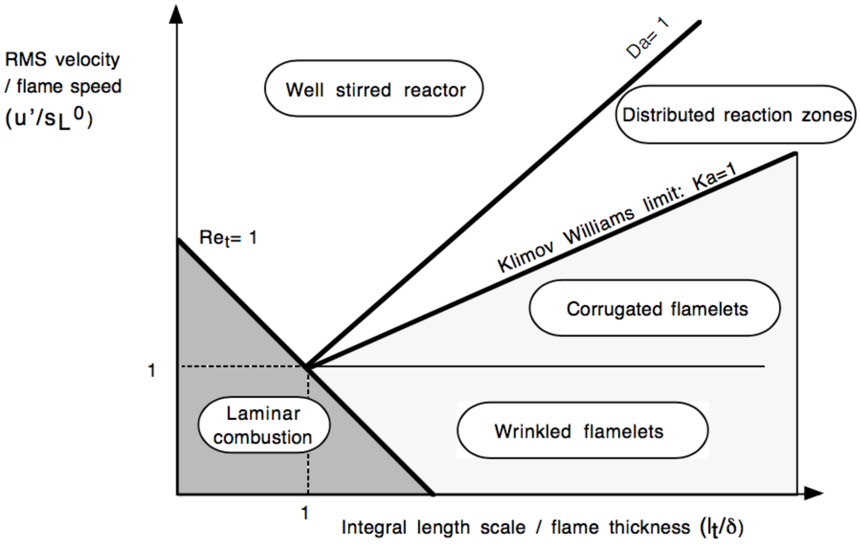

Figure 2.4: Turbulent combustion diagram by Peters [127]

structure of the flame is modified by the smallest structures and the outer structure wrinkled by largest eddies.

The combustion regimes identified with Damköhler and Karlovitz numbers are displayed on Fig. 2.4 with the limits $Da = 1$ and $Ka = 1$. An illustration of flames in different combustion regimes (Fig. 2.5) is given by Borghi and Destriau [10] in a case of premixed flames of fresh and burnt gas temperature at respectively 300 et 2000 K.

2.4.3 Computational approaches : DNS-RANS-LES

The three main approaches for computational fluid dynamics (CFD) are : DNS (Direct Numerical Simulation), RANS (Reynolds Averaged Navier-Stokes) and LES (Large Eddy Simulation). A brief presentation of them are presented below and summarized in Tab. 2.1.

DNS solves the full Navier-Stokes equations without any model. All turbulence and combustion scales are computed directly, which allows DNS to reproduce exactly an experiment. But in order to capture all the structures, the grid needs to be refined at the same level. As the Kolmogorov scale is inversely proportional to $Re^{3/4}$, the cost becomes very quickly prohibitive with high Reynolds numbers or computational domains larger than a few cm^3. Therefore DNS fits only simple academic flows.

The extreme opposite of DNS is RANS, which solves Reynolds (incompressible flows) or Favre (compressible flows) averaged balance equations by modelling all the scales of turbulence and combustion. The grid can be coarse but the results are very sensible to the model and to the constants used in the models. The model constants need to be configured before by running several computations for the studied case. Historically, first industrial case simulations were performed in RANS because of the low cost required.

LES comes in between by computing directly the large structures and modelling the smallest ones. Navier-Stokes equations are filtered to suppress small scales (wave numbers lower than k_c, see Fig. 2.6). LES can have very high accuracy with moderate computational time cost, and is therefore a good compromise between DNS and RANS. Moreover, due to the increase in high performance

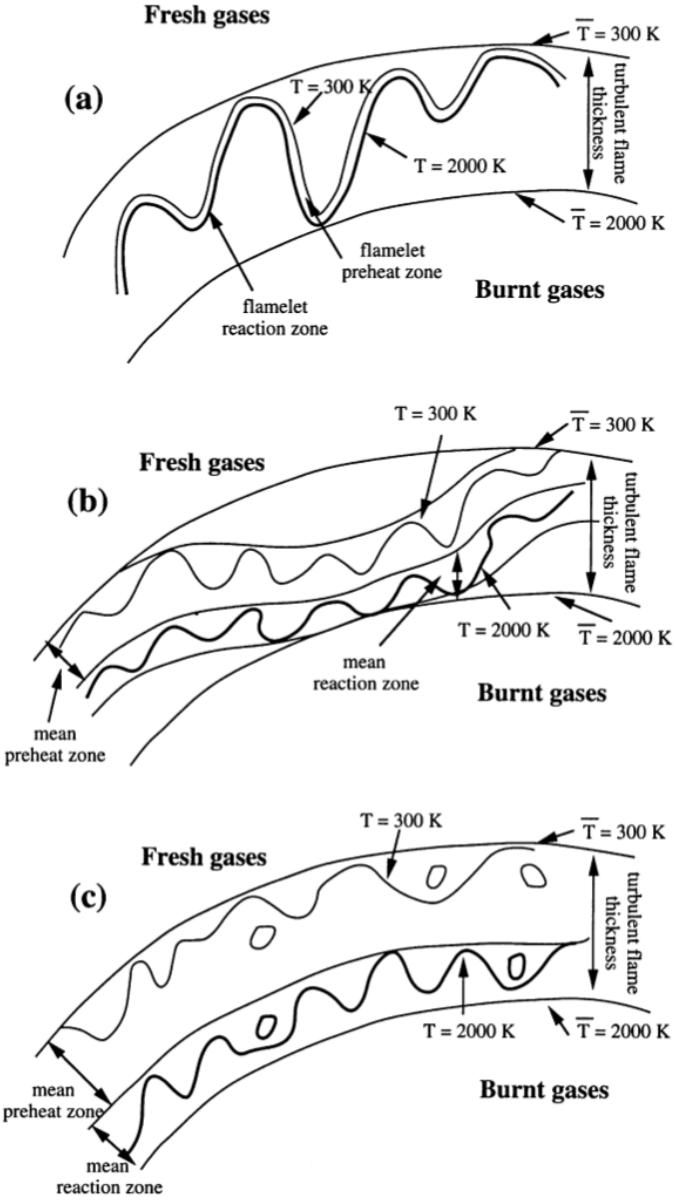

Figure 2.5: Turbulent premixed combustion regimes illustrated by Borghi and Destriau [10] : (a) wrinkled flamelet, (b) thickened-wrinkled flamelet, (c) thickened flame.

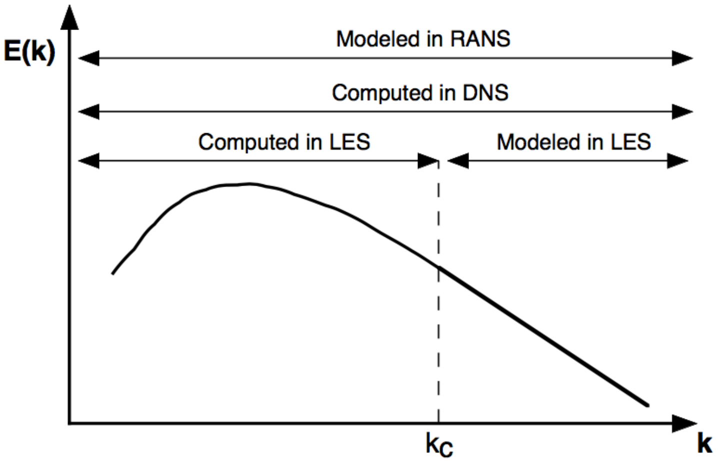

Figure 2.6: Turbulent energy spectrum vs. wave numbers. k_c is the cut-off wave number used in LES. [135]

Approaches	DNS	LES	RANS
Models	None	Partially	Fully
Accuracy	+++	++	+
Cost	+++	++	+
Application	Academic	Research & industry	Industry

Table 2.1: Summary of computational approaches.

computing, the use of LES becomes even more relevant not only in research works, but also in industry.

Chapter 3

LES : equations and modellings

Contents

Large eddy simulations compute largest structures of the flow while modelling the smallest ones. A filter is therefore applied to separate them. Filtering the balance equations produces unclosed terms which need to be handled. The current chapter also presents the in-house LES/DNS code SiTCom-B which was used for the computations.

3.1 Filtered Navier-Stokes equations

3.1.1 LES filters and Favre averaging

In this work, we are only focused on physical space filtering where the filtered quantity is averaged over a given volume. For any variable φ, the filtered quantity of φ is written $\overline{\varphi}$ and defined as:

$$\overline{\varphi}(\mathbf{x}) = \int \varphi(\mathbf{x}')F(\mathbf{x}-\mathbf{x}')d\mathbf{x}' \tag{3.1.1}$$

where F is the LES filter. The filtering operation is actually a convolution product between φ and F:

$$(\varphi * F)(\mathbf{x}) = \int_{-\infty}^{+\infty} \varphi(\mathbf{x}')F(\mathbf{x}-\mathbf{x}')d\mathbf{x}' \tag{3.1.2}$$

and satisfies all the properties of convolution product, particularly, the followings :

- Distributivity or linearity:

$$\overline{\varphi+\psi} = \overline{\varphi} + \overline{\psi} \tag{3.1.3}$$

- Differentiation

$$\overline{\frac{\partial \varphi}{\partial t}} = \frac{\partial \overline{\varphi}}{\partial t} \quad \text{and} \quad \overline{\frac{\partial \varphi}{\partial x_i}} = \frac{\partial \overline{\varphi}}{\partial x_i} \tag{3.1.4}$$

The filter F is in addition normalized:

$$\int_{-\infty}^{+\infty} F(\mathbf{x})d\mathbf{x} = 1 \tag{3.1.5}$$

The differentiation property is not satisfied for spatial commutation when the filter is not homogeneous, especially in case of non-uniform grid in near wall regions. But in the framework of this study, the spatial commutation is assumed to be always true, which is a common assumption of the LES community. The temporal commutation is false when the grid is changing with the time, i.e. in adaptative meshing, which is not our case.
In most LES codes, the filter is implicit. The filtering is done by the grid itself and the filter size Δ is usually defined as:

$$\Delta = (\Delta_1\Delta_2\Delta_3)^{1/3} \quad \text{or} \quad \Delta = (\Delta_1^2+\Delta_2^2+\Delta_3^2)^{1/2} \tag{3.1.6}$$

where Δ_i represents the cell size in the direction i. Any variable φ can be split into a filtered or resolved quantity $\overline{\varphi}$ and an unresolved or subgrid scale part φ' such that : $\varphi = \overline{\varphi} + \varphi'$.

For variable density flows, a mass-weighted or Favre averaging is introduced:

$$\widetilde{\varphi} = \frac{\overline{\rho\varphi}}{\overline{\rho}} = \frac{1}{\overline{\rho}}\int \rho\varphi(\mathbf{x}')F(\mathbf{x}-\mathbf{x}')d\mathbf{x}' \tag{3.1.7}$$

Any quantity φ may be decomposed into mean $\widetilde{\varphi}$ and fluctuation φ'' components:

$$\varphi = \widetilde{\varphi} + \varphi'' \tag{3.1.8}$$

One should be aware that some properties of RANS averaging are not true in LES filtering and Favre averaging:

$$\overline{\varphi'} \neq 0 \ , \ \overline{\overline{\varphi}} \neq \overline{\varphi} \ , \ \widetilde{\varphi''} \neq 0 \ , \ \widetilde{\widetilde{\varphi}} \neq \widetilde{\varphi} \tag{3.1.9}$$

3.1.2 Filtered equations

Filtering and applying Favre averaging to balance equations in section 2.2 leads to:

- Mass

$$\frac{\partial \overline{\rho}}{\partial t} + \frac{\partial}{\partial x_i}(\overline{\rho}\widetilde{u}_i) = 0 \tag{3.1.10}$$

- Momentum

$$\frac{\partial \overline{\rho}\widetilde{u}_i}{\partial t} + \frac{\partial}{\partial x_j}(\overline{\rho}\widetilde{u}_i\widetilde{u}_j) = -\frac{\partial \overline{p}}{\partial x_i} + \frac{\partial}{\partial x_j}\left[\overline{\tau}_{ij} - \overline{\rho}(\widetilde{u_i u_j} - \widetilde{u}_i\widetilde{u}_j)\right] \tag{3.1.11}$$

- Species

$$\frac{\partial \overline{\rho}\widetilde{Y}_k}{\partial t} + \frac{\partial}{\partial x_i}(\overline{\rho}\widetilde{u}_i\widetilde{Y}_k) = \frac{\partial}{\partial x_i}\left[-\overline{\rho V_{k,i} Y_k} - \overline{\rho}\left(\widetilde{u_i Y_k} - \widetilde{u}_i\widetilde{Y}_k\right)\right] + \overline{\dot{\omega}}_k \quad k = 1, N_{sp} \tag{3.1.12}$$

- Energy

$$\begin{aligned}\frac{\partial \overline{\rho}\widetilde{E}}{\partial t} + \frac{\partial}{\partial x_i}\left(\overline{\rho}\widetilde{u}_i\widetilde{E}\right) =& \frac{\partial}{\partial x_i}\left[\overline{\lambda\frac{\partial T}{\partial x_i}} - \overline{\rho}\left(\widetilde{u_i E} - \widetilde{u}_i\widetilde{E}\right)\right] - \frac{\partial}{\partial x_i}\left(\overline{\rho\sum_{k=1}^{N_{sp}} h_{s,k} Y_k V_{k,i}}\right) \\ &+ \frac{\partial}{\partial x_j}\left(\overline{\sigma_{ij} u_i}\right) + \overline{\dot{\omega}_T}\end{aligned} \tag{3.1.13}$$

The filtered equations lead to unknown quantities which need to be modelled to close the system:

- Filtered viscous tensor $\overline{\tau}_{ij}$.
- Unresolved Reynolds stresses $\overline{\rho}(\widetilde{u_i u_j} - \widetilde{u}_i\widetilde{u}_j)$.
- Unresolved species fluxes $\overline{\rho}\left(\widetilde{u_i Y_k} - \widetilde{u}_i\widetilde{Y}_k\right)$ and energy fluxes $\overline{\rho}\left(\widetilde{u_i E} - \widetilde{u}_i\widetilde{E}\right)$.
- Filtered laminar diffusion fluxes for species $\overline{\rho V_{k,i} Y_k}$.
- Filtered energy flux $\overline{q}_i = -\overline{\lambda\frac{\partial T}{\partial x_i}} + \overline{\rho\sum_{k=1}^{N_{sp}} h_{s,k} Y_k V_{k,i}}$
- Filtered chemical reaction rate $\overline{\dot{\omega}}_k$ presented in section 3.2.
- Filtered stress tensor fluxes $\overline{\sigma_{ij} u_i}$.

3.1.3 Unclosed terms modelling

The objective of this section is to propose commonly used models for unclosed terms found in the previous section (3.1.2).

3.1.3.1 Filtered viscous tensor and stress tensor fluxes

Neglecting any subgrid effect, the filtered viscous tensor $\overline{\tau}_{ij}$ is modelled as:

$$\overline{\tau}_{ij} = 2\overline{\mu}\left(\widetilde{S}_{ij} - \frac{1}{3}\widetilde{S}_{kk}\delta_{ij}\right) \tag{3.1.14}$$

where:

$$\widetilde{S}_{ij} = \frac{1}{2}\left(\frac{\partial \widetilde{u}_i}{\partial x_j} + \frac{\partial \widetilde{u}_j}{\partial x_i}\right) \tag{3.1.15}$$

The same simplification is done for filtered stress tensor fluxes $\overline{\sigma_{ij}u_i}$:

$$\overline{\sigma_{ij}u_i} = \widetilde{u}_i\left(\overline{\tau}_{ij} - \overline{p}\delta_{ij}\right) \tag{3.1.16}$$

3.1.3.2 Unresolved Reynolds stresses

The Reynolds stresses $\mathcal{T}_{ij} = \overline{\rho}(\widetilde{u_i u_j} - \widetilde{u}_i\widetilde{u}_j)$ is an essential part of turbulence modelling in RANS and in LES. Many models exist in the literature, only standard and dynamic Smagorinsky models are used in this work and presented hereafter.

Smagorinsky model
The Smagorinsky model [154] relies on the Boussinesq assumption [14]. The Reynolds stresses $\mathcal{T}_{ij}$ can be split into a deviatoric $\mathcal{T}_{ij}^D$ and an isotropic $\mathcal{T}_{ij}^I$ parts:

$$\mathcal{T}_{ij} = \mathcal{T}_{ij}^D + \mathcal{T}_{ij}^I \tag{3.1.17}$$

where:

$$\begin{cases} \mathcal{T}_{ij}^D = \mathcal{T}_{ij} - \dfrac{\delta_{ij}}{3}\mathcal{T}_{kk} \\ \mathcal{T}_{ij}^I = \dfrac{\delta_{ij}}{3}\mathcal{T}_{kk} \end{cases} \tag{3.1.18}$$

A subgrid scale (LES) or turbulent viscosity (RANS) ν_t is introduced to connect the deviatoric part of the Reynolds stresses to the strain rate tensor:

$$\mathcal{T}_{ij}^D = -2\overline{\rho}\nu_t\left(\widetilde{S}_{ij} - \frac{\delta_{ij}}{3}\widetilde{S}_{kk}\right) \tag{3.1.19}$$

The subgrid scale viscosity is modelled as:

$$\nu_t = (C_S\Delta)^2|\widetilde{S}| \tag{3.1.20}$$

where C_S is the Smagorinsky constant, which value depends of the flow configuration, and $|\widetilde{S}| = \left(2\widetilde{S}_{ij}\widetilde{S}_{ij}\right)^{1/2}$ the resolved shear stress.
$\mathcal{T}_{kk}$ is generally neglected (incompressible flows) or modelled (compressible flows) by the Yoshizawa's expression [180]:

$$\mathcal{T}_{kk} = 2C_I\overline{\rho}\Delta^2|\widetilde{S}|^2 \tag{3.1.21}$$

where C_I is a model constant.

A single value of the constant C_S cannot satisfy all the flow configurations, the Smagorinsky model is therefore very dissipative, especially near wall regions [143] where the flow is different from the

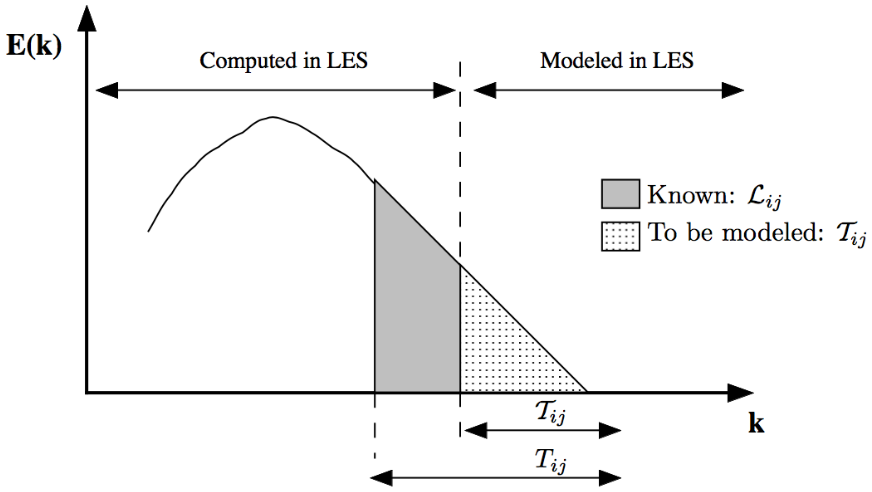

Figure 3.1: Graphical representation of the Germano identity in the energy spectrum. $\mathcal{T}_{ij}$ and T_{ij} are respectively the unresolved Reynolds stresses of LES filter and test filter, $\mathcal{L}_{ij}$ is the LES resolved part of T_{ij} [135].

far wall zones. The idea of a dynamic model has thus emerged.

Dynamic Smagorinsky model

The dynamic model was first proposed by Germano et al. [60] for incompressible flows, then extended to compressible flows by Moin et al. [117]. The model has for objective to estimate small scale dissipation from the resolved eddies by introducing a test filter of size $\widehat{\Delta}$ larger than the LES filter Δ. The ratio $\widehat{\Delta}/\Delta$ is usually 2. The test filtered unresolved Reynolds stresses are:

$$\widehat{\mathcal{T}}_{ij} = \widehat{\overline{\rho}\widetilde{u_iu_j}} - \widehat{\overline{\rho}\widetilde{u}_i\widetilde{u}_j} \tag{3.1.22}$$

Applying the test filter to the momentum balance equation leads to:

$$\begin{aligned}\frac{\partial\widehat{\overline{\rho}\widetilde{u}_i}}{\partial t} + \frac{\partial}{\partial x_j}\left(\frac{\widehat{\overline{\rho}\widetilde{u}_i}\widehat{\overline{\rho}\widetilde{u}_j}}{\widehat{\overline{\rho}}}\right) &= -\frac{\partial\widehat{\overline{p}}}{\partial x_i} + \frac{\partial}{\partial x_j}\left[\widehat{\overline{\tau}}_{ij} - \left(\widehat{\overline{\rho}\widetilde{u_iu_j}} - \widehat{\overline{\rho}\widetilde{u}_i\widetilde{u}_j}\right) - \left(\widehat{\overline{\rho}\widetilde{u}_i\widetilde{u}_j} - \frac{\widehat{\overline{\rho}\widetilde{u}_i}\widehat{\overline{\rho}\widetilde{u}_j}}{\widehat{\overline{\rho}}}\right)\right] \\ &= -\frac{\partial\widehat{\overline{p}}}{\partial x_i} + \frac{\partial}{\partial x_j}\left[\widehat{\overline{\tau}}_{ij} - \left(\widehat{\overline{\rho}\widetilde{u_iu_j}} - \frac{\widehat{\overline{\rho}\widetilde{u}_i}\widehat{\overline{\rho}\widetilde{u}_j}}{\widehat{\overline{\rho}}}\right)\right]\end{aligned} \tag{3.1.23}$$

which brings out the unresolved stresses at the test level T_{ij}:

$$T_{ij} = \widehat{\overline{\rho}\widetilde{u_iu_j}} - \frac{\widehat{\overline{\rho}\widetilde{u}_i}\widehat{\overline{\rho}\widetilde{u}_j}}{\widehat{\overline{\rho}}} \tag{3.1.24}$$

Combining Eqs. 3.1.22 and 3.1.24 leads to the Germano identity (see Fig. 3.1), by introducing the Leonard tensor $\mathcal{L}_{ij}$:

$$\mathcal{L}_{ij} = T_{ij} - \widehat{\mathcal{T}}_{ij} = \widehat{\overline{\rho}\widetilde{u}_i\widetilde{u}_j} - \frac{\widehat{\overline{\rho}\widetilde{u}_i}\widehat{\overline{\rho}\widetilde{u}_j}}{\widehat{\overline{\rho}}} \tag{3.1.25}$$

$\mathcal{L}_{ij}$ can be computed explicitly as it is only dependant of resolved velocities. Applying the Smagorinsky model to both $\mathcal{T}_{ij}$ and T_{ij} leads to:

$$\begin{cases} \mathcal{T}_{ij} - \dfrac{\delta_{ij}}{3}\mathcal{T}_{kk} = -2\overline{\rho}C\Delta^2|\widetilde{S}|\left(\widetilde{S}_{ij} - \dfrac{\delta_{ij}}{3}\widetilde{S}_{kk}\right) = -2C\alpha_{ij} \\ T_{ij} - \dfrac{\delta_{ij}}{3}T_{kk} = -2\widehat{\overline{\rho}}C\widehat{\Delta}^2|\widehat{\widetilde{S}}|\left(\widehat{\widetilde{S}}_{ij} - \dfrac{\delta_{ij}}{3}\widehat{\widetilde{S}}_{kk}\right) = -2C\beta_{ij} \end{cases} \tag{3.1.26}$$

where $C = C_S^2$, and α_{ij} and β_{ij} are introduced to simplify notations. The Germano identity can thus be rewritten as:

$$\mathcal{L}_{ij} - \frac{\delta_{ij}}{3}\mathcal{L}_{kk} = 2(\widehat{C\alpha_{ij}} - C\beta_{ij}) \tag{3.1.27}$$

The term $\widehat{C\alpha_{ij}}$ is generally approximated by $C\widehat{\alpha}_{ij}$, but can be computed using either integral [61] or relaxation [42] methods. In what follows, the approximation $\widehat{C\alpha_{ij}} = C\widehat{\alpha}_{ij}$ is assumed.
There are in total six independant equations for only one unknown C_S, the system is over-determined. Germano et al. [60] propose to multiply each side of Eq. 3.1.27 by the filtered strain rate tensor $\widetilde{S}_{ij}$, which leads to:

$$C = \frac{1}{2}\frac{(\mathcal{L}_{ij} - \frac{\delta_{ij}}{3}\mathcal{L}_{kk})\widetilde{S}_{ij}}{\widehat{\alpha}_{ij}\widetilde{S}_{ij} - \beta_{ij}\widetilde{S}_{ij}} \tag{3.1.28}$$

Using this approach, the denominator can become negative or zero, which would make C indeterminate. The negative constant C involves a negative turbulent viscosity which leads to backscatter phenomenon [20] : the direction of turbulent energy transfert is reversed, going from small scales to large scales. This issue can be overcome by averaging the rhs of Eq. 3.1.28 over a plane parallel to the wall [60]. Writting $< . >$ the averaging operation, Eq. 3.1.28 becomes:

$$C = \frac{1}{2}\frac{< (\mathcal{L}_{ij} - \frac{\delta_{ij}}{3}\mathcal{L}_{kk})\widetilde{S}_{ij} >}{< \widehat{\alpha}_{ij}\widetilde{S}_{ij} > - < \beta_{ij}\widetilde{S}_{ij} >} \tag{3.1.29}$$

Lilly [93] proposes a modification to Germano's model by optimizing with a least squares approach. Writing $M_{ij} = \widehat{\alpha}_{ij} - \beta_{ij}$, Eq. 3.1.27 becomes:

$$\mathcal{L}_{ij} - \frac{\delta_{ij}}{3}\mathcal{L}_{kk} = 2CM_{ij} \tag{3.1.30}$$

Defining Q as the square of the error, one gets:

$$Q = (\mathcal{L}_{ij} - \frac{\delta_{ij}}{3}\mathcal{L}_{kk} - 2CM_{ij})^2 \tag{3.1.31}$$

The expression for C is found by deriving Q:

$$\frac{\partial Q}{\partial C} = 0 \quad \Rightarrow \quad C = \frac{1}{2}\frac{(\mathcal{L}_{ij} - \frac{\delta_{ij}}{3}\mathcal{L}_{kk})M_{ij}}{M_{ij}^2} \tag{3.1.32}$$

Deriving twice Q shows that this value of C gives the minimum of Q since:

$$\frac{\partial^2 Q}{\partial C^2} = 8M_{ij}^2 > 0 \tag{3.1.33}$$

By contrast with the Germano model, the denominator of the constant C in the Lilly model becomes zero only if $M_{ij} = 0$, so that the numerator becomes zero too. The numerator can also locally be negative. Ghosal et al. [61] and Piomelli et al. [133] introduced the Dynamic Localization Model (DLM) which consists in filtering the constant C from Eq. 3.1.32 to soften the local variations:

$$C = \frac{1}{2}\frac{< (\mathcal{L}_{ij} - \frac{\delta_{ij}}{3}\mathcal{L}_{kk})M_{ij} >_{DLM}}{< M_{ij}^2 >_{DLM}} \tag{3.1.34}$$

where $< . >_{DLM}$ is the filtering operation. In practice, C is filtered three times at test level $\widehat{\Delta}$. Moreover, the condition $C \geq 0$ is imposed to suppress backscatter phenomenon.

As for the Smagorinsky constant, the constant C_I in the Yoshizawa expression (Eq. 3.1.21) can also differ for different flows. A dynamic value of C_I would be more precise and versatile. Moin et al. [117] propose a dynamic approach of C_I similar to the Germano model.
By analogy with the Smagorinsky constant, the stress tensor at test level is:

$$T_{kk} = 2C_I\widehat{\overline{\rho}}\widehat{\Delta}^2|\widehat{\widetilde{S}}|^2 \tag{3.1.35}$$

and the test filtered Reynolds stresses are:

$$\widehat{\mathcal{T}}_{kk} = 2C_I\widehat{\overline{\rho}\Delta^2|\widetilde{S}|^2} \tag{3.1.36}$$

The isotropizing term of the Leonard tensor $\mathcal{L}_{kk}$ is expressed by:

$$\mathcal{L}_{kk} = T_{kk} - \widehat{\mathcal{T}}_{kk} \tag{3.1.37}$$

Combining Eqs. 3.1.35, 3.1.36 and 3.1.37 leads to:

$$\mathcal{L}_{kk} = 2C_I(\widehat{\overline{\rho}}\widehat{\Delta}^2|\widehat{\widetilde{S}}|^2 - \widehat{\overline{\rho}\Delta^2|\widetilde{S}|^2}) \tag{3.1.38}$$

And finally, injecting Eq. 3.1.25 into Eq. 3.1.38 gives:

$$C_I = \frac{\widehat{\overline{\rho}\widetilde{u}_k\widetilde{u}_k} - \widehat{\overline{\rho}\widetilde{u}_k}\widehat{\overline{\rho}\widetilde{u}_k}/\widehat{\overline{\rho}}}{2(\widehat{\overline{\rho}}\widehat{\Delta}^2|\widehat{\widetilde{S}}|^2 - \widehat{\overline{\rho}\Delta^2|\widetilde{S}|^2})} \tag{3.1.39}$$

In this expression, the constant C_I can be zero or negative, therefore C_I is filtered three times at test level as for the Smagorinsky constant, and the condition $C_I \geq 0$ is imposed. This formulation of C_I has been implemented in SiTComB during this Ph.D., but its contribution to the equations is insignificant for the mesh resolutions retained, and can be neglected.

3.1.3.3 Unresolved species and energy fluxes

The species and energy fluxes are modelled by using a simple gradient assumption:

$$\overline{\rho}(\widetilde{u_iY_k} - \widetilde{u}_i\widetilde{Y}_k) = -\frac{\overline{\rho}\nu_t}{Sc_{t,k}}\frac{\partial\widetilde{Y}_k}{\partial x_i} \tag{3.1.40}$$

$$\overline{\rho}(\widetilde{u_iE} - \widetilde{u}_i\widetilde{E}) = -\frac{\overline{\rho}\nu_t}{Pr_t}\frac{\partial\widetilde{E}}{\partial x_i} \tag{3.1.41}$$

where ν_t is the subgrid scale viscosity and $Sc_{t,k}$ and Pr_t are respectively the subgrid Schmidt and Prandtl numbers, defined as:

$$Sc_{t,k} = \frac{\nu_t}{D_k} \quad \text{and} \quad Pr_t = \frac{\nu_t}{D_{th}} \tag{3.1.42}$$

3.1.3.4 Filtered laminar diffusion fluxes and energy flux

Filtering the Hirschfelder and Curtiss approximation [70] for the species diffusion leads to:

$$\overline{\rho V_{k,i}Y_k} = -\overline{\rho D_k\frac{W_k}{W}\frac{\partial X_k}{\partial x_i}} \tag{3.1.43}$$

which can be simplified as:

$$\overline{\rho V_{k,i} Y_k} \approx -\overline{\rho} D_k \frac{\widetilde{W}_k}{\widetilde{W}} \frac{\partial \widetilde{X}_k}{\partial x_i} \tag{3.1.44}$$

Finally, the filtered energy flux follows:

$$\overline{q}_i = -\overline{\lambda} \frac{\partial \widetilde{T}}{\partial x_i} - \overline{\rho} \sum_{k=1}^{N_{sp}} \widetilde{h}_{s,k} D_k \frac{\widetilde{W}_k}{\widetilde{W}} \frac{\partial \widetilde{X}_k}{\partial x_i} \tag{3.1.45}$$

3.1.4 Filtered equations including modellings

Injecting modellings from section 3.1.3 into filtered balance equations from section 3.1.2 leads to:

- Mass

$$\frac{\partial \overline{\rho}}{\partial t} + \frac{\partial}{\partial x_i}(\overline{\rho} \widetilde{u}_i) = 0 \tag{3.1.46}$$

- Momentum

$$\begin{aligned} \frac{\partial \overline{\rho} \widetilde{u}_i}{\partial t} + \frac{\partial}{\partial x_j}(\overline{\rho} \widetilde{u}_i \widetilde{u}_j) &= -\frac{\partial \overline{p}}{\partial x_i} + \frac{\partial}{\partial x_j}\left[\widetilde{\tau}_{ij} - \mathcal{T}_{ij}\right] \\ &= -\frac{\partial \overline{p}}{\partial x_i} + \frac{\partial}{\partial x_j}\left[2(\mu + \mu_t)\left(\widetilde{S}_{ij} - \frac{\delta_{ij}}{3}\widetilde{S}_{kk}\right) - \frac{2\delta_{ij}}{3} C_I \overline{\rho} \Delta^2 |\widetilde{S}|^2\right] \end{aligned} \tag{3.1.47}$$

- Species

$$\frac{\partial \overline{\rho} \widetilde{Y}_k}{\partial t} + \frac{\partial}{\partial x_i}(\overline{\rho} \widetilde{u}_i \widetilde{Y}_k) = \frac{\partial}{\partial x_i}\left[\overline{\rho} D_k \frac{\widetilde{W}_k}{\widetilde{W}} \frac{\partial \widetilde{X}_k}{\partial x_i} + \frac{\mu_t}{Sc_{t,k}} \frac{\partial \widetilde{Y}_k}{\partial x_i}\right] + \overline{\dot{\omega}}_k \quad k = 1, N_{sp} \tag{3.1.48}$$

- Energy

$$\begin{aligned} \frac{\partial \overline{\rho} \widetilde{E}}{\partial t} + \frac{\partial}{\partial x_i}\left(\overline{\rho} \widetilde{u}_i \widetilde{E}\right) =& \frac{\partial}{\partial x_i}\left[\overline{\lambda} \frac{\partial \widetilde{T}}{\partial x_i} + \frac{\mu_t}{Pr_t} \frac{\partial \widetilde{E}}{\partial x_i}\right] + \overline{\rho} \sum_{k=1}^{N_{sp}} \widetilde{h}_{s,k} D_k \frac{\widetilde{W}_k}{\widetilde{W}} \frac{\partial \widetilde{X}_k}{\partial x_i} \\ &+ \frac{\partial}{\partial x_j}\left(\widetilde{\sigma}_{ij} \widetilde{u}_i\right) + \overline{\dot{\omega}_T} \end{aligned} \tag{3.1.49}$$

where $\mu_t = \overline{\rho} \nu_t$ is the subgrid dynamic viscosity.

3.2 Turbulent combustion modelling

The modelling of reaction rate is a key issue in turbulent combustion. Readers can refer to Poinsot and Veynante [135] for a more complete list of turbulent combustion models. This section will only be focused on the quasi-laminar model (QL), thickened flame model (TFM), eddy dissipation concept (EDC), partially stirred reactor (PaSR) and flamelet progress variable (FPV).

3.2.1 Direct approach and quasi-laminar model

Let's consider a simple irreversible reaction of fuel F into oxidizer O:

$$F + O \longrightarrow P \tag{3.2.1}$$

From equations 2.1.28 and 2.1.29, the fuel reaction rate $\dot{\omega}_F$ can be expressed as:

$$\dot{\omega}_F = -W_F A_f T^\beta \exp\left(-\frac{T_a}{T}\right) [X_F] [X_O] \tag{3.2.2}$$

which can be rewritten as:

$$\dot{\omega}_F = -A\rho^2 T^\beta Y_F Y_O \exp\left(-\frac{T_a}{T}\right) \tag{3.2.3}$$

with $A = A_f / W_O$. The reaction rate is highly non-linear and its filtered value cannot be expressed easily as function of filtered values of Y_k and T, even for this simple case where only two species and one reaction are involved. Thus, the reaction rate needs to be modelled in complex chemistry simulations.

The simplest model, so-called the "no model" or quasi-laminar model, relies on the assumption:

$$\bar{\dot{\omega}}_F = \dot{\omega}_F(\widetilde{Y}_F, \widetilde{Y}_O, \widetilde{T}) \tag{3.2.4}$$

which leads to:

$$\bar{\dot{\omega}}_F = -A\bar{\rho}^2 \widetilde{T}^\beta \widetilde{Y}_F \widetilde{Y}_O \exp\left(-\frac{T_a}{\widetilde{T}}\right) \tag{3.2.5}$$

This simplification is much criticized and is only valid when the mesh is well refined enough or in the well stirred reactor regime where chemical time scales are larger than turbulent time scales. The latter regime may be encountered in specific applications such as supersonic combustion or atmospheric chemistry. Krol et al. [85] introduced a criterion based on the subgrid Damköhler number Da_{sgs} which compares the time scale of the smallest resolved structure τ_{sgs} and a chemical time scale τ_c:

$$Da_{sgs} = \frac{\tau_{sgs}}{\tau_c} \tag{3.2.6}$$

The subgrid Damköhler number needs to be largely inferior to unity to secure the soundness of the no model assumption ($Da_{sgs} \ll 1$). The definition of τ_{sgs} are multiple, for example Vinuesa et al. [169] propose to estimate the subgrid time scale from the subgrid viscosity ν_t and the subgrid kinetic energy dissipation rate ϵ_{sgs} where:

$$\tau_{sgs} = \left(\frac{\nu_t}{\epsilon_{sgs}}\right)^{1/2} \tag{3.2.7}$$

The dissipation rate can be computed from the subgrid kinetic energy k_{sgs} using the Yoshizawa expression [180]:

$$\epsilon_{sgs} = C_\epsilon \frac{k_{sgs}^{3/2}}{\Delta} \tag{3.2.8}$$

with $C_\epsilon \sim 1.05$ and k_{sgs} is estimated from the subgrid viscosity:

$$k_{sgs} = \left(\frac{\nu_t}{C_\epsilon^{1/3} C_S^{4/3} \Delta}\right)^2 \tag{3.2.9}$$

which leads to:

$$\tau_{sgs} = \frac{C_S^2 \Delta^2}{\nu_t} \tag{3.2.10}$$

The previous expression of τ_{sgs} works well for standard Smagorinsky model, but when a dynamic model is employed, the subgrid viscosity can take very small values when the constant C_S is small. Therefore, using the relation between the subgrid viscosity and the deformation tensor, the equation 3.2.10 can be rewritten as:

$$\tau_{sgs} = \frac{1}{\sqrt{2\widetilde{S}_{ij}\widetilde{S}_{ij}}} \tag{3.2.11}$$

Duwig et al. [45] linked the subgrid Damköhler number with the subgrid velocity fluctuation u'_Δ such as:

$$\tau_{sgs} = \frac{\Delta}{u'_\Delta} \tag{3.2.12}$$

where the subgrid velocity fluctuation is obtained from the subgrid viscosity $\nu_t = c_\kappa \Delta k_{sgs}^{1/2}$ and the subgrid kinetic energy $k_{sgs} = 3u'^2_\Delta/2$ following :

$$u'_\Delta = \sqrt{\frac{2}{3}}\frac{\nu_t}{c_\kappa \Delta} \tag{3.2.13}$$

with the constant $c_\kappa = 0.07$, the expression for the subgrid time scale thus becomes :

$$\tau_{sgs} = \sqrt{\frac{3}{2}}\frac{c_\kappa \Delta^2}{\nu_t} \tag{3.2.14}$$

The equation 3.2.14 is equivalent to the expression of Vinuesa et al. (Eq. 3.2.10) when the constant C_S is taken equal to $\sqrt{c_\kappa/\sqrt{2/3}} \approx 0.29$. Duwig et al. [45] also employed an alternate expression for u'_Δ based on the expression suggested by Colin et al. [25] :

$$u'_\Delta = c_2 \Delta^3 \nabla^2 (\nabla \times \widetilde{u}) \tag{3.2.15}$$

where $c_2 \approx 2$ is a model constant. Duwig et al. found little difference between those two expressions for u'_Δ which lead to the same evaluation of the subgrid Damköhler. Guven et al. [67] introduced an expression of τ_{sgs} based on the scalar dissipation rate χ :

$$\tau_{sgs} = \frac{1}{\chi} \quad \text{with} \quad \chi = 2\frac{\nu_t}{Sc_t}|\nabla Z|^2 \tag{3.2.16}$$

where Sc_t is the subgrid Schmidt number, and Z the mixture fraction. The expression 3.2.16 gives in average a higher subgrid Damköhler in the LES performed by Guven et al. [67].

The expressions for the chemical time τ_c are also multiple. Bouheraoua et al. [13] computed τ_c from the reaction rate of H_2O for a H_2/Air combustion:

$$\tau_c = \frac{\rho}{\dot{\omega}_{H_2O}} \tag{3.2.17}$$

Guven et al. [67] defined a chemical time for each species k based on the species mass fraction and reaction rate:

$$\tau_{c,k} = \frac{\rho Y_k}{\dot{\omega}_k} \tag{3.2.18}$$

Authors	Supersonic configurations	Approach
Edwards et al. [46] 2012	Burrows and Kurkov scramjet configuration [15]	RANS / LES
Boivin et al. [9] 2012	Burner of Cheng [24]	LES
Fulton et al. [56] 2014	University of Virginia's scramjet facility [84]	RANS / LES
Bouheraoua et al. [13] 2017	Burner of Cheng [24]	LES
Guven et al. [67] 2018	Rocketlike engine	LES

Table 3.1: Simulations of supersonic combustion with "no-model" for the reaction rates

and the global chemical time τ_c is taken as the minimum of all species time scale $\tau_{c,k}$. The latter formulation is more strict than the expression from equation 3.2.17 since the mass fractions are always smaller to unity. Duwig et al. [45] computed one-dimensional (1D) laminar premixed flame at stoichiometric conditions to obtain the chemical time:

$$\tau_c = \frac{\delta_L}{s_L} \tag{3.2.19}$$

This expression is maximizing the chemical time scale and is not taking in account the most reactive species. All these different definitions of the subgrid Damköhler number will be investigated in section 6.1.

Table 3.1 shows a non-exhaustive list of large eddy simulations, coupled or not with RANS for wall treatment, performed with the quasi-laminar model for supersonic combustion through the recent years. In addition, Almeida and Navarro-Martinez [1] compared the quasi-laminar model with PDF models for compressible flows in the configuration of Cheng's burner [24] for very coarse meshes: 200 000 and 2 millions points respectively to model the burner while the finest mesh in the work of Bouheraoua et al. [13] has 268 millions of points. They find out that their PDF models perform better than the quasi-laminar model with the same grids, which is predictable since the quasi-laminar model is only relevant when meshes fine enough are concerned.

3.2.2 Physical approaches

As shown in the previous section, the direct approach might be difficult to justify because of the non-linearity of the reaction rate, and the laminar model is only covering little domains of applications. Physical modellings are thus required. According to Veynante and Vervisch [168], the models are usually based on one of the three following approaches (Fig. 3.2):

- Geometrical approach : the flame front is considered as a thin and mobile geometrical surface separating the fresh gases from the burnt gases (premixed flames) or the fuel from the oxidizer (diffusion flames). This approach gave rise to the G-equation model, the flame surface density model or the thickened flame model.

- Turbulent mixing : the chemical time scales are assumed to be shorter than turbulent time scales ($Da \gg 1$), the reaction rate depends on the turbulent mixing which can be expressed using scalar dissipation rate χ. This analysis leads to the Eddy-Break-Up (EBU) model for premixed combustion or the Eddy-Dissipation Concept (EDC) for non-premixed.

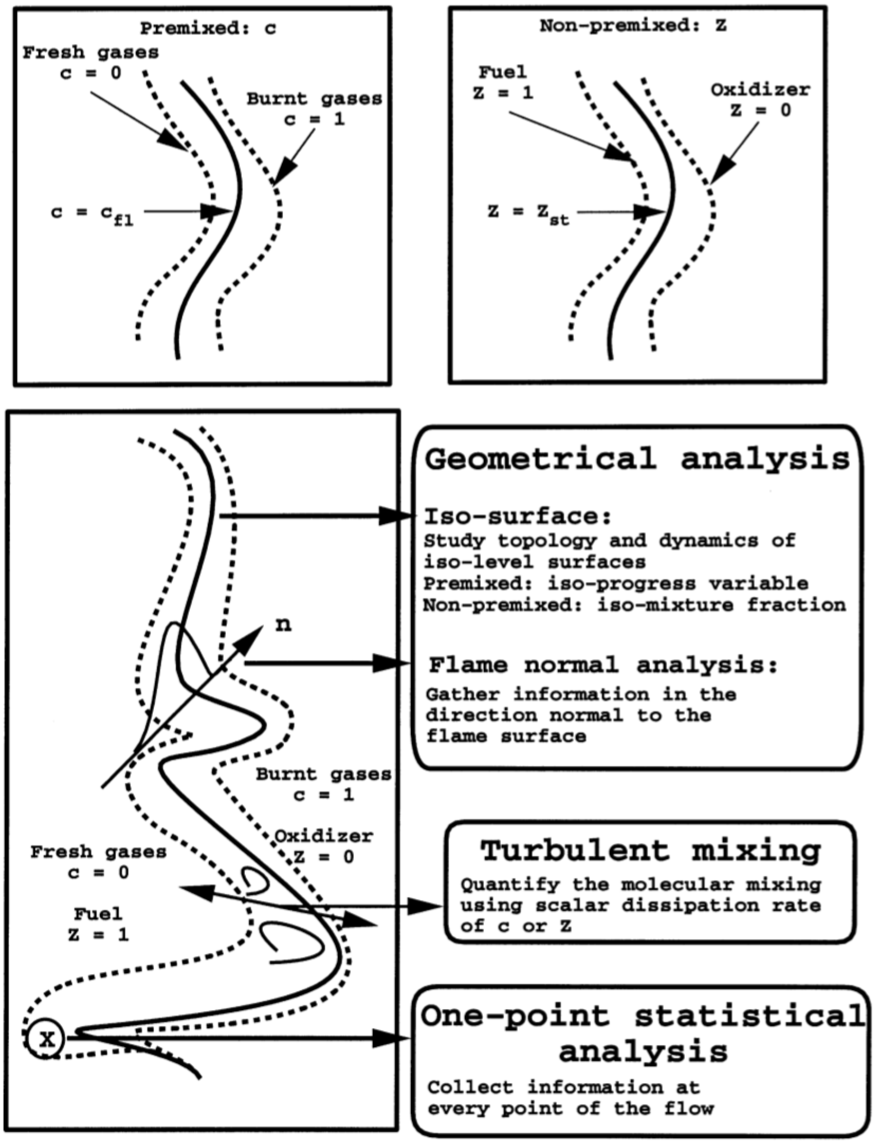

Figure 3.2: Three types of approach for turbulent flames [168].

- Statistical approach : the flame structure is described at every point by a probability density function (PDF). This approach leads to the flamelet progress variable (FPV) model and the partially stirred reactor (PasR) model.

3.2.3 Thickened flame model

The original idea of Thickened Flame Model was introduced by Butler and O'Rourke [16, 124]. The actual flame is simply replaced by a thicker flame featuring the same laminar flame speed which does not require any subgrid scale model for the reaction rate. To thicken the flame, the diffusivity D is multiplied by the thickening factor $\mathcal{F}$ and the reaction rate is divided by this same factor to ensure the conservation of the flame speed:

$$\begin{cases} D_k \mapsto \mathcal{F} D_k \\ \dot{\omega}_k \mapsto \dfrac{\dot{\omega}_k}{\mathcal{F}} \end{cases} \tag{3.2.20}$$

The usual transport equation of a reactive specie k:

$$\frac{\partial \rho Y_k}{\partial t} + \frac{\partial}{\partial x_i}(\rho u_i Y_k) = \frac{\partial}{\partial x_i}\left(\rho D_k \frac{\partial Y_k}{\partial x_i}\right) + \dot{\omega}_k \tag{3.2.21}$$

then becomes:

$$\frac{\partial \rho Y_k}{\partial t} + \frac{\partial}{\partial x_i}(\rho u_i Y_k) = \frac{\partial}{\partial x_i}\left(\rho \mathcal{F} D_k \frac{\partial Y_k}{\partial x_i}\right) + \frac{\dot{\omega}_k}{\mathcal{F}} \tag{3.2.22}$$

The thickening factor is chosen in order to have enough points to resolve the flame with a given resolution of the grid:

$$\mathcal{F}_{max} = \frac{n\Delta}{\delta_L^0} \tag{3.2.23}$$

where n is the number of numerical points desired in the flame, Δ the local LES filter cutoff and δ_L^0 the laminar flame thickness.

Studies [135, 25, 112] have shown that an artificially thickened flame is less sensitive to the turbulence since by thickening the flame, the Damköhler number is decreased by $\mathcal{F}$:

$$Da(\mathcal{F}\delta_L^0) = \frac{l_t}{u'}\frac{S_L^0}{\mathcal{F}\delta_L^0} = \frac{Da(\delta_L^0)}{\mathcal{F}} \tag{3.2.24}$$

A flame efficiency coefficient $\mathcal{E}$ was then introduced by Colin et al. [25] to overcome this defect. The transformations done to the diffusivity and the reaction rate thus become:

$$\begin{cases} D_k \mapsto \mathcal{E}\mathcal{F} D_k \\ \dot{\omega}_k \mapsto \dfrac{\mathcal{E}\dot{\omega}_k}{\mathcal{F}} \end{cases} \tag{3.2.25}$$

The efficiency function is defined by Colin et al. [25] as the ratio between the wrinkling factor Ξ of the actual flame and the thickened flame:

$$\mathcal{E} = \frac{\Xi(\delta_L^0)}{\Xi(\mathcal{F}\delta_L^0)} = \frac{1 + \alpha\Gamma\left(\dfrac{\Delta}{\delta_L^0}, \dfrac{u'_\Delta}{S_L^0}\right)\dfrac{u'_\Delta}{S_L^0}}{1 + \alpha\Gamma\left(\dfrac{\Delta}{\mathcal{F}\delta_L^0}, \dfrac{u'_\Delta}{S_L^0}\right)\dfrac{u'_\Delta}{S_L^0}} \tag{3.2.26}$$

where α and Γ are the parameters defined by the model:

$$\begin{cases} \alpha = \beta \dfrac{2\ln(2)}{3c_{ms}\left[\mathrm{Re_t}^{1/2} - 1\right]} \\ \Gamma\left(\dfrac{\Delta}{\delta_L}, \dfrac{u'_\Delta}{S_L^0}\right) = 0.75\exp\left[-\dfrac{1.2}{(u'_\Delta/S_L^0)^{0.3}}\right]\left(\dfrac{\Delta}{\delta_L}\right)^{2/3} \end{cases} \tag{3.2.27}$$

with the model constants $\beta = 1$ and $c_{ms} = 0.28$, and the subgrid scale velocity u'_Δ is evaluated from equation 3.2.13.

With a constant flame thickening factor $\mathcal{F}$, the TFM can only be employed for premixed flames. Legier et al. [91] introduced a dynamic model of TFM by giving a dynamic version of thickening factor which depends on a flame sensor $\mathcal{S}$:

$$\mathcal{F} = 1 + (\mathcal{F}_{max} - 1)\mathcal{S} \tag{3.2.28}$$

where $\mathcal{F}_{max}$ is computed using the equation 3.2.23. Multiple formulations of the flame sensor exist in the literature [91, 86, 55, 6, 76] and are not discussed here.

A dynamic formulation of the efficiency function is available in the literature [22, 23, 172, 148, 170]. The thickened flame model is widely used in subsonic flows to model turbulent combustion [6, 51, 52], but its implementation in supersonic flows is still scarce. Fureby [58] compared the thickened flame model with the eddy dissipation concept (EDC, presented in the next paragraph) in large eddy simulations of the ONERA/JAXA supersonic combustion rig [159] by using a seven-step chemical mechanism for H_2 [33]. EDC is found to be slightly better than TFM in the previous configuration.

3.2.4 Eddy Dissipation Concept

Introduced by Magnussen [108], the Eddy Dissipation Concept (EDC) consists in splitting the flow into two zones : a dissipative or mixing zone with fine structures where reactions take place (denoted by $*$) and a surrounding area with large-scale flow structures (denoted by $^\circ$). The dissipative zone ($*$) is supposed to behave like a perfectly stirred reactor (PSR) while almost no chemical reaction occurs in the surrounding zone ($^\circ$). The filtered reaction rate $\bar{\dot{\omega}}_k$ can be expressed as:

$$\bar{\dot{\omega}}_k = \int_\psi \mathcal{P}(\psi)\dot{\omega}_k(\psi)d\psi \tag{3.2.29}$$

where $\psi = [Y_k, T]^T$ and $\mathcal{P}$ is the bimodal joint scalar probability density function (PDF) defined as:

$$\mathcal{P}(\psi) = \gamma^*\delta(\psi - \psi^*) + (1-\gamma^*)\delta(\psi - \psi^\circ) \tag{3.2.30}$$

where γ^* is the fine structures volume fraction and δ the Dirac function. The reaction rate becomes:

$$\bar{\dot{\omega}}_k = \gamma^*\dot{\omega}_k(\psi^*) + (1-\gamma^*)\dot{\omega}_k(\psi^\circ) \tag{3.2.31}$$

which can be simplified to $\bar{\dot{\omega}}_k = \gamma^*\dot{\omega}_k(\psi^*)$ as the reaction rate is vanishing in the surrounding area. The reaction rate of the fine structures $\dot{\omega}_k(\psi^*)$ can be computed using the subgrid balance equations between the fines structures and the surroundings:

$$\begin{cases} \bar{\rho}(Y_k^* - Y_k^\circ) = \tau^*\dot{\omega}_k(Y_k^*, T^*) \\ \bar{\rho}\sum_{k=1}^{N_{sp}}(Y_k^* h_k^* - Y_k^\circ h_k^\circ) = \tau^* \sum_{k=1}^{N_{sp}} \Delta h_{f,k}^0 \dot{\omega}_k(Y_k^*, T^*) \end{cases} \tag{3.2.32}$$

where τ^* is the subgrid mixing time. The system of equations 3.2.32 has 4 unknowns (Y_k^*, T^*, Y_k° and T°; h_k can be computed from T and $\dot{\omega}_k$ from Y_k^* and T^*) for only two equations. The system is under-resolved and requires two additional equations. The fine structure variables can be linked to the surrounding variables by applying the PDF on the resolved fields $\widetilde{Y}_k$ and $\widetilde{T}$ such as:

$$\begin{cases} \widetilde{Y}_k = \gamma^* Y_k^* + (1-\gamma^*)Y_k^\circ \\ \widetilde{T} = \gamma^* T^* + (1-\gamma^*)T^\circ \end{cases} \tag{3.2.33}$$

Injecting 3.2.33 into 3.2.32 leads to:

$$\begin{cases} \bar{\rho}(Y_k^* - \widetilde{Y}_k) = (1-\gamma^*)\tau^*\dot{\omega}_k(Y_k^*, T^*) \\ \bar{\rho}\sum_{k=1}^{N_{sp}}(Y_k^* h_k^* - \widetilde{Y}_k\widetilde{h}_k) = (1-\gamma^*)\tau^* \sum_{k=1}^{N_{sp}} \Delta h_{f,k}^0 \dot{\omega}_k(Y_k^*, T^*) \end{cases} \tag{3.2.34}$$

The subgrid mixing time τ^* and the volume fraction γ^* can be estimated from the subgrid kinetic energy k such as $\gamma^* \approx 1.02(\mu/\bar{\rho}\Delta k^{1/2})^{3/4}$ and $\tau^* \approx 1.23(\Delta\mu/\bar{\rho}k^{3/2})^{1/2}$ [58].

3.2.5 Partially Stirred Reactor

Initially introduced by Correa [28], then modified by Sabel'nikov and Figueira da Silva [142], the Partially Stirred Reactor (PaSR) model relies on the same principle as the EDC model which consists in dividing the flow into a fine structure zone and a surrounding zone. The PaSR model thus follows the same closure equations (Eq. 3.2.34) but with different subgrid mixing time τ^* and volume fraction γ^*. τ^* is estimated as the harmonic mean of the Kolmogorov time scale $\tau_K = \eta_k/u'_k$ and the large scales time $\tau_\Delta = \Delta/u'_\Delta$:

$$\tau^* = \sqrt{\tau_K \tau_\Delta} \tag{3.2.35}$$

with $\eta_k = (\nu^3/\epsilon)^{1/4}$, $u'_k = (\nu\epsilon)^{1/4}$, $u'_\Delta = \sqrt{2k/3}$, $\epsilon = k^{3/2}/\Delta$ and $k = (\nu_t/(0.069\Delta))^2$ [7, 118], the subgrid mixing time can be expressed as:

$$\tau^* = 0.039\Delta^2 \frac{\nu^{1/4}}{\nu_t^{5/4}} \tag{3.2.36}$$

and the fine structure volume fraction is expressed as:

$$\gamma^* = \frac{\tau_c}{\tau_c + \tau^*} \tag{3.2.37}$$

where τ_c is a chemical time scale usually estimated from one-dimensional laminar premixed flames [7, 118, 57, 141] such as $\tau_c = \delta_L^0/S_L^0$. The PaSR model has been validated in LES by Berglund et al. [7] on the ONERA/LAERTE scramjet and by Fureby et al. [59] on the HyShot II configuration.

Sabel'Nikov and Fureby [141] modified the PaSR model to the Extended PaSR (EPaSR) model by adding convection and diffusive terms to the subgrid balance equations (Eq. 3.2.34) and a transport equation for γ^* such as:

$$\begin{cases} \dfrac{\partial \overline{\rho}\gamma^* Y_k^*}{\partial t} + \dfrac{\partial}{\partial x_i}(\overline{\rho}\widetilde{u}_i\gamma^* Y_k^*) = \dfrac{\partial}{\partial x_i}\left[\overline{\rho}\gamma^* D_k \dfrac{\widetilde{W}_k}{\widetilde{W}}\dfrac{\partial X_k^*}{\partial x_i} + \dfrac{\mu_t\gamma^*}{Sc_{t,k}}\dfrac{\partial Y_k^*}{\partial x_i}\right] + \gamma^*\dot{\omega}_k + M_k^* \quad k = 1, N_{sp} \\ \dfrac{\partial \overline{\rho}\gamma^* h^*}{\partial t} + \dfrac{\partial}{\partial x_i}(\overline{\rho}\widetilde{u}_i\gamma^* h^*) = \dfrac{\partial \overline{p}}{\partial t} + \dfrac{\partial}{\partial x_i}\left[\overline{\lambda}\gamma^*\dfrac{\partial \widetilde{T}}{\partial x_i} + \dfrac{\mu_t\gamma^*}{Pr_t}\dfrac{\partial h^*}{\partial x_i}\right] + \overline{\rho}\gamma^*\displaystyle\sum_{k=1}^{N_{sp}}\widetilde{h}_{s,k}D_k\dfrac{\widetilde{W}_k}{\widetilde{W}}\dfrac{\partial X_k^*}{\partial x_i} \\ \qquad\qquad + \dfrac{\partial}{\partial x_j}(\widetilde{\tau}_{ij}\widetilde{u}_i) + \gamma^*\overline{\dot{\omega}_T} + M_h^* \\ \dfrac{\partial \overline{\rho}\gamma^*}{\partial t} + \dfrac{\partial}{\partial x_i}(\overline{\rho}\widetilde{u}_i\gamma^*) = -\dfrac{\overline{\rho}(\gamma^* - \gamma_{eq}^*)}{\tau^*} \end{cases} \tag{3.2.38}$$

with the exchange terms between the fine structures and the surroundings M_k^* and M_h^* defined as:

$$\begin{cases} M_k = \dfrac{1}{2}(\dot{m}_e + |\dot{m}_e|)Y_k^\circ + \dfrac{1}{2}(\dot{m}_e - |\dot{m}_e|)Y_k^* - \dfrac{\gamma^*\overline{\rho}(Y_k^* - \widetilde{Y}_k)}{\tau^*(1-\gamma^*)} \\ M_h = \dfrac{1}{2}(\dot{m}_e + |\dot{m}_e|)h^\circ + \dfrac{1}{2}(\dot{m}_e - |\dot{m}_e|)h^* - \dfrac{\gamma^*\overline{\rho}(h^* - \widetilde{h})}{\tau^*(1-\gamma^*)} \end{cases} \tag{3.2.39}$$

where $\dot{m}_e = -\overline{\rho}(\gamma^* - \gamma_{eq}^*)/\tau^*$ is the exchange mass flow rate from the surroundings to the fine structures. The system is totally closed when an expression for γ_{eq}^* is found. In the EPaSR model, the equivalent volume fraction γ_{eq}^* has the same definition of the volume fraction γ^* of PaSR model such as:

$$\gamma_{eq}^* = \frac{\tau_c}{\tau_c + \tau^*} \tag{3.2.40}$$

The definition for τ_c and τ^* remains the same as the PaSR model. Sabel'Nikov and Fureby [141] validated their model by comparing the LES-EPaSR data with DNS data of a planar turbulent flame in homogenous isotropic turbulence and with experimental data for an axisymmetric dump combustor.

Moule et al. [118] found that the consideration of the convective and diffusive terms in the EPaSR model does not play a huge role, and can be neglected. They thereby simplified the EPaSR to the U-PaSR (Unsteady PaSR) model by keeping only the time derivative, and adding it to the subgrid balance equations (Eq. 3.2.34):

$$\begin{cases} \dfrac{\partial \overline{\rho} Y_k^*}{\partial t} + \overline{\rho}\dfrac{(Y_k^* - \widetilde{Y}_k)}{(1-\gamma^*)\tau^*} = \dot{\omega}_k(Y_k^*, T^*) \\ \dfrac{\partial \overline{\rho} h^*}{\partial t} + \overline{\rho}\displaystyle\sum_{k=1}^{N_{sp}} \dfrac{(Y_k^* h_k^* - \widetilde{Y}_k \widetilde{h}_k)}{(1-\gamma^*)\tau^*} = \displaystyle\sum_{k=1}^{N_{sp}} \Delta h_{f,k}^0 \dot{\omega}_k(Y_k^*, T^*) \end{cases} \tag{3.2.41}$$

Moule et al. [118] performed a LES of the Cheng's burner [24] with the U-PaSR model and found the comparison with the experimental data satisfying.

3.2.6 Flamelet model

Solely non-premixed diffusion flamelet model can be found in the literature for supersonic flows, therefore, premixed flamelet model is not discussed in this section. Initially introduced by Peters [127], the flamelet model assumes that the chemical time scales are shorter than the turbulent time scales, so the flame can be assimilated to one-dimensional laminar flamelets. Instead of solving $N_{species}$ transport equations, only a set of variables are transported and the chemical processes are mapped in a table controlled by this set of variables. The steady laminar model of Peters [127] transports only one variable, the mixture fraction Z, which tracks the mixing of fuel and oxidizer. This model is criticized for its inability to predict properly ignition and extinction. One additional parameter is required to improve these phenomena prediction. Pierce and Moin [129] introduced the Flamelet Progress-Variable (FPV) model in which the progress variable C is transported additionally to the mixture fraction Z. The equations are:

$$\begin{cases} \dfrac{\partial \overline{\rho}\widetilde{Z}}{\partial t} + \dfrac{\partial}{\partial x_i}(\overline{\rho}\widetilde{u}_i\widetilde{Z}) = \dfrac{\partial}{\partial x_i}\left[\overline{\rho}\left(D_Z + \dfrac{\nu_t}{Sc_t}\right)\dfrac{\partial \widetilde{Z}}{\partial x_i}\right] \\ \dfrac{\partial \overline{\rho}\widetilde{C}}{\partial t} + \dfrac{\partial}{\partial x_i}(\overline{\rho}\widetilde{u}_i\widetilde{C}) = \dfrac{\partial}{\partial x_i}\left[\overline{\rho}\left(D_C + \dfrac{\nu_t}{Sc_t}\right)\dfrac{\partial \widetilde{C}}{\partial x_i}\right] + \overline{\rho}\dot{\omega}_C \end{cases} \tag{3.2.42}$$

where D_Z and D_C are respectively the diffusivity of mixture fraction and progress variable. Filtered variables are constructed from the mixture fraction and the progress variable by integrating over the joint subgrid PDF of Z and C, $\widetilde{P}(Z,C)$, to take into account the subgrid effects. For any filtered variable $\widetilde{\Phi}$, it follows:

$$\widetilde{\Phi} = \int \Phi(Z,C)\widetilde{P}(Z,C)dZdC \tag{3.2.43}$$

where $\Phi(Z,C)$ is obtained from the flamelet library. The joint PDF $\widetilde{P}(Z,C)$ can be decomposed into two separated PDF:

$$\widetilde{P}(Z,C) = \widetilde{P}(C \mid Z)\widetilde{P}(Z) \tag{3.2.44}$$

where $\widetilde{P}(C \mid Z)$ can be approximated by a delta function:

$$\widetilde{P}(C|Z) = \delta(C- < C|Z >) \tag{3.2.45}$$

where $< C \mid Z >$ is the conditional mean of C by Z. Furthermore, $\widetilde{P}(Z)$ is generally given by an assumed beta PDF:

$$\widetilde{P}(Z) = \frac{Z^{a-1}(1-Z)^{b-1}}{\int (Z*-1)^{a-1}(1-Z*)^{b-1}dZ*} \tag{3.2.46}$$

with the coefficient a and b determinated through the relations:

$$\begin{cases} a = \widetilde{Z}\left(\dfrac{1}{S_Z} - 1\right) \\ b = a\left(\dfrac{1}{\widetilde{Z}} - 1\right) \end{cases} \tag{3.2.47}$$

and the segregation factor S_Z is defined as the ratio of variance of Z, $\widetilde{Z''^2}$, on the maximum level of variance $\widetilde{Z}(1-\widetilde{Z})$:

$$S_Z = \frac{\widetilde{Z''^2}}{\widetilde{Z}(1-\widetilde{Z})} \tag{3.2.48}$$

An algebraic formulation is used to model the variance of mixture fraction:

$$\widetilde{Z''^2} = C_Z \Delta^2 |\nabla \widetilde{Z}|^2 \tag{3.2.49}$$

where C_Z is determined dynamically [129] and Δ is the filter size. Finally, each filtered variable $\widetilde{\Phi}$ is function of a set of three parameters ($\widetilde{Z}$,$\widetilde{Z''^2}$,$\widetilde{C}$) from LES: two of them are required ($\widetilde{Z}$ and $\widetilde{C}$) to read from the flamelet library and all of them are needed to evaluate the beta PDF.

The previous flamelet model is designed for low Mach number flows and does not suit supersonic flows since compressibility effects and viscous heating are not accounted. Terrapon et al. [163] developped a flamelet model for supersonic combustion in RANS, tested it on the HyShot II configuration. Saghafian et al. [145] extended this model to LES and called it Compressible Flamelet/Progress Variable (CFPV) approach. A table with five entries would be too large to be stored properly, the idea of CFPV is to decompose any quantity Φ into a reference value Φ_0 and a fluctuation part Φ':

$$\Phi(\widetilde{Z},\widetilde{Z''^2},\widetilde{C},\overline{p},\widetilde{e}) = \Phi_0(\widetilde{Z},\widetilde{Z''^2},\widetilde{C};\overline{p}_0,\widetilde{e}_0) + \Phi'(\overline{p},\widetilde{e};\widetilde{Z},\widetilde{Z''^2},\widetilde{C}) \tag{3.2.50}$$

The reference value Φ_0 is read directly from the flamelet library (as the model proposed by Pierce et Moin [129]) at corresponding conditions p_0 and e_0. The fluctuating term Φ' is function of two variables (p and e) that are additionally dependant of three parameters ($\widetilde{Z}$, $\widetilde{Z''^2}$ and $\widetilde{C}$). In order to determinate the fluctuating term for the temperature, two assumptions are made. The first consists in stating that a small deviation in pressure and temperature will not change the mass fractions, that is to say:

$$Y_k(\widetilde{Z},\widetilde{Z''^2},\widetilde{C},\overline{p},\widetilde{e}) = Y_{k,0}(\widetilde{Z},\widetilde{Z''^2},\widetilde{C};\overline{p}_0,\widetilde{e}_0) \tag{3.2.51}$$

which naturally leads to the same conclusion for the gas constant:

$$r(\widetilde{Z},\widetilde{Z''^2},\widetilde{C},\overline{p},\widetilde{e}) = r_0(\widetilde{Z},\widetilde{Z''^2},\widetilde{C};\overline{p}_0,\widetilde{e}_0) \tag{3.2.52}$$

The second assumption is to approximate the internal energy $\widetilde{e} = \widetilde{h} - \widetilde{rT}$ by:

$$\widetilde{e} \approx \widetilde{e}_0 + \int_{T_0}^{\widetilde{T}} \frac{\widetilde{r}}{\widetilde{\gamma}(T) - 1} dT \tag{3.2.53}$$

where $\widetilde{\gamma}(T)$ is computed using a linear expansion equation:

$$\widetilde{\gamma}(T) = \widetilde{\gamma}_0 + a_\gamma(\widetilde{T} - T_0) \tag{3.2.54}$$

The variables $\widetilde{e}_0$, $\widetilde{r}_0$, $\widetilde{\gamma}_0$, a_γ and T_0 are computed in a preprocessing step and then tabulated in the flamelet library. The analytical relationship between temperature and internal energy becomes:

$$\widetilde{T} = T_0 + \frac{\widetilde{\gamma}_0 - 1}{a_\gamma}\left[\exp\left(a_\gamma \frac{\widetilde{e} - \widetilde{e}_0}{\widetilde{r}}\right) - 1\right] \tag{3.2.55}$$

The molecular viscosity $\widetilde{\mu}$ and the thermal diffusivity $\widetilde{\lambda}$ are corrected by a power-law function:

$$\begin{cases} \widetilde{\mu} = \widetilde{\mu}_0 \left(\dfrac{\widetilde{T}}{T_0}\right)^{a_\mu} \\ \widetilde{\lambda} = \widetilde{\lambda}_0 \left(\dfrac{\widetilde{T}}{T_0}\right)^{a_\lambda} \end{cases} \tag{3.2.56}$$

where a_μ and a_λ are two coefficients dependant of $\widetilde{Z}$, $\widetilde{Z''^2}$ and $\widetilde{C}$ computed by perturbing the flamelet solution, and tabulated. The pressure is from the perfect gas equation of state by assuming $\widetilde{rT} = \widetilde{r}\widetilde{T}$:

$$\overline{p} = \overline{\rho}\widetilde{r}\widetilde{T} \tag{3.2.57}$$

Finally, the source term of the progress variable is also corrected from the reference value:

$$\overline{\dot{\omega}}_C = \overline{\dot{\omega}}_{C_0} \left(\frac{\overline{\rho}}{\overline{\rho}_0}\right)^{a_\rho} \exp\left[-T_a\left(\frac{1}{\widetilde{T}} - \frac{1}{T_0}\right)\right] \tag{3.2.58}$$

The values of ρ_0, a_ρ and T_a are computed during preprocessing and tabulated. Saghafian et al. [144] validated this model for supersonic combustion on the HIFiRE 2 configuration.

3.3 Wall-layer model for LES

3.3.1 Generalities

In wall bounded turbulent flows, the boundary layer can be divided into an inner layer (near the wall) where the viscous effets are dominating and an outer layer in which they are negligible (see Fig. 3.3). A wall-resolved LES requires almost the same description of the near wall region as the DNS [21, 116, 130, 157, 132], which involves a huge number of points, since the resolution of inner layer strongly scales with the Reynolds number such that [21]:

$$N_x N_y N_z \propto Re^{1.8} \tag{3.3.1}$$

Chapman [21] also estimated the number of points required for the outer layer:

$$N_x N_y N_z \propto Re^{0.4} \tag{3.3.2}$$

While the number of points required to resolve the outer layer is affordable, the one required for the inner layer quickly becomes prohibitive, especially at high Reynolds number flows. The wall-resolved LES is therefore often discarded at the expense of the wall-modeled LES [37]. It is important to highlight that wall-modeled LES (WMLES) only models the inner layer of the boundary layer and leaves the outer layer fully resolved, which is different from the Detached Eddy Simulation (DES) introduced by Spalart [97] that models the whole boundary layer. Many approaches of the

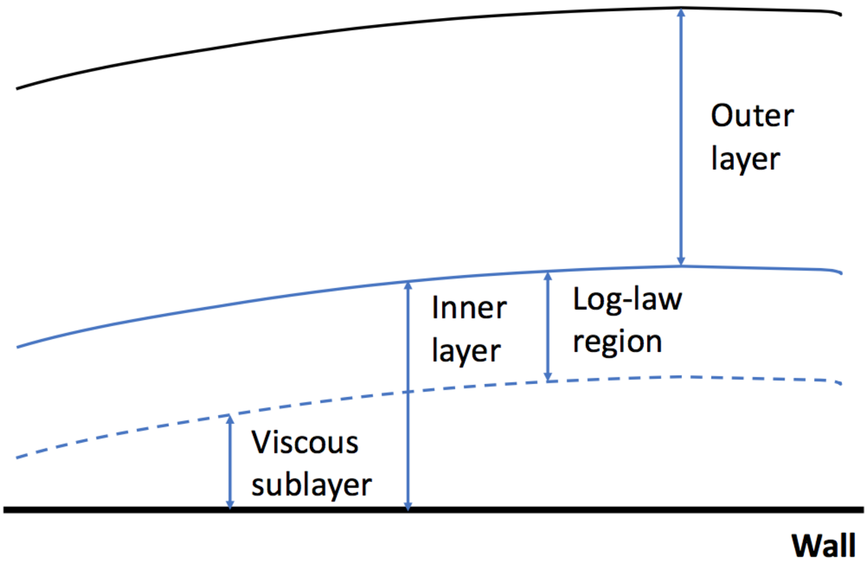

Figure 3.3: Schematic of different regions in turbulent boundary layer.

WMLES are proposed in the literature [132, 131, 89]. Two families of wall model approaches can be distinguished and are classified in figure 3.4.

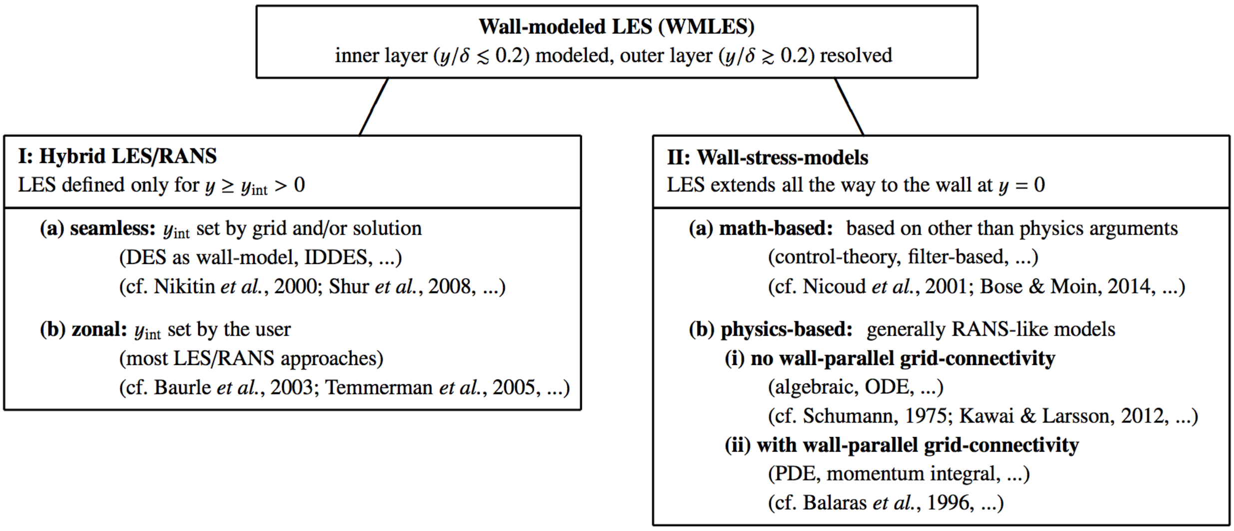

Wall-modeled LES (WMLES)
inner layer ($y/\delta \lesssim 0.2$) modeled, outer layer ($y/\delta \gtrsim 0.2$) resolved

I: Hybrid LES/RANS
LES defined only for $y \geq y_{\text{int}} > 0$

(a) seamless: y_{int} set by grid and/or solution
(DES as wall-model, IDDES, ...)
(cf. Nikitin *et al.*, 2000; Shur *et al.*, 2008, ...)

(b) zonal: y_{int} set by the user
(most LES/RANS approaches)
(cf. Baurle *et al.*, 2003; Temmerman *et al.*, 2005, ...)

II: Wall-stress-models
LES extends all the way to the wall at $y = 0$

(a) math-based: based on other than physics arguments
(control-theory, filter-based, ...)
(cf. Nicoud *et al.*, 2001; Bose & Moin, 2014, ...)

(b) physics-based: generally RANS-like models
(i) no wall-parallel grid-connectivity
(algebraic, ODE, ...)
(cf. Schumann, 1975; Kawai & Larsson, 2012, ...)
(ii) with wall-parallel grid-connectivity
(PDE, momentum integral, ...)
(cf. Balaras *et al.*, 1996, ...)

Figure 3.4: Classification of wall-modeled LES approaches, from Larsson et al. [89].

The first approach, called hybrid LES/RANS method consists in spliting the computional domain into two sub-regions solved with either LES or RANS equations. Generally, the RANS region covers the inner layer and extends from the wall to a certain interface y_{int} which can be calculated during the simulations (seamless), or defined by the user (zonal) [89]. This interface will be the area of exchange between RANS and LES and is used as boundary conditions to the LES domain which is above y_{int}. The RANS domain may require very refined grids that can become expensive. The second family of models belongs to the wall-stresses models, where the whole computational domain is solved with LES equations. In the present work, we will be using the latter model, and the reader can refer to the references cited above for more detailed descriptions of the models.

3.3.2 Definition of wall dimensionless numbers

Before tackling the wall stress model, dimensionless numbers relative to the wall are presented in this section. The non-dimensional wall distance y^+ is expressed as:

$$y^+ = \frac{u_\tau y}{\nu} \tag{3.3.3}$$

where y is the distance to the wall and u_τ the friction velocity at the wall defined as:

$$u_\tau = \sqrt{\frac{\tau_w}{\rho}} \tag{3.3.4}$$

with $\tau_w = \mu \left(\frac{\partial u}{\partial y}\right)_{y=0}$ the wall shear stress. Finally, y^+ becomes:

$$y^+ = y\sqrt{\frac{1}{\nu}\left(\frac{\partial u}{\partial y}\right)_{y=0}} \tag{3.3.5}$$

The dimensionless velocity u^+ is defined as the ratio of the streamwise velocity u on the friction velocity u_τ:

$$u^+ = \frac{u}{u_\tau} \tag{3.3.6}$$

A friction Reynolds number Re_τ can be constructed from the friction velocity u_τ and a characteristic length H which corresponds to the half-height of the channel:

$$Re_\tau = \frac{u_\tau H}{\nu} \tag{3.3.7}$$

The dimensionless wall distance y^+ can be rewritten as:

$$y^+ = \frac{y Re_\tau}{H} \tag{3.3.8}$$

3.3.3 Wall stress model

Wall stress model has been chosen for its simplicity to implement and its low computional cost. Assuming that x is the direction parallel to the wall and y is the direction normal to the wall, the conservation of momentum projected in the $x-$direction for the first cells becomes:

$$\begin{aligned}\frac{\partial}{\partial t}\overline{\rho}\widetilde{u}_x + \frac{\partial}{\partial x_i}\overline{\rho}\widetilde{u}_i\widetilde{u}_x =& -\frac{\partial \overline{p}}{\partial x} + \frac{\partial}{\partial x}\left[2\mu\left(\frac{\partial \widetilde{u}_x}{\partial x} - \frac{1}{3}\frac{\partial \widetilde{u}_i}{\partial x_i}\right)\right] \\ &+ \frac{\partial}{\partial y}\left[\mu\frac{\partial \widetilde{u}_y}{\partial x} + (\mu + \mu_{t,wm})\frac{\partial \widetilde{u}_x}{\partial y}\right] + \frac{\partial}{\partial z}\left[\mu\left(\frac{\partial \widetilde{u}_z}{\partial x} + \frac{\partial \widetilde{u}_x}{\partial z}\right)\right]\end{aligned} \tag{3.3.9}$$

where $\mu_{t,wm} = \rho\nu_{t,wm}$ and the eddy viscosity of the wall model $\nu_{t,wm}$ is given by a zero-equation mixing length model [18] based on the van Driest damping function:

$$\nu_{t,wm} = \kappa u_\tau y \left[1 - \exp(-u_\tau y/\nu A^+)\right]^2 \tag{3.3.10}$$

with u_τ the friction velocity at the wall and y the distance to the wall. The previous expression can be rewritten with the dimensionless wall distance y^+:

$$\nu_{t,wm} = \kappa\nu y^+ \left[1 - \exp(-y^+/A^+)\right]^2 \tag{3.3.11}$$

$\kappa = 0.41$ is the von Karman constant and $A^+ = 17$. The same eddy-viscosity is added to the energy equation for the temperature gradient and the velocity gradient in the wall normal direction:

$$\begin{cases} \dfrac{\partial}{\partial y}\left(\lambda \dfrac{\partial \widetilde{T}}{\partial y}\right) \mapsto \dfrac{\partial}{\partial y}\left[(\lambda + \lambda_{t,wm})\dfrac{\partial \widetilde{T}}{\partial y}\right] \\ \dfrac{\partial}{\partial y}\left(\mu \widetilde{u}_x \dfrac{\partial \widetilde{u}_x}{\partial y}\right) \mapsto \dfrac{\partial}{\partial y}\left[(\mu + \mu_{t,wm})\widetilde{u}_x \dfrac{\partial \widetilde{u}_x}{\partial y}\right] \end{cases} \tag{3.3.12}$$

where $\lambda_{t,wm} = \rho C_p \nu_{t,wm}/Pr_{t,wm}$, with $Pr_{t,wm} = 0.9$. The wall shear stress can be computed using directly the velocity provided by the LES (see Eq. 3.3.9) or by solving an ODE with equilibrium assumption based on the simplified momentum and energy equations:

$$\begin{cases} \dfrac{d}{dy}\left[(\mu + \mu_{t,wm})\dfrac{dU}{dy}\right] = 0 \\ \dfrac{d}{dy}\left[(\lambda + \lambda_{t,wm})\dfrac{dT}{dy}\right] = -\dfrac{d}{dy}\left[(\mu + \mu_{t,wm})U\dfrac{dU}{dly}\right] \end{cases} \tag{3.3.13}$$

The ODE based model provides more accurate results, but is considerably more expensive. In practice, those equations are solved only in presence of other physical effects, such as strongly non-adiabatic compressible flow [89]. Therefore, in the current work, the wall shear stress is computed from the velocity provided by the LES and results are shown in section 4.5.5.

3.4 Description of the CFD code SiTCom-B

In this section, a brief overview of the main features of the code is given, followed by a more detailed description of Immersed Boundary Method (IBM).

3.4.1 Overview

SiTCom-B (Simulation of Turbulent Combustion with Billions of points) [153] is a parallel solver developped in CORIA and written in Fortran 90 that solves compressible reacting Navier-Stokes equations in cartesian meshes. Immersed Boundary Method (IBM, see Sec. 3.4.2) is employed to deal with complex geometries. It has been designed to perform DNS and highly resolved LES on multiple processors with the MPI (Message Passing Interface) libraries. The spatial discretization is performed with the finite volume method where the fluxes are computed with the fourth order centered skew-symmetric-like numerical scheme from Ducros et al. [44]. The temporal discretization is explicit and is ensured by a 4th order Runge-Kutta method [150]. Boundary conditions can be prescribed with NSCBC (Navier Stokes Characteristic Boundary Conditions), initially developped by Poinsot and Lele [134] and extended to 3D by Lodato et al. [102]. Four turbulence models are available in the solver SiTCom-B for the LES: Smagorinsky model [154], dynamic Smagorinsky model [93, 117], Wall-Adapting Local Eddy-viscosity (WALE) model [43] and the model of Vreman [171]. Solely the Smagorinsky models (constant and dynamic) are used in this work. If needed, Homogeneous Isotropic Turbulence (HIT) can be injected at the inlet of the computational domain using the expressions given in [11]. Besides the perfect gas assumption for the equation of state (EoS), cubic equations are also available to take in account the effects of real gas which is not the case in this study. Finally, second and fourth order artificial dissipation terms [162, 161, 160] are implemented to overcome spurious oscillations and damp high-frequency modes. The later terms are only applied in zones where strong gradients of density or pressure are detected [128]. For all the simulations performed in this thesis, the hyperviscosity constants α_1, α_2 (second order terms for shock capturing), β_1 and β_2 (fourth order terms) are set to 1.5, 1.5, 0.4 and 1.0 respectively.

Three chemistry modeling solvers are available in SiTCom-B: multi-species formulation, tabulated solver (FPI) and a hybrid solver (HTTC). In this work, solely simulations with multi-species formulation are performed. In this solver, chemical mechanisms written in CHEMKIN format are read to compute quantities involved in reacting flows, such as forward and reverse rates of each reaction j (K_{fj}, K_{rj}), heat capacity, enthalpy or entropy of each species k (C_{pk}, h_k, s_k). A transport equation (Eq. 2.2.7) is solved for each species and thermodynamic properties are computed thereafter for the next iteration. The species diffusion velocities are modeled with the Hirschfelder and Curtiss approximation [70] coupled to a velocity correction. During my Ph.D., the multi-species solver has been optimized to perform simulations almost twice faster than initially.

Three timesteps (convective, diffusive and chemical) are computed in SiTCom-B, and the smallest is chosen to ensure the stability of simulations. The convective timestep Δt^C is based on the Courant-Friedrichs-Lewy (CFL) criterion which imposes the velocity of any perturbation $|u_i| + c$ (c is the soundspeed) to be lower than a limit velocity $V_L = \min(\Delta x_i)/\Delta t^C$, where Δx_i is the cell size in the direction i. The soundspeed is computed from the relation $c = \sqrt{\gamma r T}$. The CFL number is introduced to limit the timestep:

$$\Delta t^C = CFL \times \min_i \left(\frac{\Delta x_i}{|u_i| + c} \right) \tag{3.4.1}$$

The diffusive timestep Δ_t^D is based on the Fourier criterion which imposes the overall timestep to be lower than the diffusive timestep. The Fourier number Fo is introduced to compute the diffusive timestep for each transported scalar Φ:

$$\Delta t_\Phi^D = Fo \times \min_i \left(\frac{\Delta x_i^2}{D_\Phi} \right) \tag{3.4.2}$$

The diffusive timestep Δt^D is taken as the minimum of timestep of each transported scalar Δt_Φ^D. The chemical timestep is based on the species mass fraction Y_k and reaction rate $\dot{\omega}_k$, and is defined as:

$$\Delta t^{chem} = \min_k \left(\frac{a_{tol} + r_{tol} \rho Y_k}{|\dot{\omega}_k|} \right) \tag{3.4.3}$$

where a_{tol} and r_{tol} are model parameters. In this work, the CFL and the Fourier numbers are both equal to 0.5, and $a_{tol} = 10^{-3}$ and $r_{tol} = 0.1$. Finally, the solver timestep Δt is taken as the lowest among the three defined previously:

$$\Delta t = \min(\Delta t^C, \Delta t^D, \Delta t^{chem}) \tag{3.4.4}$$

3.4.2 Immersed Boundary Method

Immersed Boundary Method (IBM) is used here to model complex geometries. A description of the original version of IBM implemented in SiTCom-B is given in this section, but this version has shown some limits for the complex geometry simulated in this thesis. The coding has therefore been modified to deal with the issues. In addition, isothermal wall condition at the interface between the fluid and the immersed domain is implemented in the code and presented below.

3.4.2.1 Original IBM implementation

The immersed boundary method has been introduced by Peskin [126] to investigate interaction between fluid and surrounding walls for biomecanical applications. IBM was implemented by Bouheraoua in SiTCom-B during her Ph.D. [12], based on the work of Merlin [113]. This method consists in creating boundaries inside the computational domain and is composed of five steps:

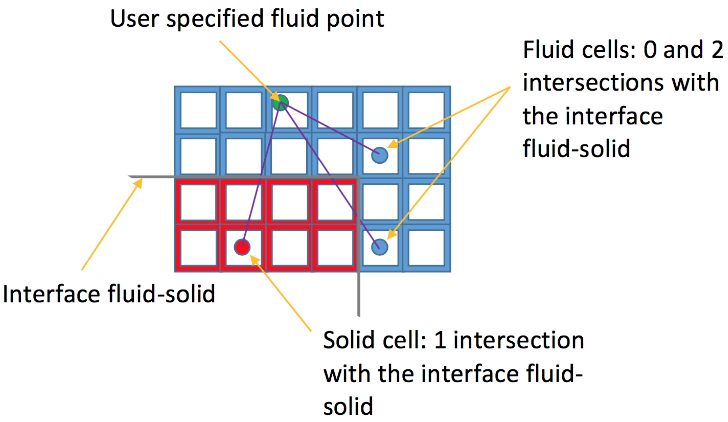

Figure 3.5: Method to locate fluid (even number of intersections) and solid (odd number of intersections) cells.

- Read the geometry of immersed domain.
- Separate the immersed domain from the rest of the computational domain.
- Identify ghost cells (first solid cells at the interface fluid-solid).
- Find images points for each ghost cell.
- Update ghost cells respectively to their images, and use them as boundary cells to compute the first fluid cells.

The geometry of immersed domain (solid region) is created in stereolithography (STL) format to get the coordinates of each triangular face and the normal to each face, which are used then to find the images points. The separation of the regions is performed by computing the number of intersection between each cell and a fluid point that the user specifies. If this number is even, the cell is marked as fluid, and solid otherwise (see Fig. 3.5). The marking is done with the variable called “in fluid”, I_f which is assigned 1 if the cell is in fluid region and -1 in the solid region.

As the code runs in fourth order, two layers of ghost cells (see Fig. 3.6) are required to compute the first fluid cells. The first layer of ghost cells can easily be identified since these cells have at least one neighbor cell which is fluid. This condition is expressed by the relation:

$$I_f + I_{f,n} = 0 \tag{3.4.5}$$

where $I_{f,n}$ is the in fluid value of a neighbor cell. And the second layer of ghost cells are identified by having a neighbor which belongs to the first layer, that is a neighbor verifying Eq. 3.4.5. Once the ghost cells are identified, the image points of each ghost cell can be found. An image point is actually a virtual point which is the opposite symmetric of the ghost cell with respect to the interface fluid-solid (see Fig. 3.6). It has therefore no reason to be at the same coordinate as a fluid cell. Values at an image point are computed by interpolating surrounding fluid cells, called interpolants (maximum $3 \times 3 \times 3 = 27$). For any quantity Φ_I of the image point:

$$\Phi_I = \sum_k \Phi_k W_k^{int} \tag{3.4.6}$$

where Φ_k is the same quantity of the k-th interpolant, and W_k^{int} its weight based on the distance between the image point and the k-th interpolant h_k:

$$W_k^{int} = \frac{1}{h_k^2} \left(\sum_k \frac{1}{h_k^2} \right)^{-1} \tag{3.4.7}$$

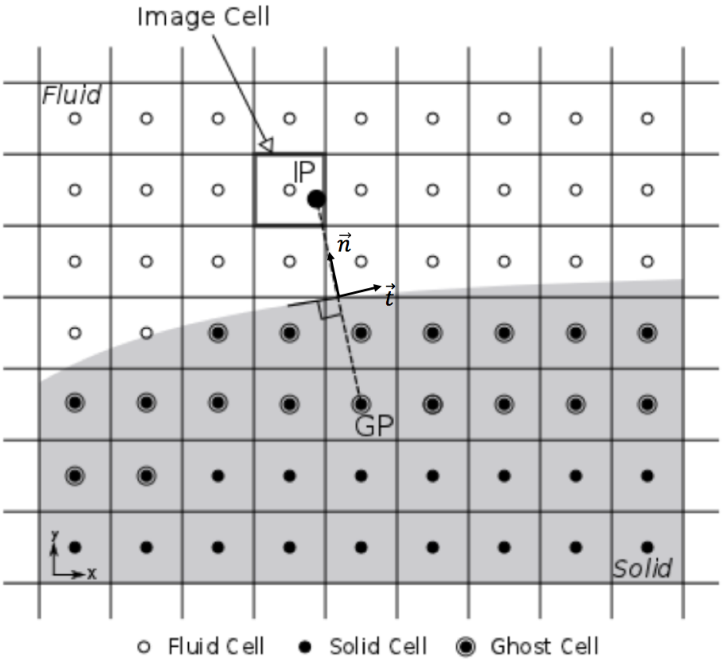

Figure 3.6: Schematic from [12] showing the principle of immersed boundary method: finding an image point (IP) located in the fluid region from a ghost cell (GP) located in the solid region.

In the original method, there is no equation for the interface between fluid and solid, the symmetry is done with respect to each triangular face, to the edge and the vertex of each face that forms the solid region. This method leads to a huge amount of candidates to become an image point. A selection based on the distance of the candidate and the solid d_{IS} is applied. Noting d_{min} the minimum distance between the ghost cell and the solid, every candidate in the fluid region verifying $d_{IS} < 2d_{min}$ is selected as an image point of this ghost cell. The schematic of algorithm for finding image points from a ghost cell is shown in Fig. 3.7. With this method, a ghost cell can have many image points. Each image point k has its weight W_k^{im} defined as:

$$W_k^{im} = \frac{1}{d_k^2}\left(\sum_k \frac{1}{d_k^2}\right)^{-1} \tag{3.4.8}$$

where d_k is the distance between the ghost cell and the image point k. The ghost cells are finally updated from the image points for scalar variables using the following relation if a zero-gradient condition is to be prescribed:

$$\Phi_G = \sum_k \Phi_{I,k} W_k^{im} \tag{3.4.9}$$

The vector and tensor formulations are different depending on the wall conditions. The update of all variables is shown below in the case each ghost cell is associated with only one image point for non-slip adiabatic wall conditions and zero wall gradient for species concentrations, with n and t ($= t_1$ or t_2) being the normal and the transverse vector to the wall respectively:

$$\begin{cases} (\rho E)_G = (\rho E)_I & \overrightarrow{U}_G = -\overrightarrow{U}_I & Y_G = Y_I \\ (\nabla T.\overrightarrow{n})_G = -(\nabla T.\overrightarrow{n})_I & (\nabla T.\overrightarrow{t})_G = (\nabla T.\overrightarrow{t})_I & \\ (\nabla Y.\overrightarrow{n})_G = -(\nabla Y.\overrightarrow{n})_I & (\nabla Y.\overrightarrow{t})_G = (\nabla Y.\overrightarrow{t})_I & \\ \left(\frac{\partial U_i}{\partial n}\right)_G = \left(\frac{\partial U_i}{\partial n}\right)_I & \left(\frac{\partial U_i}{\partial t}\right)_G = -\left(\frac{\partial U_i}{\partial t}\right)_I, & i = n,\ t_1,\ t_2 \end{cases} \tag{3.4.10}$$

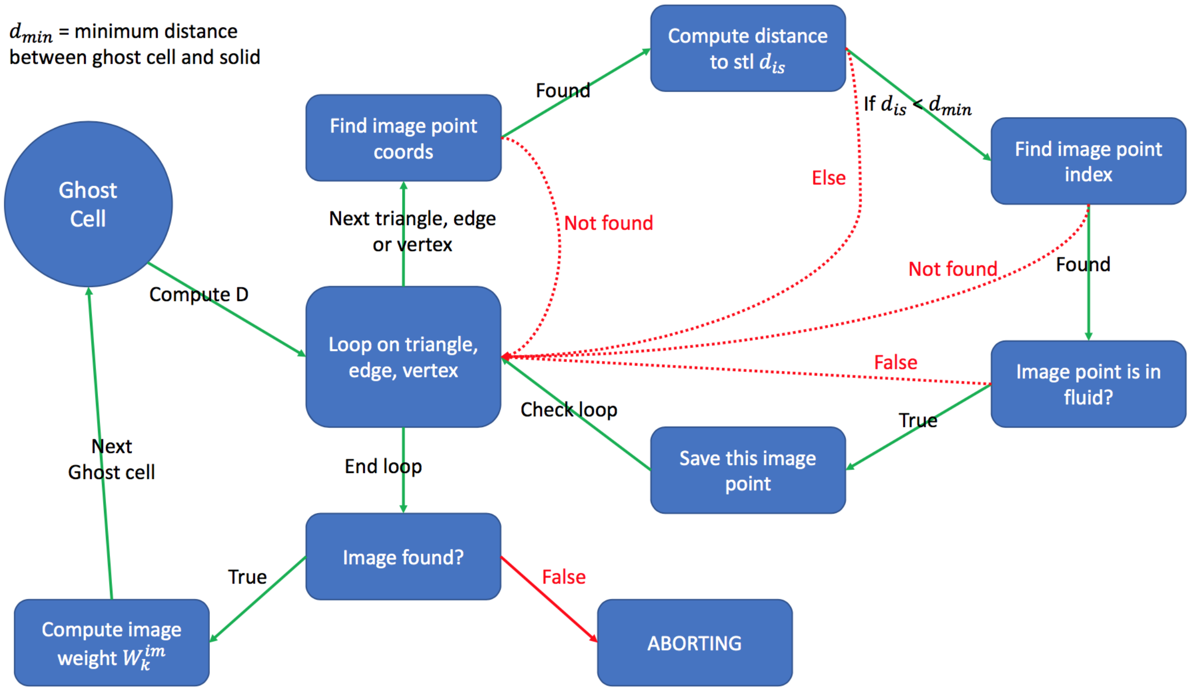

Figure 3.7: Schematic of algorithm for finding image points from ghost cells.

and slip wall conditions:

$$\begin{cases} (\rho E)_G = (\rho E)_I & Y_G = Y_I \\ (\vec{U}.\vec{n})_G = -(\vec{U}.\vec{n})_I & (\vec{U}.\vec{t})_G = (\vec{U}.\vec{t})_I \\ (\nabla T.\vec{n})_G = -(\nabla T.\vec{n})_I & (\nabla T.\vec{t})_G = (\nabla T.\vec{t})_I \\ (\nabla Y.\vec{n})_G = -(\nabla Y.\vec{n})_I & (\nabla Y.\vec{t})_G = (\nabla Y.\vec{t})_I \\ \left(\dfrac{\partial U_i}{\partial x_i}\right)_G = \left(\dfrac{\partial U_i}{\partial x_i}\right)_I & \left(\dfrac{\partial U_i}{\partial x_j}\right)_G = -\left(\dfrac{\partial U_i}{\partial x_j}\right)_I, \quad i,\ j = n,\ t_1,\ t_2 \text{ and } i \neq j \end{cases} \tag{3.4.11}$$

While the formulations for scalars and vectors are straightforward, the tensor update (∇U) requires some clarifications. The velocity gradient is composed of 9 components, and the update for some of them differs whether the wall is slipping or not. The relationships between image points and ghost cells for the velocity gradient are based on the conditions on the velocity (U_n, U_{t_1}, U_{t_2}) at the wall, being 0 in the direction normal to the wall, and either 0 for non-slipping conditions or U_t^G for slipping conditions in the transverse directions. Readers are reminded that the image point is located in the fluid region, while the ghost cell is in the solid region. The demonstration of relationships shown above for ∇U is displayed below, where the superscripts I and G corresponds to cells in the fluid and solid regions respectively:

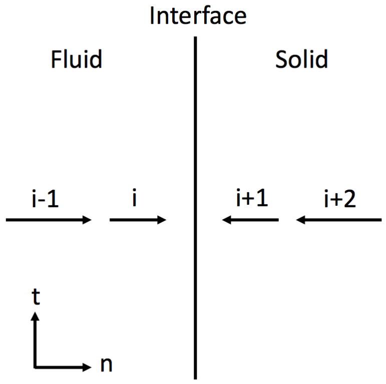

- $U_n^I = -U_n^G \Rightarrow U_{n,i} = -U_{n,i+1}\ ,\ U_{n,i-1} = -U_{n,i+2}$
- $\left(\dfrac{\partial U_n}{\partial n}\right)_I = \dfrac{U_{n,i} - U_{n,i-1}}{\Delta n}$
- $\left(\dfrac{\partial U_n}{\partial n}\right)_G = \dfrac{U_{n,i+2} - U_{n,i+1}}{\Delta n} = \dfrac{-U_{n,i-1} + U_{n,i}}{\Delta n}$

$$\Rightarrow \boxed{\left(\frac{\partial U_n}{\partial n}\right)_I = \left(\frac{\partial U_n}{\partial n}\right)_G}$$

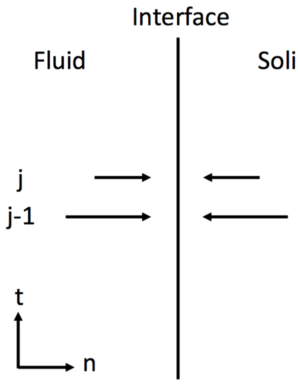

- $U_n^I = -U_n^G \Rightarrow U_{n,j}^I = -U_{n,j}^G\ ,\ U_{n,j-1}^I = -U_{n,j-1}^G$
- $\left(\dfrac{\partial U_n}{\partial t}\right)_I = \dfrac{U_{n,j}^I - U_{n,j-1}^I}{\Delta t}$
- $\left(\dfrac{\partial U_n}{\partial t}\right)_G = \dfrac{U_{n,j}^G - U_{n,j-1}^G}{\Delta t} = \dfrac{-U_{n,j}^I + U_{n,j-1}^I}{\Delta t}$

$$\Rightarrow \boxed{\left(\frac{\partial U_n}{\partial t}\right)_I = -\left(\frac{\partial U_n}{\partial t}\right)_G}$$

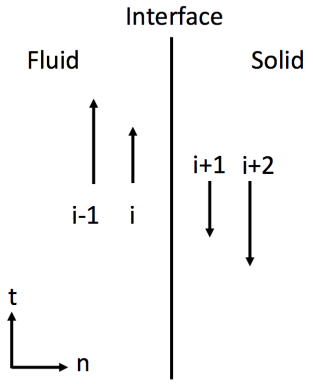

- $U_t^I = -U_t^G \Rightarrow U_{t,i} = -U_{t,i+1}\ ,\ U_{t,i-1} = -U_{t,i+2}$
- $\left(\dfrac{\partial U_t}{\partial n}\right)_I = \dfrac{U_{t,i} - U_{t,i-1}}{\Delta n}$
- $\left(\dfrac{\partial U_t}{\partial n}\right)_G = \dfrac{U_{t,i+2} - U_{t,i+1}}{\Delta n} = \dfrac{-U_{t,i-1} + U_{t,i}}{\Delta n}$

$$\Rightarrow \boxed{\left(\frac{\partial U_t}{\partial n}\right)_I = \left(\frac{\partial U_t}{\partial n}\right)_G}$$

wall no slip

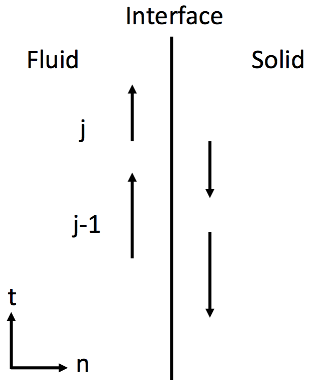

- $U_t^I = -U_t^G \Rightarrow U_{t,j}^I = -U_{t,j}^G\ ,\ U_{t,j-1}^I = -U_{t,j-1}^G$
- $\left(\dfrac{\partial U_t}{\partial t}\right)_I = \dfrac{U_{t,j}^I - U_{t,j-1}^I}{\Delta t}$
- $\left(\dfrac{\partial U_t}{\partial t}\right)_G = \dfrac{U_{t,j}^G - U_{t,j-1}^G}{\Delta t} = \dfrac{-U_{t,j}^I + U_{t,j-1}^I}{\Delta t}$

$$\Rightarrow \boxed{\left(\frac{\partial U_t}{\partial t}\right)_I = -\left(\frac{\partial U_t}{\partial t}\right)_G}$$

wall no slip

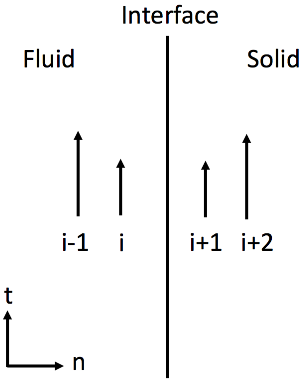

- $U_t^I = U_t^G \Rightarrow U_{t,i} = U_{t,i+1}\ ,\ U_{t,i-1} = U_{t,i+2}$
- $\left(\dfrac{\partial U_t}{\partial n}\right)_I = \dfrac{U_{t,i} - U_{t,i-1}}{\Delta n}$
- $\left(\dfrac{\partial U_t}{\partial n}\right)_G = \dfrac{U_{t,i+2} - U_{t,i+1}}{\Delta n} = \dfrac{U_{t,i-1} - U_{t,i}}{\Delta n}$

$$\Rightarrow \boxed{\left(\frac{\partial U_t}{\partial n}\right)_I = -\left(\frac{\partial U_t}{\partial n}\right)_G} \qquad \text{wall slip}$$

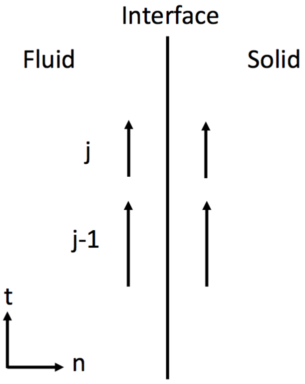

- $U_t^I = U_t^G \Rightarrow U_{t,j}^I = U_{t,j}^G\ ,\ U_{t,j-1}^I = U_{t,j-1}^G$
- $\left(\dfrac{\partial U_t}{\partial t}\right)_I = \dfrac{U_{t,j}^I - U_{t,j-1}^I}{\Delta t}$
- $\left(\dfrac{\partial U_t}{\partial t}\right)_G = \dfrac{U_{t,j}^G - U_{t,j-1}^G}{\Delta t} = \dfrac{U_{t,j}^I - U_{t,j-1}^I}{\Delta t}$

$$\Rightarrow \boxed{\left(\frac{\partial U_t}{\partial t}\right)_I = \left(\frac{\partial U_t}{\partial t}\right)_G} \qquad \text{wall slip}$$

Finally, for $i = n$ or t, the non-slipping wall condition for the velocity gradient is:

$$\left(\frac{\partial U_i}{\partial n}\right)_G = \left(\frac{\partial U_i}{\partial n}\right)_I \quad \text{and} \quad \left(\frac{\partial U_i}{\partial t}\right)_G = -\left(\frac{\partial U_i}{\partial t}\right)_I \tag{3.4.12}$$

and the slipping wall condition:

$$\left(\frac{\partial U_i}{\partial x_i}\right)_G = \left(\frac{\partial U_i}{\partial x_i}\right)_I \quad \text{and} \quad \left(\frac{\partial U_i}{\partial x_j}\right)_G = -\left(\frac{\partial U_i}{\partial x_j}\right)_I \quad i \neq j \tag{3.4.13}$$

3.4.2.2 Issues of the original method

The first issue appears when parallel computations are involved. Indeed, in SiTCom-B, two rows of cells are exchanged between processors, but sometimes, the image point can be located at the third or fourth row, so is never exchanged. Therefore, the image cannot be found and the ghost cell not be updated. Three failing cases are displayed on Fig. 3.8. The respective positioning of the fluid-solid interface and the interface between two blocks is controlling the position of the image point: if the fluid-solid interface is below the block interface, the cell containing the image point is located at the first or second row and is always exchanged, otherwise this cell is not exchanged (third or fourth row) if the distance between the ghost cell and the fluid-solid interface d_{GS} is greater than 1.25 times the cell size Δx. Actually, the issue can only occur for ghost cells located at the second layer, and can be corrected if the numerical scheme is degenerated into second order in the vicinity of the interface between fluid and solid regions. The second layer of ghost cells is thus not needed. In order not to increase the computational time, the degeneration is performed by using a mask α taking values 0 or 1, which is computed only once at the initialization of the solver, and every flux Φ is changed to:

$$\Phi = \alpha\Phi_2 + (1-\alpha)\Phi_4 \tag{3.4.14}$$

where Φ_2 and Φ_4 are the flux calculated with a second order and fourth order numerical schemes respectively.
The second problem is an interpolation issue. One ghost cell needs actually only one image point, the current implementation leads to multiple image points, sometimes non-desired. As shown on Fig. 3.9, the ghost cell filled with red color has one image above and one image at its right which is undesired because the ghost cell should not have any interaction with that image. If the geometry of the solid can easily be described mathematically, the image point can be computed analytically to avoid the previous issue.

3.4.2.3 Analytical implementation of IBM

In this implementation, the STL file is removed, the fluid-solid interface is localized by mathematical formulas. This method can deal with the interpolation error shown in the previous section, but has the drawback of not being universal: each geometry needs to be described mathematically. Fluid or solid region can easily be identified depending if the region is below or above the interface. While the research of ghost cells is performed the same way as the original method, the research of image points is completely different. In the current work, the scramjet walls are composed of straight lines without any curvature, and the injector is a cylinder, both are quite easy to describe mathematically. In case where the interface is a line, slanted by a angle of θ (see Fig. 3.10), the image point (x_I, y_I, z_I) can be computed from the ghost cell (x_G, y_G, z_G) through the following relations:

$$\begin{cases} x_I = x_G + 2d_{GS}\sin(\theta) \\ y_I = y_G + 2d_{GS}\cos(\theta) \\ z_I = z_G \end{cases} \tag{3.4.15}$$

where d_{GS} is the shortest distance between the ghost cell and the interface defined as:

$$d_{GS} = |y_G - y_d(x_G)|\cos(\theta) \tag{3.4.16}$$

where y_d is the linear equation of the interface. And when the interface is a circle (see Fig. 3.11), the image point is computed in the following way:

$$\begin{cases} x_I = x_G \\ y_I = (z_G - z_O)\dfrac{r_0 - d_{GS}}{r_0 + d_{GS}} + y_O \\ z_I = (z_G - z_O)\dfrac{r_0 - d_{GS}}{r_0 + d_{GS}} + z_O \end{cases} \tag{3.4.17}$$

where r_0 is the radius of the cercle and y_O and z_O are the coordinates of the center of the circle. The distance between the ghost cell and the interface d_{GS} is here defined as:

$$d_{GS} = |r - r_0| \quad \text{with} \quad r = \sqrt{(y_G - y_O)^2 + (z_G - z_O)^2} \tag{3.4.18}$$

This implementation works well since every ghost cell has now only one image and the user knows exactly where its image should be located, except for points in the corners (see Fig. 3.12). Indeed, those ghost cells have at least two images (I_1 and I_2), the equations are modified in this case to force the ghost cell to take the image point at the opposite side of the corner (point I):

$$\begin{cases} x_I = x_G + \sqrt{2}d_{GC} \\ y_I = y_G + \sqrt{2}d_{GC} \\ z_I = z_G \end{cases} \tag{3.4.19}$$

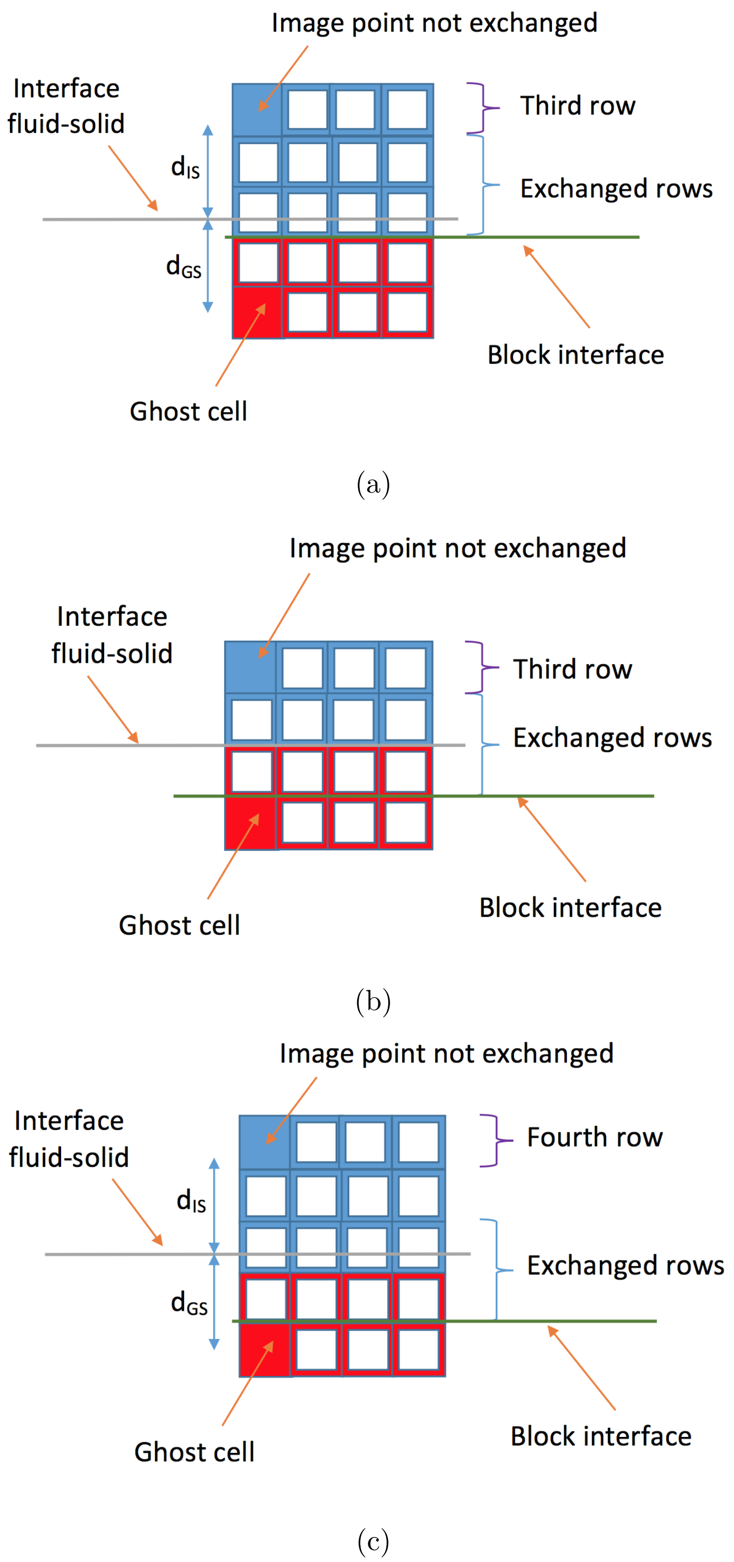

Figure 3.8: Example of cases where the image point is not exchanged between processors. Blue: fluid cells; red: solid cells.

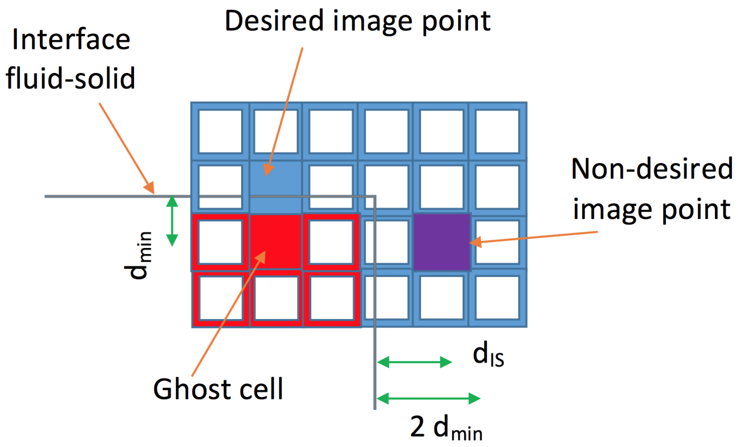

Figure 3.9: Case with undesired image point.

where d_{GC} is the distance from the ghost cell to the corner defined as:

$$d_{GC} = \sqrt{d_{GS_1}^2 + d_{GS_2}^2} \tag{3.4.20}$$

with d_{GS_1} and d_{GS_2} being respectively the distance from the ghost cell to the interface 1 and the interface 2 computed with expression 3.4.16. Once all the image points are associated to their respective ghost cells, the values at the image points are computed by interpolating fluid cells around them (see Eq. 3.4.6). Finally, values at ghost cells are updated from the image points.

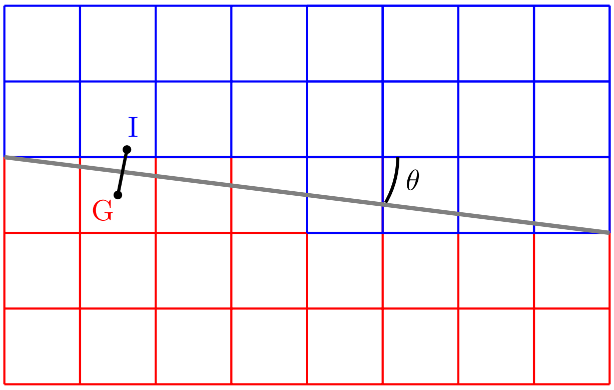

Figure 3.10: Case where the fluid-solid interface is a straight line slanted by θ with axis x: fluid cells (blue), solid cells (red) and fluid-solid interface (gray). XY plane.

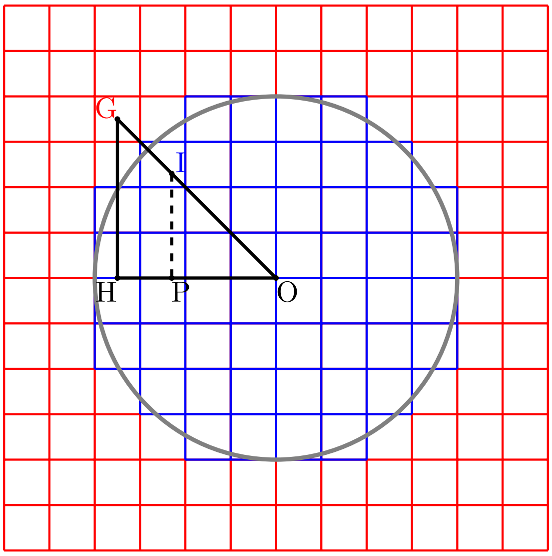

Figure 3.11: Case of a circular interface: fluid cells (blue), solid cells (red) and fluid-solid interface (gray). YZ plane.

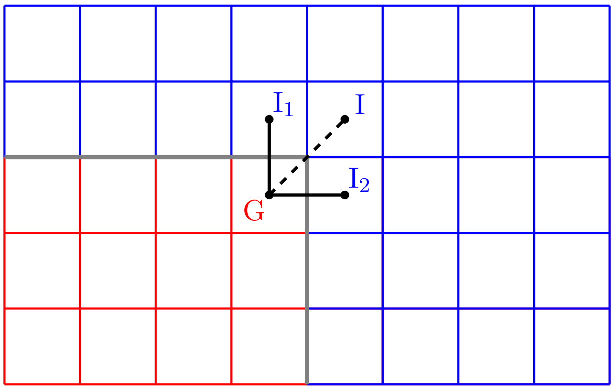

Figure 3.12: Case of a ghost cell located at a corner: fluid cells (blue), solid cells (red) and fluid-solid interface (gray). XY plane.

3.4.2.4 Isothermal wall condition coupled with IBM

The isothermal wall condition at the fluid-solid interface has been implemented during this Ph.D. As shown in Eq. 3.4.10, values at ghost cells are updated from the image points for 6 variables which are ρE, ρU, ρY, ∇T, ∇U and ∇Y. For an adiabatic wall, the conservative variables ρE, ρU and ρY are first updated in ghost cells from image points and then used to compute T, U and Y in the ghost cells. The gradients of the latter variables are then calculated in the image points, and finally ∇T, ∇U and ∇Y are updated in the ghost cells from image points. When the wall is isotherm, the temperature at the wall is different from the fluid domain, so unlike the adiabatic case, the norm of temperature gradient is not equal anymore in fluid and solid regions. The temperature of the ghost cell becomes:

$$T_G = 2T_w - T_I \tag{3.4.21}$$

where T_G, T_I and T_w are the temperature of the ghost cell, the image point and the wall respectively. The temperature gradient of the ghost cell is now:

$$\left(\frac{\partial T}{\partial n}\right)_G = 2\frac{T_w - T_G}{\Delta n} \tag{3.4.22}$$

The initial code is modified to take into account the isothermal wall condition:

- Update U and Y in ghost cells. The update of ρE is not mandatory since it will be recomputed by taking into account the wall temperature.
- Update P and T in the ghost cells:

$$\begin{cases} P_G = P_I \\ T_G = 2T_w - T_I \end{cases} \tag{3.4.23}$$

- Compute gradients (∇T, ∇U and ∇Y) from face values. This step is kept the same, except for the temperature gradient in ghost cells where expression 3.4.22 is used.
- Update ∇U and ∇Y in ghost cells. There is no need to update the temperature gradient since it has been computed correctly in ghost cells at the previous step.

In this work, the wall temperature is only prescribed when its value exceeds the maximum wall temperature imposed by the user (800 K here), so the wall temperature is:

$$T_w = \min(800, T_I) \tag{3.4.24}$$

and the ghost cell temperature is:

$$T_G = \begin{cases} T_I & \text{if} \quad T_w < 800 \text{ K} \\ 2T_w - T_I & \text{if} \quad T_w = 800 \text{ K} \end{cases} \tag{3.4.25}$$

This is actually a hybrid implementation: the wall behaves like an adiabatic wall when the temperature of the image point T_I is lower than 800 K, and starts being isotherm at 800 K only if this temperature exceeds this value. Note that when the temperature of the image point is higher than twice the wall temperature ($T_I > 2T_w$), the temperature of the ghost cell T_G becomes negative. A minimum temperature T_{min} is necessary. When $T_w = 800$ K, the temperature of the ghost cell is modified to:

$$T_G = \max(T_{min},\ 2T_w - T_I) \tag{3.4.26}$$

In the scramjet computation, T_{min} is fixed at 300 K. The code was tested on a 2D case where the fluid domain, initiated at 350 K, is cooled down by a rectangular wall at 300 K. Results are shown in Fig. 3.13 and are satisfying. Furthermore, the new implementation is not slowing the code, performing at the same speed.

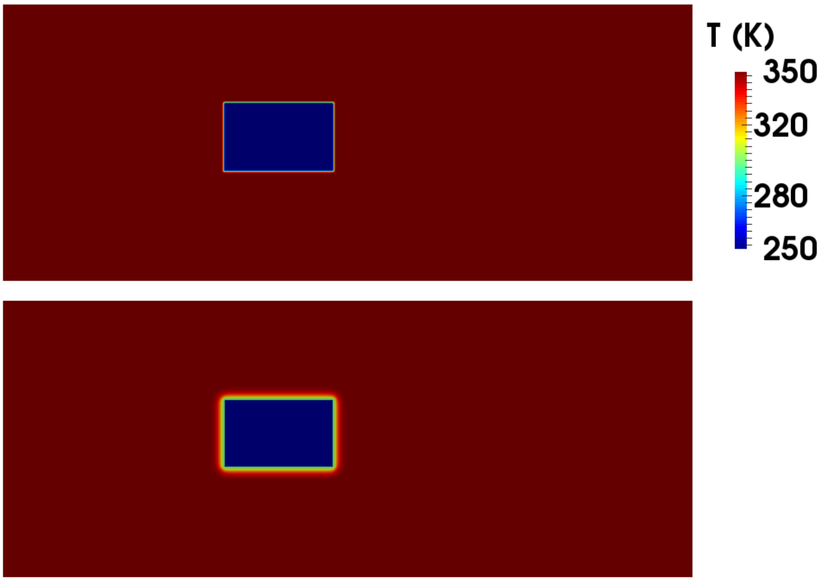

Figure 3.13: 2D test case of the isothermal wall conditions: initial state (top) and converged solution (bottom). The imposed wall temperature is 300 K.

Chapter 4

Large eddy simulation of supersonic airflow

Contents

4.1 Generalities on cavity flows

4.2 Design of cavity-based scramjet

Cavities are efficient flameholders due to the induced large recirculation of hot mixture of fuel and burnt gases. The velocity disparity between the supersonic freestream and the subsonic cavity leads to a shear layer, which controls the mass exchange with the recirculation area. The performance of a scramjet is found highly dependent of the choice of the fuel, the cavity geometry and the injection area (see Fig. 4.1).

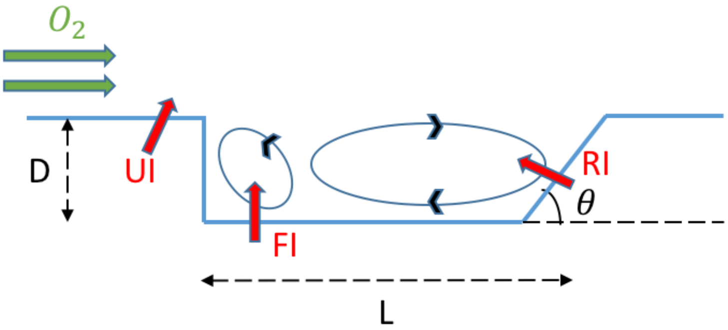

Figure 4.1: Schematic of slanted cavity with 3 injection zones: Upstream Injection (UI), Floor Injection (FI) and Ramp Injection (RI).

4.2.1 Impact of fuel choice

As the fuel spends a very short time in the engine core, its delay to ignite needs to be low to enable combustion. Hydrogen (H_2) is known to burn very easily and quickly, due to its high energy density and small molecular structure. But hydrocarbon fuels are logistically more attractive than hydrogen since they require less space (higher density) and less safety measures. Some hydrocarbon fuels also have the advantage of being liquid at ambiant temperature, thus facilitating the storage.

Kerosene ($C_{10}H_{22}$) is widely used for subsonic combustion jet engines (turbofan and ramjet), but does not fit in supersonic combustion since its delay to ignite is too important. Neely et al. studied in [120] the performance of ethylene and hydrogen fueled cavity-based scramjet by varying the equivalence ratio of each fuel. Hydrogen seems to generate a higher combustion-induced pressure rise in the cavity, but produces less combustion downstream than ethylene. Rasmussen et al. investigated the stability of ethylene and methane flames in [137]. Ethylene flames appear to have a wider range of stability than methane, because the ignition delay of ethylene is shorter and its flame speed higher.

Ethylene is generally used as a surrogate for heavier hydrocarbon fuels in ground tests, as it is an intermediate product in the combustion of most heavy hydrocarbons, and it is the fastest hydrocarbon to burn [26]. However, auto-ignition of hydrocarbon fuels can hardly be obtained in a scramjet combustor. A spark plug or a pilot flame (hydrogen) can be used to solve that issue.

4.2.2 Effect of cavity geometry

The cavity geometry is determined by its aspect ratio L/D and rear ramp angle θ. The first parameter is responsible for the shape of the shear layer and the cavity residence time, while the second controls the oscillations inside the cavity.

The cavity aspect ratio is defined as the ratio of cavity length L[1] over cavity depth D. Depending on its value, the flowfield can be split into two regimes [5, 64]: open or closed cavity flow (Fig. 4.2). The first regime occurs when the ratio $L/D < 10$, which is characterized by the upper shear layer reattaching the back face of the cavity. However, when the ratio is too low (< 3), transverse oscillations appear to disturb the main stream [181]. In the other case, the mechanism involved is the longitudinal oscillations. The cavity flow is considered as closed for $L/D > 10$, when the free shear layer is impinging the lower cavity wall. The drag penalties are amplified due to the strong pressure difference involved in this case (pressure increasing at the downstream and decreasing at

---

[1] The cavity length L is defined as the sum of the cavity floor length L_f and half of the cavity rear length $D\cot(\theta)$: $L = L_f + D\cot(\theta)$

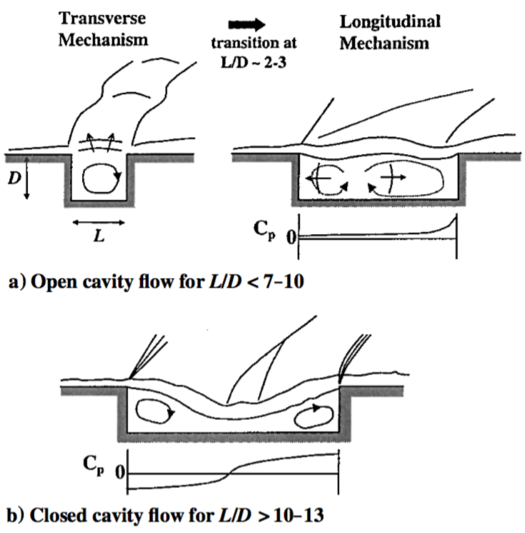

Figure 4.2: Flowfield schematics of cavities with different L/D in a supersonic flow [5]

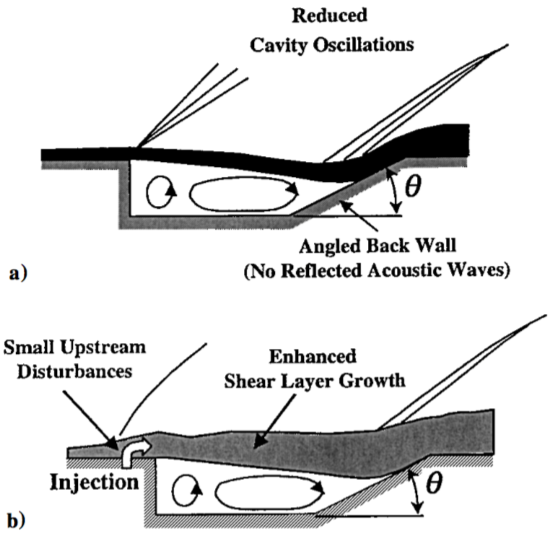

Figure 4.3: Cavity oscillations stabilization techniques: a) slanted cavity back wall, b) upstream disturbance [5]

the upstream). The aspect ratio should take value between 3 and 10 to avoid any undesired phenomenon.

The longitudinal oscillations are caused by the freestream flow entering the cavity from the back wall. The cavity pressure then increases and creates an acoustic wave, which propagates upstream at the local sound speed and induces small vortices. This phenomenon can be avoided by using oscillation stabilization techniques [5] shown in figure 4.3. The first method (a) consists in slanting the cavity back wall of a certain angle θ, which avoids, the generation of the traveling shocks due to the free shear layer impingement, inside the cavity. The pressure waves are thus not reflected to the upstream [182]. Ben-Yakar and Hanson [5] suggest there might be a critical rear wall angle between 16° and 45° at which the drag penalties are minimal. The second method (b) lies in adding a small disturbance at the upstream to enhance free shear layer growth rate, which can also attenuate the oscillations in the cavity [71, 125]. The previous methods are termed passive as the devices are permanent features. Several active control methods have been studied elsewhere [88, 146, 166], but not discussed herein. The passive methods are very effective and simple to implement, but can alter the cavity performance (adding drag penalties).

The cavity residence time τ is defined as the time required for the cavity fluid to leave the cavity, due to the mass exchange $\dot{m}_{exchange}$ with the freestream:

$$\tau = \frac{m_{cav}}{\dot{m}_{exchange}} = \frac{\rho_{cav} V_{cav}}{\dot{m}_{exchange}} = \frac{\rho_{cav} WLD}{\dot{m}_{exchange}} \tag{4.2.1}$$

where m_{cav} and ρ_{cav} are the mass of fluid and the mean fluid density in the cavity, and W, L and D are respectively the cavity width, length and depth. Neglecting the cavity velocity and approximating the shear layer velocity, Davis [34] developed an analytical expression to estimate the mass exchange:

$$\dot{m}_{exchange} = \frac{\rho_\infty U_\infty WL}{2\sigma\sqrt{\pi}} \tag{4.2.2}$$

where ρ_∞ and U_∞ are respectively the density and the velocity of the freestream, and $13 \leq \sigma \leq 30$

depends on the convective Mach number. The residence time can be written as:

$$\tau = 2\sigma\sqrt{\pi}\left(\frac{\rho_{cav}}{\rho_\infty}\right)\left(\frac{D}{U_\infty}\right) \tag{4.2.3}$$

Without reaction, the cavity temperature can be related to the total temperature, which gives:

$$\frac{\rho_{cav}}{\rho_\infty} = \frac{T_\infty}{T_{total}} = \frac{1}{1+\frac{\gamma-1}{2}M_\infty^2} \tag{4.2.4}$$

The residence time thus becomes:

$$\tau = \frac{2\sigma\sqrt{\pi}}{1+\frac{\gamma-1}{2}M_\infty^2}\frac{D}{U_\infty} \tag{4.2.5}$$

The cavity residence time depends only on the cavity depth and the freestream velocity, the length seems to have no impact on it. Ben-Yakar and Hanson [5] found that the residence time in a cavity with $L/D = 5$ is smaller than a cavity with $L/D = 3$, which may appear at first sight unexpected, since assuming a constant depth, a higher length leads to larger volume inside the cavity (increase $/tau$), but also leads to a larger exchange area with the freestream which increases the mass exchange (decrease τ). These two phenomena somehow balance, so increasing the length L does not really increase the residence time. On the other hand, assuming a constant length and increasing the cavity depth leads to larger cavity volume with the same exchange area, which can in this case increase the residence time. This study confirms that the cavity depth has a higher influence than the length in terms of residence time. Besides, Davis and Bowersox [35, 36] obtained empirically a relation between D, τ and U_∞:

$$\tau = \frac{40D}{U_\infty} \tag{4.2.6}$$

4.2.3 Influence of injection zone

The injection area plays a crucial role in the performance of the cavity-based scramjet. Whether the fuel is injected at the upstream, from the floor or by the ramp (Fig. 4.1), the mixing and the combustion in the recirculation area differ.

Gruber et al. [65] investigated experimentally the cavity injections using planar laser-induced fluorescence of nitric oxide (NO-PLIF) and the hydroxyl radical (OH-PLIF). The upstream injection appears to be attractive since it provides fuel both to the mainstream and the cavity. But in practice, the fuel remains above the shear layer, only a small portion goes into the cavity, because the cavity fueling is highly dependent of the fuel pressure. Decreasing the fuel injection pressure can increase the amount of fuel going into the cavity, since the fuel, being less pressurized, can hardly penetrate into the mainstream, and is more likely pushed down into the cavity. Compared to the upstream injection, the floor injection improves the cavity fueling but leads to a nonuniform fuel distribution because of the small recirculation zone at the leading edge. The ramp injection provides fuel directly into the large recirculation area and establishes a uniform fuel distribution in the cavity, except in the corner between the leading edge and the side walls.

The fuel lean and rich blowout limits for cavity floor and ramp injections have been studied by Rasmussen et al. in [137]. The injection from the floor performed better at the rich blowout limit, while the ramp injection provided better stability at the lean blowout limit. Both statements can be explained using the same observation: injection from the cavity floor allows the fuel to escape to the shear layer without reacting, whereas injection from the cavity ramp provides longer residence time and more uniform mixing and combustion. At the lean blowout, the quantity of fuel is insufficient due to the leak for combustion in the floor injection case. While at the rich blowout, the recirculation zone is flooded of fuel and is not flammable anymore in the ramp injection case.

Name	Symbol	Value
Cavity length	L	66 mm
Cavity depth	D	16.5 mm
Cavity angle	θ	22.5°
Tunnel width	W	152.4 mm
Isolator length	L_{iso}	177.8 mm
Isolator height	H	50.8 mm
Divergent length	L_{div}	740 mm
Divergent angle	α	2.5°
Injector diameter	d	1.6 mm

Table 4.1: AFRL supersonic wind tunnel dimensions.

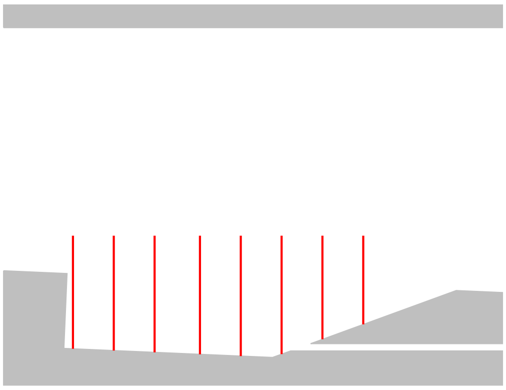

Figure 4.5: Velocity profiles location.

4.3 Experimental set-up

In the experiment of AFRL, the air flow is accelerated through a nozzle to reach supersonic speed and enters the isolator at nominal Mach 2, with respectively a total temperature and pressure of 589 K and 483 kPa. The simulations in the present work will only start at the isolator. The supersonic wind tunnel is therefore modeled as a simple rectangular duct with a ramped cavity at its rear (see Fig. 4.4). The air flow meets the fuel ethylene inside the cavity where combustion has been shown experimentally to take place. Ethylene (C_2H_4) is injected at 310 K which makes the auto-ignition impossible to occur, spark plugs are set at the cavity floor to help ignition. The isolator, spans 177.8 mm (L_{iso}) of the wind tunnel and has a constant area section $H \times W$ of 50.8×152.4 mm^2. At the exit of the isolator, the lower wall of the duct is diverging by an angle α of 2.5°. The cavity is located at 76.2 mm further from the diverging section. Its length and depth are respectively 66 and 16.5 mm, which gives an aspect ratio L/D of 4, corresponding to an open cavity flow regime. The aft wall of the cavity is slanted by 22.5° to avoid oscillations of acoustic waves inside the cavity [5]. An array of 11 fuel injection ports of diameter $d = 1.6$ mm are evenly distributed on the back cavity wall.

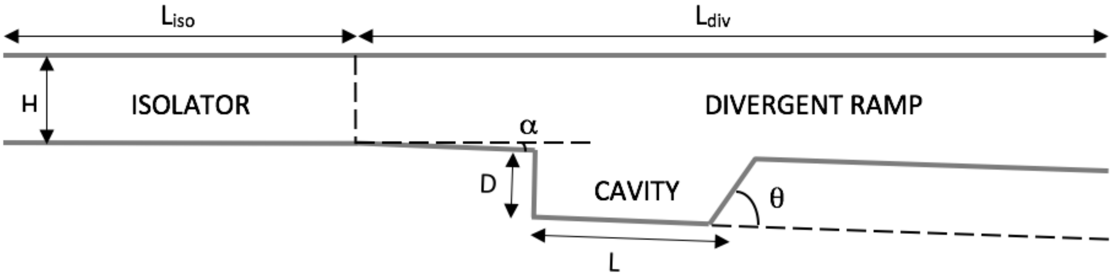

Figure 4.4: Schematic of AFRL supersonic wind tunnel, injectors are not shown.

Tuttle et al. [164] performed five experiments by varying the fuel mass flow rate (Tab. 4.2), which correspond to different flow regimes (Fig. 4.6). The total temperature, total pressure and freestream velocity are kept the same for every cases. The particle image velocimetry (PIV) method was used to determine the velocity inside the cavity in both nonreacting and reacting conditions. Streamwise (U) and transverse (V) velocity profiles are measured at 8 locations in the cavity which are located respectively 2, 11, 20, 30, 39, 48, 57 and 66 mm from the cavity leading edge for the five cases (Fig. 4.5).

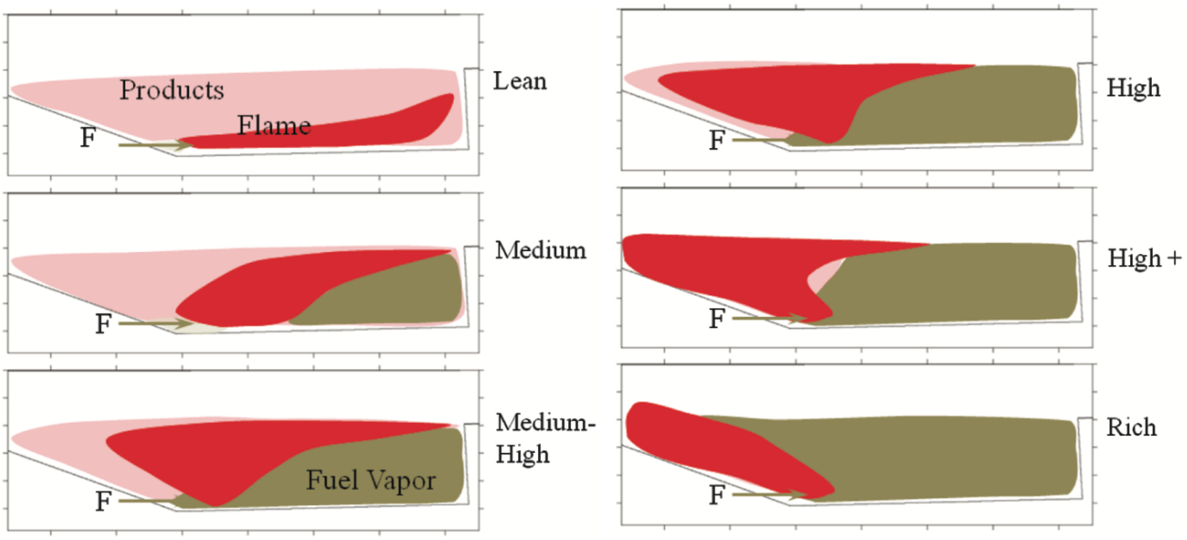

Figure 4.6: Fuel flow regimes [164].

Case	1	2	3	4	5
T_0 [K]	589	589	589	589	589
P_0 [kPa]	483	483	483	483	483
Mach	2	2	2	2	2
U_∞ [m/s]	727	727	727	727	727
Fuel [SLPM]	0	56	99	$39 \rightarrow 36$	110

Table 4.2: Rig conditions for the experimental cases.

Tuttle et al. [164] built a diagram (Fig. 4.6) showing the approximate, averaged distribution of the heat release (red), combustion products (pink), and fuel vapor (green), based on the studies of Hsu et al. [71], Rasmussen et al. [137] and Lin et al. [96]. At low fuel loading ($\sim$ 40 Standard Liters Per Minute, SLPM), the entire fuel is consumed and the flame is attached to the cavity floor. As the fuel flow rate increases, some unburnt fuel vapor appears at the front of the cavity, and the flame is shifted at the rear. The reaction zone is all the further from the cavity front as the fuel loading is high, which means that the mixture is sufficiently rich to extinguish combustion within the cavity. As the fuel flow approaches the rich limit, combustion disappears from the shear layer and is only present at the exit of the injector and the cavity ramp.

4.4 Numerical set-up

The portion of the experimental device which is simulated is displayed in Fig. 4.7. The objective of this work is to investigate combustion near the cavity, therefore the computational domain includes the whole insolator (177.8 mm), followed by a small part of the divergent (212.2 mm) where the cavity is located.

In the experiment performed by Tuttle et al. [164], stagnation conditions P_0 and T_0 are provided. The injection pressure and temperature need therefore to be estimated by assuming an ideal gas with isentropic evolution from the reservoir (state 0) to the throat (state 1). The Mach 2 facility nozzle is displayed in Fig. 4.8.

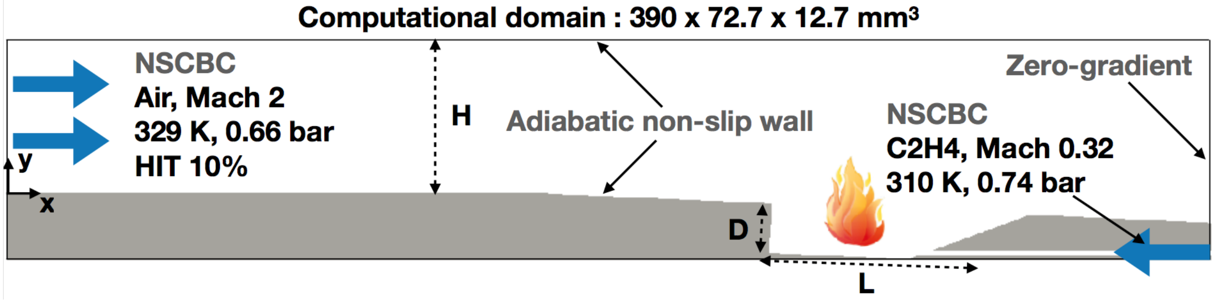

Figure 4.7: Sketch of the computational domain. The region colored in grey corresponds to solid parts. $L = 66$ mm, $D = 16.5$ mm, $H = 50.8$ mm. The centerline of each injector is located at $x = 305.50$ mm and $y = -19.57$ mm.

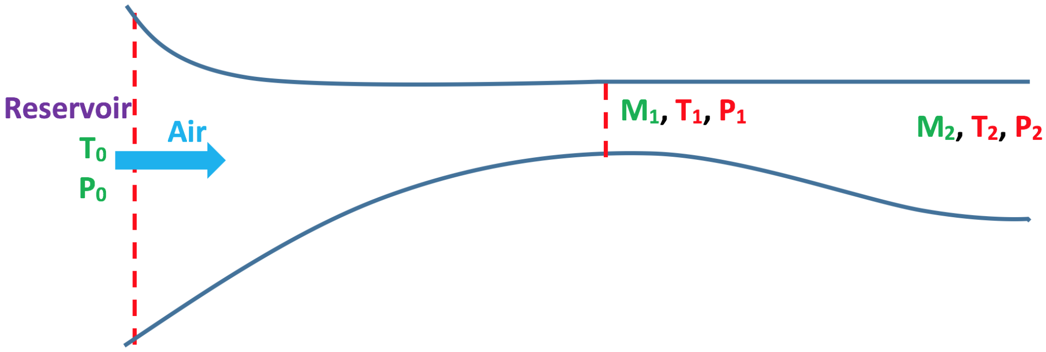

Figure 4.8: Mach 2 facility nozzle.

Using the energy conservation equation:

$$C_pT_0 + \frac{1}{2}U_0^2 = C_pT_1 + \frac{1}{2}U_1^2 \tag{4.4.1}$$

and assuming that the velocity in the reservoir U_0 is zero, the temperature at the throat T_1 can be linked to T_0 following:

$$T_1 = \frac{C_p}{C_p + \frac{1}{2}M_1^2\gamma r}T_0 \tag{4.4.2}$$

The pressure can be determined with the isentropic relationship:

$$P_1T_1^{\frac{\gamma}{1-\gamma}} = P_0T_0^{\frac{\gamma}{1-\gamma}} \tag{4.4.3}$$

which leads to:

$$P_1 = P_0\left(\frac{T_0}{T_1}\right)^{\frac{\gamma}{1-\gamma}} \tag{4.4.4}$$

Knowing that the Mach number is equal to 1 at the throat, T_1 and P_1 can be calculated. The same analysis is done from state 1 to state 2, and with the injection mach number M_2 being 2 (the state 2 corresponds to the inlet of the isolator), the injection temperature and pressure can be computed:

$$\begin{cases} T_2 = 329 \text{ K} \\ P_2 = 65.8 \text{ kPa} \end{cases} \tag{4.4.5}$$

Case	**Mesh**	**Width (mm)**	**HIT**	**Wall model**	**CPU time (h)**
NRC1	Coarse	12.7	×	×	40 000
NRF1	Fine	12.7	×	×	150 000
NRC2	Coarse	25.4	×	×	80 000
NRC1H	Coarse	12.7	√	×	40 000
NRC1W	Coarse	12.7	×	√	40 000
NRC1HW	Coarse	12.7	√	√	40 000

Table 4.3: Non reactive simulations studied in section 4.5. The CPU times are based on the MYRIA cluster of CRIANN [29] which is equipped of Xeon cores of 403 Tflops.

These values are consistent with those given by Baurle [4] for his simulations.

The 3D Navier Stokes Characteristic Boundary Conditions (NSCBC) [102] are applied to describe the air and fuel inflows. The outflow of the computational domain is using a zero-gradient condition. The upper and lower walls of the scramjet are modeled with an adiabatic non-slip condition, while the side sections use periodic conditions since, in non-reactive flow simulations, only one or two injectors are considered. The size of the whole computational domain with one injector is then $390 \times 72.7 \times 12.7\text{mm}^3$.

Unsolved subgrid-scale fluxes are modeled by the dynamic Smagorinsky closure [93, 117]. Subgrid Prandtl and Schmidt numbers, are set to 0.9.

4.5 LES of non-reactive flow

In this section, before addressing the scramjet simulation with fuel injection and combustion, the airflow velocity profile is first determined, followed by an investigation on the mesh resolution. The computations of one and two injectors are then presented and compared to the experimental data. Finally, an investigation on the impact of homogeneous isotropic turbulence injection at inlet and wall modeling is performed. Tab. 4.3 shows all the non-reactive simulations presented in this section.

4.5.1 Effect of inlet velocity

The shape of the inlet velocity profile has to be provided to initialize correctly the simulation. Since no experimental information is available, the impact of the chosen shape of the velocity has first to be investigated. Two different velocity profiles are first tested in 2D and compared. The first profile (P1) is a classical turbulent channel flow profile:

$$U(y) = P_{Vel} U_{max} \quad \text{with} \quad P_{Vel} = 2^{2/7} \left(\frac{y^{\frac{1}{7}} (h-y)^{\frac{1}{7}}}{h^{\frac{2}{7}}} \right) \tag{4.5.1}$$

where $U_{max} = 1.0845 U_0$ is the velocity at the center ($y = h/2$) and $U_0 = 727$ ms is the bulk velocity corresponding to a Mach number of 2 for the given pressure and temperature conditions.
The second velocity profile (P2) is obtained by running 400 000 iterations, corresponding to 16 ms

of physical time, on a 2D square modelizing a small part of the isolator with periodic inlet/outlet conditions. The velocity of computational domain is initialized with the profile P1. The square, which side is 50.8 mm long, is modelized uniformly with cells of 100 μm. The velocity field obtained is then approximated by three polynomial functions at different locations to get the profile P2:

$$U(y) = ay^6 + by^5 + cy^4 + dy^3 + ey^2 + fy + g \tag{4.5.2}$$

- $y < 3.99$ mm:

$$\begin{cases} a = -5.25676456894792 \times 10^{16} \\ b = -1.03409770509107 \times 10^{15} \\ c = 1.661943438336 \times 10^{13} \\ d = -6.586436785 \times 10^{10} \\ e = 2.512518796 \times 10^{7} \\ f = 3.685606 \times 10^{5} \\ g = 19.29 \end{cases}$$

- 3.89 mm < y < 46.91 mm:

$$\begin{cases} a = -4.65446273 \times 10^{11} \\ b = 7.095180944 \times 10^{10} \\ c = -4.606748162 \times 10^{9} \\ d = 1.628278018 \times 10^{8} \\ e = -3.428392038 \times 10^{6} \\ f = 4.284133112 \times 10^{4} \\ g = 536.42 \end{cases}$$

- $y > 46.81$ mm:

$$\begin{cases} a = -5.40854891115971 \times 10^{16} \\ b = 1.74985742989092 \times 10^{16} \\ c = -2.33449474333157 \times 10^{15} \\ d = 1.6466815160124 \times 10^{14} \\ e = -6.485579509973 \times 10^{12} \\ f = 1.35373716828 \times 10^{11} \\ g = -1.170882269 \times 10^{9} \end{cases}$$

Both profiles are displayed in Fig. 4.9 and there is only a slight difference between P1 and P2 near the wall region. Computations using both formulations for the inlet velocity were performed in 2D and averaged velocity profiles inside the cavity at positions $x = 2$, 30 and 57 mm from the cavity front were compared. The velocity is non-dimensionalized by the bulk velocity $U_0 = 727$ m/s. Comparison is shown in Fig. 4.10. Differences are not significant enough to be accounted for. This result is expected since the difference between P1 and P2 is very small, and the isolator is long enough to retrieve the correct velocity profile regardless of the velocity profile at the inlet. Therefore, the profile P1 is chosen for its simplity for all the following simulations.

4.5.2 Impact of resolution

Two meshes were used for the large eddy simulation of the non-reactive case with the dimension of only one injector (12.7 mm in the span direction). There is no injector in the non-reactive case

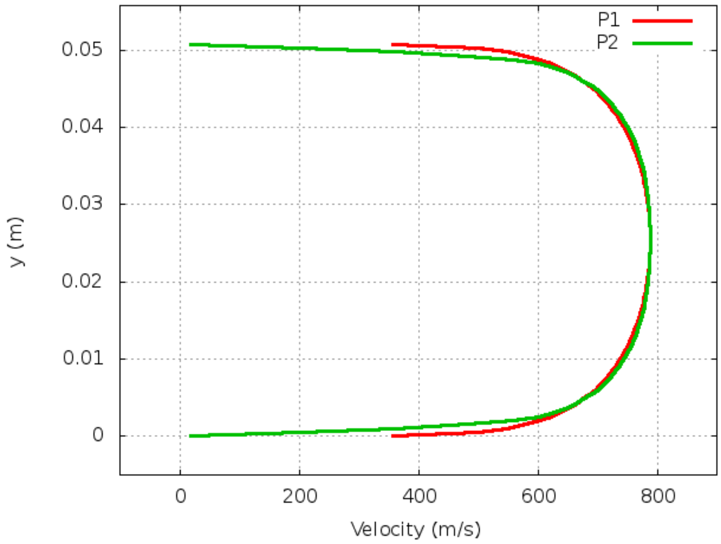

Figure 4.9: Inlet velocity profiles P1 and P2.

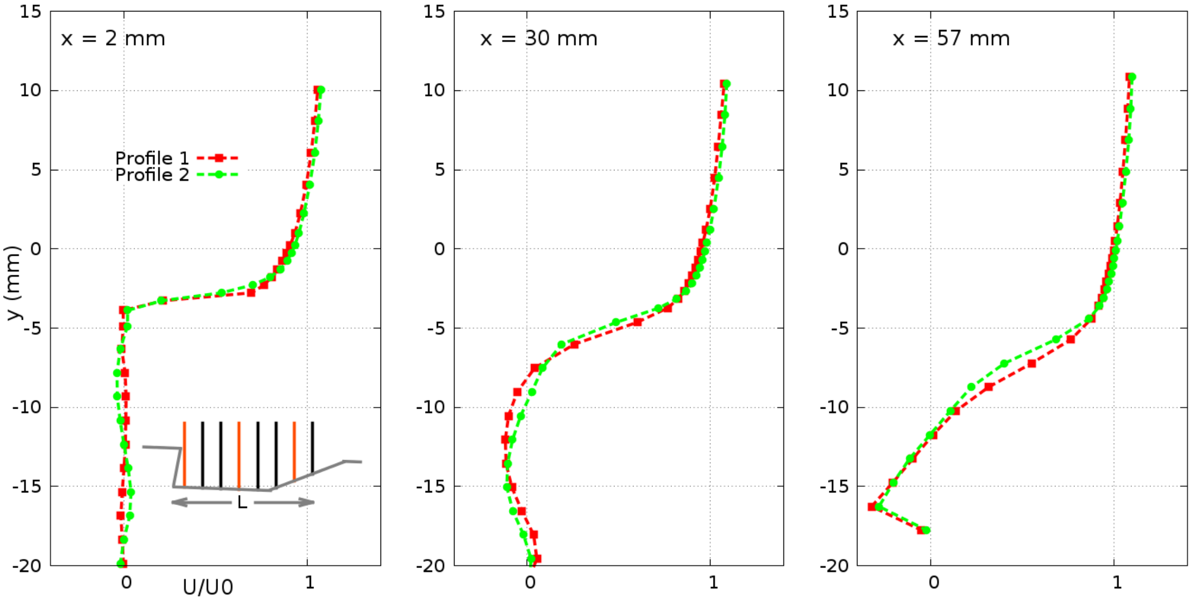

Figure 4.10: Averaged streamwise velocity profile with the inlet velocity profiles P1 and P2.

Mesh	Δx (μm)	Δy (μm)	Δz (μm)	Cells
Fine	100	80 - 150	100 - 150	300M
Coarse	200	150 - 200	160 - 300	45M

Table 4.4: Description of meshes used for computations. M $\equiv 10^6$.

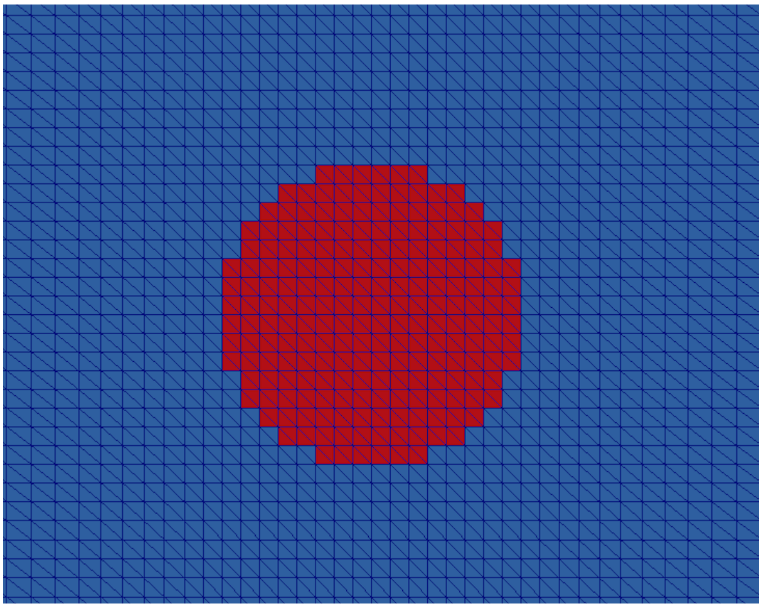

Figure 4.11: Mesh around the injector: fluid (red) and solid (blue) regions. Fine grid.

simulations, but the meshes are designed as if the injector were present to maintain the same grid for reactive and non-reactive simulations. The coarse mesh contains 45 millions of points with the cell size varying between 150 and 300 μm. The fine mesh features cell sizes almost twice smaller in all direction, leading to 300 millions of points (see Tab. 4.4).

While the cell size is kept constant in the x direction, the cells near the walls and the mixing layer between the freestream and the cavity are refined down to 80 μm in the direction y for the fine mesh and 150 μm for the coarse mesh. The cell size is 100 μm (fine) or 160 μm (coarse) in the injector, which leaves 16 cells to describe the diameter of the injector for the fine mesh (see Fig. 4.11) and 10 for the coarse mesh. The cell size in the spanwise direction, Δz, is increased to 150 μm (fine mesh) or 300 μm (coarse mesh) in the direction of the sides of the domain. The cell size evolution is performed slowly by introducing a factor f_c to avoid numerical error induced by two neighbour cells having too large size difference. The maximum difference between two neighbour cells should be 5%, leading to:

$$f_c = \frac{\delta_n}{\delta_{n-1}} \leq 1.05 \tag{4.5.3}$$

which is equivalent to a geometric sequence of scale factor δ_0 and common ratio f_c:

$$\delta_n = \delta_0 \times f_c^n \tag{4.5.4}$$

The dimensionless wall distance y^+ computed at the upper wall of the simulation domain and inside the cavity is displayed in Fig. 4.12 for both meshes. This value being on average 10 for the fine mesh and 18 for the coarse mesh at the upper wall, a wall model is probably needed to improve

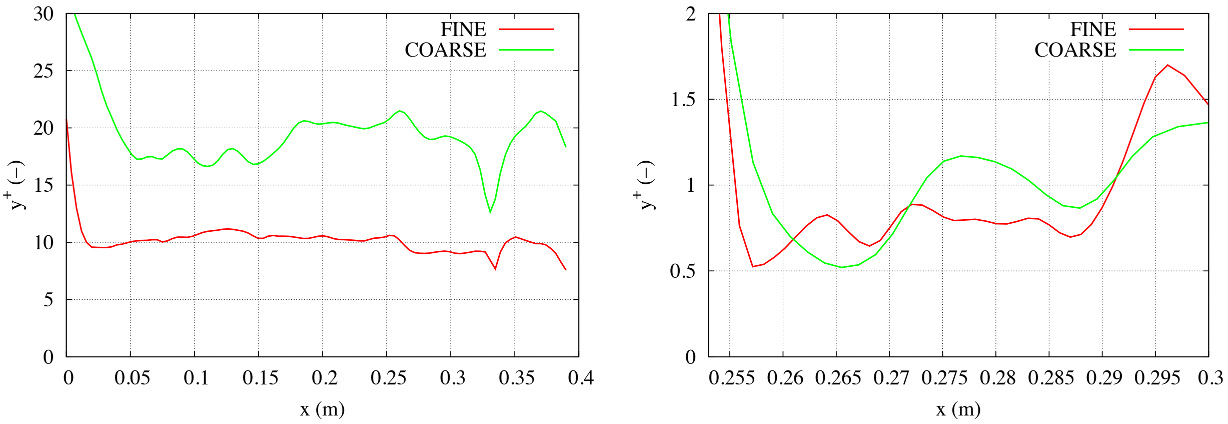

Figure 4.12: Dimensionless wall distance y^+ for coarse and fine meshes at the upper wall (left) and inside the cavity (right).

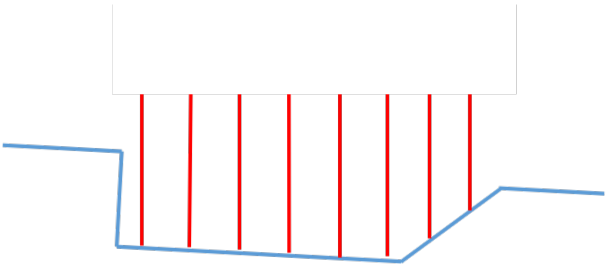

Figure 4.13: Positions where the data are computed: 2, 11, 20, 30, 39, 48, 57 and 66 mm respectively from the cavity front corner.

the simulation results. The dimensionless wall distance inside the cavity stays relatively low (≈ 1) for both meshes, no model is required in this region. An investigation relative to wall model is discussed in section 4.5.5.

Computations were performed in 3D. Statistics on velocities (averaged and rms) are compared at 8 positions (see Fig. 4.13). The positions are located by their distance to the cavity front which are respectively: 2, 11, 20, 30, 39, 48, 57 and 66 mm. Fig. 4.14 shows a comparison between the meshes for averaged streamwise velocity and velocity fluctuations. The velocity profiles near the cavity front ($x = 2$ and 11 mm) and at the rear of the cavity ($x = 66$ mm) are almost superimposed for the two grids, while the profiles in between differ slightly at the mixing layer. On the other hand, the fine mesh leads to much more velocity fluctuations at the front of the cavity than the coarse mesh. But this difference is reversed as we get closer to the cavity rear.

4.5.3 Simulation with one injector

4.5.3.1 Analysis of the flow

Averaged streamlines of the non-reactive flow are shown in Fig. 4.15 for the fine mesh. As discussed in previous works [64, 5], the velocity disparity between the supersonic air flow and the one inside the cavity, creates a clockwise large recirculation area, which is responsible of the mass exchange at the shear layer. This recirculation zone is the main feature of flame stabilization by a cavity, as it is intended to trap the hot combustion products to maintain the cavity at high temperature thus insuring pre-heating and ignition of the fresh reactants. The primary recirculation zone is at high

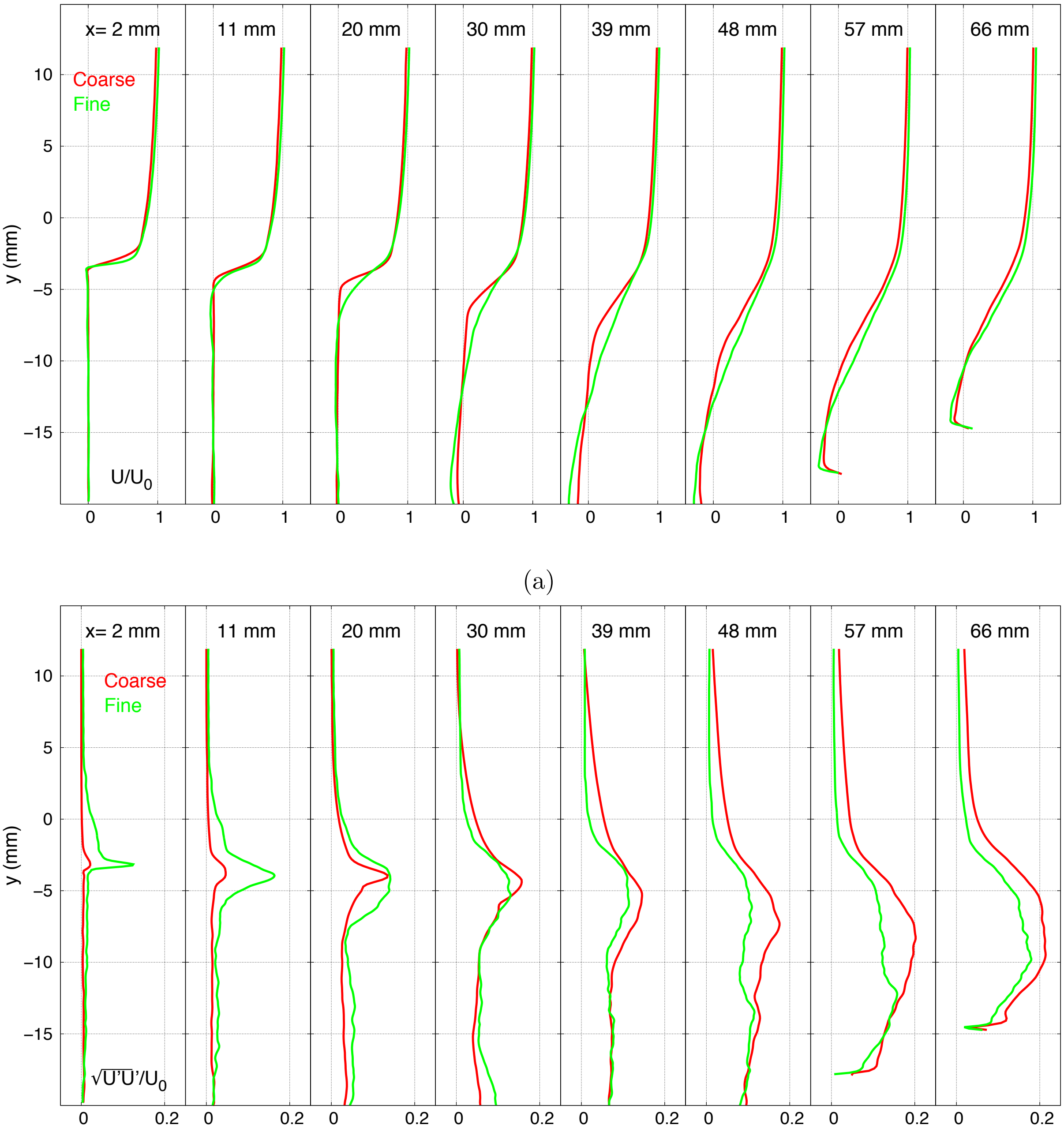

(a)

(b)

Figure 4.14: Streamise velocity (a) and velocity fluctuations (b) inside the cavity for coarse (red) and fine (green) meshes.

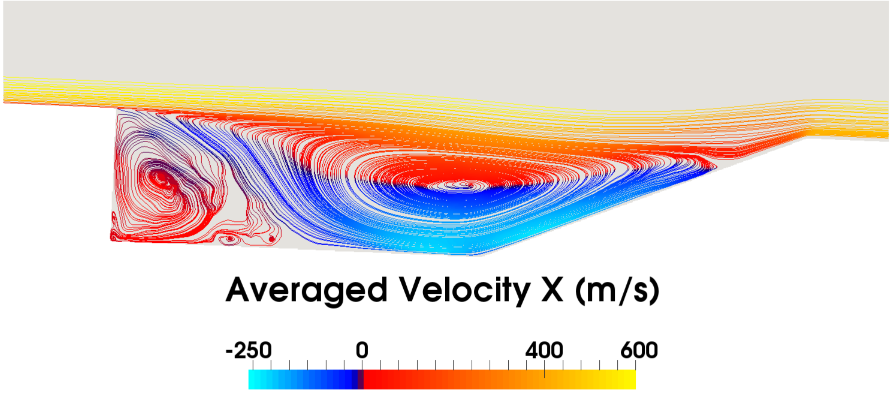

Figure 4.15: Averaged streamlines inside the cavity, colored by axial velocity fied for fine mesh.

speeds, approaching Mach 0.5. A much smaller secondary anti-clockwise recirculation area is found at the front of the cavity with very low speed. The shape of the recirculation areas is similar to the one in the work of Baurle [4], and the velocity of the primary recirculation zone is very close to the experimental data of Tuttle et al. [164]. A small part of the front of the cavity is cut in the experiment, so no comparison can be made for the small recirculation area.

A variety of averaged flow properties for non-reactive case are displayed in Fig. 4.16. The coarse and the fine meshes are showing the same flow characteristics. As shown previously, the Mach number inside the cavity is very low, approaching 0 at the cavity front, and is under 0.5 in the large recirculation area. The whole cavity is at subsonic speeds. A strong reattachment shock system where the pressure is equal to 90 kPa is identified from the aft wall of the cavity to the exit of the computational domain. This system of shocks is also present at the same position in the RANS/LES performed by Baurle [4]. This shock system is actually responsible of the temperature increase inside the cavity: the shock hitting the aft wall of the cavity is heating the surrounding flow, which is brought to the front and the middle of the cavity due to the recirculation bubbles. There is also a small preheating due to the frictions with the wall upstream the cavity. All these heatings lead to an average temperature of 450 K in the cavity, which is 120 K higher than the freestream. Finally, the pressure inside the cavity is heterogeneous, varying from 40 to 90 kPa.

An instantaneous field of subgrid viscosity adimensionalized by laminar viscosity is displayed in Fig. 4.17 for the fine mesh. Values are as expected for supersonic flows: high in the boundary layers where turbulent intensity is strong, mixing layer and at the oblique shock where subgrid viscosity adds to numerical artificial dissipations.

4.5.3.2 Comparison with the experimental results

Comparisons between results obtained with coarse and fine meshes and the experimental data are performed in this section. Statistics correspond to 6 ms physical time simulations for the coarse mesh and 2 ms for the fine mesh. The residence time of the cavity being the order of 1 ms, the statistics are performed on approximately 6 and 2 residence times for the coarse and fine meshes respectively. The Fig. 4.18 shows the streamwise and transverse velocity profiles inside the cavity at the positions given in Fig. 4.13. The experiment is fairly well predicted by both meshes for streamwise velocity, except at the front of the cavity where the mixing layer is not well described. The velocity evolution at this area is smoother in the experiment. The transverse velocity is better described by the coarse mesh probably because the statistics are longer. The statistics of fine mesh

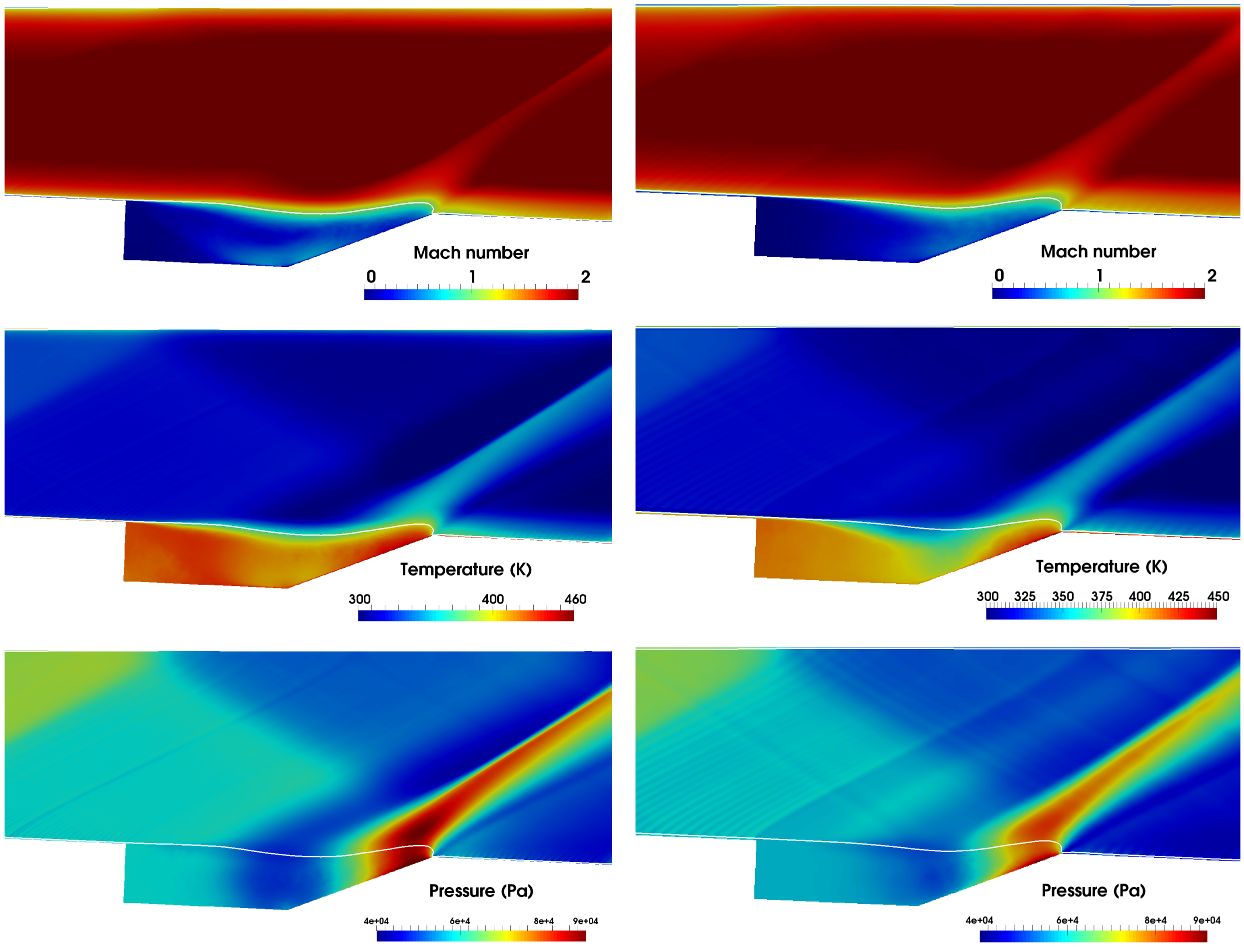

Figure 4.16: Various averaged properties of the flow for fine (left) and coarse (right) meshes: Mach number (top), temperature (middle) and pressure (bottom). The isoline Mach = 1 is displayed with a white line.

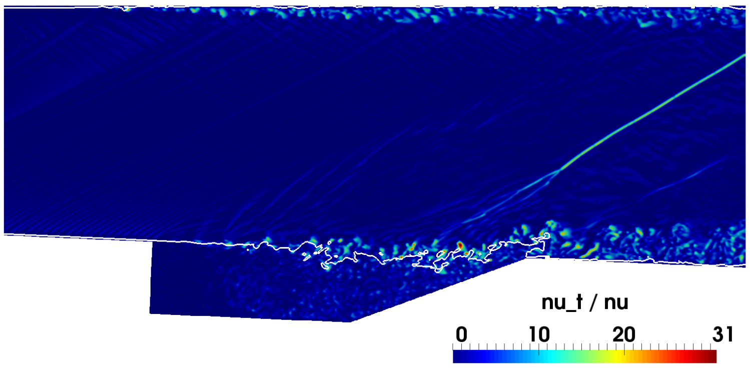

Figure 4.17: Instantaneous field subgrid viscosity adimensionalized by laminar viscosity ν_t/ν for fine mesh. The isoline Mach = 1 is displayed with a white line.

simulation are not extended because the non-reactive simulation with the fine mesh is expensive (150 000 hours for 2 ms of physical time). The computational results are close to the experimental data at the front and middle of the cavity, but are out of phase when reaching the rear of the cavity. The difference at the rear is probably due to the strong reattachment shock system hitting the wall of the cavity at this region, which might be not well captured.

A comparison on cavity wall pressure is performed for both meshes, and displayed in Fig. 4.19. The pressure of the simulations differs from the experiment by approximately 10% in the cavity for both meshes. The simulations are therefore not well reproducing the experimental pressure. However, the study done by Gruber et al. [64] on non reactive cases of cavity-based scramjet shows the same shape of profiles as the present computations (see Fig. 1.12): the pressure being almost constant from the region before the cavity to the cavity aft wall, then increasing due to the shock. On the other hand, the pressure of the experiment is higher in the cavity than in the area before the cavity, which means that the airflow of the freestream will not be able to enter the cavity (hypothesis on a roughly constant pressure in the cavity). Consequently, this result is very confusing and would need to be investigated further.

The averaged streamwise velocity, transverse velocity and vorticity fields in the cavity of the coarse mesh are compared to the experiment. Fig. 4.20 shows that the main features of the flow is recovered by the simulations. It is shown that the mixing layer at the front the cavity is thinner in the computations, but becomes thicker at the rear of the cavity.

4.5.4 Simulation with two injectors

A non reactive simulation with two injectors (25.4 mm) has been performed for the coarse mesh and compared to the one injector simulation. The two injectors case NRC2 has been initialized with the one injector solution NRC1 (12.7 mm) by symmetry to the axis $z = 0$. The boundaries at $z = -12.7$ mm and $z = 12.7$ mm are still prescribed as periodic. The mesh is composed of 90 millions of cells and needs approximately 80 000 hours CPU time to get statistics cumulated on 6 ms. The averaged velocity profiles inside the cavity are compared and displayed in Fig. 4.21. The streamwise velocity is not modified by the addition of one extra injector. NRC2 is performing slightly better at positions corresponding to the front of the cavity for the transverse velocity. At the other positions, both cases are not recovering the experimental data, and NRC1 is closer to the experiment at $x = 57$ mm. NRC2 and NRC1 are also compared to the experiment for the wall pressure inside the cavity (Fig. 4.22). The difference in wall pressure is negligible at the cavity bottom floor between the numerical cases, but the pressure in NRC2 is higher at the cavity ramp, resulting in a maximum difference of 4000 Pa in the vicinity of the shock. The two injectors simulation leads to results quite similar to the one obtained with one injector. In fact, the disparity between NRC1 and NRC2 is smaller than what is obtained between NRC1 and the fine mesh (NRF1).

4.5.5 Impact of HIT and wall model on the flow

Previous comparisons to the experiment show that the largest discrepancy in streamwise velocity appears at the mixing layer at the front of the cavity. This might be caused by the turbulence in the boundary layer of the isolator which is not developped enough. Therefore, injection of homogeneous isotropic turbulence (HIT) at inlet and wall modeling are studied in this section to find out the optimum numerical configuration for the simulations. A brief description on HIT is first presented. Then, computations with HIT and wall modeling (see Sec. 3.3) are performed and compared.

The implementation of HIT follows the formulations given in [11] where the energy spectrum E^+ from Passot-Pouquet is used. The turbulence injection is not desired at the whole inlet face, but

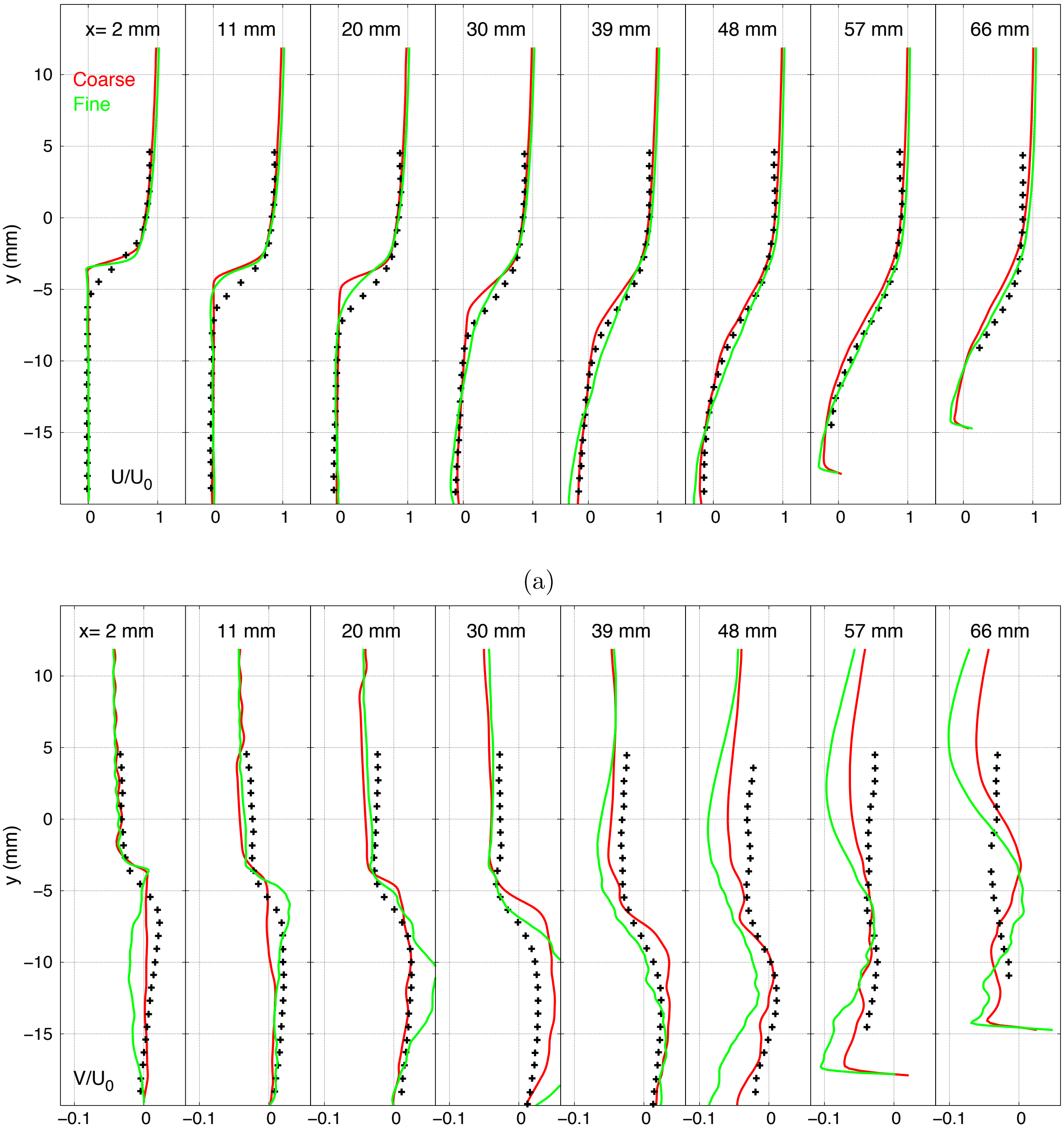

(a)

(b)

Figure 4.18: Comparison of the coarse and fine mesh computations with the experimental data [164]: (a) averaged streamwise velocity and (b) averaged transverse velocity.

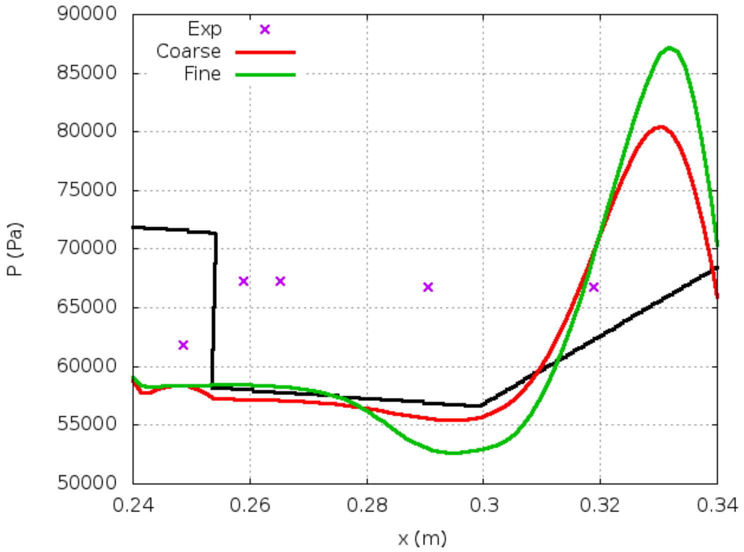

Figure 4.19: Averaged wall pressure field: comparison between coarse and fine meshes.

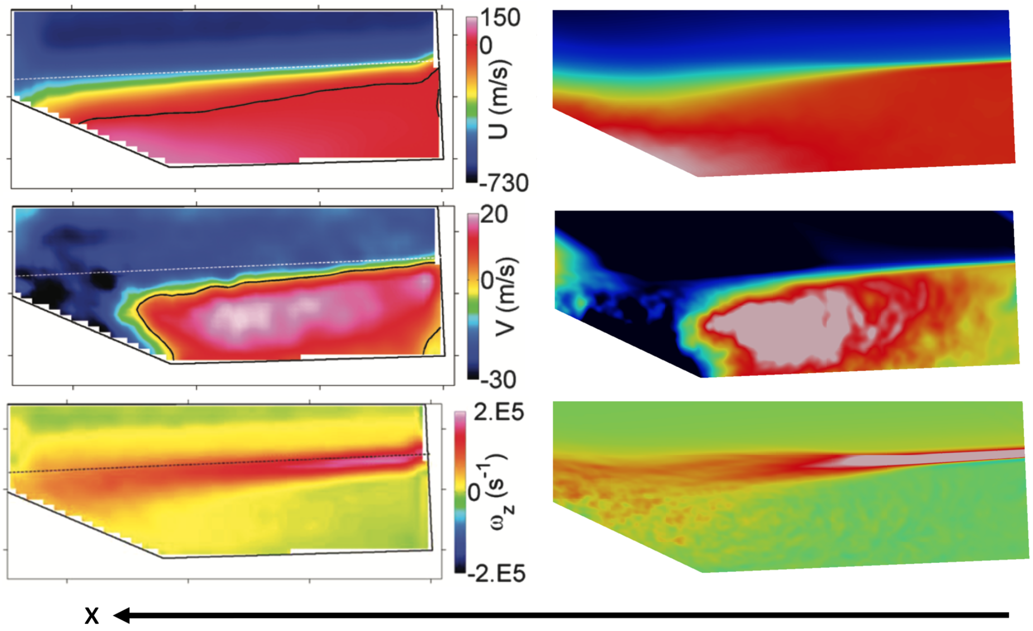

Figure 4.20: Comparison of averaged velocities and vorticity fields to the experiments [164]: experiment (left) and simulation (right). The direction of the axis x is reversed. The black line represents the isocontour U or $V = 0$. Coarse mesh.

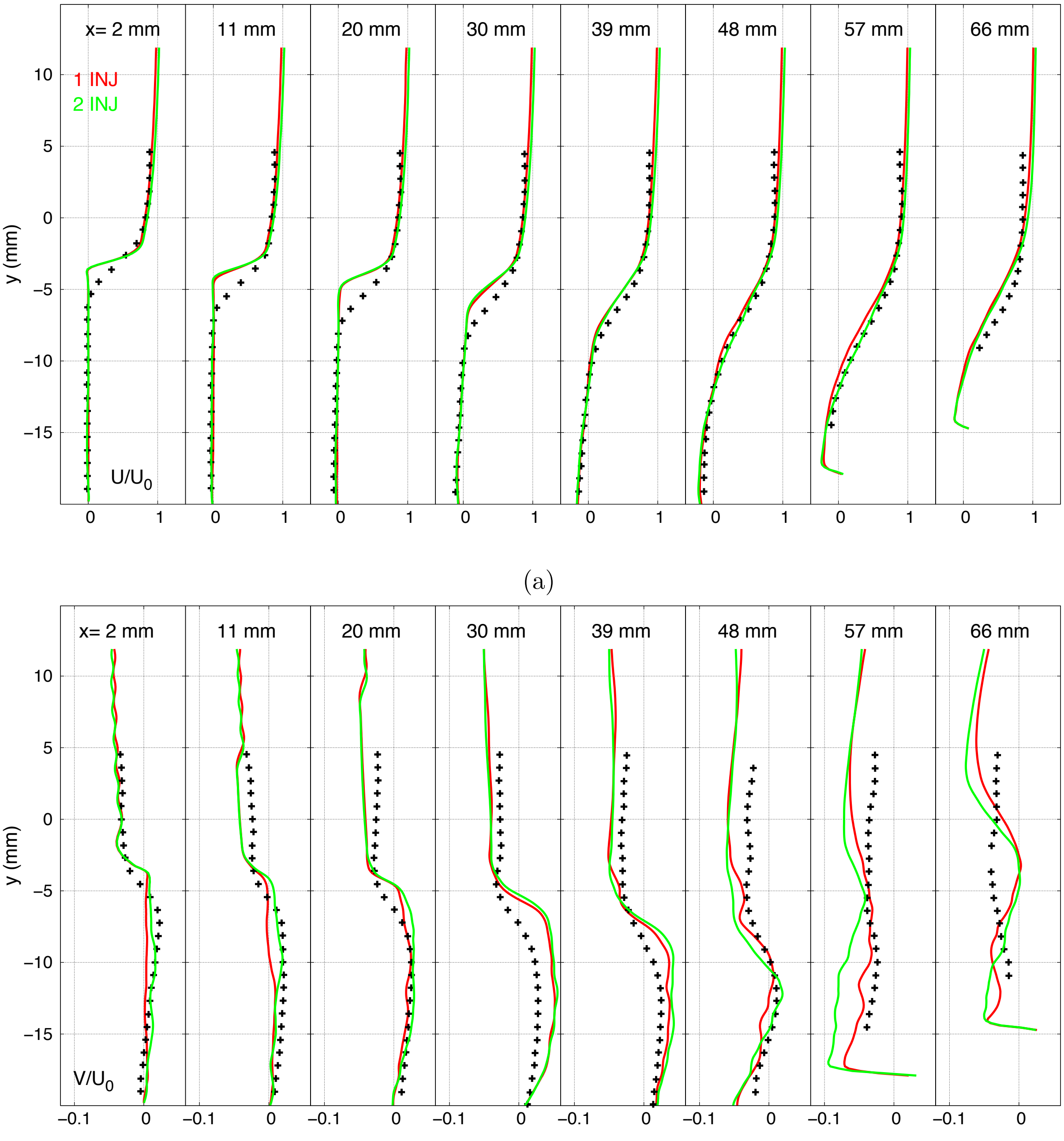

(a)

(b)

Figure 4.21: Comparison of the one and two injector size computations with the experimental data [164]: (a) averaged streamwise velocity and (b) averaged transverse velocity.

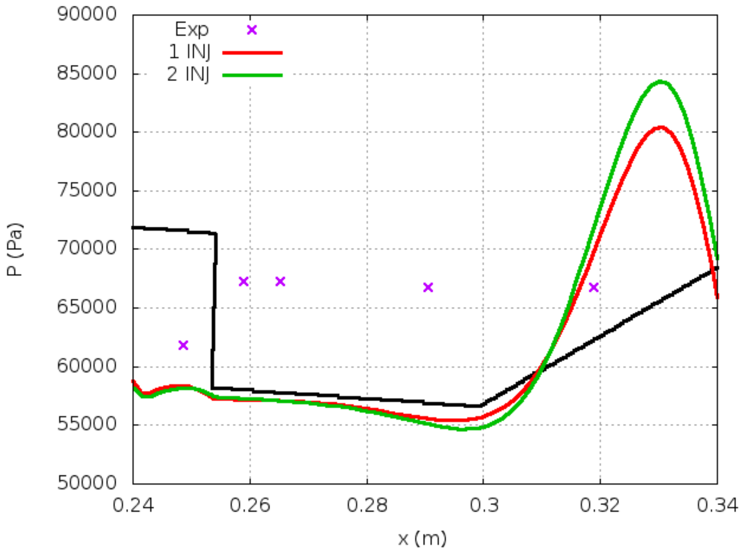

Figure 4.22: Averaged wall pressure field: comparison between one and two injector size simulations for the coarse mesh.

only in areas close to the wall. Thus, a hyperbolic tangente function is added to have injection only at the vicinity of upper and lower walls. The HIT injection profile P_{HIT} is expressed as:

$$P_{HIT} = \tanh\left[\max\left(0, |y - \frac{h-h_0}{2}| - (\frac{h-h_0}{2} - h_t)\right)\frac{\pi}{h_t}\right] \tag{4.5.5}$$

where $h_0 = 0$ and $h = 50.8$ mm are the ordinates of lower and upper walls respectively, and $h_t = 10$ mm is the distance to the wall where turbulence is injected. The HIT profile, along with the velocity profile P_1 are displayed in Fig. 4.23. The injection velocity is defined as:

$$\begin{cases} U_{inj} = (1 + P_{HIT} I_t) P_1 U_0 \\ V_{inj} = P_{HIT} I_t P_1 U_0 \\ W_{inj} = P_{HIT} I_t P_1 U_0 \end{cases} \tag{4.5.6}$$

where $U_0 = 727$ m/s is the bulk velocity, and I_t is the turbulence intensity computed by the solver dependent of the mean intensity $I_{t,m}$ imposed by the user. Three cases with $I_{t,m} = 10\%$, 20% and 50% are investigated, and the RMS profiles in the isolator (region prior to the cavity) are displayed on Fig. 4.24 at six positions: $x = 0.3$, 50, 100, 150, 200 and 250 mm, showing the profile evolution through the isolator, the cavity being located at $x = 253$ mm. The differences between the studied cases are solely significant in the streamwise direction. The case with 20% turbulence intensity has the strongest fluctuations, with values reaching 20% of bulk velocity in the plane near the cavity front (position $x = 250$ mm). This level of turbulence is found to be too strong. The simulation with $I_{t,m} = 50\%$ leads to lower turbulence levels than the previous case. In fact, such a high level of fluctuations at inlet triggers high subgrid scale viscosity which reduces the level of fluctuations down to realistic values. The case with 10% turbulence intensity has its streamwise fluctuations pike at 12% of freestream velocity, which is sufficient to generate significant turbulence at the front of the cavity. The latter case is chosen to be compared with the case without injection of HIT.

A comparison between a simulation with HIT injection of 10% intensity, and one without HIT is now performed for the coarse mesh. The instantaneous Mach number field in the cavity is displayed on Fig. 4.25. The mixing layer with HIT appears more turbulent than in the case without HIT. A thicker in average mixing layer is then expected for the case with HIT injection.

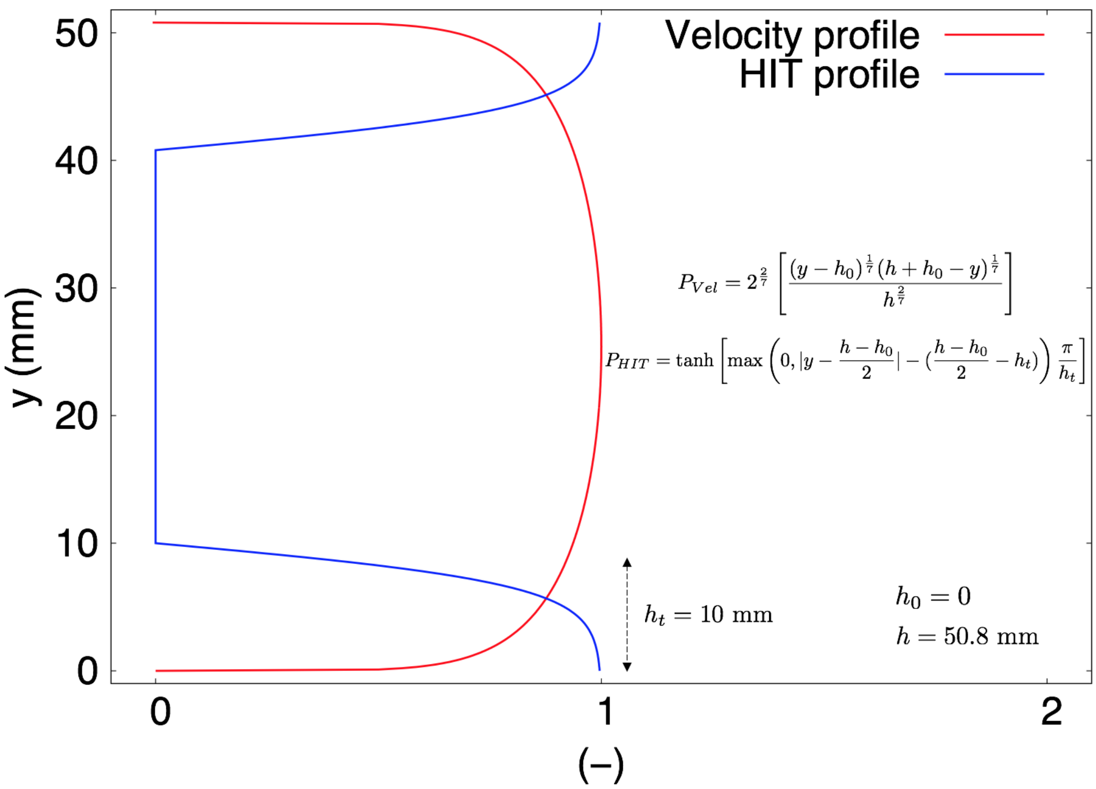

Figure 4.23: Velocity and HIT profiles.

Four computations were performed and compared for non-reactive flows with coarse mesh to investigate the impact of HIT and of the wall modeling. These computations are described in Tab. 4.3 and correspond to NRC1, NRC1W, NRC1H, NRC1HW respectively. The computation NRC1, named case 1 in the figures, was done without using any model and will be represented in red color. Case 2 corresponds to NRC1W, is only provided with wall model while case 3 (NRC1H) has HIT injection at the inlet with an intensity of 10% of local speed. The case 4 (NRC1HW) has both wall model and HIT injection. Case 1 will be compared to case 2, and case 3 to case 4.
As shown in section 4.5.2, $y^+ \approx 1$ in the cavity region and $y^+ \approx 18$ elsewhere for the coarse mesh. The cavity wall is therefore well resolved and does not require any wall modeling. Statistics were performed on 6 ms of physical time computation, corresponding to approximately 6 cavity residence times. The averaged wall pressure, temperature profiles, velocities profiles and velocity fluctuations profiles are displayed respectively on figures 4.26, 4.27, 4.28 and 4.29. The profiles spread from $y = -19$ mm to $y = 12$ mm at 8 different positions inside the cavity where the distance to the front corner of the cavity is respectively $x = 2$, 11, 20, 30, 39, 48, 57 and 66 mm.
The pressure inside the cavity remains the same for cases with HIT injection (NRC1H and NRC1HW), and differs for less than 500 Pa for cases without HIT. The wall modeling (NRC1W and NRC1HW) leads to higher pressure peak at the cavity ramp, about 800 Pa, compared to the cases without wall modeling (NRC1 and NRC1H). But, all the cases still underpredict the wall pressure inside the cavity compared to the experimental measurements. The impact of wall modeling is very limited for the wall pressure inside the cavity, as there is only a slight difference between activating or not the wall modeling, whereas the HIT injection has a larger influence on pressure.

The temperature inside the cavity is not modified by the wall modeling when HIT is used (NRC1H and NRC1HW). Otherwise (NRC1 and NRC1W), the difference is only observed at the front of the cavity where the largest discrepancy, 35 K, is found at the position $x = 2$ mm (Fig. 4.27). The strongest difference is found between cases with and without HIT injection where the temperature

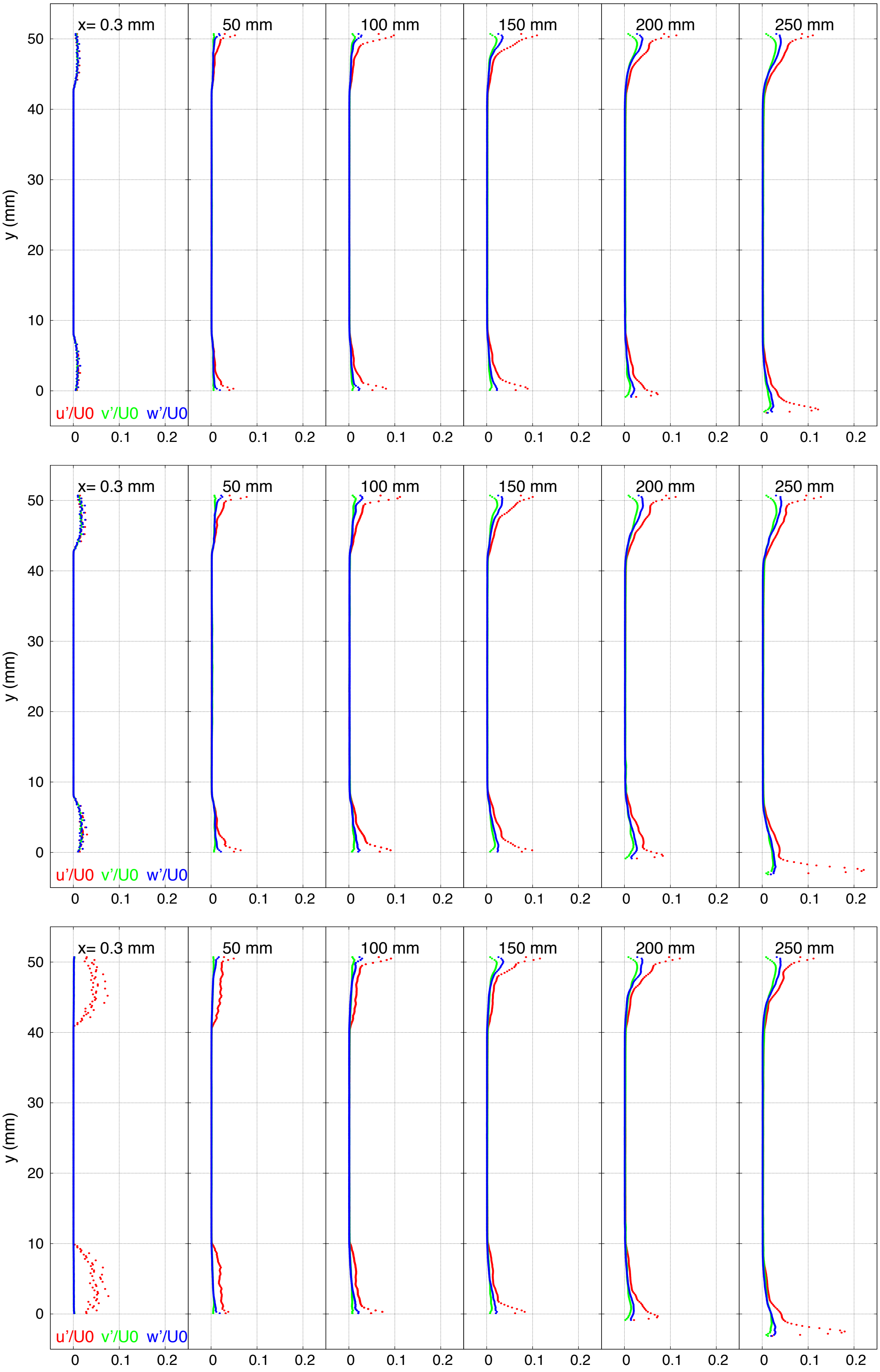

Figure 4.24: Velocity fluctuations inside the isolator for three turbulence intensities: 10% (top), 20% (middle) and 50% (bottom).

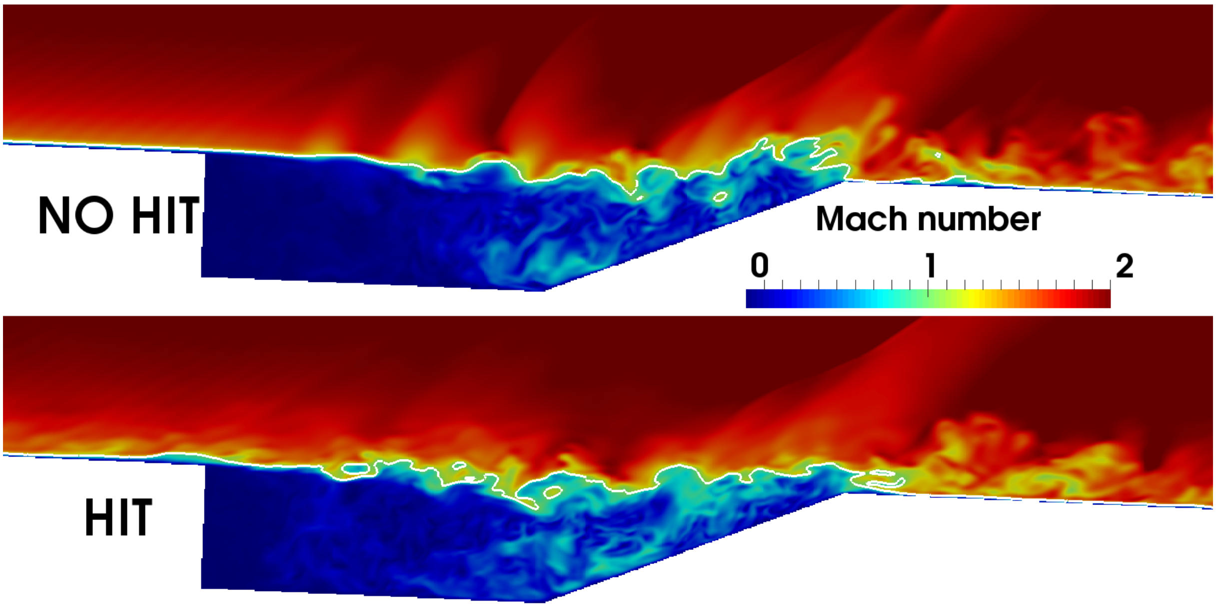

Figure 4.25: Instantaneous Mach number field of non reacting flows for case without HIT (top) and with 10% HIT injection (bottom). The iso-Mach = 1 is displayed with a white line.

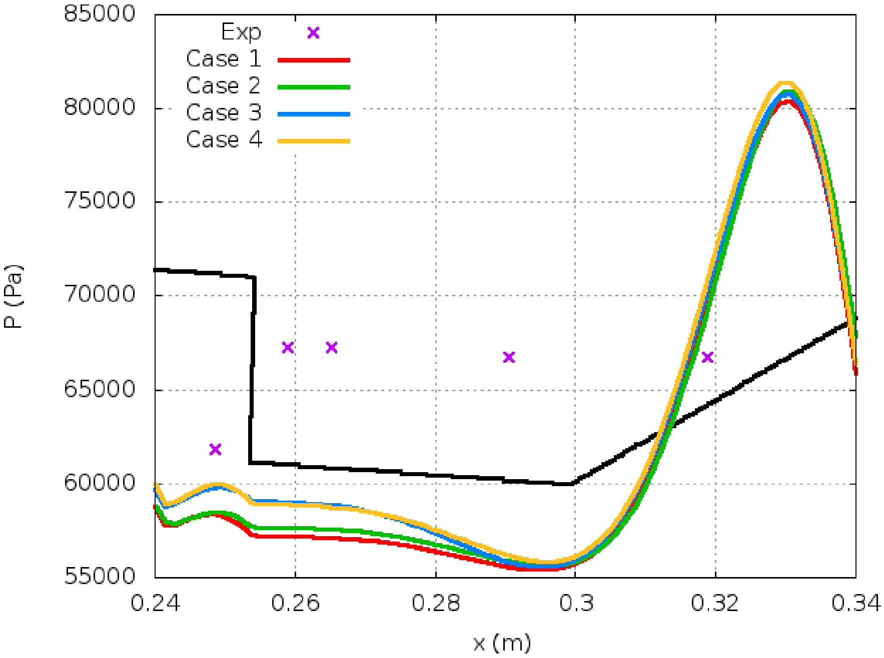

Figure 4.26: Averaged wall pressure of the cavity. Case 1 = NRC1, Case 2 = NRC1W, Case 3 = NRC1H and Case 4 = NRC1HW.

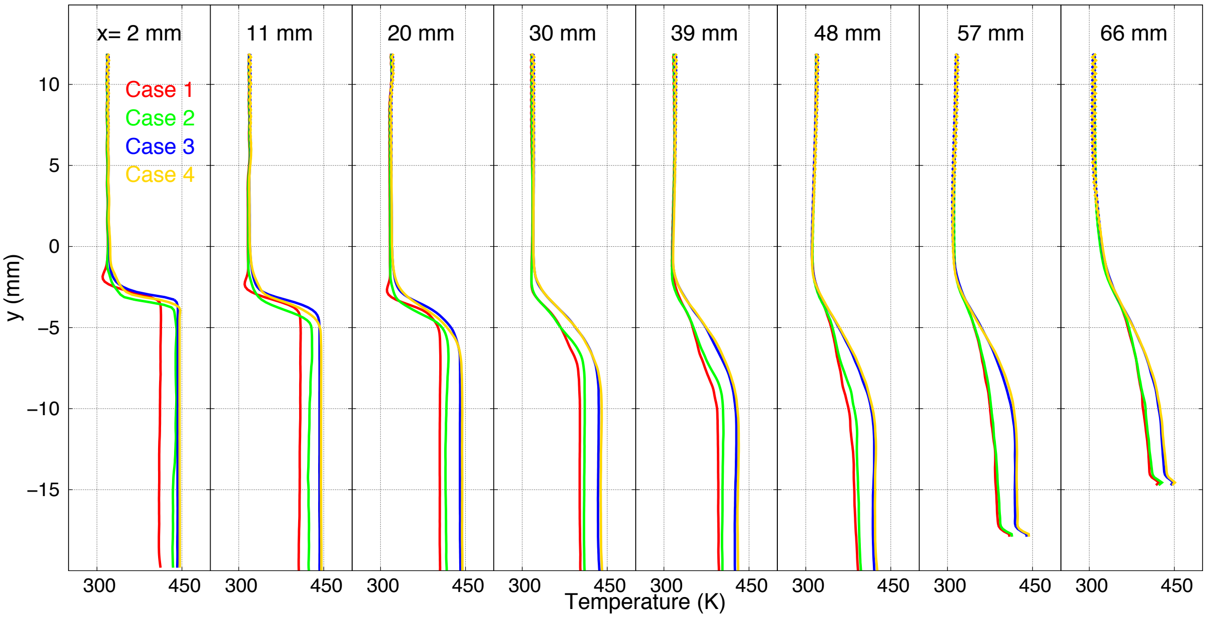

Figure 4.27: Averaged temperature profiles inside the cavity. Case 1 = NRC1, Case 2 = NRC1W, Case 3 = NRC1H and Case 4 = NRC1HW.

discrepancy can reach 45 K at any positions of the cavity.

The streamwise, transverse and spanwise velocities, adimensionalized by the bulk velocity U_0 are displayed in figure 4.28 respectively at top, middle and bottom positions. The streamwise velocity is only slightly modified by using HIT or the wall model. For the transverse velocity, while the differences become noticeable from position $x = 30$ mm when using HIT, the impact of the wall modeling is still not significant, except at the rear of the cavity, in the vicinity of the region where the shock system is reattached to the wall. Figure 4.29 shows the velocity fluctuations adimensionalized by the bulk velocity. The case with solely wall modeling (NRC1W) is performing the same as the case 1, which uses neither HIT nor wall model. On the other hand, cases with HIT (NRC1H and NRC1HW) provide higher fluctuations in the mixing layer at the front of the cavity, but slightly lower at the rear of the cavity. As the cavity temperature depends on the level of turbulence of the mixing layer, the velocity fluctuations may explain the differences found in Fig. 4.27.

The wall modeling has an overall very limited impact on the pressure, the temperature and the velocity inside the cavity, even more in the case with HIT injection. The implemented wall modeling was the simplest of the literature, but also the most disruptive model with high values of u_τ (≈ 5.5 m/s), therefore the impact of more precise wall modelings will be less significant than this simple one. The use of HIT provides more turbulence at the mixing layer between the mainstream and the cavity, which can facilitate fuel-air mixing at this region. Further computations will be performed only with HIT.

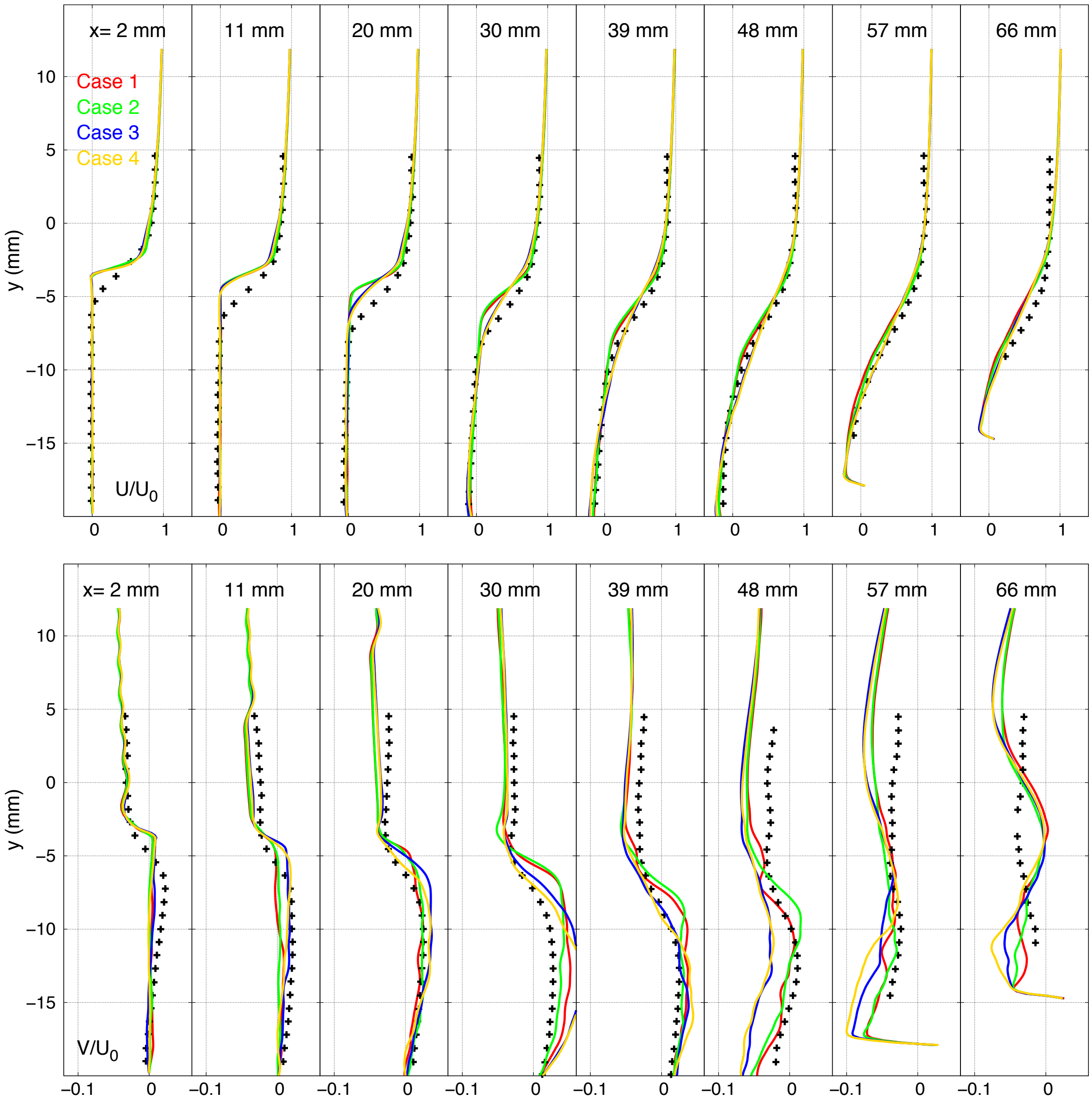

Figure 4.28: Velocity profiles inside the cavity: streamwise (top) and transverse (bottom) velocities. Case 1 = NRC1, Case 2 = NRC1W, Case 3 = NRC1H and Case 4 = NRC1HW.

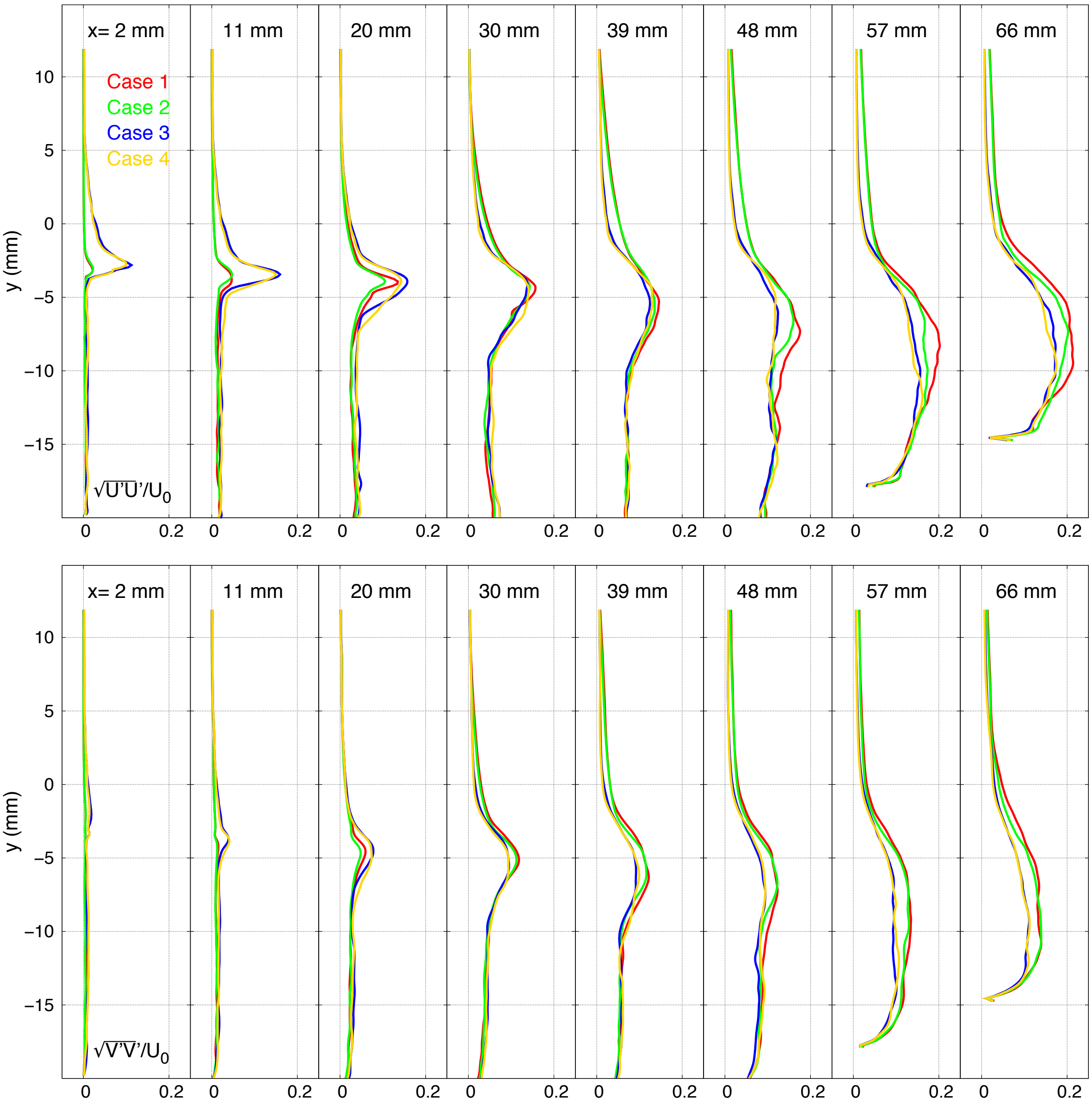

Figure 4.29: Velocity fluctuations inside the cavity: streamwise (top) and transverse (bottom) velocity fluctuations. Case 1 = NRC1, Case 2 = NRC1W, Case 3 = NRC1H and Case 4 = NRC1HW.

Chapter 5

Large eddy simulation of supersonic combustion

Contents

5.1 Generalities on ethylene

In this work, air is assumed to be composed solely of O_2 (21%) and N_2 (79%), which gives the molar ratio $n_{N_2}/n_{O_2} = 3.76$. The global combustion mechanism of ethylene with air is:

$$C_2H_4 + 3(O_2 + 3.76N_2) \rightleftharpoons 2CO_2 + 2H_2O + 11.28N_2 \tag{5.1.1}$$

The mass fractions of the reactives are function of the equivalence ratio ϕ, and follow:

$$\begin{aligned} Y_{C_2H_4} &= \frac{\phi W_{C_2H_4}}{\phi W_{C_2H_4} + 3(W_{O_2} + 3.76 W_{N_2})} \\ Y_{O_2} &= \frac{3W_{O_2}}{\phi W_{C_2H_4} + 3(W_{O_2} + 3.76 W_{N_2})} \\ Y_{N_2} &= \frac{11.28 W_{N_2}}{\phi W_{C_2H_4} + 3(W_{O_2} + 3.76 W_{N_2})} \end{aligned} \tag{5.1.2}$$

For a stoichiometric mixture ($\phi = 1$), the mass fractions are:

$$\begin{aligned} Y_{C_2H_4,st} &= 0.06366 \\ Y_{O_2,st} &= 0.21826 \\ Y_{N_2,st} &= 0.71808 \end{aligned} \tag{5.1.3}$$

The stoichiometric ratio s is therefore:

$$s = \left(\frac{Y_{O_2}}{Y_{C_2H_4}} \right)_{st} = 3.4285 \tag{5.1.4}$$

In the case of a pure ethylene injection mixed with pure air $Y_{C_2H_4,1} = 1$ and $Y_{O_2,2} = 0.2331$, the terms in the Bilger mixture fraction equation (Eq. 2.1.15) can be expressed as:

- $Y_{C,1} = \frac{2W_C}{W_{C_2H_4}} Y_{C_2H_4,1} = \frac{6}{7}$
- $Y_{C,2} = 0$
- $Y_{H,1} = \frac{4W_H}{W_{C_2H_4}} Y_{C_2H_4,1} = \frac{1}{7}$
- $Y_{H,2} = 0$
- $Y_{O,1} = 0$
- $Y_{O,2} = \frac{2W_O}{W_{O_2}} Y_{O_2,2} = 0.2331$

and Eq.2.1.15 can be simplified into:

$$Z = 4.3696 \left[\frac{Y_C}{6} + \frac{Y_H}{2} - \frac{Y_O - 0.2331}{16} \right] \tag{5.1.5}$$

Using Eq. 2.1.17, the stoichiometric mixture fraction is retrieved at $Z_{st} = 0.06366$.

The flammability limit of a fuel in an oxidizer is the value below (lower limit) or beyond (upper limit) which the combustion of the fuel in the oxidizer cannot occur anymore. The flammability limits of ethylene in air are provided by performing experiments at standard conditions of pressure and temperature using a 2 inch tube with spark ignition [179], the lower and upper limits, defined as the ratio between fuel and air concentrations, were found respectively at $F_L = 0.027$ and $F_U = 0.36$. The limits in terms of equivalence ratio are expressed as:

$$\begin{cases} \phi_L = \dfrac{s M_{C_2H_4}}{0.21 M_{air}} F_L = 0.425 \\ \phi_U = \dfrac{s M_{C_2H_4}}{0.21 M_{air}} F_U = 5.67 \end{cases} \tag{5.1.6}$$

where ϕ_L and ϕ_U are respectively the lower and the upper equivalence ratio limits.

5.2 Reduced kinetic schemes of ethylene

SiTCom-B is a numerical code with complex molecular transport properties [32] where all species are transported. The computational time increases strongly with the number of species. This is even more true in presence of short life species with characteristic time of the order of picoseconds. The computational cost of simulations of a real size combustor with detailed chemistry is thus prohibitive. The kinetic reduction consists of suppressing unimportant species and reactions from the detailed mechanism for conditions representative of the case under study, this procedure decreases the number of species involved, and at the same time increases the timestep since minor species are removed. Among the reduction techniques, the directed relation graph (DRG) is widely used to generate a skeletal mechanism from the detailed one by removing secondary species and associated reactions. Then the quasi-steady-state (QSS) assumptions can be made over some species of the skeletal mechanism to generate an even smaller scheme. However a reduced mechanism cannot mimic perfectly the detailed scheme in any conditions and can only be used in the conditions it was designed for. Therefore having a relevant reduced kinetic scheme leads to a compromise between computational costs and consistent simulations.

5.2.1 Presentation of studied reduced schemes

In the present work, four different reduced kinetic schemes from the literature are studied (see Table 5.1). The first scheme S10 is a 10 species 10 steps kinetic scheme from Singh and Jachimowski [152], reduced from the detailed model of Jachimowski [73] which has 25 species and 77 reactions. This simple reduced scheme has been compared in [152] to the detailed scheme for auto-ignition at a wide range of initial conditions : pressure $P \in [0.5, 2.0]$ bar, temperature $T \in [1200, 2000]$ K and equivalence ratio $\phi \in [0.5, 2.0]$. The reduced scheme is found to give good predictions near $\phi = 1.0$, but overpredicts the adiabatic flame temperature and the concentration of CO_2 with rich mixtures ($\phi = 2.0$). Also, in every studied case, combustion starts earlier in the reduced scheme than it does in the detailed model.

The scheme S19 consisting of 19 species and 167 reactions comes from the work of Lu and Law [104], and Lignell et al. [92]. The Qin 2000 mechanism for C1-C3 [136], composed of 70 species and 205 elementary reactions, has first been reduced to a skeletal mechanism of 29 species using DRG, then to a 19-species scheme with QSS assumptions on 10 species [104]. A comparison between the detailed, the skeletal and the reduced mechanisms has been performed for auto-ignition, 1D laminar flame propagation and counterflow ignition at different conditions : pressure $P \in [0.1, 30]$ bar, temperature $T \in [1000, 1800]$ K and equivalence ratio $\phi \in [0.5, 1.5]$. It is shown in [104] that the reduced scheme reproduces the detailed mechanism with high fidelity for all tested cases. The two last schemes S22 and S32 [105] are reduced from a detailed mechanism [173] base on USC-Mech II of the University of South California, composed of 75 species and 529 elementary reactions. S32 is a 32-species skeletal scheme, obtained by applying DRG to the detailed mechanism. S22 is obtained by applying QSS approximations to the skeletal scheme S32 (10 QSS species). S22 has been compared in [105] to its detailed mechanism for auto-ignition and extinction in Perfectly-Stirred Reactor (PSR) configuration and premixed laminar flames for a large range of initial conditions : pressure $P \in [1, 50]$ bar, temperature $T \in [1000, 1800]$ K and equivalence ratio $\phi \in [0.5, 1.5]$. Once again, the reduced scheme mimics with high fidelity the detailed mechanism, with a disparity below 10% for the extinction time and the ignition time, and below 4 cm/s for the laminar flame speed. These mechanisms will be compared for auto-ignition and laminar flame propagation in the following sections for conditions of pressure and temperature of 1 bar and 300 K respectively.

Schemes	Species	Reactions	Authors
S10	10	10	Singh and Jachimowski (1993) [152]
S19	19	167	Lu and Law (2005) [104], Lignell et al. (2007) [92]
S22	22	206	Luo et al. (2012) [105]
S32	32	206	Luo et al. (2012) [105]
S53	53	325	GRI-Mech 3.0 (1999) [155]
S75	75	529	USC-Mech II (2007) [173]

Table 5.1: Studied reduced mechanisms and two detailed mechanisms (S53 and S75) for ethylene.

5.2.2 Auto-ignition of ethylene

Auto-ignition has been performed using the solver SENKIN from Lutz et al. [106]. SENKIN is a 0 D solver, written in Fortran, that computes the time evolution of a homogeneous reacting gas mixture in a closed system. Before addressing reduced mechanisms, auto-ignition computations were performed for two detailed mechanisms and compared to the shock-tube experiments of ethylene-air combustion from Kopp et al. [83]. These mechanisms are the GRI-Mech 3.0 [155] with 53 species (S53) and the USC-Mech II [173] from which S22 and S32 are reduced, composed of 75 species (S75). The GRI-Mech 3.0 has mainly been designed for methane since the experimental data used to optimize this scheme are principally those from methane. However, it could also be used for ethylene and propane.
The experiments of Kopp et al. [83] were performed at $P = 1.1$ bar, $T \in [1100, 1300\ K]$ for lean ($\phi = 0.5$), stoichiometric ($\phi = 1$) and rich ($\phi = 2$) ethylene-air mixtures. Comparisons are shown in Fig. 5.1. S53, despite having some discrepancies with the experiments, reproduces that a lean mixture would ignite faster than a rich one. On the other hand, S75 is doing the opposite since rich mixtures are found to ignite faster. The case $\phi = 2$ for S75 is nevertheless very close to the experimental data, and the results for $\phi = 1$ are acceptable.

Actually, the experiments found in the literature are mostly oxy-fuel combustion in shock-tube with strong dilution by argon ($> 90\%$). A detailed review can be found in [167]. The detailed mechanisms S53 and S75 are thus compared to another experiment performed at $P = 1.07$ bar and $\phi = 1$, where the mixture is composed of 98% of argon (molar ratio). This leads to very low mass fractions for the fuel $Y_{C_2H_4} = 0.00352$ and the oxidant $Y_{O_2} = 0.01207$ which are about 20 times lower than in the previous case. Fig. 5.2 shows that autoignition times from S75 are very close to the experimental times, and S75 is performing better than S53. That leads to a conclusion that S75 was optimized with autoignition data from experiments with strong dilution by argon, and difference in autoignition time between cases with or without dilution is considerable.

In the case without dilution by argon, a lean mixture having a lower ignition delay is actually more intuitive, since a molecule of ethylene can react more easily if it is surrounded by oxygen than by other ethylene molecules. In contrary, when the mixture is highly diluted, the chance of finding a molecule of ethylene surrounded by oxygen is much lower, therefore a richer mixture can ignite faster. Kopp et al. [83] have proposed a detailed mechanism, Aramco 1.3 [114], which could overcome the defect of S75 in prediction of autoignition times for fuel-air combustion without dilution. The Aramco 1.3 mechanism is composed of 346 species and thus does not fit a 3D large eddy simulation, therefore it has not been considered for the LES performed in this thesis.

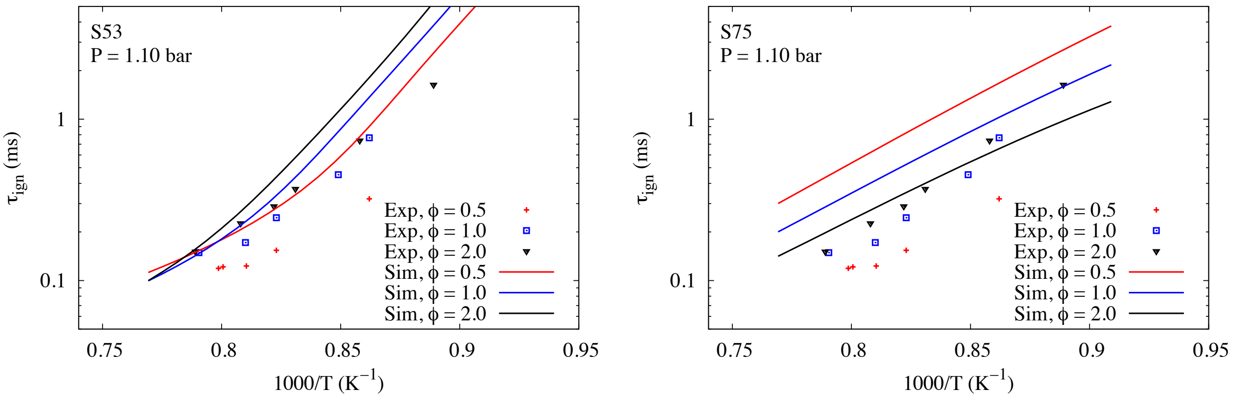

(a) (b)

Figure 5.1: Comparaison of ignition delay for S53 (a) and S75 (b) with experimental data [83] at $P = 1.1$ bar and $\phi \in [0.5, 2.0]$ for ethylene-air mixture.

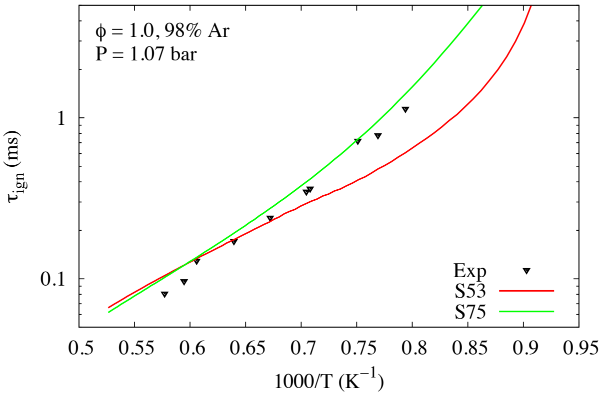

Figure 5.2: Comparaison of ignition delay for S53 and S75 with experimental data [78] at $P = 1.07$ bar and $\phi = 1$ for ethylene-oxygen mixture, diluted by argon (98% molar ratio).

A wide range of initial conditions (pressure $P \in [0.66, 1]$ bar, temperature $T \in [800, 2000]$ K and equivalence ratio $\phi \in [0.5, 2.0]$) have then been investigated for the four reduced mechanisms for autoignition of ethylene-air mixtures. The temperature profile over time is shown in Fig. 5.3 for ambient pressure and equivalence ratio of unity. The adiabatic flame temperature remains the same for all the studied schemes regardless of the initial temperatures : $T_{ad} = 2725$ K for $T_{ini} = 1200$ K and $T_{ad} = 2950$ K for $T_{ini} = 2000$ K. However, the ignition delays differ largely among the mechanisms, especially at low temperatures. While the difference between S10, S22 and S32 is not significant, the delay for S19 is almost an order of magnitude higher than for S22 or S32. The long ignition time of S19 is consistent with the detailed mechanism (Qin 2000) which also has a very long ignition time at low temperatures ($T < 1400$ K) [104]. S19 could fail to predict auto-ignition regions in the cavity where the temperature is relatively low, around 1200 K.

The mixing in the cavity not being uniform, a large range of equivalence ratios need to be investigated. In addition to the stoichiometric case displayed in Fig. 5.3, a lean ($\phi = 0.5$) and a rich ($\phi = 2$) cases are shown in Fig. 5.4. While the adiabatic flame temperature is constant for all mechanisms at the stoichiometric conditions, it differs slightly between S10 and the other mechanisms for lean and rich cases: lower at lean mixtures and higher at rich mixtures. At the conditions of

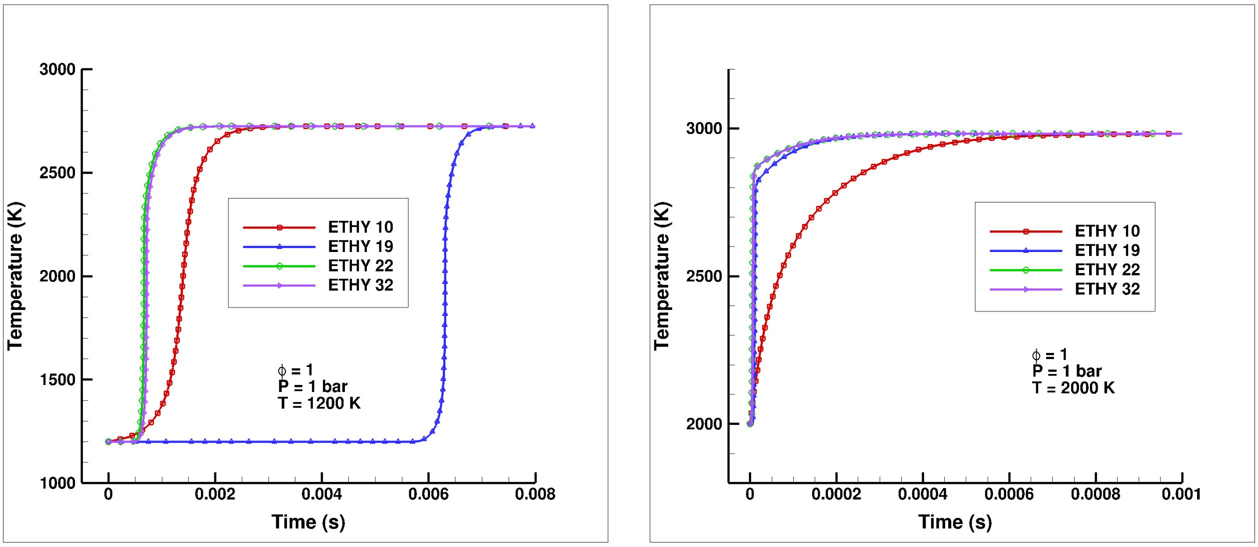

Figure 5.3: Autoignition of ethylene at T = 1200 K (left) and T = 2000 K (right) for different reduced schemes: S10, S19, S22 and S32 ($\phi = 1$).

$P = 1$ bar and $T = 1200$ K, the autoignition delay increases when the equivalence ratio decreases for all the mechanisms studied.

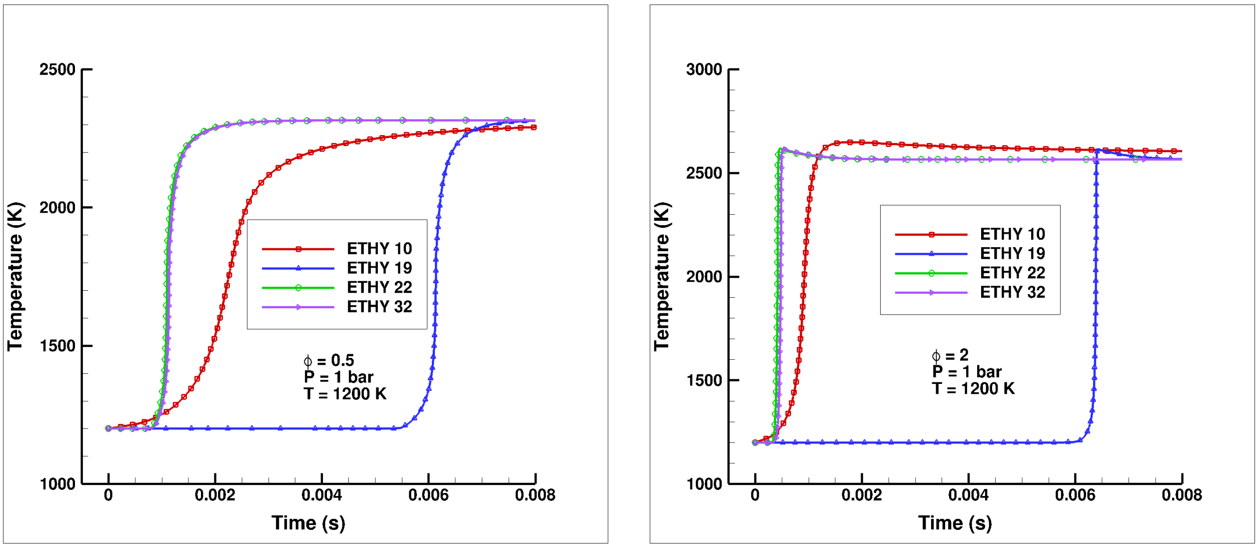

Figure 5.4: Autoignition of ethylene at $\phi = 0.5$ (left) and $\phi = 2$ (right) for different reduced schemes.

The concentration time evolution of ethylene (C_2H_4) and of three main products (CO_2, CO, H_2O) mass fractions is shown in Fig. 5.5 at $P = 1$ bar, $T = 1200$ K and $\phi = 1$ for all schemes. It appears that S19 has the same behaviour as S22 or S32 except for the shift in ignition delay. S10 behaves differently since ethylene starts to be consumed earlier, and the CO peak (at 1.5 ms) is weaker than with the other mechanisms. Nevertheless, the composition of the major combustion products in the burnt gas is identical for all the schemes: $Y_{CO_2} = 0.118$, $Y_{H_2O} = 0.067$ and $Y_{CO} = 0.052$. Fig. 5.6 compares the time evolution of main species for S10 and S22. The delay between CO_2 and CO production is very high, around 0.15 ms for S10 while being insignificant for S22. The difference is even stronger with lean ($\phi = 0.5$) and rich ($\phi = 2$) mixtures. A very peculiar behaviour of species concentration time evolution is observed for S10, especially at the beginning, around $t = 0.0002$ s. These differences will lead to a different behaviour of combustion in the cavity.

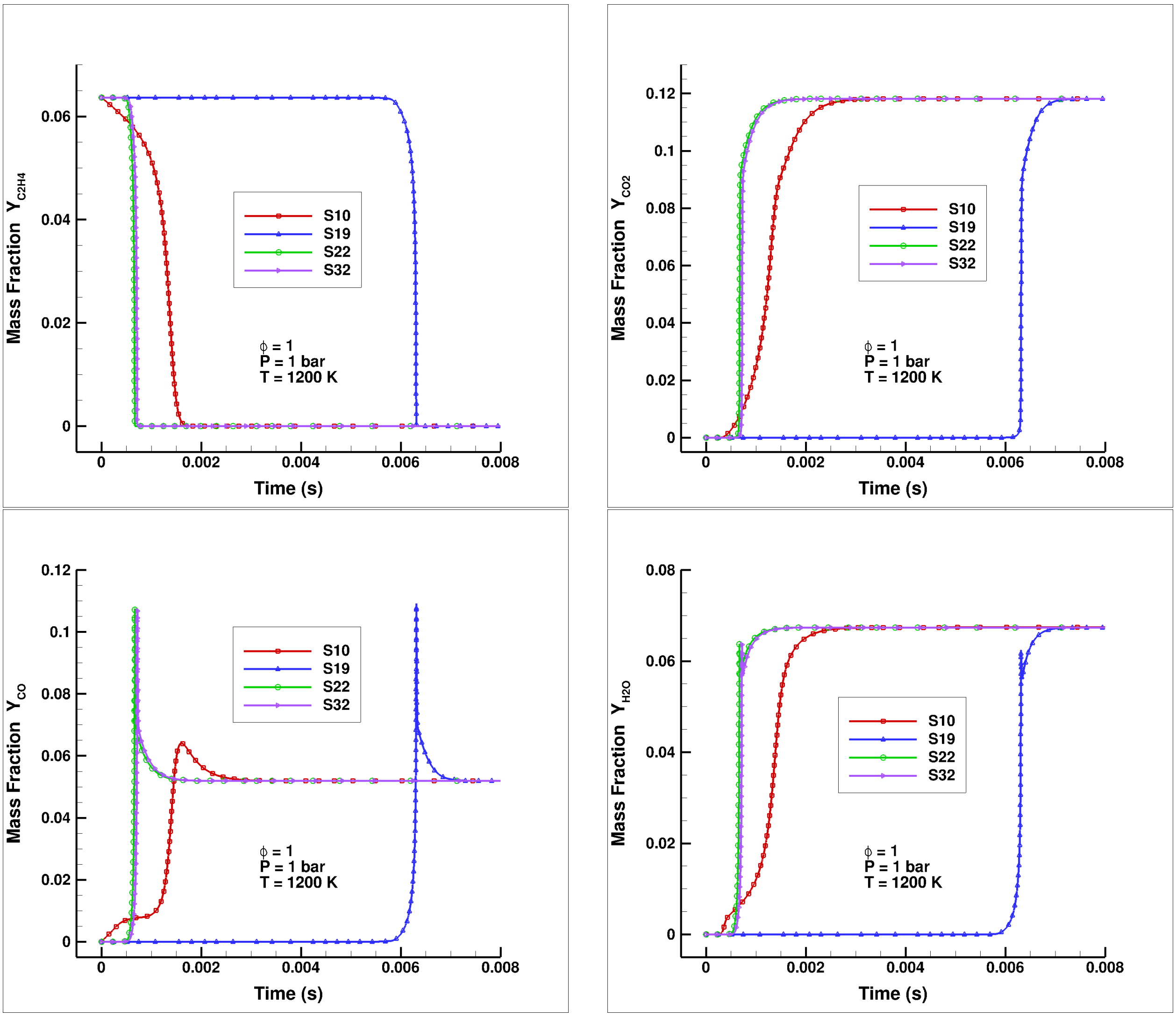

Figure 5.5: Mass fraction of ethylene and main products of its combustion during autoignition at $\phi = 1$, $P = 1$ bar and $T = 1200$ K.

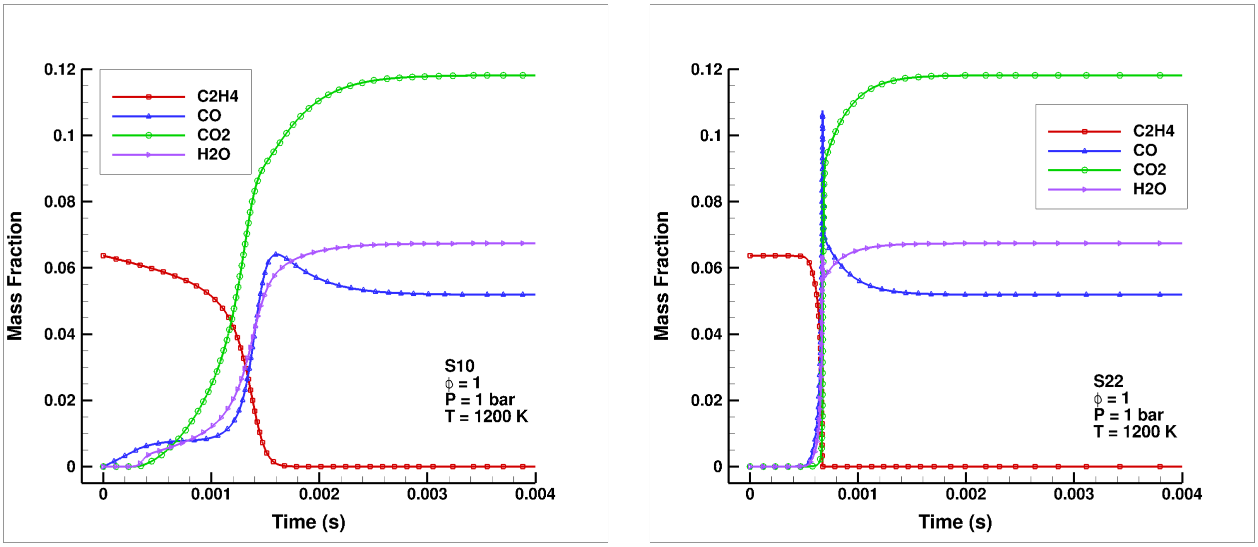

Figure 5.6: Mass fraction of main species for S10 (left) and S22 (right) at $\phi = 1$, $P = 1$ bar and $T = 1200$ K.

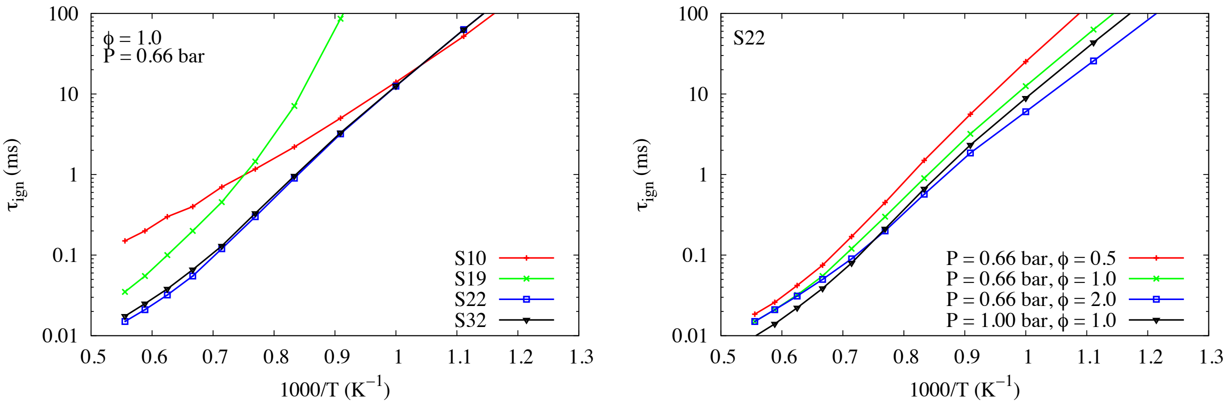

(a)

(b)

Figure 5.7: Comparaison of ignition delay between the reduced mechanisms at $P = 0.66$ bar and $\phi = 1.0$ (a), and for S22 at various initial conditions (b).

The pressure inside the cavity being around 0.66 bar, the ignition delay has been computed again for all reduced schemes at equivalence ratio $\phi = 1.0$, pressure $P = 0.66$ bar and temperature $T \in [800, 1800]$ and shown in Fig. 5.7 (a). The ignition delay will be compared to the cavity residence time, which has been estimated as approximately 1 ms with the empirical relationship from Davis and Bowersox [35, 36]. A reduced mechanism with an ignition delay far longer than the cavity residence time will be discarded for the reactive simulations of the scramjet. At this pressure and equivalence ratio, S10, despite being the longest to ignite at high temperatures ($T > 1400$), is having acceptable ignition delays until $T = 1200$ K. On the other hand, the ignition delay for S19 is satisfactory at high temperatures, but the delay increases exponentially below 1400 K to reach values that are too far from the cavity residence time. Thus, the scheme can hardly be used for LES of this scramjet. S22 and S32 are having similar results for auto-ignition and have the lowest ignition delay among the studied schemes. Their ignition delays stay under 1 ms until $T = 1100$ K. While S19 can easily be discarded because of its ignition delay, S10 remains interesting since it is very simple, with few species and still having acceptable auto-ignition delays. Therefore, S10 will be used in preliminary simulations to investigate the dynamics of the reactive cavity before using a more precise, but also more CPU time consuming mechanism (S22), which will grant more accurate results. The skeletal scheme S32 is also discarded as it gives the same results as S22, but with some additional secondary species that limit the chemical timestep to picoseconds.

A more detailed study is now performed for the reduced scheme S22. The combustion products of ethylene-air flame are split into major (Fig. 5.6), intermediate and minor products (Fig. 5.8) based on the concentration of species. A major species has in average a mass fraction with two orders of magnitude higher than a minor species at stoichiometric conditions with $P = 1$ bar and $T = 300$ K. While the major species constitute the burnt gas, most of the intermediate and the minor species are only present in the preheat and flame regions, with some species exclusively present in the flame, such as $HCCO$.

Autoignition computations for lean and rich mixtures have been performed for S22 at $P = 0.66$ bar (see Fig. 5.7 (b)). The ignition delay appears to be higher at lower pressures with $\phi = 1.0$ and the interval of studied temperatures. By varying the equivalence ratio and with the pressure kept at 0.66 bar, one can notice that the ignition delay is decreasing when the equivalence ratio is increasing. A comparison has been made to the experimental data from Kopp et al. [83] for S22 (see Fig. 5.9). S22 has the same behaviour as S75 which is expected since S22 is derived from S75.

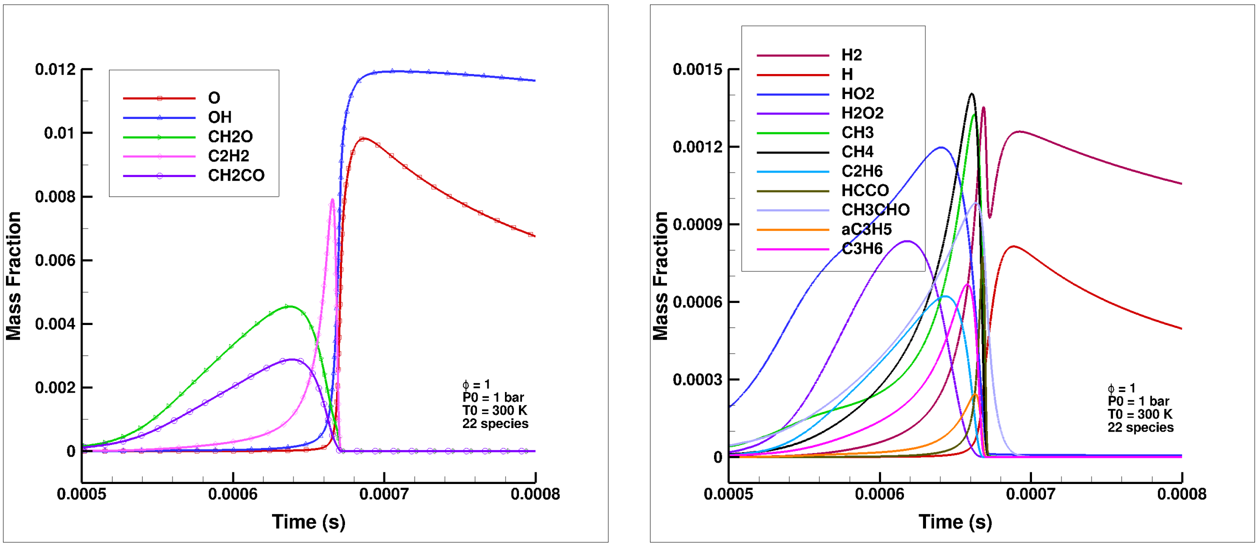

Figure 5.8: Mass fraction of intermediate (left) and minor (right) products of ethylene-air combustion with S22 at $\phi = 1$, $P = 1$ bar and $T = 1200$ K.

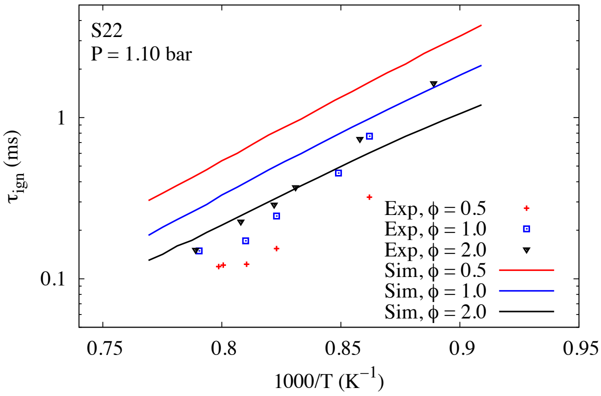

Figure 5.9: Comparaison of ignition delay for S22 with experimental data [83] at $P = 1.1$ bar and $\phi \in [0.5 - 2.0]$.

As for S75, the results of S22 are not that inconsistent in rich mixtures. It will be shown later (see Sec. 5.3.3.3) that the composition in the cavity is very rich, thus S22 will be kept. Future work could aim at reducing Aramco 1.3 with the inhouse ORCh code developed by Jaouen et al. [75] to render it compatible with CFD.

5.2.3 Premixed laminar flames of ethylene

The autoignition study shows that S19 and S32 should be eliminated respectively because of the unrealistic ignition delay and the tiny chemical timestep. The 1D simulation of S10 could not result in a converged solution, since this very reduced scheme has originally been designed only for auto-ignition. Therefore, only S22 will be studied for premixed laminar flame propagation. The 1D simulations are firstly performed with the solver REGATH, and then compared with the inhouse code SiTComB.

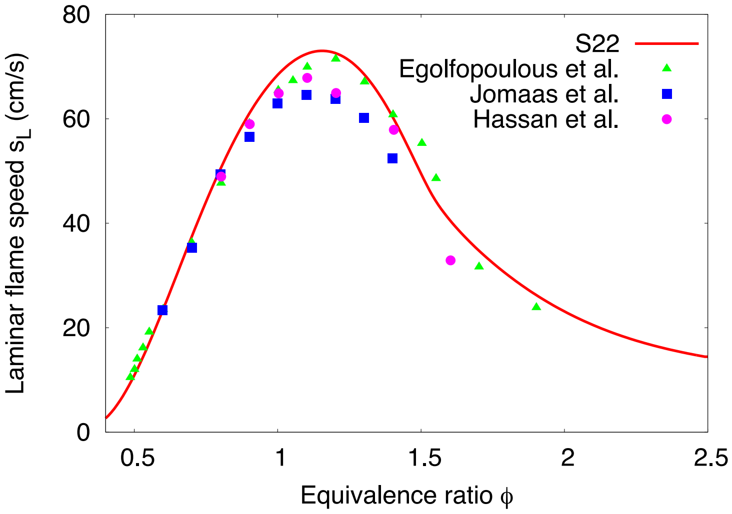

Figure 5.10: Performance of reduced scheme S22 (line) against experimental data (patterns) of laminar flame speeds for ethylene at $P = 1$ bar and $T = 300$ K.

5.2.3.1 1D premixed flames with REGATH

One dimensional laminar premixed flame propagations were computed with REGATH [19], an incompressible solver from the Ecole Centrale de Paris that solves 1D steady transport equations of primitive variables T, Y and U with a Newton-Raphson iterative algorithme to converge from an initial solution, which must be "close" to the final solution. The latter condition imposes the upper limit of equivalence ratio step $\Delta\phi$ beyond which the algorithm will not converge.
Simulations were performed on S22 at pressure and temperature of 1 bar and 300 K respectively and equivalence ratio from 0.45 to 2.5. Converged solutions could not be obtained at leaner mixtures. Laminar flame speed against equivalence ratio is computed and displayed in Fig. 5.10 and compared to three experimental data of: (E1) Egolfopoulous et al. [47], (E2) Jomaas et al. [77] and (E3) Hassan et al. [69]. The peak of laminar flame speed and the equivalence ratio at which the peak is found are reported in Tab. 5.2.

Data	**Equivalence Ratio**	**Maximum flame speed (cm/s)**
E1	1.2	71.5
E2	1.1	64.5
E3	1.1	68
S22	1.15	73

Table 5.2: Maximum laminar flame speeds for experimental (E1, E2, E3) and numerical (S22) data.

Compared to the experiments E2 and E3, simulations are overpredicting the flame speed, especially around $\phi = 1.1$. On the other hand, simulations are also shifting the peak of flame speed by 0.05 to the rich mixtures, increasing the discrepancies between E2, E3 and the simulations. However S22 reproduced with high fidelity E1, except in a small region around the peak, where the simulations are shifted by 0.05 to the lean mixtures.

Some of the ethylene-air combustion products at stoichiometric conditions with $P = 1$ bar and

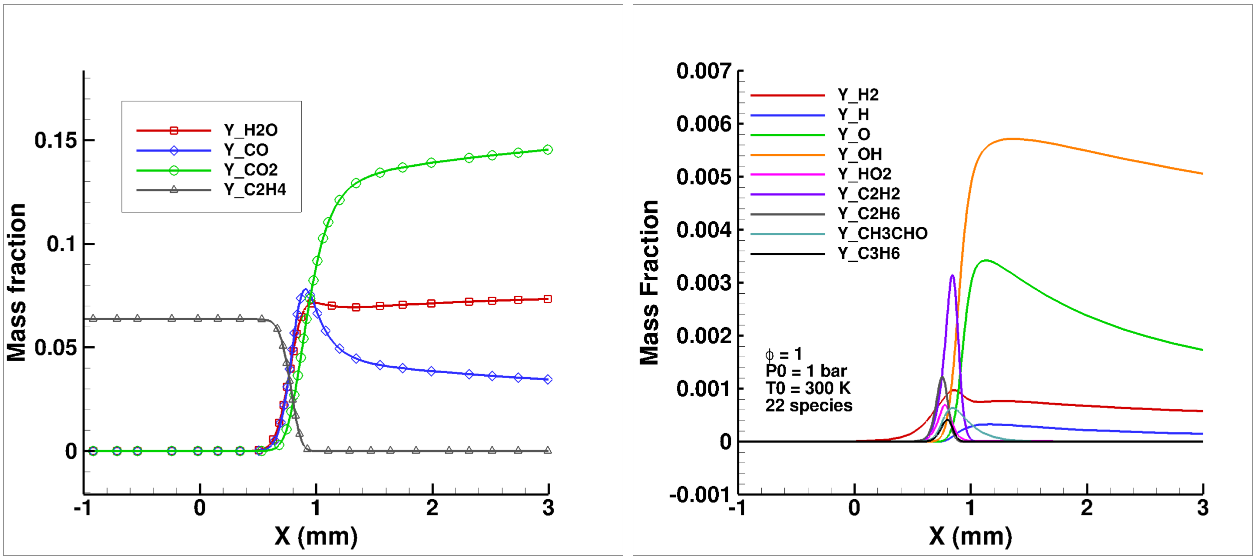

Figure 5.11: Ethylene-air combustion products at $P = 1$ bar, $T = 300$ K and $\phi = 1$ for S22.

$T = 300$ K are shown on Fig. 5.11. The laminar flame thickness δ_L can be computed using the following expression:

$$\delta_L = \frac{T_b - T_f}{\max \nabla T} \tag{5.2.1}$$

where T_b and T_f are the temperature of the burnt and the fresh gases respectively. 1D laminar premixed flames have also been computed for conditions close to the experiment of Tuttle et al. [164]: $P = 0.66$ bar and $T = 329$ K for $\phi \in [0.4, 75]$. Results are detailed in section 6.5.2. Flame speed and thickness at these conditions are displayed in Tab. 5.3 for $\phi \in [0.5, 2.5]$. The maximum flame speed and the minimum flame thickness are found near the stoichiometry. The minimum flame thickness being 0.4 mm, the flame will be described with at least four points when the LES will be performed with the fine mesh ($\Delta x = 0.1$ mm).

ϕ	**Flame speed (cm/s)**	**Flame thickness (mm)**
0.5	14.8	1.24
0.75	55.0	0.50
1	82.7	0.40
1.5	63.9	0.47
2	30.7	0.80
2.5	18.5	1.15

Table 5.3: Ethylene-air laminar flame speed and thickness for $P = 0.66$ bar and $T = 329$ K.

5.2.3.2 1D premixed flames with a compressible code: SiTComB

REGATH is an incompressible solver that does not take into account the compressibility effect, the pressure stays constant through the flame. Differently, a compressible solver like SiTComB could predict the pressure jump through the flame front which can be calculated analytically by using the

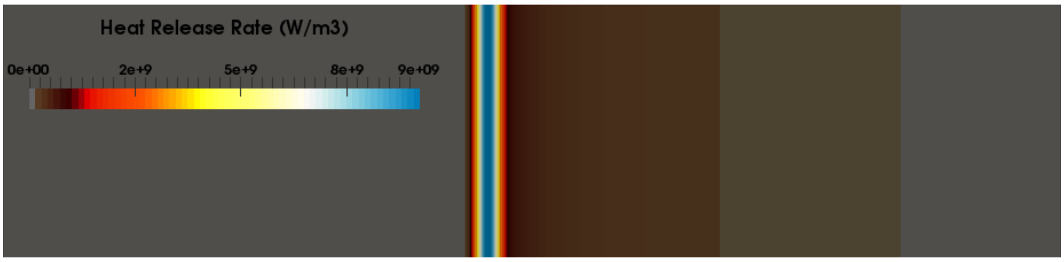

Figure 5.12: Heat release rate field for 1D laminar premixed flame on SiTComB with S22.

conservation of momentum and mass flow rate:

$$\begin{cases} (P_f - P_b) = \rho_b U_b^2 - \rho_f U_f^2 \\ \rho_b U_b = \rho_f U_f \end{cases} \tag{5.2.2}$$

where the subscripts f and b refer to the fresh and burnt gases, respectively. The pressure jump through the flame front $\Delta P = P_f - P_b$ is therefore:

$$\Delta P = \rho_f U_f^2 \left(\frac{\rho_f}{\rho_b} - 1 \right) \tag{5.2.3}$$

Taking ρ_f, ρ_b and U_f from REGATH solution at $P = 1$ bar and $T = 300$ K at stoichiometry with S22, the pressure jump is found equal to 3.66 Pa.

In order to check the capability of SiTComB to predict the pressure jump through the flame front, an one-dimensional computation has been performed at $P = 1$ bar and $T = 300$ K with stoichiometric mixtures using the 22 species chemical mechanism. The computational domain is initialized with an incompressible solution from REGATH with the same parameters. The heat release rate is shown in Fig. 5.12 and an 1D laminar premixed ethylene-air flame can reach a heat release of 9 GW/m^3 at the flame front. The temperature and pressure profiles from SiTComB are then compared to REGATH and displayed in Fig. 5.13. While the temperature profile is identical regardless which solver is used, the pressure differs by $\Delta P_{sim} = 3.5$ Pa between the solvers. This pressure difference is also the gap between fresh and burnt gases captured by SiTComB, which is very close to the theoretical value. The previous study validates the prediction of pressure jump through a flame front using the SiTComB solver and then its accuracy.

5.3 Reactive flow study

This section is dedicated to the simulation of the experimental device with only one injector included. The numerical modelling is first presented. Then some 2D computations are shown, followed by 3D simulations with 10 or 22 species to represent the chemistry between ethylene and air. Tab. 5.4 lists all the different cases studied in this section.

5.3.1 Numerical modelling

The scramjet geometry in the reactive case is the same as in the non-reactive case (see Fig. 4.7) with an additionnal injector modelized by immersed boundary method at the rear of the cavity, located at $y = -19.57$ mm. This injector is modeled by a cylindrical channel with adiabatic slipping wall conditions. The diameter of the cylinder is 1.6 mm which leaves 10 and 16 cells in the coarse and fine meshes respectively to describe its width. Pure fuel is injected uniformly at $P = 73.8$ kPa

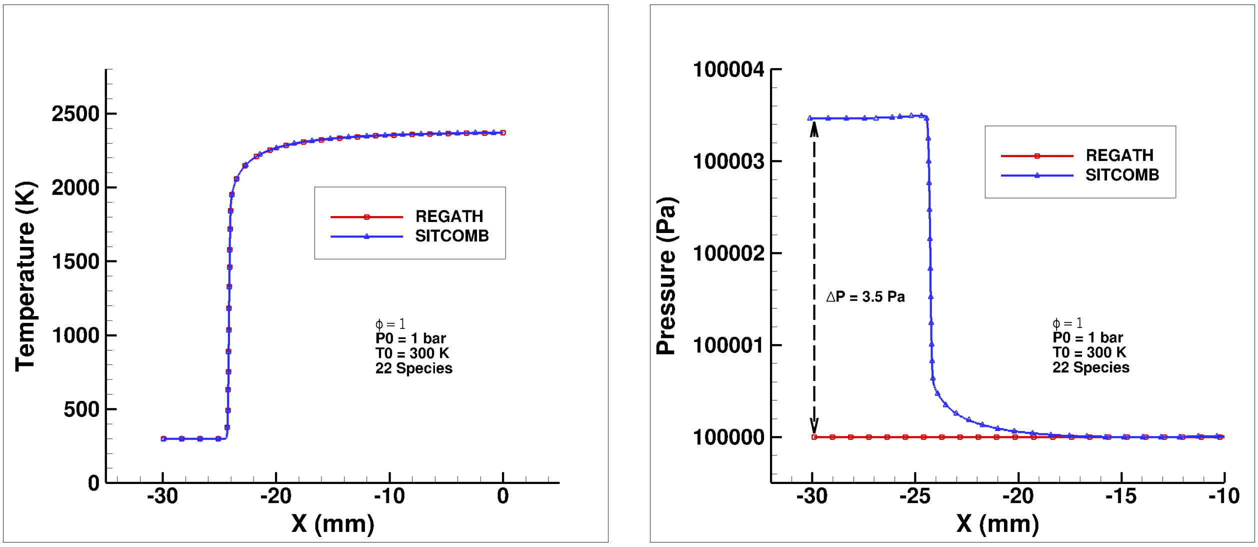

Figure 5.13: Comparison of temperature profile and pressure jump through a flame front between REGATH and SiTComB for 1D simulations with S22.

Case	Dimension	Injectors	Chemistry	Wall	Mesh	Cells (M)
R2D	2D	-	S22	Adiabatic	Fine	3
NRCS22	3D	1	None	Adiabatic	Coarse	45
RCS10	3D	1	S10	Adiabatic	Coarse	45
RCA1	3D	1	S22	Adiabatic	Coarse	45
RCA1L	3D	1	S22	Adiabatic	Coarse	45
RCA1M	3D	1	S22	Adiabatic	Coarse	45
RFA1	3D	1	S22	Adiabatic	Fine	300
RCI1	3D	1	S22	Isothermal	Coarse	45
RFI1	3D	1	S22	Isothermal	Fine	300
RCA2	3D	2	S22	Adiabatic	Coarse	90
RCA11	3D	11	S22	Adiabatic	Coarse	542

Table 5.4: Simulations studied in the current chapter. The fuel loading of all cases is 99 SLPM (Case 3 of Tuttle et al. [164]), except for RCA1L and RCA1M which are featuring fuel loadings of 36 and 56 SLPM respectively (Cases 4 and 2 respectively of Tuttle et al. [164]).

and $T = 310$ K with 3D-NSCBC conditions [102]. A mid-high fuel loading, corresponding to the case 3 (99 SLPM) of the experiments performed by Tuttle et al. [164], is considered in this section to obtain a stable flame. As the injector wall is provided with slip conditions, the fuel injection velocity is uniform and equal to $U_F = 115$ m/s. The airflow injection has the same velocity profile as the non-reactive case with a bulk velocity of $U_0 = 727$ m/s, coupled with a 10% intensity of homogeneous isotropic turbulence injection in the boundary layer (see Sec. 4.5.5).

Unsolved subgrid-scale fluxes are still modeled by the dynamic Smagorinsky closure [117, 93]. Fourth-order artificial dissipation terms [162, 161, 160] are applied in zones with strong gradients of density or pressure to overcome spurious oscillations and damp high-frequency modes. Full multi-species formulation is considered with complex molecular transport properties [70]. The reaction rates are modeled with the quasi-laminar model (see 3.2.1) which will be further discussed in section 6.1. Subgrid Prandtl and Schmidt numbers, are set to 0.9.

Due to the low temperatures of the flows, firing the cavity requires an artificial ignition source. The experiments performed at AFRL [164] used spark plugs in the middle of the cavity to start combustion. In the simulation, the local temperature will be forced to $T^{imp} = 1800$ K in an ignition spot, modelized by a cylinder of 10 mm diameter and placed in the center of the cavity at $x_0 = 0.277$ m and $y_0 = -0.0147$ m (Fig. 5.14). In SiTComB, because the conservative variables are transported, the value of the total energy in the ignition spot is modified at each time step (t^n) during 1 ms to force a local temperature of $T^{imp} = 1800$ K. The implemented equations are described below:

$$\rho E^n_{modif} = \max\left(\rho E^n, \rho E^{spark}\right) \tag{5.3.1}$$

where ρE^n is the total energy provided by the simulation and ρE^{spark} the total energy representing the effect of a spark which is defined as:

$$\rho E^{spark} = \rho E_c + \alpha \rho C_v^n T^{spark} \tag{5.3.2}$$

with α a model constant set to 1.1 which could be modified to reproduce a stronger energy deposit. The temperature difference between the ignition spot (1800 K) and the rest of the cavity (≈ 450 K) can be huge and leads to numerical errors. The temperature transition at the surface of the ignition spot has therefore been made smooth by using a hyperbolic tangente law. Consequently, T^{spark} has been built from the temperature of the simulation T^n and the imposed temperature T^{imp}:

$$T^{spark} = S_r T^n + (1 - S_r) T^{imp} \tag{5.3.3}$$

where S_r is the disk of origin (x_0, y_0) and radius $(r_0 + dr)$ that is equal to unity everywhere except at the borders where its evolves from 1 to 0, S_r is defined as:

$$S_r = \frac{1}{2}\left[1 + \tanh\left(\frac{r_0 - r}{dr}\right)\right], \tag{5.3.4}$$

with $r_0 = 4$ mm and $dr = 1$ mm. S_r is actually the equation that delimits three domains:

- the inner ignition spot where the position (x, y) verifies $(x - x_0)^2 + (y - y_0)^2 \leq r_0$: the temperature is forced at $T^{imp} = 1800$ K or kept at T^n if $T^n > T^{imp}$.
- the outer ignition spot where the position (x, y) verifies $r_0 < (x - x_0)^2 + (y - y_0)^2 \leq r_0 + dr$: the temperature varies from $\max(T^n, T^{imp})$ to T^n following a hyperbolic tangente law.
- the outer zone representing the rest of the cavity where the position (x, y) verifies $(x - x_0)^2 + (y - y_0)^2 > r_0 + dr$: the temperature of the simulation is unchanged (T^n).

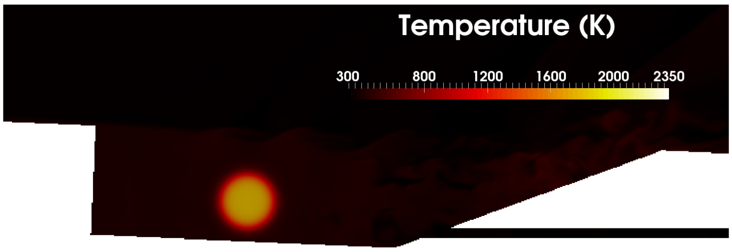

Figure 5.14: Imposed temperature inside the cavity at the injector centerplane.

When combustion starts, the temperature T^n can then become higher than the maximum imposed temperature T^{imp}, therefore taking the maximum in Eq. 5.3.1 allows the energy forcing to be activated only in area where it is needed.

5.3.2 2D reactive flows

Before addressing 3D simulations, a first investigation in 2D is performed with the 22 species chemical mechanism with the fine mesh. In order to keep the same ratio of ethylene injected as the 3D case, either the injection velocity or the fuel concentration can be modified to meet the needs. A modification on the injection velocity would impact strongly the dynamics of the flow, therefore, ethylene is diluted with N_2 in the 2D case. The 2D ethylene concentration is calculed from the fuel mass balance:

$$\dot{m}^{3D} Y_F^{3D} = \dot{m}^{2D} Y_F^{2D} \quad , \quad Y_F^{2D} = Y_F^{3D} \frac{\rho^{3D} U^{3D} S^{3D}}{\rho^{2D} U^{2D} S^{2D}}. \tag{5.3.5}$$

As discussed above, $\rho^{3D} \approx \rho^{2D}$ and $U^{3D} = U^{2D}$, the injector is circular in 3D, so $S^{3D} = 11\pi d^2/4$ (11 injectors) and rectangular in 2D leading to $S^{2D} = d \times W$, where $d = 1.6$ mm and $W = 152.4$ mm are the injector diameter and the cavity width of the whole geometry, respectively. $Y_F^{3D} = 1$ because pure fuel is injected in the 3D case. Finally, the fuel concentration injected becomes:

$$Y_F^{2D} = \frac{11\pi d}{4W} \tag{5.3.6}$$

That leaves $Y_F^{2D} = 0.0907$ and $Y_{N_2}^{2D} = 0.9093$ at the fuel injection ports. Combustion was installed inside the cavity by forcing the energy value at the center of the cavity during 0.25 ms. Snapshots showing evolution of temperature and equivalence ratio are displayed in Fig. 5.15. Initially, at $t = 0.25$ ms, almost all the fuel inside the cavity is burnt, and there is a non-negligible amount of fuel which flows upstream of the cavity. The second instant ($t = 0.50$ ms) shows on the one hand the cold fuel (310 K) flowing through the cavity at high speed (115 m/s), and on the other hand the cold airflow (329 K) entering the cavity by the rear. Ethylene is not burnt anymore, which could be due to two different phenomena: the strong dilution by N_2 that could increase the ignition time of ethylene and the strong dynamics of the flow with low temperatures. The instant $t = 0.75$ ms shows that the equivalence ratio in the large recirculation zone is very high, so the fuel has completely occupied this area, and the only remaining combustion zone is in the small recirculation area, featuring gases at low speed.

In 2D, flame stabilization cannot be achieved because of the injection area spreading on the whole cavity width. This is completely different in 3D where the injector occupies only 1/8-th of the cavity width, leaving areas at the sides of the injector with low speeds which help to stabilize the flame. 2D simulations are therefore not relevant for reactive cases and tests can only be done in 3D, which lead to high computational costs to find out the well fitted numerical parameters for the LES of this scramjet.

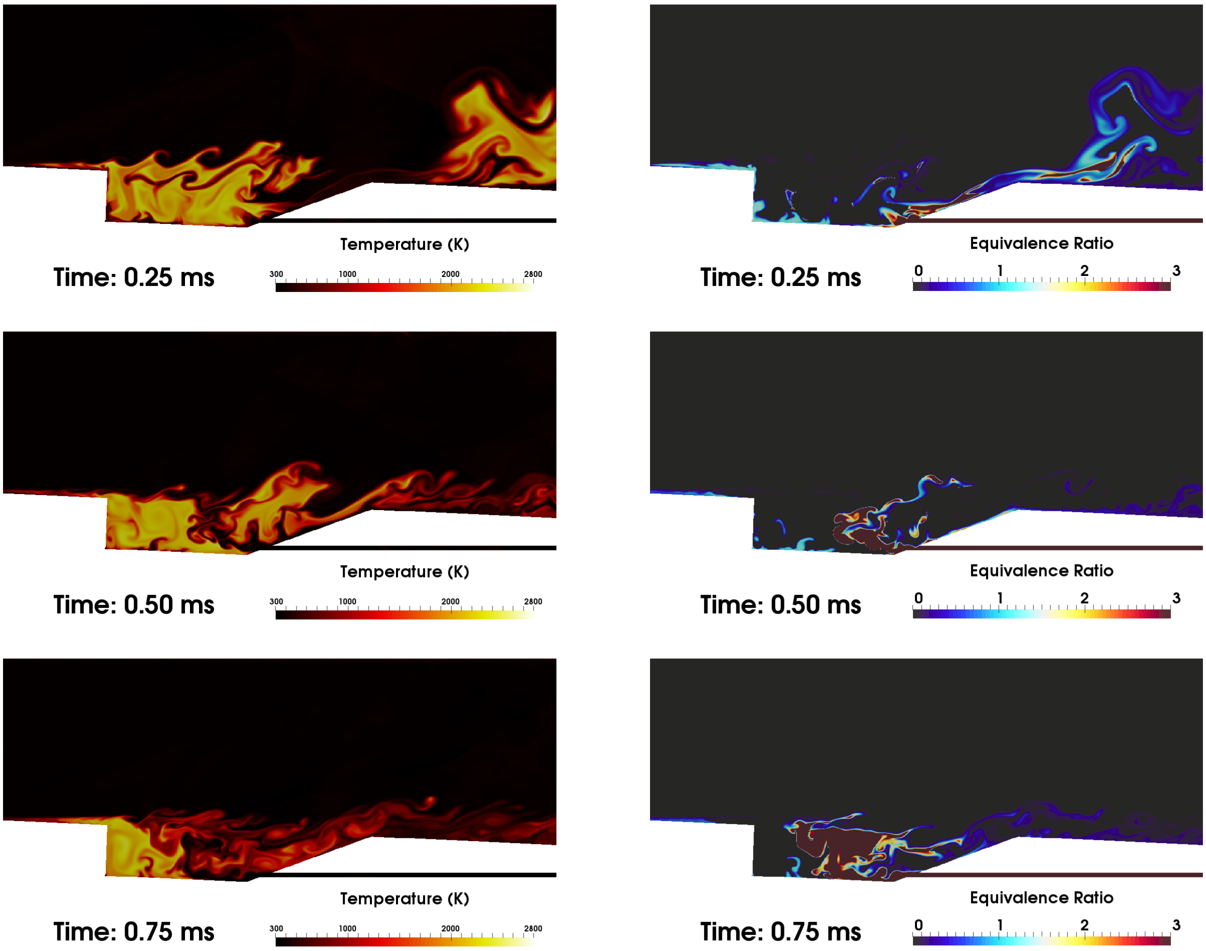

Figure 5.15: Instantaneous temperature (left) and Equivalence Ratio (right) of 2D reactive flows at (from top to bottom) 0, 0.25 ms and 0.5 ms respectively after removing the ignition source, which was kept for 0.25 ms. The simulation was performed with fine mesh using S22.

5.3.3 3D reactive flows

Before running reactive flow computations, a non-reactive case with fuel injection and no ignition in 3D has been performed to investigate the distribution of the fuel inside the cavity. Then the 3D reactive flow simulations have been performed with the 10 species reduced chemical mechanism (S10) [152] to have some preliminary results of combustion inside the cavity. Finally, the more accurate mechanism composed of 22 species (S22) [104, 92] is used for the simulations to get more precise results.

5.3.3.1 Non-reactive flow with fuel injection

Using the previous 3D non-reactive simulation on a coarse mesh as an initial solution, an injector providing ethylene at 99 SLPM has been added to the computational domain using immersed boundary method. Chemistry is not activated in this case, so combustion between ethylene and air cannot occur. The average fuel distribution is displayed in Fig. 5.16. The injector provides enough momentum to the fuel to reach the middle of the cavity, but can barely reach the front of it. Ethylene is spread into two directions when reaching the middle of the cavity: the first one mainly goes into the large recirculation area and a few portion of fuel flows to the small recirculation zone; and the second flow spreads in the spanwise direction. The rear of the cavity stays very poor in fuel, mainly due to air entering the cavity from this area. The result is similar to the non-reactive simulation performed by Baurle [4] in the case with turbulent Schmidt number $Sc_t = 1$.

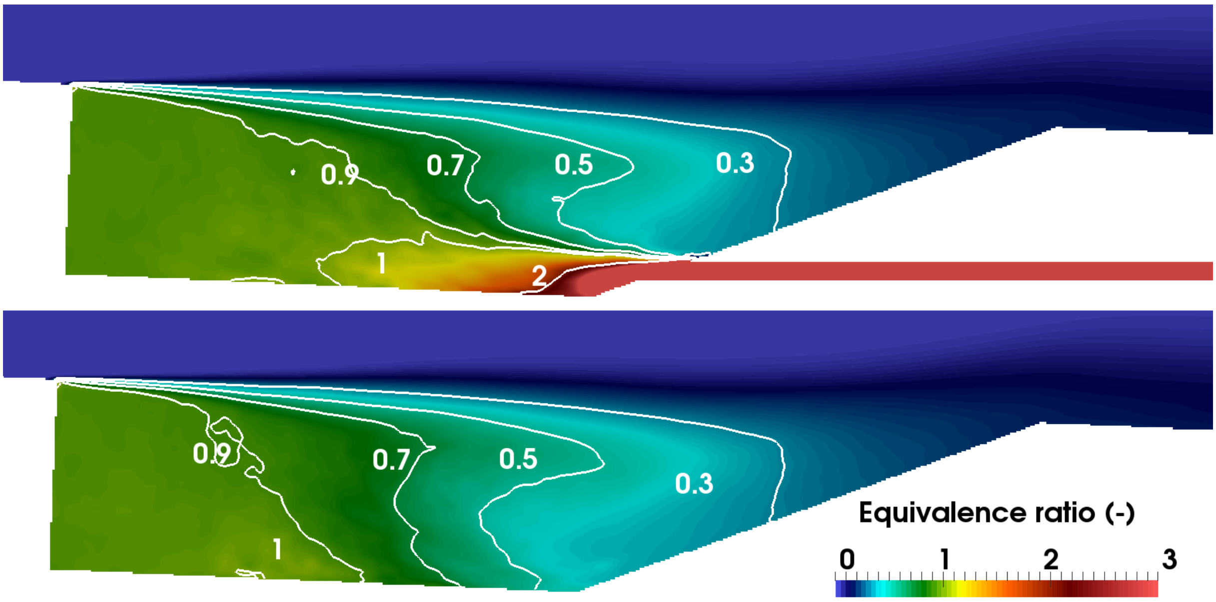

Figure 5.16: Averaged fuel-air equivalence ratio inside the cavity for non-reactive case in the injector centerplane (top) and in the centerplane between two injectors (bottom). Coarse mesh.

5.3.3.2 10 species chemical mechanism

Reactive computations with 10 species 10 steps chemical mechanism (S10) are first performed for the coarse mesh. Numerical solution of non-reactive case with fuel injection is used to initialize the computational domain. The ignition source is kept for 1 ms, then removed. Due to rather low heat release rates produced by combustion with S10, the flame quenches very quickly. The snapshots of temperature and heat release rate in the injector centerplane are presented in Fig. 5.17 to understand how the flame quenching phenomenon occurs inside the cavity. The heat release rate fields indicates that the maximum value of this field is around 0.3 GW/m^3 for S10 against 9 GW/m^3

for S22 in the case of one dimensional laminar premixed flame. Although the premixed flame heat release rate is generally not reached in 3D simulations of a real configuration, the difference should nevertheless stay small. The underprediction of heat release rate by S10 shows that this scheme, initially designed for 0D autoignition, does not fit 3D simulations featuring different combustion regimes. Combustion quickly becomes difficult to sustain and the flame front is pushed back by the airflow from the rear of the cavity to the front through the snapshots shown in Fig. 5.17.
The reduced scheme S10 was initially designed for autoignition under certain conditions only. Its inability to compute a laminar premixed flame was indeed a first warning of its inadequaty for real flow simulations. This result is similar to the one of Liu et al. [99] who found that the extinction residence time of S10 is largely higher that the cavity residence time which is 1 ms (see Sec. 1.3). This test shows the importance in the choice of chemical mechanism to reproduce properly the combustion in the cavity.

5.3.3.3 22 species chemical mechanism

Computations with S22 have then been performed with the coarse and fine meshes (RCA1 and RFA1 respectively). In this case, a stable flame has been obtained and a variety of flow and mixture properties are displayed in Fig. 5.18 and 5.19 respectively, at the injector centerplane and the centerplane between two injectors, for the fine mesh. The whole cavity is at subsonic speed. While the large recirculation zone is featuring high velocities (until 350 m/s), the velocity of the flow in the small recirculation area is rather low. The temperature can reach 2500 K in the cavity, and the coolest area remains the cavity front where the temperature is below 1500 K. The flow near the cavity aft wall is also very warm, approximately 2000 K which allows the incoming airflow to be heated before encountering ethylene present in the cavity which will facilitate ignition. The heat release rate snapshots (Fig. 5.18) show that the flame fronts are located at the exit of the injector, the interface between the two recirculation zones and the mixing layer between the cavity and the freestream. The isoline Mach = 1 indicates that combustion occurs preferencially at subsonic speeds, this will be quantified in section 6.2. The middle of the cavity and the interface between recirculation areas are driven by moderately strong positive and weak negative heat release rate respectively. Negative values of heat release rate occur when the local mixture is at overequilibrium state. This latter phenomenon is further described in section 6.5.

Fig. 5.19 displays the mixture fraction computed with Bilger et al.'s formulation (Eq. 2.1.15), the mass fractions of reactants and two major products in the injector centerplane and in the centerplane between two injectors for the fine mesh. Snapshots in plane with constant x are displayed in Fig. 5.20 and 5.21 for fuel mass fraction and heat release rate respectively, along with stoichiometric line. The constant x planes are taken at $x = 2$, 20, 39 and 66 mm from the injector, which correspond to (1) the small recirculation area, (2) the interface between recirculation areas, (3) the large recirculation area and (4) the rear of the cavity respectively. The stoichiometric mixture fraction Z_{st} being equal to 0.06366, the cavity is therefore globally very rich, except near the cavity aft wall region where the mixture is lean ($Z \approx 0.05$). The small recirculation area at the front of the cavity is only filled with fuel and burnt gases, and no oxygen left. Combustion cannot occur in this area because of the absence of oxygen. At the top of the small recirculation zone, ethylene, heated by burnt gases to 1500 K, is carried away by the airflow to the mixing layer between the large recirculation area and the freestream, and reacts in that region providing energy to heat the airflow entering at the rear of the cavity. Then, the heated airflow reacts with a small part of cold fuel from the injector to form burnt gases that will heat the remaining cold fuel, and the circle is complete. Ethylene entering the large recirculation area reacts immediately with air available in that region due to preheating by burnt gases, so the mass fraction of ethylene is almost zero. This reaction maintains a very high temperature in the large recirculation zone. This process of flame stabilization is shown in Fig. 5.22. Four combustion zones can be identified: (I) the mixing layer above

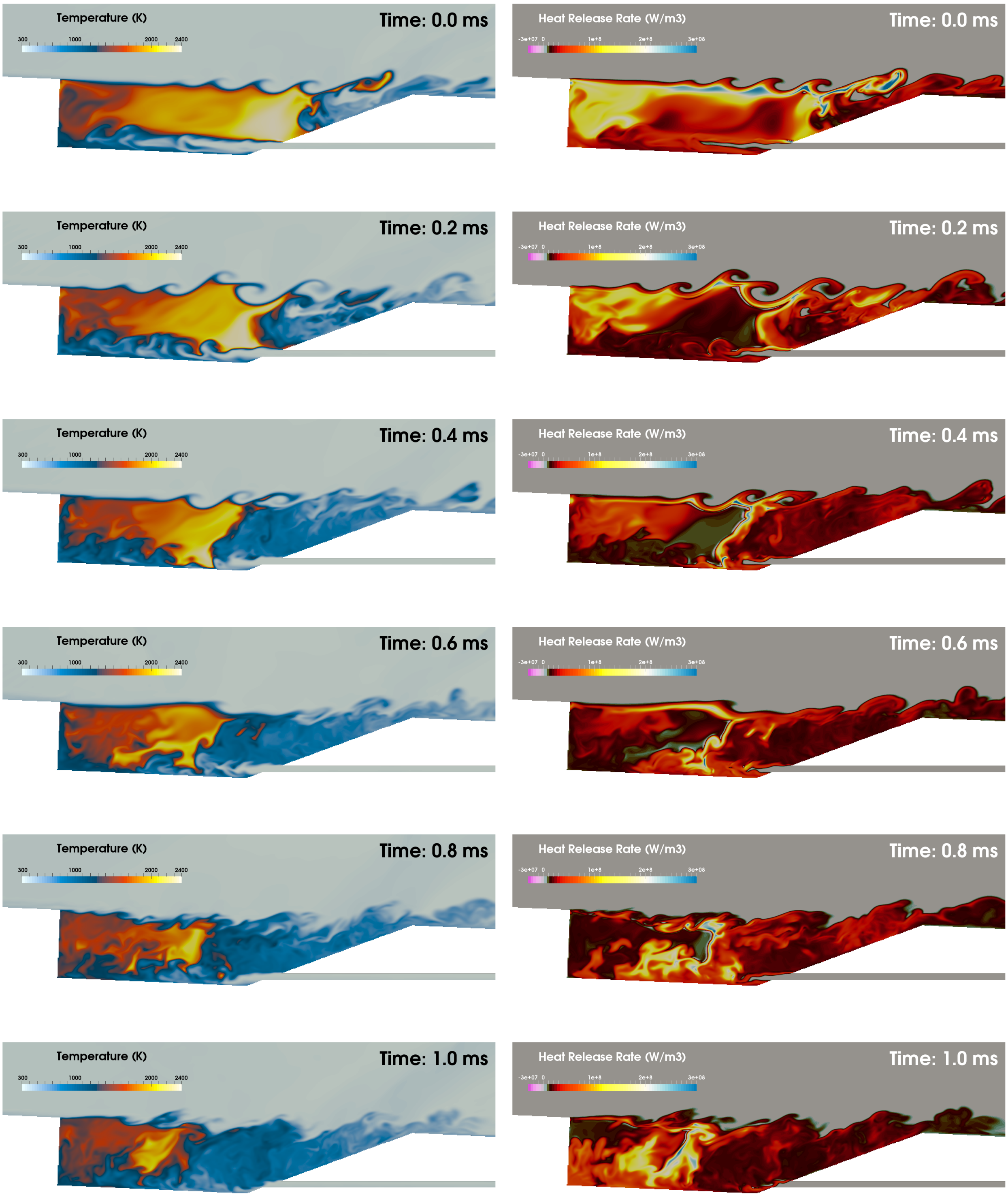

Figure 5.17: Snapshots of temperature (left) and heat release rate (right) for S10, presented every 0.2 ms from $t = 0$ to 1 ms. Coarse mesh.

the small recirculation area with weak combustion occuring, (II) the mixing layer above the large recirculation zone featuring strong combustion in the middle of the cavity, which intensity decreases when approaching the rear of the cavity, (III) the region between the two recirculation zones where the combustion intensity is moderate and finally (IV) the exit of the injector with strong combustion.

To summarize, the flame stabilization inside the cavity is performed the following away:

- Fuel from the injector reacts with heated oxygen present in the cavity;
- Burnt gases from combustion provide high temperature in the small and large recirculation areas;
- Ethylene in the small recirculation area is heated, then carried away by the freestream airflow to the mixing layer where it burns;
- The combustion released energy heats cold airflow entering the cavity.

Q-criterion colored by CO mass fraction is displayed in Fig. 5.23 to identify vortex structures in the cavity-based scramjet. The cavity flow is animated by strong vortices from the middle to the rear of the cavity. The front of the cavity has only weak vortices with low values of Q-criterion.

Statistics started a few cavity residence times later after removing the ignition forcing to evacuate possible transitory phenomenon, and then are computed on several residence times. The whole process of reactive flow statistics extraction is shown in Fig. 5.24. Comparisons between the numerical solutions and the experiment [164] are displayed in Fig. 5.25 for pressure and Fig. 5.26 for the velocity profiles at $x = 2$, 11, 20, 30, 39, 48, 57, 66 mm from the cavity front corner. Contrary to the non-reactive case, the wall pressure in the reactive case is very close to the experimental data for both meshes, except for the last point at the cavity aft wall. This point is not very well captured certainly because of the strong reattachment shock system in that region which may be not exactly located. The pressure peak, located in the shock system is higher by 2500 Pa in the case with fine mesh than the one with coarse mesh due to a better refinement in this region. The velocity profiles comparison shows only a slight difference between the experiment and the numerical data for streamwise velocity. The discrepancies are located in first planes ($x = 2$ and 11 mm), at the mixing layer. As in the non-reactive case, the mixing layer of the experiment is thicker in the small recirculation area, but the correct thickness is recovered further downstream. The largest difference between coarse and fine meshes also appears in that region, where fine mesh performs better due to better refinement. However, the transverse velocity is not well predicted for both meshes, the coarse mesh even performs better than the fine mesh at multiple locations compared to the experiment. Particular attentions need to be paid to averaged fields to have a better understanding of this phenomenon. A variety of averaged fields will be studied in the following paragraphs.

The averaged streamlines colored by streamwise velocity values in the centerplane between two injectors are displayed in Fig. 5.27. Like the non-reactive case, two recirculation zones can be identified: a primary clockwise recirculation zone, spreading all over the cavity, is at very high speeds, reaching an average speed of 250 m/s; the secondary anti-clockwise recirculation area is located at the front of the cavity, and spins slowly ($U < 50$ ms) compared to the primary one. The direct fuel injection into the large recirculation area has no impact on the flow in that region. The averaged temperature in Fig. 5.28 shows that the large recirculation zone is featuring high temperatures (until 2200 K), while the cavity front is much cooler and can only reach 1500 K. The airflow above the recirculation zones are heated on average to 1000 K before entering the cavity. The averaged pressure field is displayed in Fig. 5.29. The pressure initially increases through the compression wave at the leading edge of the cavity, then decreases by approximately 1.5 kPa from the middle of the cavity. The rear of the cavity is animated by a shock structure where the pressure can reach

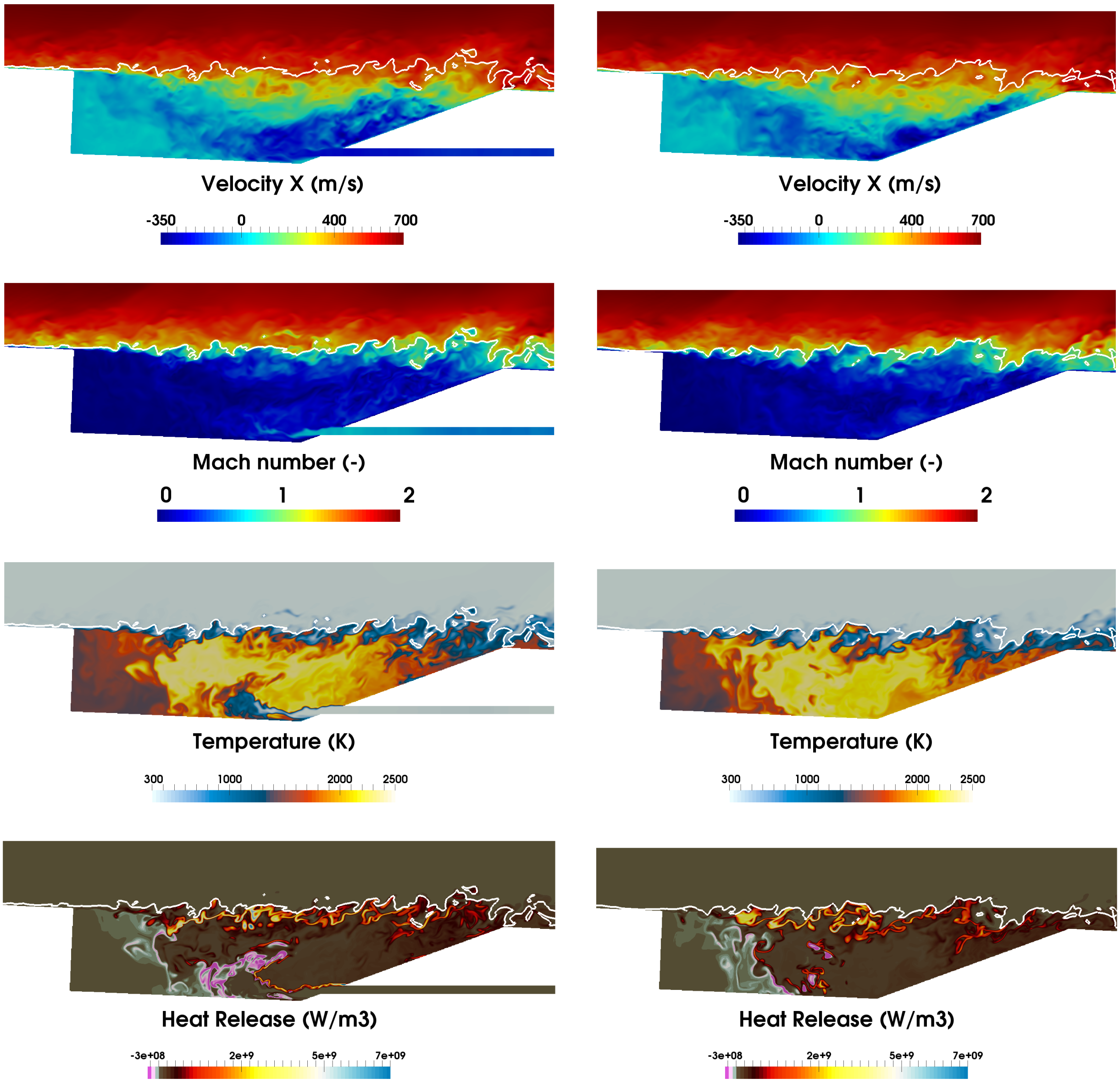

Figure 5.18: Instantaneous fields of streamwise velocity, Mach number, temperature and heat release rate at the injector centerplane (left) and the centerplane between two injectors (right). The isoline Mach = 1 is displayed with a white line. Fine mesh.

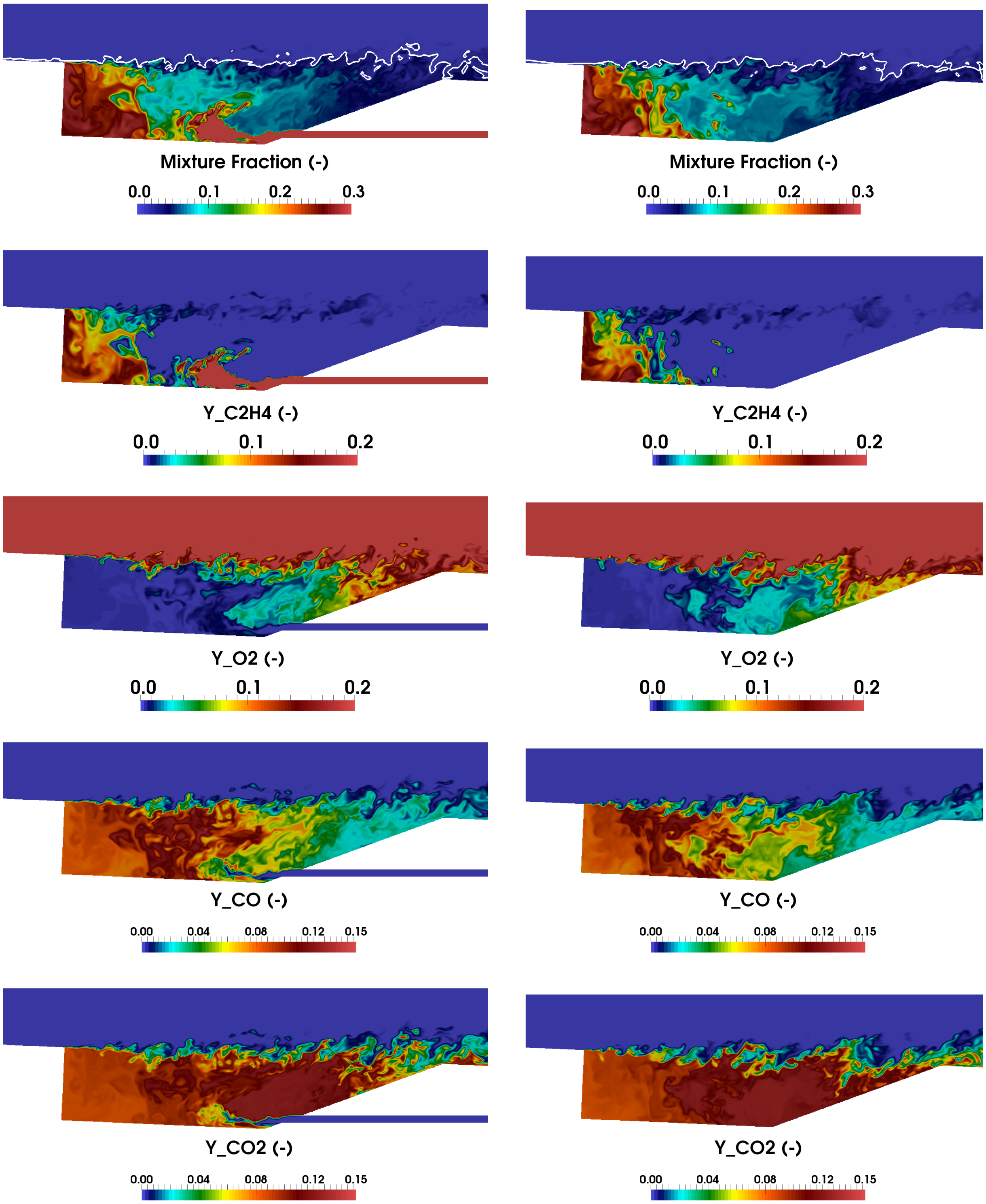

Figure 5.19: Instantaneous fields of mixture fraction and mass fractions of C_2H_4, O_2, CO and CO_2 at the injector centerplane (left) and the centerplane between two injectors (right). The isoline Mach $= 1$ is displayed with a white line. Fine mesh.

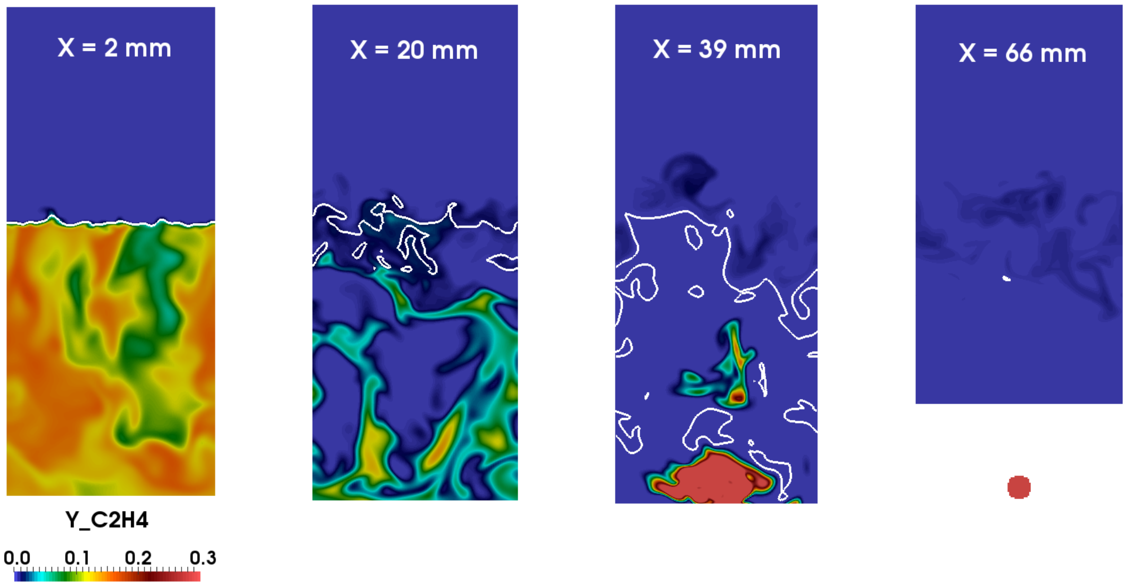

Figure 5.20: Instantaneous mass fraction of ethylene inside the cavity in planes with constant x. The stoichiometric mixture isoline is displayed with a white line. Fine mesh.

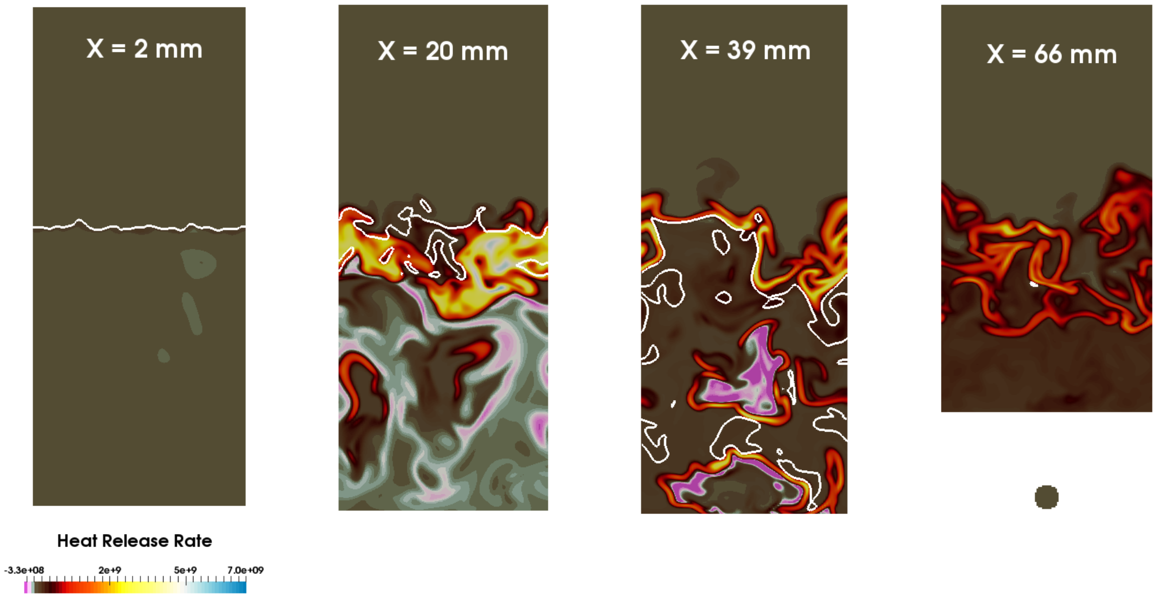

Figure 5.21: Instantaneous heat release rate inside the cavity in planes with constant x. The stoichiometric mixture isoline is displayed with a white line. Fine mesh.

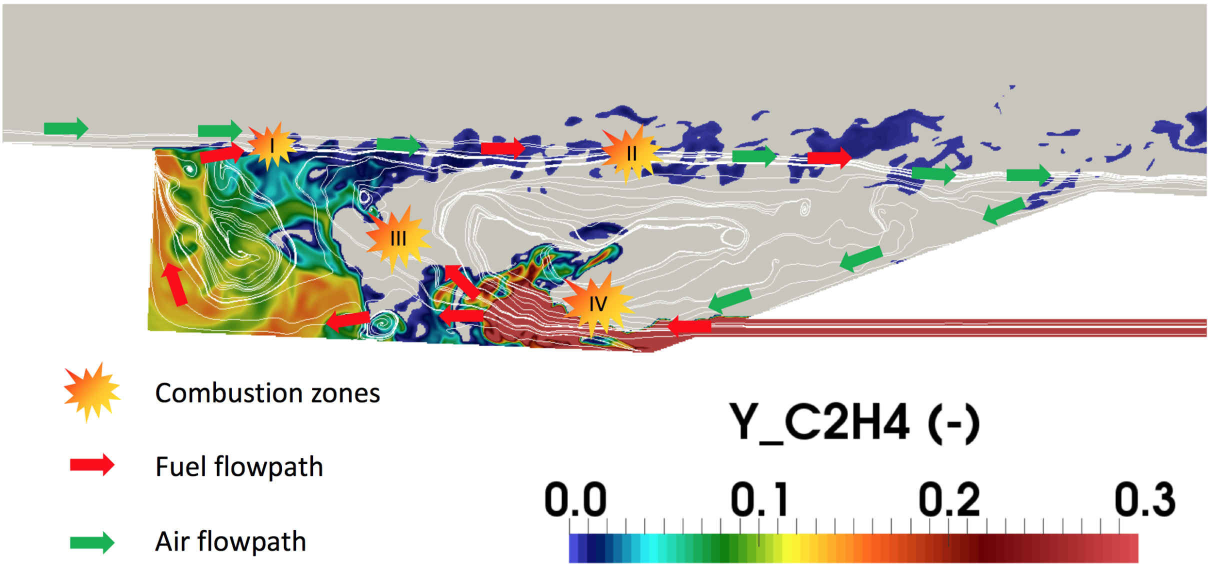

Figure 5.22: Schematic of the cavity flame stabilization.

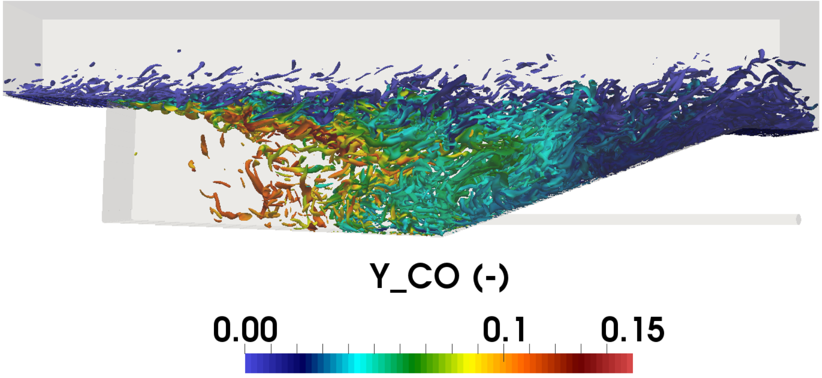

Figure 5.23: Q-criteron colored by Y_{CO} concentrations. Fine mesh.

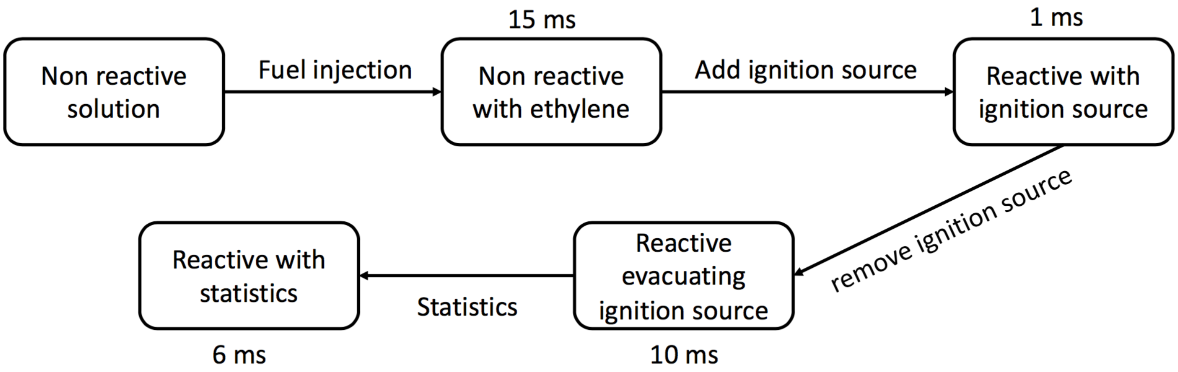

Figure 5.24: Process of establishment of reactive case with S22 from the cold simulation.

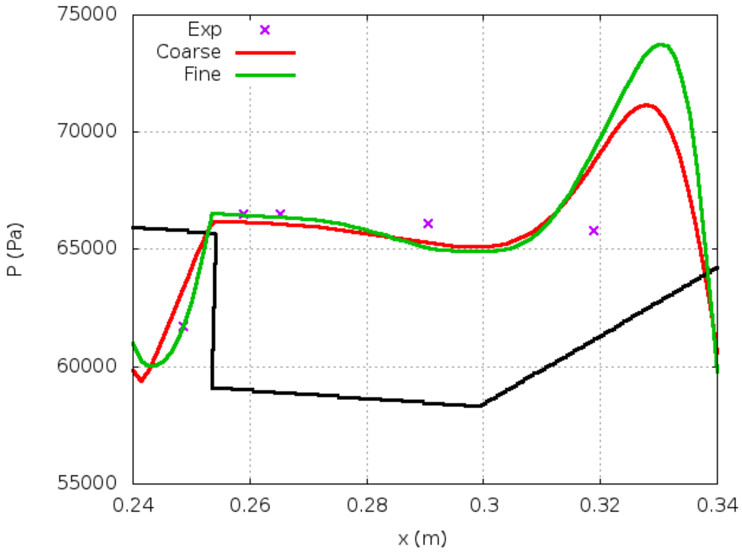

Figure 5.25: Averaged cavity wall pressure: comparison between the numerical and the experimental data for coarse and fine mesh at the centerplane between two injectors.

75 kPa, and is followed by an expansion wave where the pressure hits 48 kPa. The total pressure loss in this configuration is around 17 kPa.

Averaged velocity profiles are displayed in Fig. 5.30. The white line indicates the zero speed contour for each velocity: $U_x = 0$, $U_y = 0$ or $U_z = 0$ depending on the figure. The thickness of the mixing layer between the freestream and the cavity can be easily identified on the averaged streamwise velocity figures, the mixing layer being thin above the small recirculation zone and thick above the large one. The isoline $U_x = 0$ indicates in fact the mid-line of the recirculation areas. The transverse velocity is positive and high in the middle of the cavity where the large recirculation is flowing up and in the shock region at the rear of the cavity. The strongest negative values are found near the cavity aft wall where air is flowing down to the cavity. The spanwise velocity should be on average zero, but there are still some regions where $U_z \neq 0$, probably because the statistics performed are not converged enough in that direction.

Averaged velocity fluctuations are displayed in Fig. 5.31. Very strong velocity fluctuations can be observed in the region above the small recirculation area and at the cavity ramp in all directions. These fluctuations are higher than those in the experiment performed by Tuttle et al. [164], especially in the mixing layer in the vinicity of the cavity corner. The simulation is thus more turbulent in this region which may be the origin of the difference between the averaged velocity profiles inside the cavity between the numerical and the experimental data.

5.4 Simulation of an unstable case

An unstable reactive computation using S22 has then been performed with the coarse mesh to check if the LES can reproduce quenching induced by low fuel loading (RCA1L). This case corresponds to the case 4 of the experiments of Tuttle et al. [164] where ethylene is injected at 36 SLPM. The computational domain is initialized with the stable case presented in section 5.3.3.3. The fuel injection velocity is decreased from 99 SLPM to 36 SPLM linearly within 1 ms.

The snapshots of temperature, heat release and ethylene mass fraction are displayed in Fig. 5.32, 5.33 and 5.34 respectively, in the injector centerplane and the centerplane between two injectors.

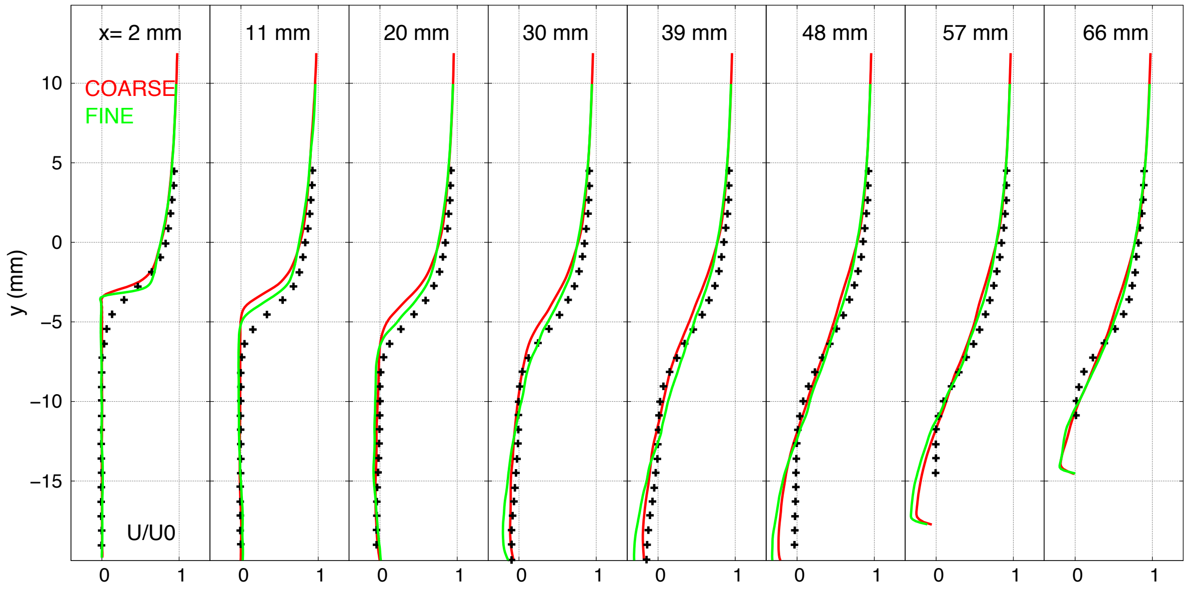

(a)

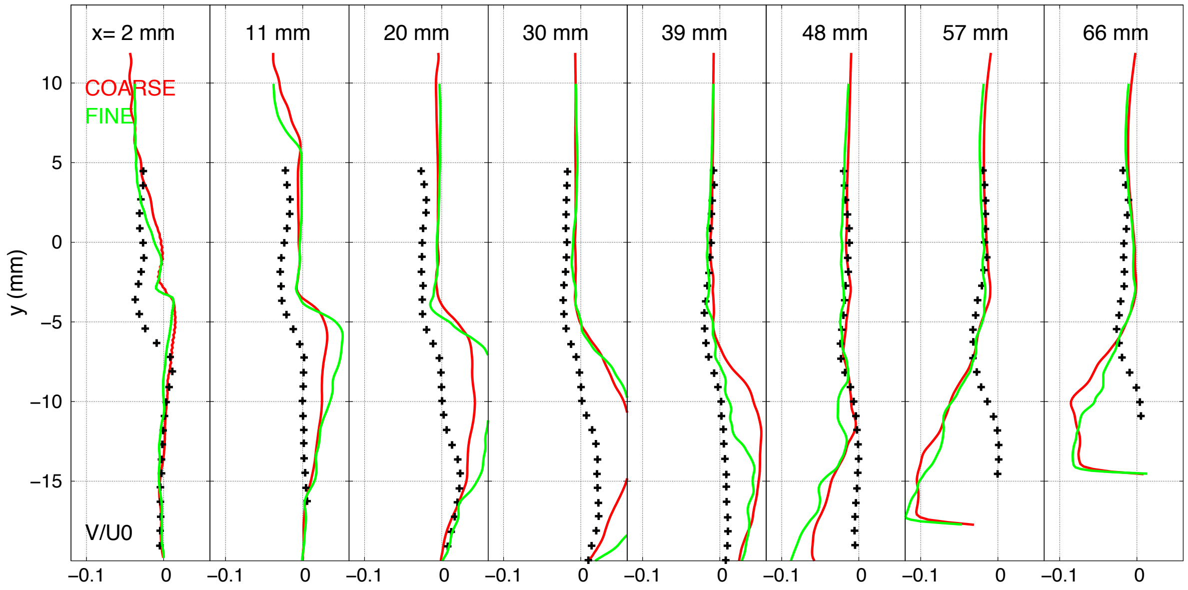

(b)

Figure 5.26: Averaged streamwise (a) and tranverse (b) velocity profiles inside the cavity: comparison between the numerical and the experimental data for coarse and fine mesh at the centerplane between two injectors.

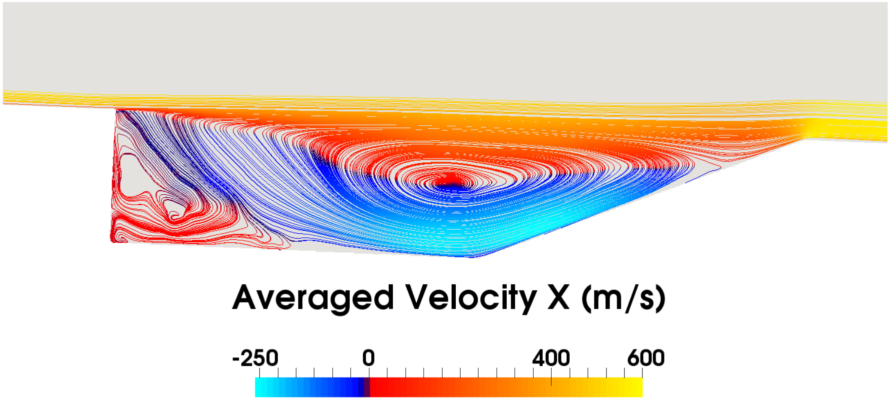

Figure 5.27: Averaged values of the pathline, colored by streamwise velocity at the centerplane between two injectors. Fine mesh.

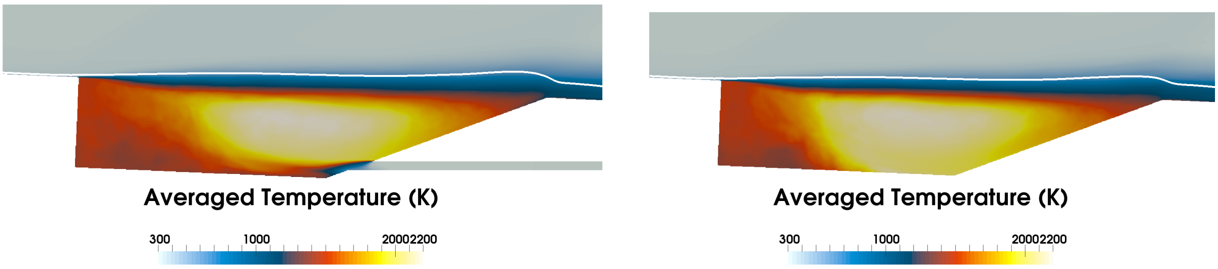

Figure 5.28: Averaged temperature fields in the injector centerplane (left) and the centerplane between two injectors (right). The isoline Mach = 1 is displayed with a white line. Fine mesh.

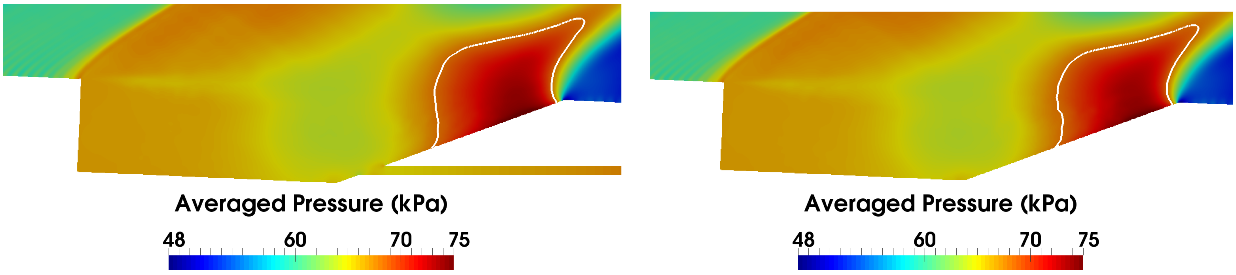

Figure 5.29: Averaged pressure fields in the injector centerplane (left) and the centerplane between two injectors (right). The isoline $P = 68$ kPa is displayed with a white line. Fine mesh.

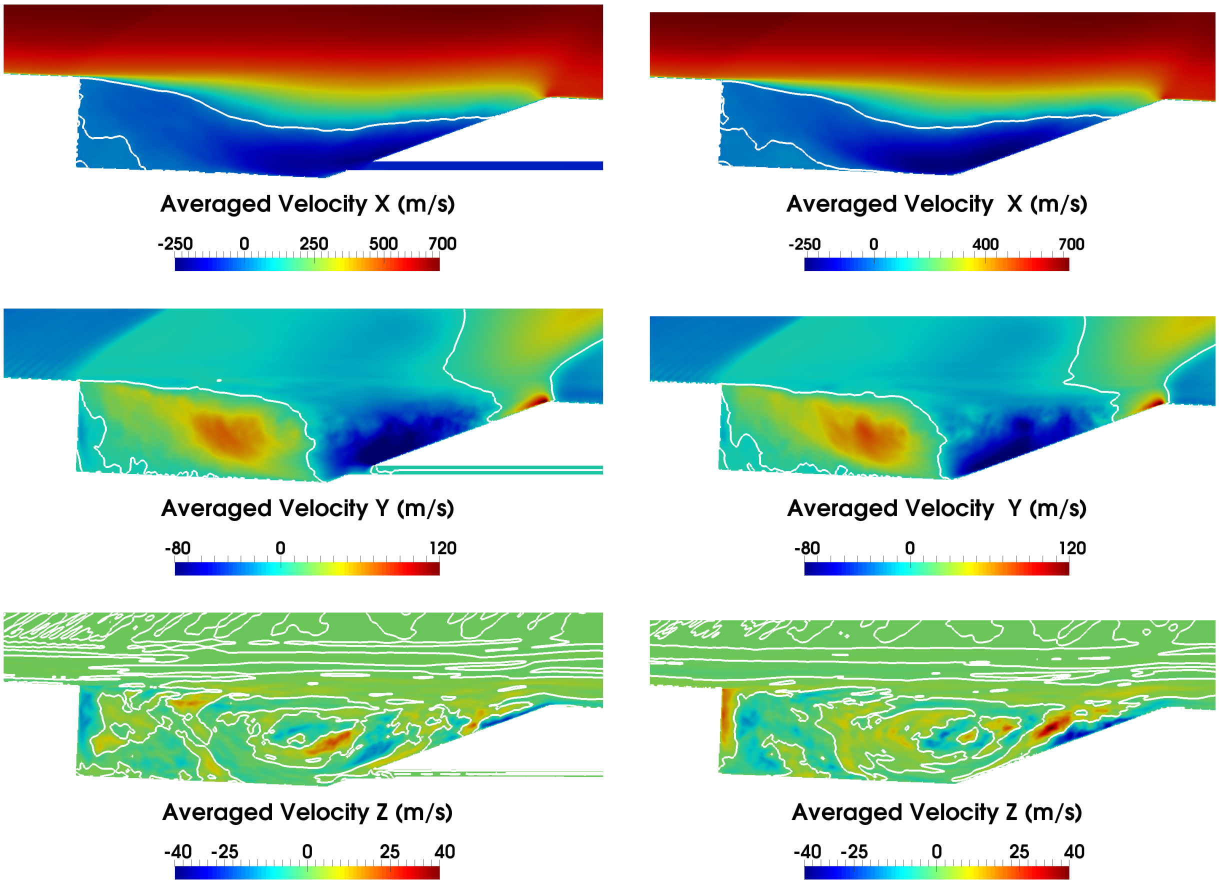

Averaged Velocity X (m/s)

Averaged Velocity X (m/s)

Averaged Velocity Y (m/s)

Averaged Velocity Y (m/s)

Averaged Velocity Z (m/s)

Averaged Velocity Z (m/s)

Figure 5.30: Averaged fields of velocity components: streamwise, tranverse and spanwise at the injector centerplane (left) and the centerplane between two injectors (right). The isoline Ux, Uy or Uz = 0 is displayed with a white line. Fine mesh.

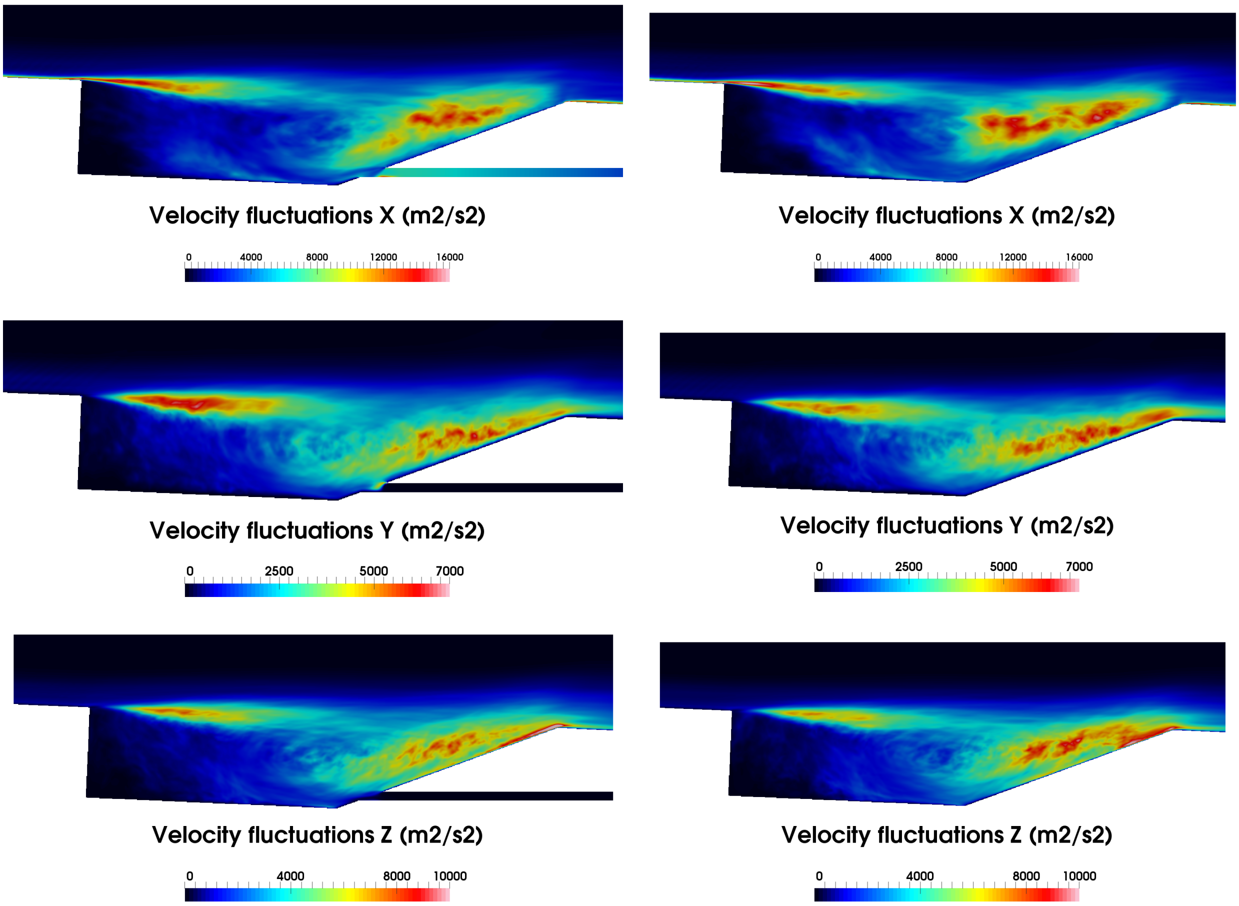

Figure 5.31: Averaged fields of velocity fluctuation components: streamwise, tranverse and spanwise at the injector centerplane (left) and the centerplane between two injectors (right). Fine mesh.

The instant $t = 0$ corresponds to the solution of the stable case with high fuel loading where injection is strong enough to reach the middle of the cavity and feed the small recirculation area by the cavity wall. Combustion mainly occurs at the exit of the injector and the mixing layer between the cavity and the freestream. The injection velocity then is decreased linearly to 36 SPLM until $t = 1$ ms, which corresponds to a transitional regime where the successive velocity damping leads to combustion inside the injector. The injection velocity decrease could have been performed on a longer time to avoid this transitional effect. But this transitory result disappears at $t = 2$ ms where the low fuel loading makes impossible for the fuel to reach the middle of the cavity, ethylene is immediately consumed at the exit of the injector. Combustion at the mixing layer is only fed by the initial huge stock of fuel at the front of the cavity which is starting to be cleared out. The lack of ethylene in the large recirculation zone causes a fuel shortage at the rear of the cavity, where the air entering is not mixed anymore with burnt products leading to a cooling of the cavity. At the next instants $t = 3$ and 4 ms, ethylene is still burning at the exit of the injector, and the spare fuel at the cavity front has almost totally been consummed. The mixing layer between the freestream and the cavity is not anymore fed by the fuel from the small recirculation zone, so combustion vanishes in this region and the airflow entering the cavity cannot be heated. The flame at the exit of the injector will eventually faint. The quenching is in this case marked by a lack of fuel inside the cavity, which is caused by an unsufficient fuel loading.

Additionally to the stable case, the simulation has shown its ability to predict the unstable fuel loading case provided by the experiment, showing the great accuracy of the LES.

5.5 Simulation of a medium fuel loading case

A medium fuel loading simulation has then been performed using S22 with the coarse mesh to investigate first the capability of the LES to reproduce this stable reactive case and second the difference between a medium and a high fuel loadings. This case corresponds to the case 2 of the experiments performed by Tuttle et al. [164] where ethylene is injected at 56 SLPM. The computational domain is still initialized with the stable case presented in section 5.3.3.3. The fuel injection velocity is decreased from 99 SLPM to 56 SPLM linearly within 1 ms. Afterwards, the computation continued during 9 ms to evacuate the possible transitory effects. Finally, statistics are computed on 6 ms leading to a total of 16 ms physical time computations from the solution of RCA1.

A variety of flow and mixture properties is displayed in Fig. 5.35 at the injector centerplane and at the centerplane between two injectors. The LES has again reproduced successfully a stable case using a 22 species chemical mechanism. The heat release rate fields show that strong combustion is observed here (RCA1M) at the front of the cavity instead of at the mixing layer above the large recirculation zone in the case RCA1. Due to a lower fuel loading, the quantity of fuel going into the small recirculation area is smaller. The amount of fuel flowing from the small recirculation area to the mixing layer is also reduced compared to RCA1. The fuel shortage in the mixing layer above the large recirculation area and near the cavity ramp is responsible of the low heat release rate present in this area. This results in high temperatures at the front of the cavity and the only "cold" area of the cavity is located at near the ramp. It is also observed in the RANS simulations performed by Baurle [4] that the temperature at the front of the cavity is globally higher in the case 2 (RCA1M) than the case 3 (RCA1), and the temperature at the cavity ramp is lower in the case 2. The concentration of fuel is also in agreement with the simulation of Baurle [4], where the mass fraction of ethylene is found around 0.03. The fuel mass fraction found by Hassan et al. [68] is much higher at the front of the cavity, $Y_{C_2H_4} \approx 0.12$. However, the oxidizer mass fraction of the current LES is similar to the simulation of Hassan. The discrepancy in fuel concentration could probably due to the kinetic mechanism used by Hassan which is only composed of 6 species and 3

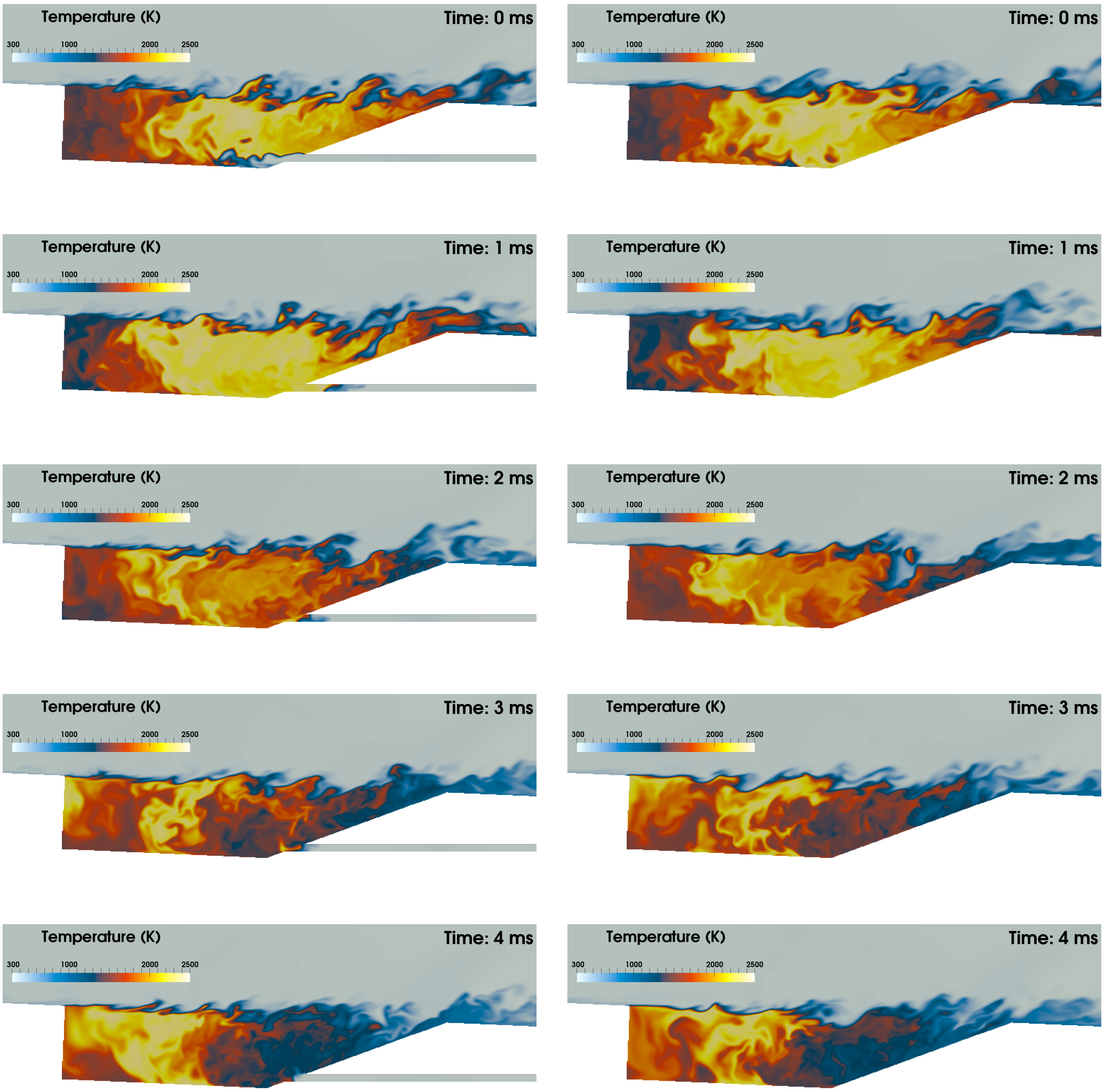

Figure 5.32: Snapshots of temperature at injector centerplane (left) and centerplane between two injectors (right) for a lean fuel loading (RCA1L), presented every ms from $t = 0$ to 4 ms. Coarse mesh.

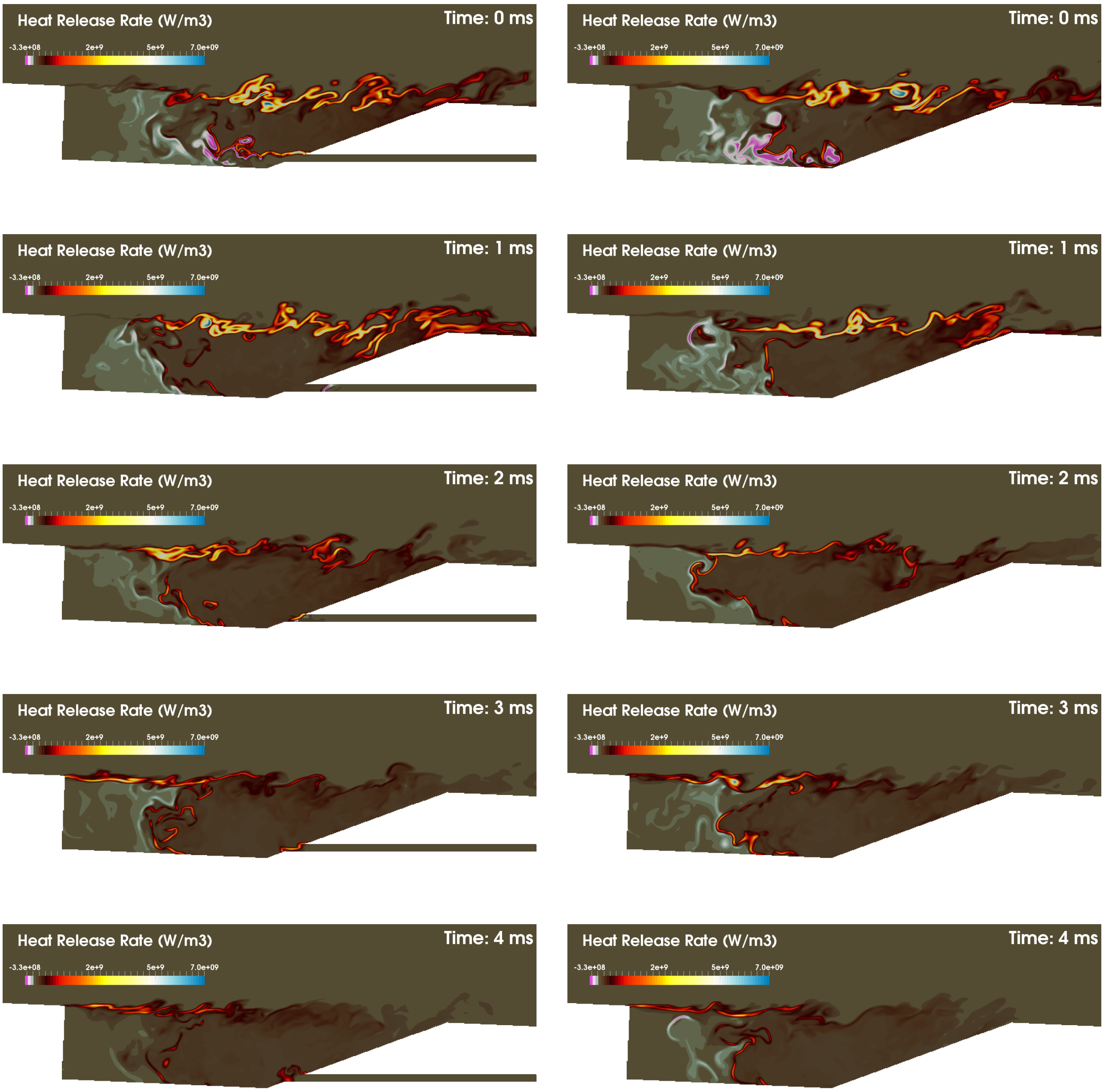

Figure 5.33: Snapshots of heat release rate at injector centerplane (left) and centerplane between two injectors (right) for a lean fuel loading (RCA1L), presented every ms from $t = 0$ to 4 ms. Coarse mesh.

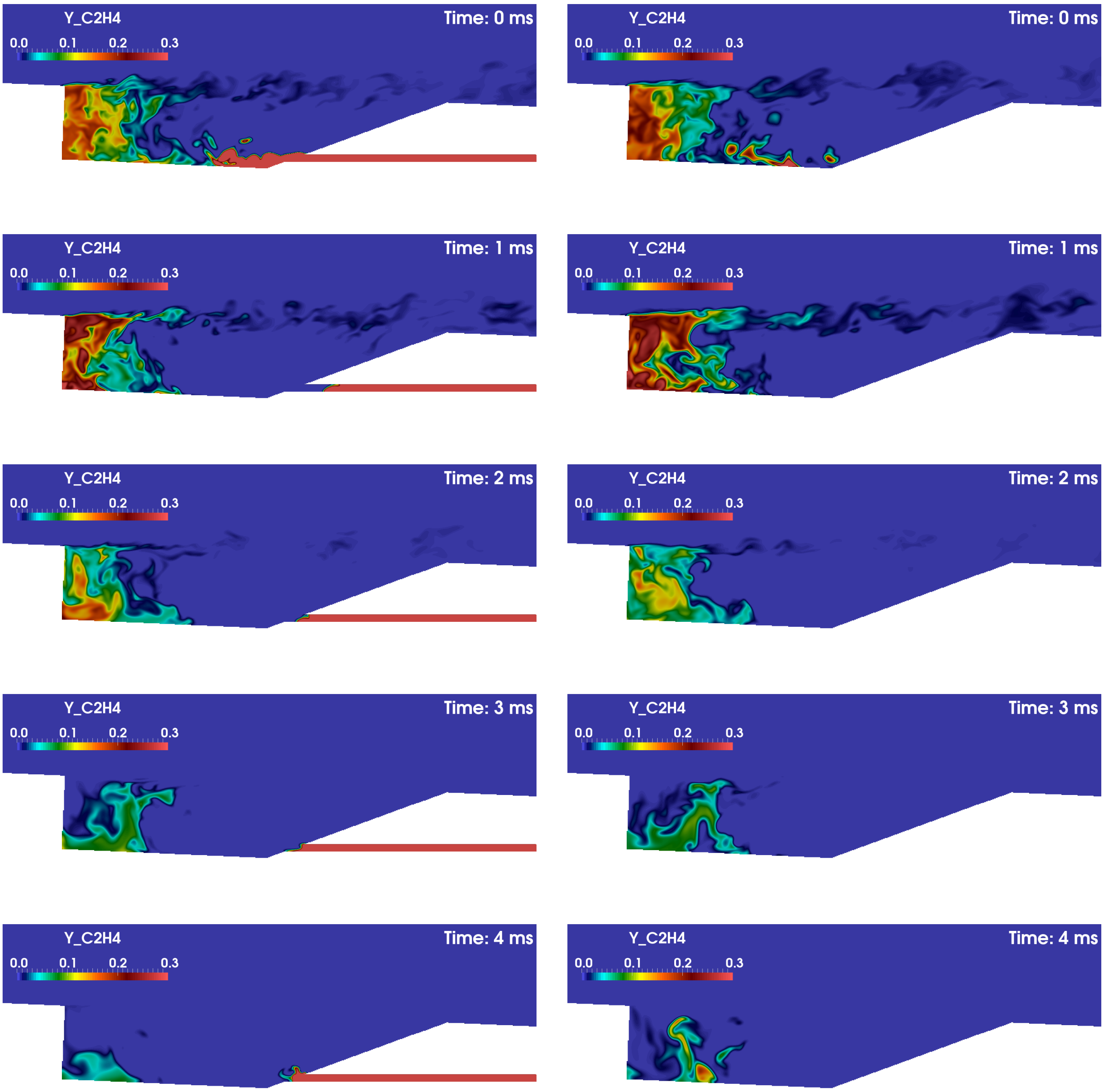

Figure 5.34: Snapshots of ethylene mass fraction at injector centerplane (left) and centerplane between two injectors (right) for a lean fuel loading (RCA1L), presented every ms from $t = 0$ to 4 ms. Coarse mesh.

steps, while the mechanism used in this study and by Baurle has 22 species and 206 reactions. The 6 species scheme is not accounting for the ethylene decomposition.

An investigation on the combustion regime of the medium fuel loading case has been performed and is shown in Sec. 6.3.

5.6 Adiabatic vs. isothermal wall conditions

In order to investigate the impact of wall temperature on the flow, simulations with isothermal wall condition are performed with coarse and fine mesh, and compared to the stable case studied in section 5.3.3.3, the geometry considered is still composed of only one injector with periodic conditions on the sides. The airflow is injected with homogeneous isotropic turbulence which intensity is 10% of the local speed. Ethylene-air combustion is modelled with the 22 species (S22) from Luo et al. [105]. The isothermal wall condition is actually a combination of a real isothermal and an adiabatic wall condition. The walls become isothermal only when the initial wall temperature exceeds 800 K. Otherwise, walls are considered adiabatic. This implementation of isothermal wall condition is similar to the one in the RANS simulation performed by Baurle [4]. He also compared the isothermal wall condition to a steady-state one-dimensional coupled fluid/solid heat transfer boundary condition [177]. Baurle [4] found that the cavity combustion process is not sensitive to the wall boundary treatment. As a more refined mesh provides more precise results, the comparison is made only for the fine mesh.

Averaged temperature fields in the injector centerplane and the centerplane between two injectors are displayed in Fig. 5.36 for adiabatic and isothermal wall conditions (RFA1 and RFI1 respectively). The shape of the averaged temperature fields is the same for both cases, but the isothermal case is cooler at the front and the rear of the cavity. The temperature at the front of the cavity of RFI1 is similar to the RANS performed by Baurle [4], but not in the middle of the cavity where the current simulation is showing higher temperatures. In the simulation of Baurle, only the region of the large recirculation zone close to the rear of the cavity is having extremely high temperatures (> 2100 K), while the current simulation indicates that the core of the large recirculation area has the same temperature, regardless of its proximity to the middle or the rear of the cavity.
Temperature profiles at positions $x = 2$, 11, 20, 30, 39, 48, 57, 66 mm from the front of the cavity are displayed in Fig. 5.37 to better quantify the differences between adiabatic and isothermal simulations. The profiles go from $y = -20$ mm to $y = 10$ mm, the cavity wall can go until $y = -21.9$ mm at certain positions, so the points near the wall for positions $x = 20$, 30, 39 and 48 mm are not shown. At the front of the cavity, $x = 2$ mm, the temperature difference grows from 50 K at the mixing layer until 700 K as we get to the cavity bottom wall. As we advance in the cavity, only the mixing layer and the region near the wall are affected by the isothermal wall conditions. The temperature gap at the mixing layer can reach 200 K from $x = 39$ mm until $x = 66$ mm. The temperature evolution near the wall is very stiff from $x = 39$ mm, since it varies from 800 K at the wall to 1800 K only a few cells further, because of the strong recirculation of hot burnt gases. As a consequence, this region needs to be treated with particular attentions experimentally, since the cooling of the wall at this region can be difficult.

Instantaneous heat release rate and ethylene and oxygen mass fractions in the injector centerplane and the centerplane between two injectors are displayed in Fig. 5.38, Fig. 5.39 and Fig. 5.40 respectively, to investigate if the isothermal wall conditions modify strongly the chemistry and the reactants distribution in the cavity. The heat release is globally lower in the mixing layer, especially at the front of the cavity where combustion seems to be absent. The difference in heat release rate is due to the flow being cooler in the isothermal case. So combustion is less likely to take place

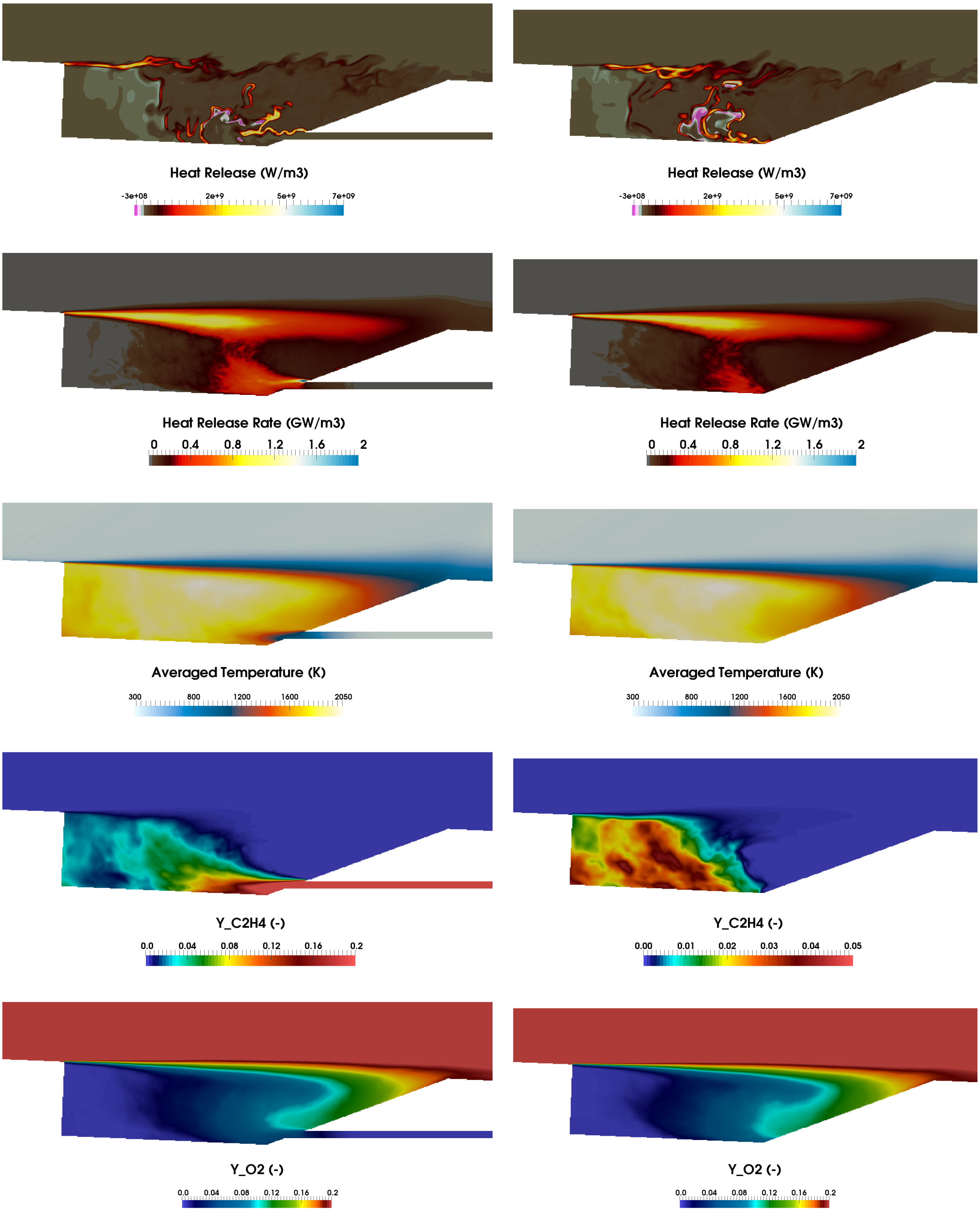

Figure 5.35: Various fields at the injector centerplane (left) and the centerplane between two injectors (right) for a medium fuel loading; from top to bottom: instantaneous heat release rate, averaged heat release rate, averaged temperature, averaged fuel and oxidizer mass fractions. Case RCA1M.

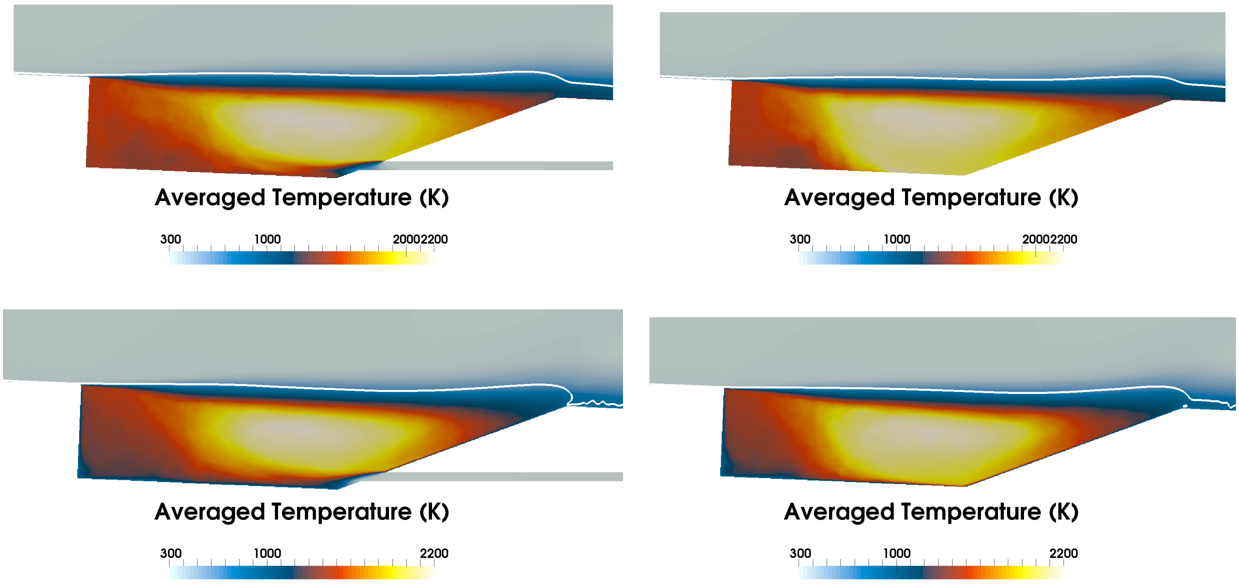

Figure 5.36: Averaged temperature fields in the injector centerplane (left) and the centerplane between two injectors (right) for adiabatic (top) and isothermal (bottom) cases. The isoline Mach = 1 is displayed with a white line. Fine mesh.

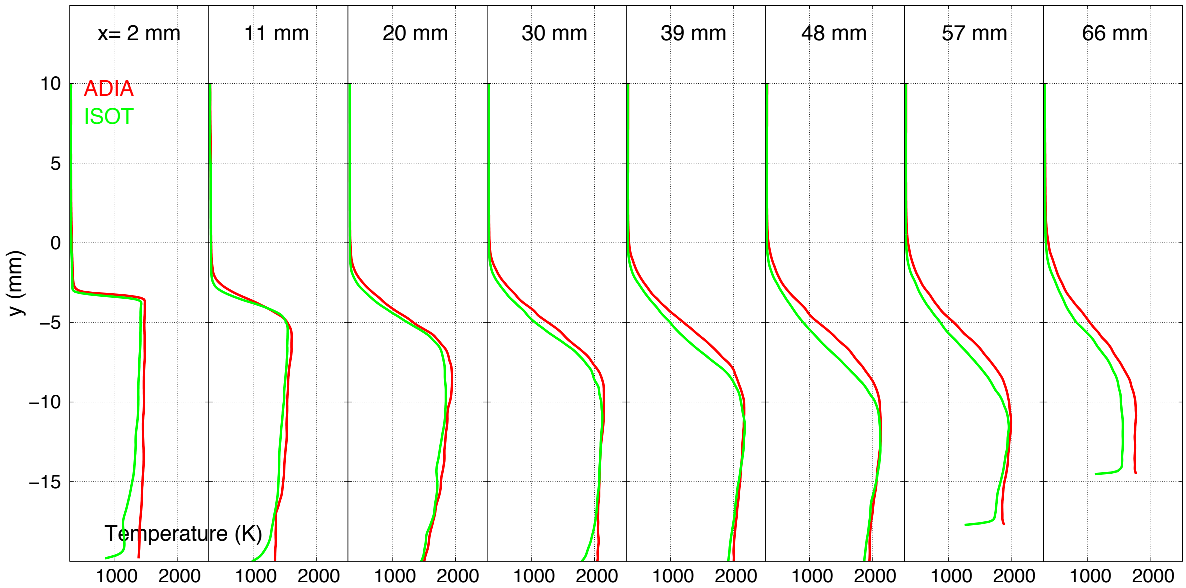

Figure 5.37: Averaged temperature profiles inside the cavity, comparison between the adiabatic and isothermal simulations for fine mesh at the centerplane between two injectors.

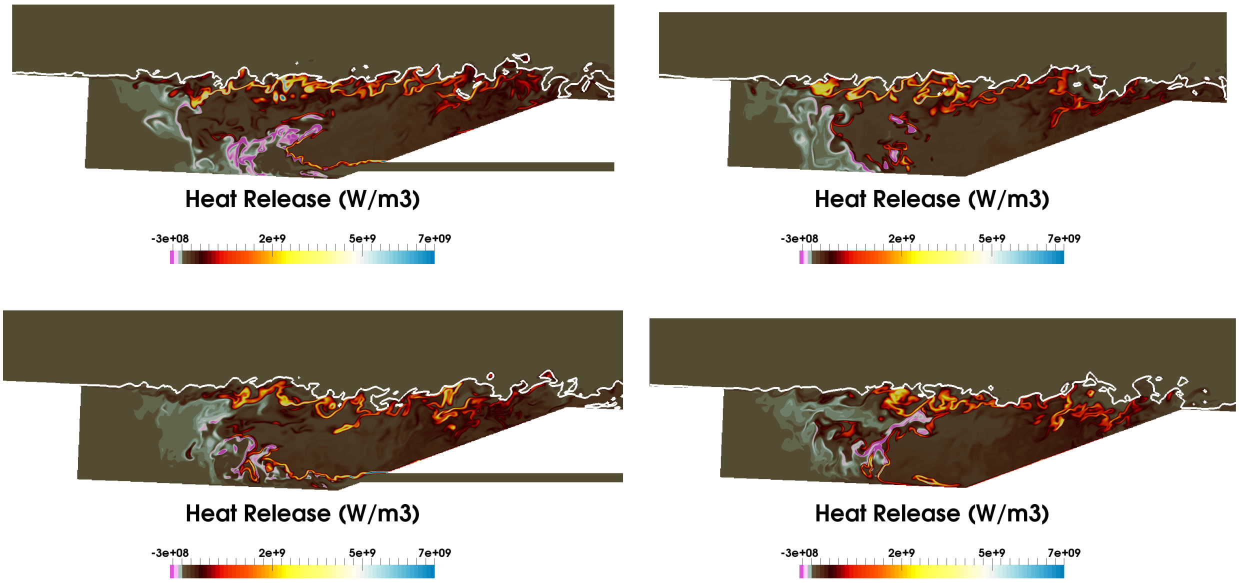

Figure 5.38: Instantaneous heat release rate fields in the injector centerplane (left) and the centerplane between two injectors (right) for adiabatic (top) and isothermal (bottom) cases. The isoline Mach = 1 is displayed with a white line. Fine mesh.

at the cavity front, and is weaker in the rest of the mixing layer. This can be identified in Fig. 5.39 by higher ethylene concentration at the mixing layer for the isothermal case. At the injector centerplane, the reaction is spreading further from the exit of the injector until the middle of the cavity in the isothermal case, which means that more air is available in this scenario. Less combustion in the mixing layer allows more air to enter the cavity and react with ethylene from the injector. Because the reaction area at the exit of the injector is larger, more fuel is consumed and the fuel concentration arriving in the small recirculation area is lower. At the centerplane between two injectors, the combustion zone is shifted from the interface between the recirculation areas in the adiabatic case to the middle of the cavity in the isothermal case. The previous phenomenon is also caused by higher concentration of oxidant entering the cavity, sufficient to allow combustion before arriving the to interface between the recirculation zones. Consequently, a perturbation in temperature at the cavity front can trigger the butterfly effect that modifies the reacting zones and the species distribution inside the cavity.

Averaged fields of the mixture composition inside the cavity are displayed in Fig. 5.41 for the isothermal case (RFI1) in the centerplane between two injectors. The equivalence ratio is computed from the mixture fraction using the Eq. 2.1.18. As expected, the mixture at the front of the cavity is very rich, mainly composed of fuel and burnt gases, without any oxygen. The large recirculation zone is mainly composed of burnt gases ($Y_{CO_2} = 0.12$), and only a small amount of fuel and oxidizer can be found in this area. Compared to the RANS simulation performed by Baurle [4], the composition in the cavity of the current simulation is largely richer, especially in the small recirculation area where the average equivalence ratio is found to be 1.5 in the simulation of Baurle and 4 here. However, the concentrations of C_2H_4 and CO_2 are quite similar between the RANS and the LES, where their values are in average 0.12 and 0.09 respectively. The large discrepancy in equivalence ratio is probably due to a different definition of ϕ, as it is not given in the article of Baurle [4].

Simulation with isothermal wall conditions is compared to the experiment for fine mesh. The averaged cavity wall pressure is displayed on Fig. 5.42. The isothermal case is underestimating the wall pressure at the front and the middle of the cavity by about 2500 Pa, but is overestimating it

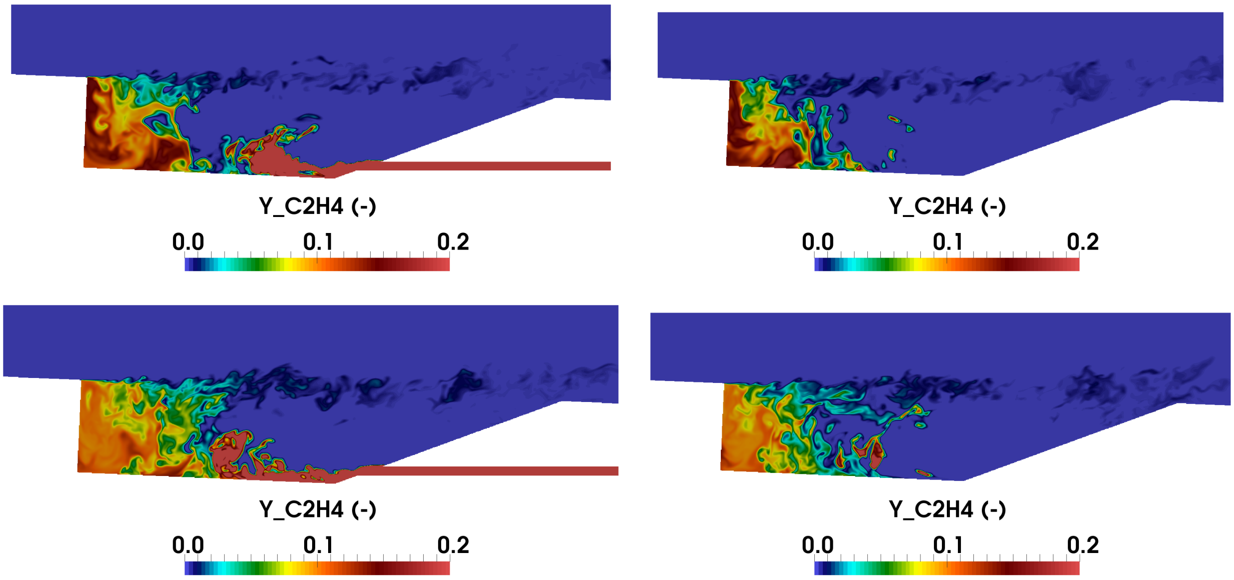

Figure 5.39: Instantaneous fuel mass fraction in the injector centerplane (left) and the centerplane between two injectors (right) for adiabatic (top) and isothermal (bottom) cases. Fine mesh.

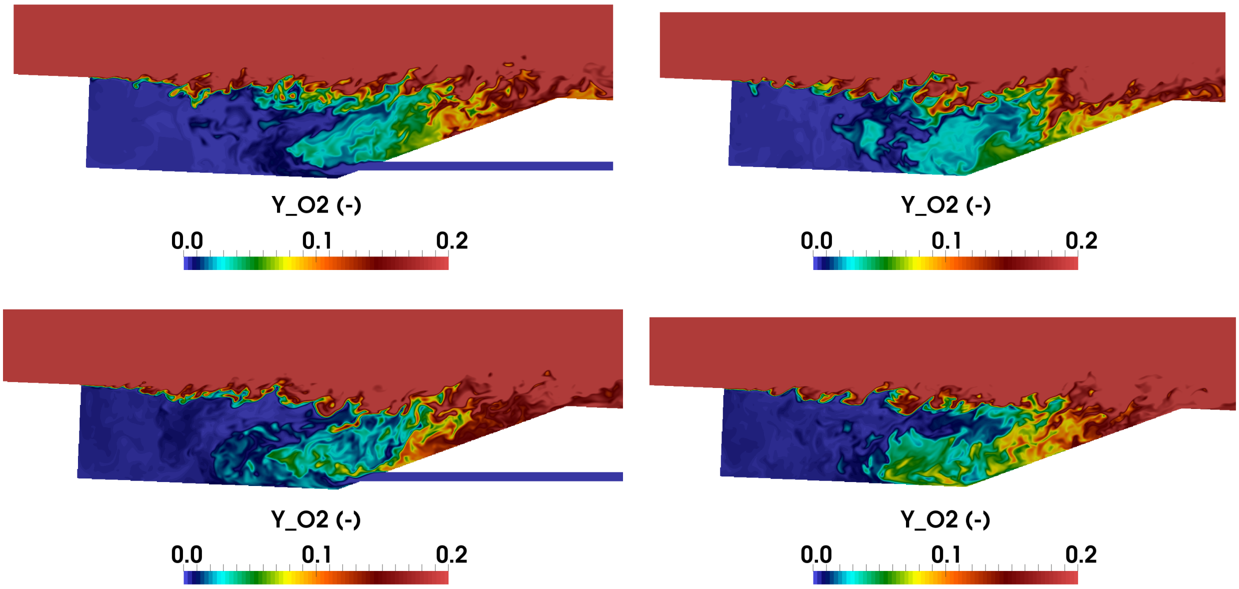

Figure 5.40: Instantaneous oxidant mass fraction in the injector centerplane (left) and the centerplane between two injectors (right) for adiabatic (top) and isothermal (bottom) cases. Fine mesh.

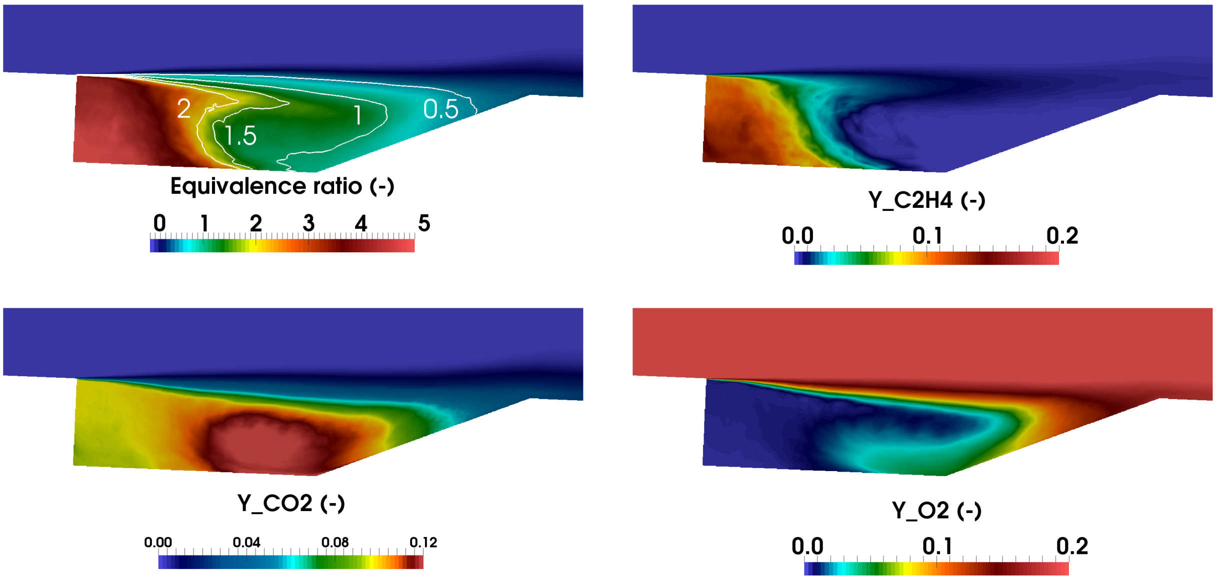

Figure 5.41: Averaged equivalence ratio and mass fractions of C_2H_4, CO_2 and O_2 for RFI1 in the centerplane between two injectors. The white line indicates the isolines $\phi = 0.5$, 1, 1.5 and 2.

at the cavity aft wall by 3500 Pa. The velocity profiles comparison is shown on Fig. 5.43. The streamwise velocity profiles are equivalent for both cases. As for the transverse velocity profiles, both cases are not well predicting the experimental results, but stay quite close to each other. Note that the transverse velocity is higher by norm in the mixing layer for the isothermal case, showing that the flow is more likely to go into the cavity. Compared to the experiment, the adiabatic simulation is performing better than the isothermal case for the cavity wall pressure, and they feature similar velocity profiles. An accurate isothermal simulation requires precise wall conditions (temperature, fluxes) that the experiment of Tuttle et al. [164] does not provide. As the conditions of the isothermal case are not certain, and the adiabatic case is closer to experimental measurements for wall pressure and not that different from the isothermal case, further simulations with two and eleven injectors will be done with adiabatic wall conditions.

5.7 Impact of number of injectors on the flame

5.7.1 Comparison between 1, 2 and 11 injectors

In addition to the adiabatic wall conditions case with only one injector, simulations with two and eleven injectors (whole geometry) have been performed using the coarse mesh to investigate the effect of number of injectors on the flame (see Tab. 5.5). The two injectors case RCA2 ($z \in [-12.7\text{ mm}, 12.7\text{ mm}]$) has been initialized with the one injector solution RCA1 ($z \in [-12.7\text{ mm}, 0]$) by symmetry to the axis $z = 0$. The center of each injector is at $z = -6.35$ mm and $z = 6.35$ mm respectively. The boundaries at $z = -12.7$ mm and $z = 12.7$ mm are prescribed as periodic. The mesh is composed of 90 millions of cells and needs approximately 200 000 hours CPU time to gather statistics of 4 ms physical time. The eleven injectors case RCA11 ($z \in [-82.55\text{ mm}, 69.85\text{ mm}]$) has also been initialized from the one injector solution by duplicating the solution for each injector, located at $z = -69.85$, -57.15, -44.45, -31.75, -19.05, -6.35, 6.35, 19.05, 31.75, 44.45, 57.15 mm respectively. Note that the width of the case RCA11 is 152.4 mm which is equal to 12×12.7 mm and not 11. Actually, the distance between the first/last injector and the wall is 1.5 times higher than the distance between two injectors: 19.05 mm instead of 12.7 mm. The centerplane of the whole geometry is the centerplane of the 6-th injector which is located at $z = -6.35$ mm.

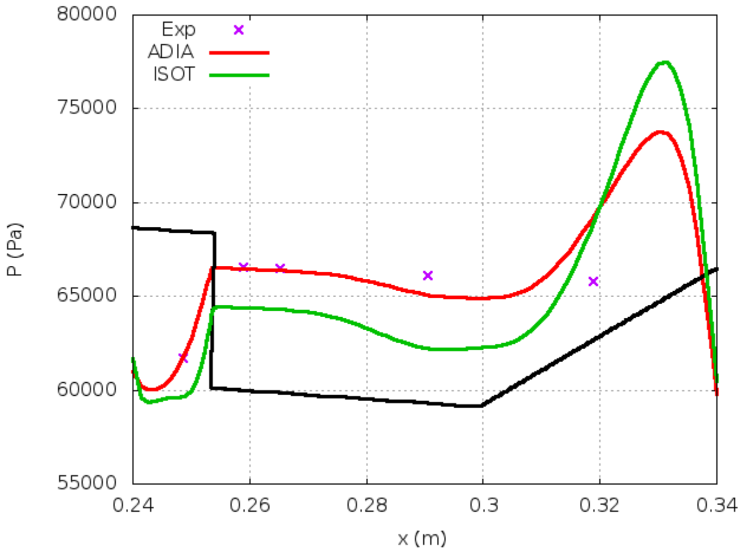

Figure 5.42: Averaged cavity wall pressure, comparison between the numerical and the experimental data for fine mesh at the centerplane between two injectors: experiment (pattern), adiabatic wall simulation (red line), isothermal wall simulation (green line).

The side walls are modeled with adiabatic non-slipping wall conditions. The mesh of the complete domain has 542 millions of cells and requires about 3 000 000 hours CPU time for 4 ms of statistics. The airflow is injected with homogeneous isotropic turbulence with an intensity of 10% of the local speed. Ethylene-air combustion is still modeled with the 22 species (S22) from Luo et al. [105]. Like the one injector simulation, each injector has the same mass flow rate, which is 1/11 × 99 SLPM, leading to a velocity of 115 m/s per injector.

Case	**Cavity width (mm)**	**Injector center coordinate (mm)**	**Side boundary conditions**
RCA1	12.7	$z = -6.35$	Periodic
RCA2	25.4	$z = -6.35, 6.35$	Periodic
RCA11	152.4	$z = -69.85, -57.15, -44.45, -31.75, -19.05, -6.35, 6.35, 19.05, 31.75, 44.45, 57.15$	Adiabatic non-slip wall

Table 5.5: Parameters of reactive cases with different number of injectors. Coarse mesh.

Averaged fields of temperature, heat release rate and fuel mass fraction are displayed at the centerplane of the injector in the transverse direction ($y = -19.57$ mm) in Fig. 5.44, Fig. 5.45 and Fig. 5.46 for RCA1, RCA2 and RCA11 respectively. Instantaneous fields can be found in the Appendix 7.2. The cases RCA1 and RCA2 are showing very similar results where each injector is performing the same way. The injection jet is parallel to the direction of the injection and the resulted flame has a V-shape with the same intensity. The case with eleven injectors RCA11 is performing differently, especially for the injection jets which are not parallel to each other, and the combustion is found more intense in the vicinity of the injectors located at the centerplane. The difference is probably due to the side walls, which were prescribed as periodic in the cases RCA1 and RCA2, that create an oscillatory mode in that direction that deviates the injection jets. In addition, the average temperature is also higher in RCA11 than in RCA1 or RCA2 by 100 K in the most reactive zones.

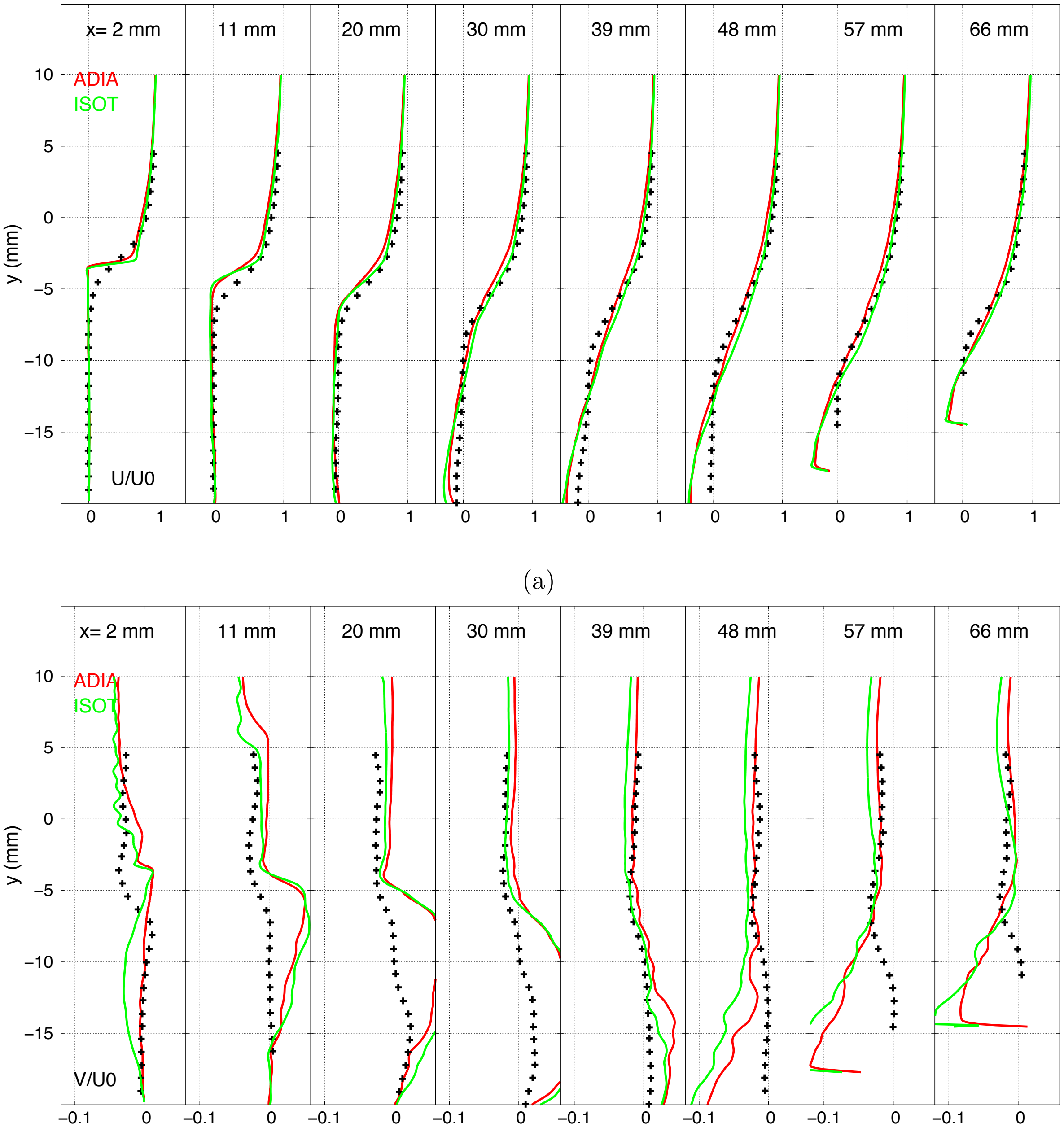

(a)

(b)

Figure 5.43: Averaged streamwise (a) and tranverse (b) velocity profiles inside the cavity, comparison between the numerical and the experimental data for fine mesh at the centerplane between two injectors: experiment (pattern), adiabatic wall simulation (red line), isothermal wall simulation (green line).

The simulations are then compared to the experimental data of Tuttle et al. [164] in the centerplane between two injectors (between 6-*th* and 7-*th* for RCA11). The averaged wall pressure is displayed in Fig. 5.47. RCA1 and RCA2 have very similar wall pressure, whereas the discrepancy between RCA1 and RCA11 is about 1 kPa. However, the experiment is fairly well predicted by all cases, except for the last point in the cavity ramp. The averaged streamwise and transverse velocities profiles are displayed in Fig. 5.48. The averaged streamwise velocity is still very well predicted by all the cases, only slight differences are observed between them. The simulations still overpredict the tranverse velocity, regardless of the number of injectors involved. The difference between RCA1 and RCA2 is in average smaller than the one with RCA11, probably due to the periodic conditions prescribed at the side walls.

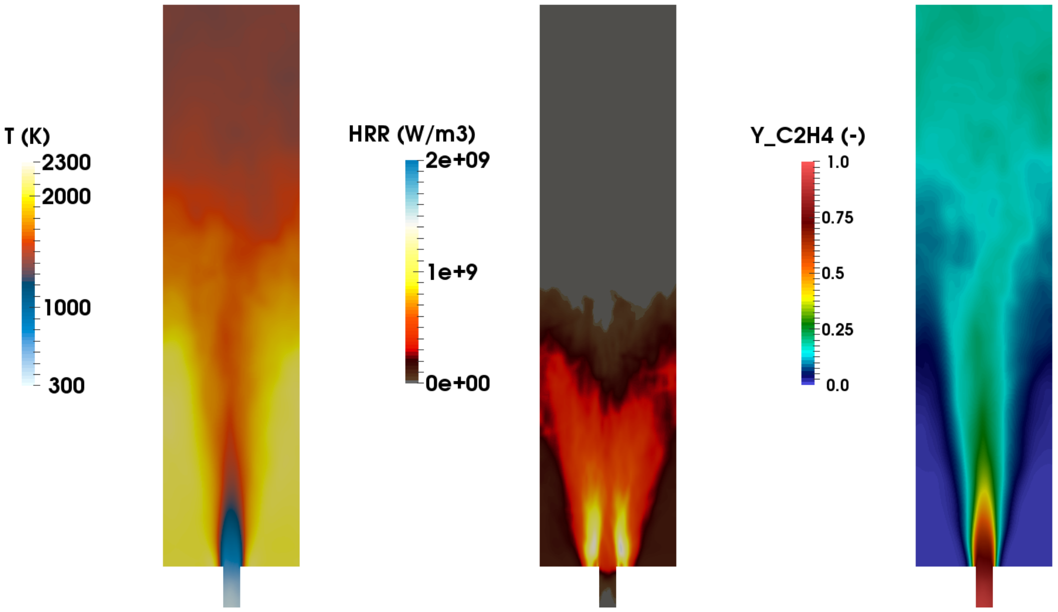

Figure 5.44: Averaged temperature, heat release rate and fuel mass fraction at $y = -19.57$ mm (injector center) for RCA1. Coarse mesh.

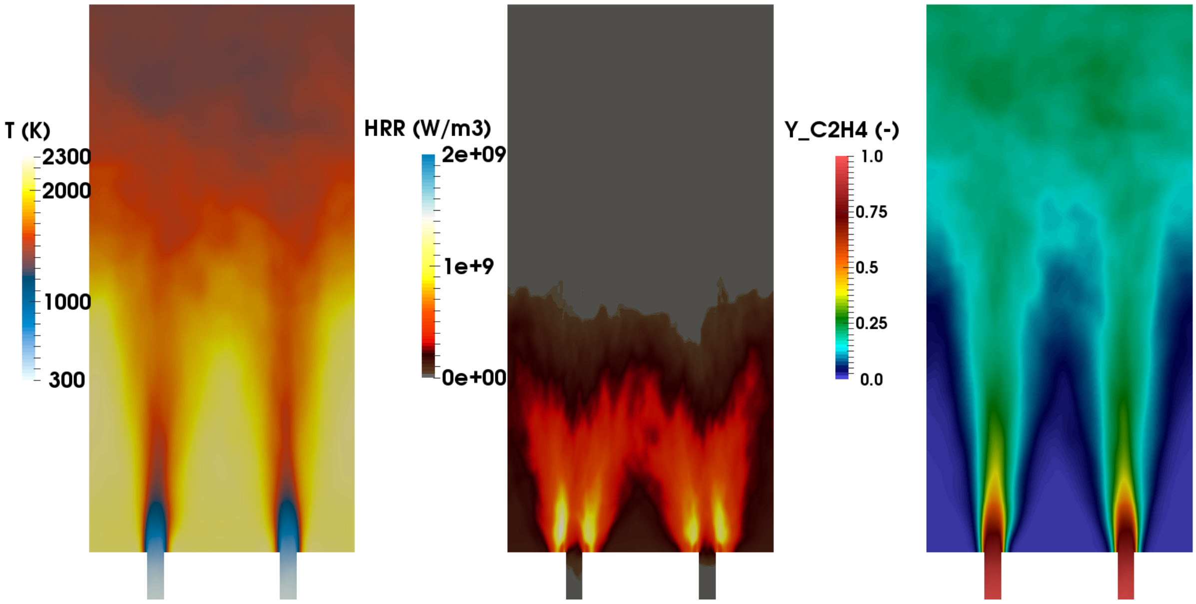

Figure 5.45: Averaged temperature, heat release rate and fuel mass fraction at $y = -19.57$ mm (injector center) for RCA2. Coarse mesh.

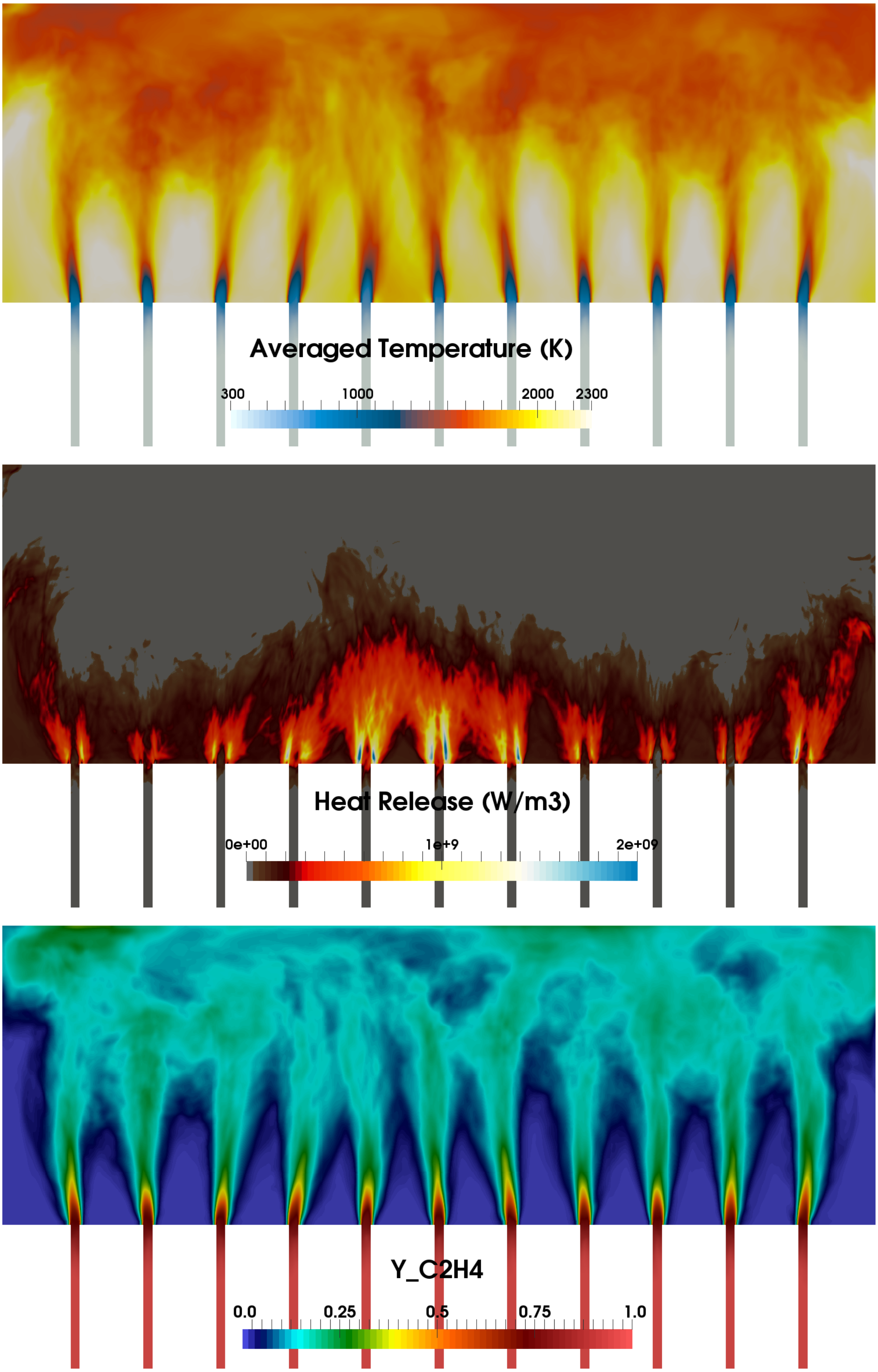

Figure 5.46: Averaged temperature, heat release rate and fuel mass fraction at $y = -19.57$ mm (injector center) for RCA11. Coarse mesh.

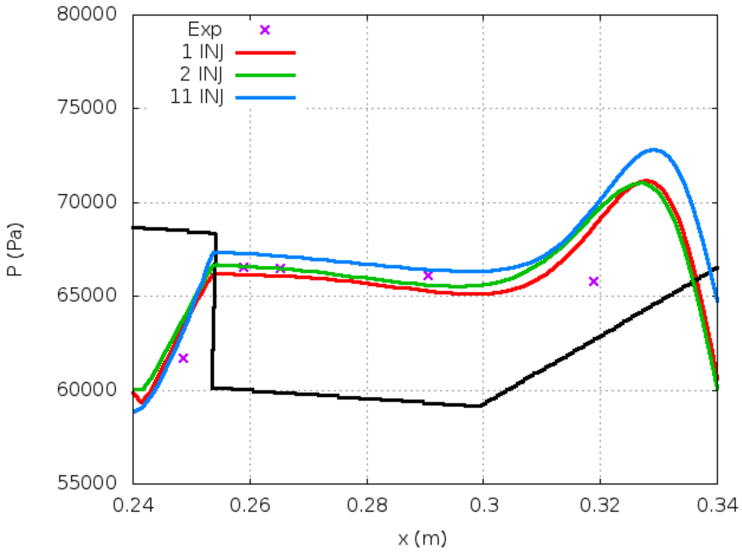

Figure 5.47: Averaged cavity wall pressure, comparison between the numerical and the experimental data for fine mesh at the centerplane between two injectors: experiment (pattern), numerical data of one (red line), two (green line) and eleven (blue line) injectors (between 6-*th* and 7-*th*).

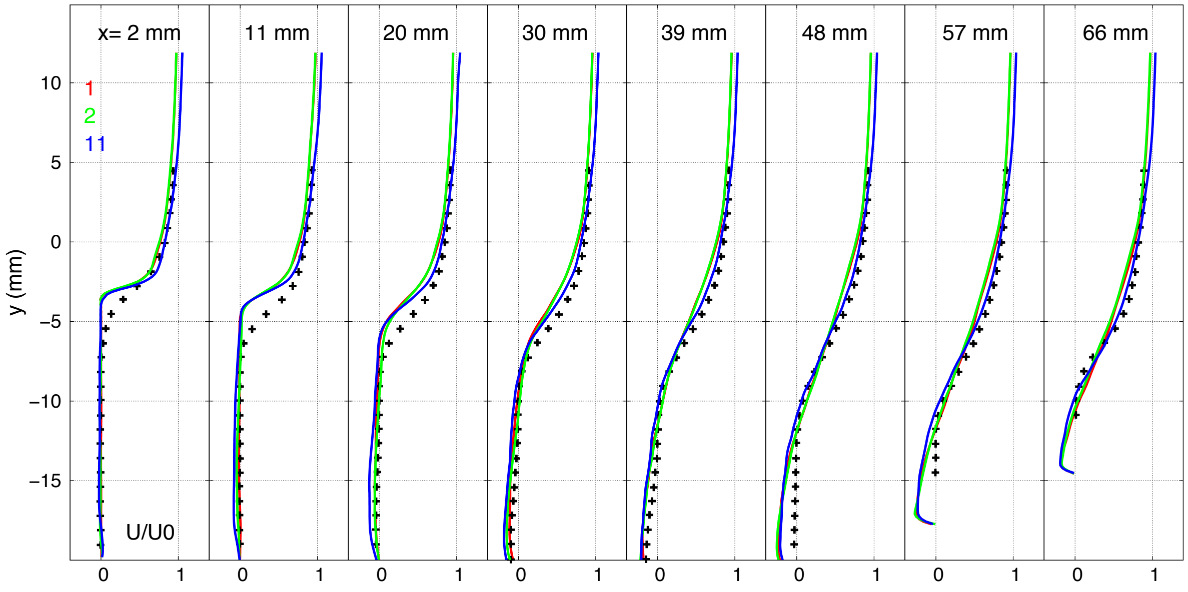

(a)

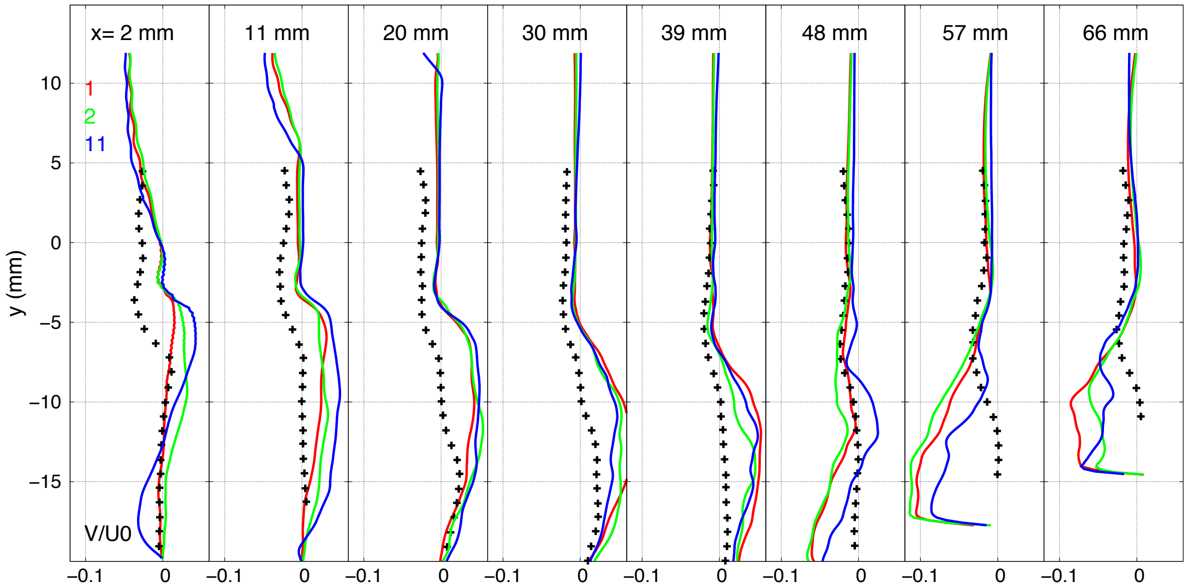

(b)

Figure 5.48: Averaged streamwise (a) and tranverse (b) velocity profiles inside the cavity, comparison between the numerical and the experimental data for coarse mesh at the centerplane between two injectors: experiment (pattern), numerical data of one (red line), two (green line) and eleven (blue line) injectors (between 6-*th* and 7-*th*).

5.7.2 Comparison between injectors of the 11 injectors case

The eleven injectors case (RCA11) is showing some disparities between each injector, therefore a more detailed investigation on some of these injectors is performed in this section. Comparisons have been done on the centerplane between injectors 4-5, 6-7, 9-10, and 10-11 for averaged wall pressure inside the cavity (Fig. 5.49), averaged temperature profiles (Fig. 5.50) and averaged velocity profiles (Fig. 5.51). In the region prior to the cavity, the wall pressure is higher at the centerplane between injectors 10 and 11, which is closer to the side wall. The pressure stays relatively the same

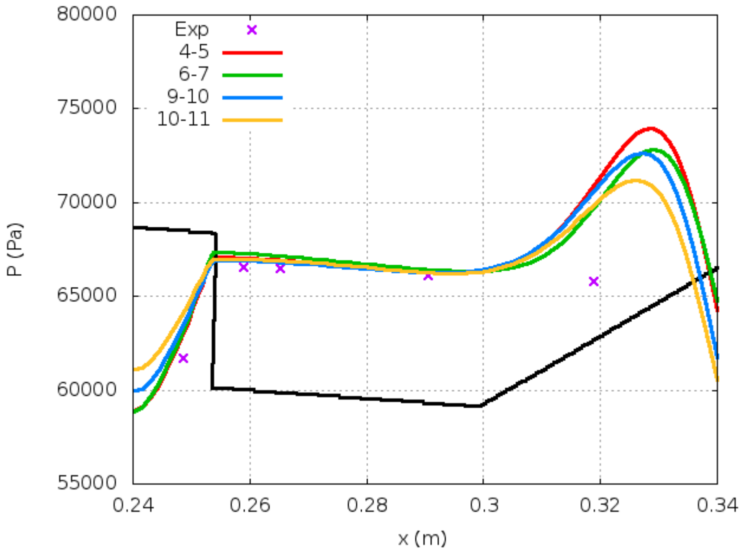

Figure 5.49: Averaged cavity wall pressure, comparison between the numerical and the experimental data for coarse mesh at the centerplane between two injectors for RCA11: experiment (pattern), injectors 4-5 (red line), 6-7 (green line), 9-10 (blue line) and 10-11 (magenta line).

for each centerplane in the cavity, except in the vicinity of the reattachment shock system where a higher wall pressure is found for the centerplane between injectors 4 and 5 and the lowest one between injectors 10 and 11. The discrepancy in temperature is slight between centerplanes 4-5, 9-10 and 10-11. But the centerplane near the central injector behaves differently. This centerplane has a higher temperature at the front of the cavity and a lower temperature at the rear of the cavity. The temperature discrepancy can reach 250 K in certain regions. The combustion zone is in fact shifted from the large recirculation area to the small recirculation area in the centerplanes near the central injector (6-th), resulting in a difference in temperature. The averaged streamwise velocity is still not changing and stays relatively the same at each centerplane. The averaged transverse velocity is dependent of the location of the centerplane, especially at the vicinity of the shock system.

The isosurface of temperature ($T = 2000$ K) colored by the values of mixture fraction is displayed in Fig. 5.52. A lower temperature and a leaner mixture can be observed in the vinicity of the central injector. This indicates that the amount of cold airflow entering through the rear of the cavity is higher in the central injector region, thus decreasing the temperature and the mixture fraction. The origin of the airflow massively entering in the central injector region is difficult to capture and in the absence of more complete experimental results, it is difficult to decide if this is a real feature of the experimental set-up or a numerical artefact. However the differences between the simulation of the complete set-up and one or two injectors simulations can be considered unimportant if only stability issues or combustion regime analysis are considered.

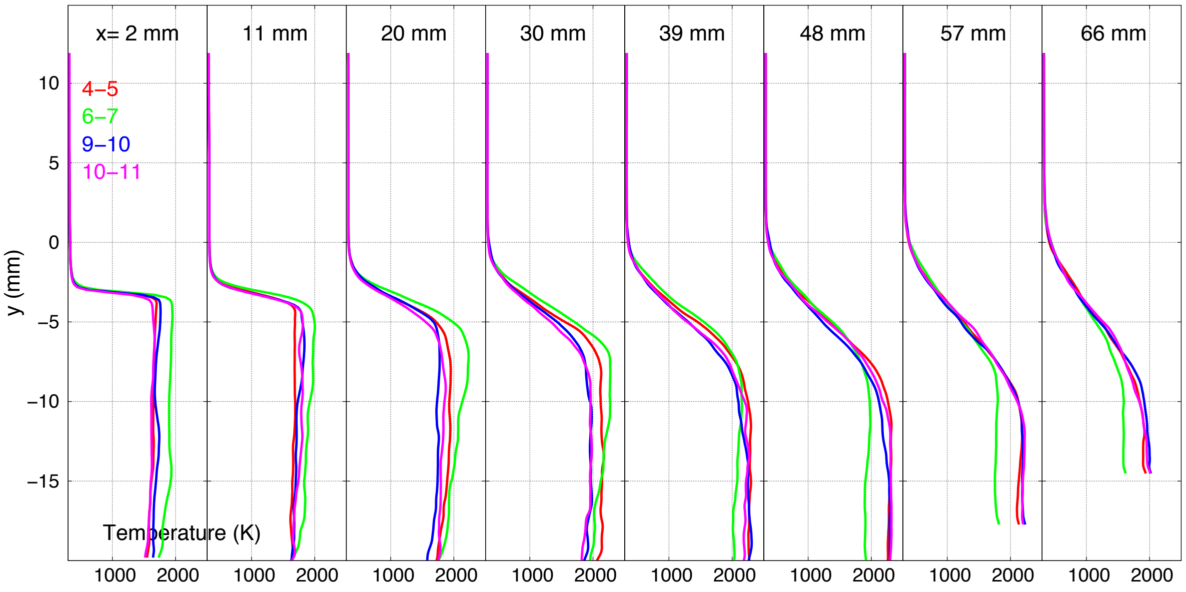

Figure 5.50: Averaged temperature inside the cavity for RCA11: comparison between injectors. Coarse mesh.

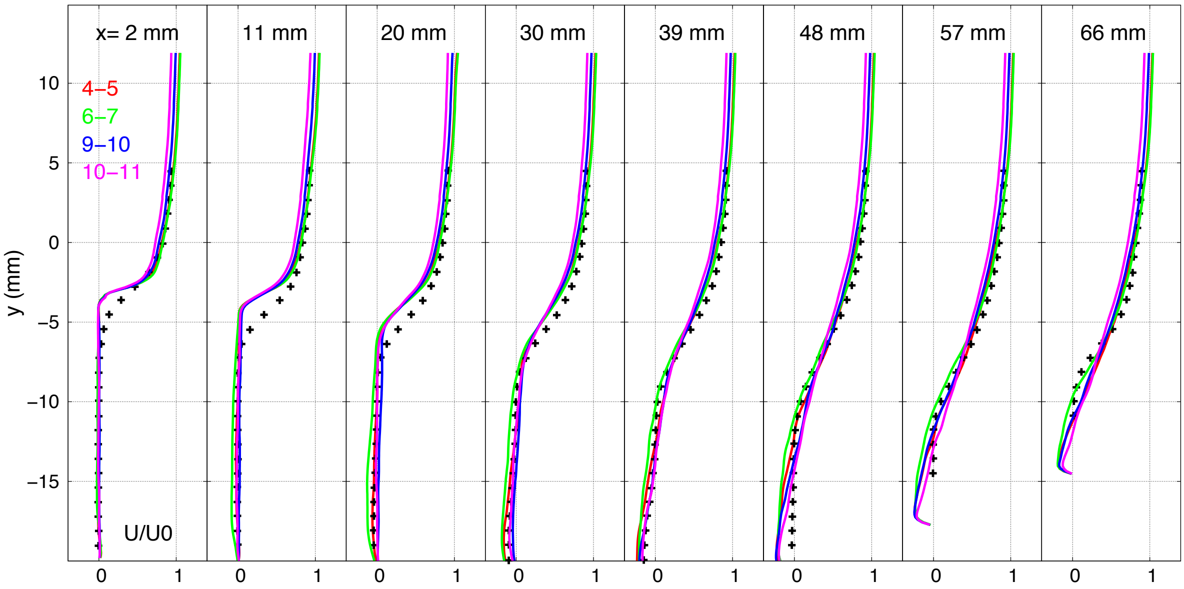

(a)

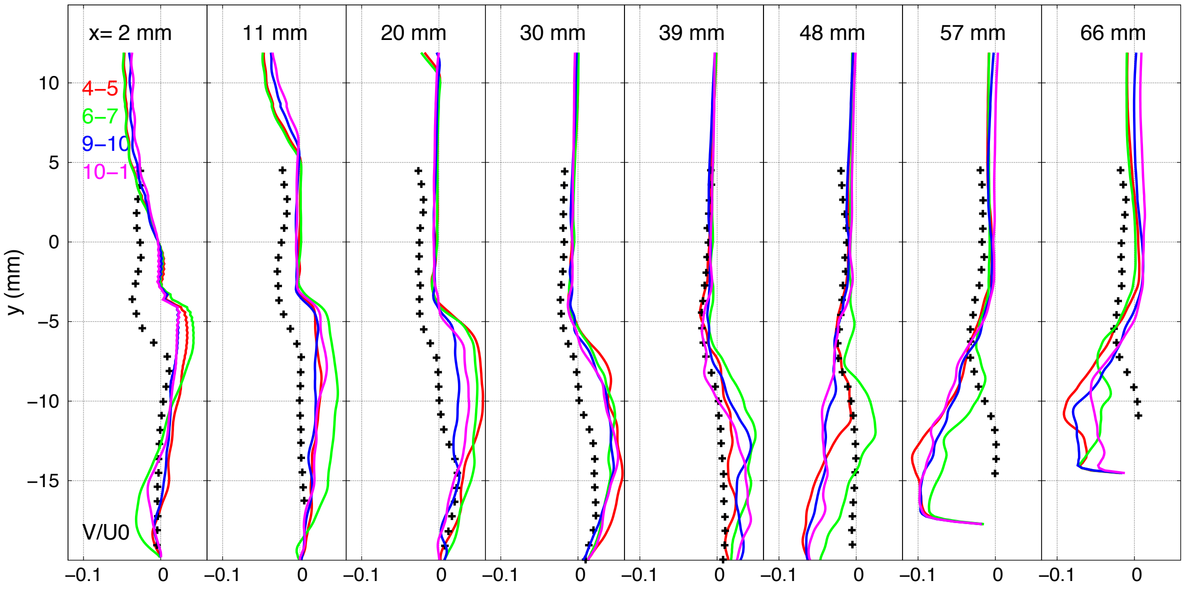

(b)

Figure 5.51: Averaged streamwise (a) and tranverse (b) velocity profiles inside the cavity, comparison between the numerical and the experimental data for coarse mesh at the centerplane between the two injectors for RCA11: experiment (pattern), injectors 4-5 (red line), 6-7 (green line), 9-10 (blue line) and 10-11 (magenta line).

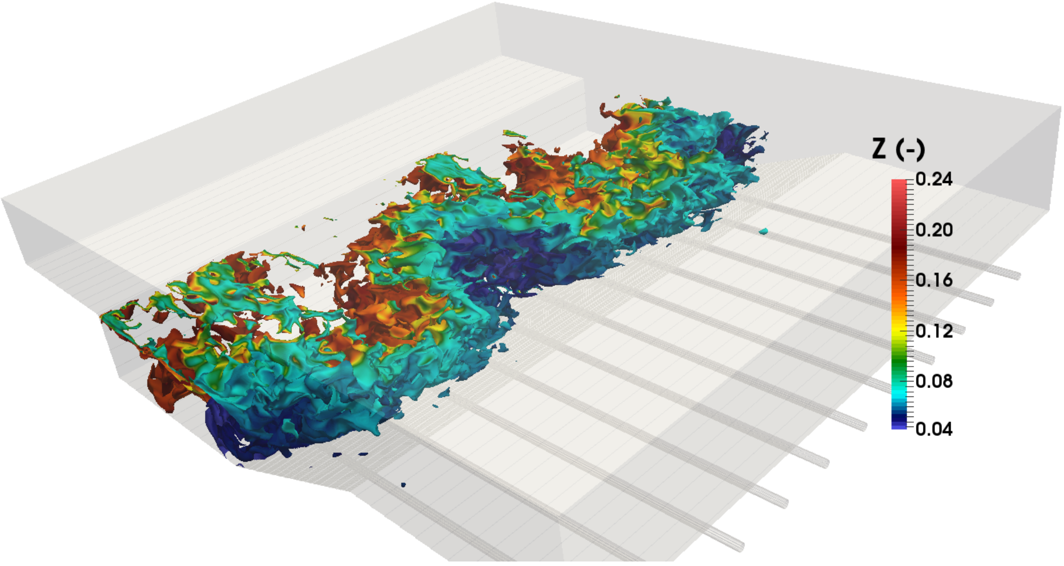

Figure 5.52: Instantaneous isosurface of temperature at 2000 K for RCA11, colored by the values of mixture fraction.

Chapter 6

Analysis of flame structures

Contents

6.1 Validity of quasi-laminar model

Computations in previous sections were performed with the quasi laminar model which is theoretically only valid in cases where the mesh is sufficiently refined. Section 3.2.1 showed that the subgrid Damköhler number Da_{sgs} can be used to check the validity of the quasi laminar model. This number needs then to be very small to unity, therefore Da_{sgs} is computed in this section to justify a posteriori the use of this model.

6.1.1 Expressions of subgrid Damköhler number

Four formulations are employed and compared. The first expression uses the subgrid time scale from Vinuesa et al. [169] adapted to dynamic Smagorinsky model and the chemical time scale from Guven et al. [67]:

$$Da_{sgs,1} = \frac{(2\widetilde{S}_{ij}\widetilde{S}_{ij})^{-1/2}}{\min(\rho Y_k/\dot{\omega}_k)} \tag{6.1.1}$$

The second expression is different by replacing the chemical time scale by a formulation based on one dimensional laminar premixed flame at stoichiometric condition characteristic time, $\tau_{c,2} = \delta_L / s_L = 0.48$ ms:

$$Da_{sgs,2} = (2\widetilde{S}_{ij}\widetilde{S}_{ij})^{-1/2}\frac{s_L}{\delta_L} \tag{6.1.2}$$

The third and fourth expressions are respectively from Duwig et al. [45] and Moule et al. [118], and are based on the same chemical time scale than the second formulation. The smallest resolved time scale being $\tau_{sgs,2} = \Delta / u'_\Delta$ for the third expression and $\tau_{sgs,3} = \sqrt{\tau_K \tau_{sgs,2}}$ for the fourth expression. With the approximation $u'_\Delta = \sqrt{2/3}\nu_t/(c_\kappa \Delta)$ [7, 45], the subgrid Damköhler number expressions become:

$$\begin{aligned} Da_{sgs,3} &= \sqrt{\frac{3}{2}}\frac{c_\kappa \Delta^2}{\nu_t}\frac{s_L}{\delta_L} \\ Da_{sgs,4} &= \left(\sqrt{\frac{3}{2}}c_\kappa\right)^{2.25}\frac{\Delta^2 \nu^{1/4}}{\nu_t^{5/4}}\frac{s_L}{\delta_L} \end{aligned} \tag{6.1.3}$$

approximating c_κ to 0.7, one gets:

$$\begin{aligned} Da_{sgs,3} &= 0.86\frac{\Delta^2}{\nu_t}\frac{s_L}{\delta_L} \\ Da_{sgs,4} &= 0.039\frac{\Delta^2 \nu^{1/4}}{\nu_t^{5/4}}\frac{s_L}{\delta_L} \end{aligned} \tag{6.1.4}$$

The four expressions are assembled in Tab. 6.1. Two comparisons are performed, the first one by comparing $Da_{sgs,1}$ and $Da_{sgs,2}$ to investigate which chemical time scale is more restrictive. And the second comparison is related to $Da_{sgs,2}$, $Da_{sgs,3}$ and $Da_{sgs,4}$ to study the different subgrid turbulent time scales.

Da_{sgs}	**Subgrid time scale**	**Chemical time scale**
1	$(2\widetilde{S}_{ij}\widetilde{S}_{ij})^{-1/2}$	$\min(\rho Y_k / \dot{\omega}_k)$
2	$(2\widetilde{S}_{ij}\widetilde{S}_{ij})^{-1/2}$	δ_L / s_L
3	$0.86\Delta^2\nu_t^{-1}$	δ_L / s_L
4	$0.039\Delta^2\nu^{1/4}\nu_t^{-5/4}$	δ_L / s_L

Table 6.1: Different formulations of subgrid Damköhler number Da_{sgs}.

The computation of subgrid Damköhler number is relevant exclusively in zones with combustion, that is in zone with significant heat release rates. The criterion used in this study is that only cells with heat release rate higher than 1% of maximum heat release rate are considered:

$$|\dot{\omega}_{E,cell}| \geq 0.01\dot{\omega}_{E,max} \tag{6.1.5}$$

The comparison between these expressions of subgrid Damköhler number will first be done for the fine mesh ($\Delta_x \approx 100\ \mu$m) to find the most restrictive formulation. The latter is then used to compute Da_{sgs} on the coarse mesh ($\Delta_x \approx 200\ \mu$m). The computations were performed using only one injector with adiabatic wall conditions and injection of HIT.

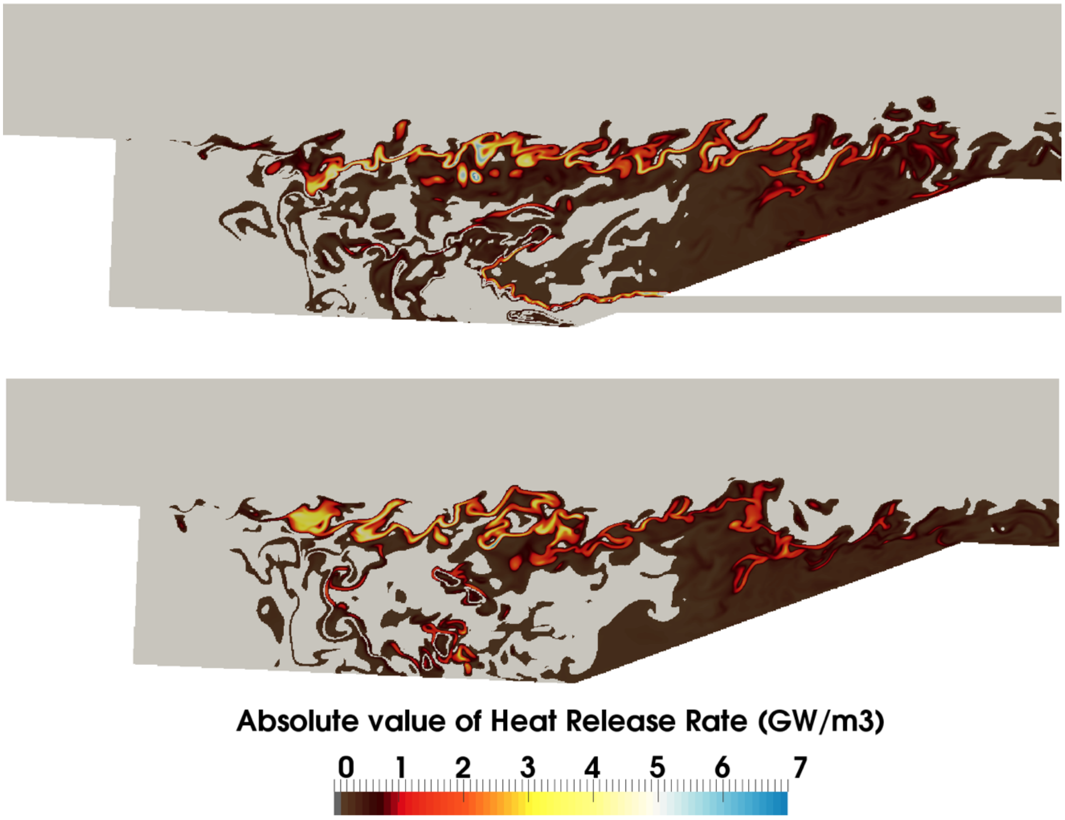

Figure 6.1: Instantaneous field of absolute value of heat release rate in the injector centerplane (top) and the centerplane between two injectors (bottom) for the fine mesh. Cells with heat release rate lower than 1% of maximum heat release are not shown.

6.1.2 Comparison of subgrid Damköhler numbers

Fig. 6.1 displays cuts of the injector centerplane and the centerplane between two injectors of the domain taking in consideration the criterion on heat release rate from Sec. 6.1.1. The zones of interest are the mixing layer, the middle and the rear of the cavity. The heat release rate in the front of the cavity is not significant, showing that no reaction occurs in the vicinity of the small recirculation bubble.

A cell ratio is introduced in order to measure the subgrid Damköhler number, and is defined as the ratio between the number of cells in a given interval of Da_{sgs} on the total number of cells where Eq. 6.1.5 is verified:

$$C_{Da,i} = \frac{N_{c,Da,i}}{N_T} \tag{6.1.6}$$

with $N_{c,Da,i}$ the number of cells verifying $Da_{sgs} \in [Da_i, Da_i + \epsilon_{Da}]$, where ϵ_{Da} is the interval range. A study on the number of species controlling $Da_{sgs,1}$ is first investigated. The chemical time scale $\tau_{c,1}$ of $Da_{sgs,1}$ is:

$$\tau_{c,1} = \min\left(\tau_{c,1}^{k}\right) \quad \text{where} \quad \tau_{c,1}^{k} = \frac{\rho Y_k}{\dot{\omega}_k} \tag{6.1.7}$$

where the subscript k corresponds to a species. In order to avoid division by zero, a criterion based on the species reaction rate $\dot{\omega}_k$ similar to the heat release criterion is applied for all cells. At a given

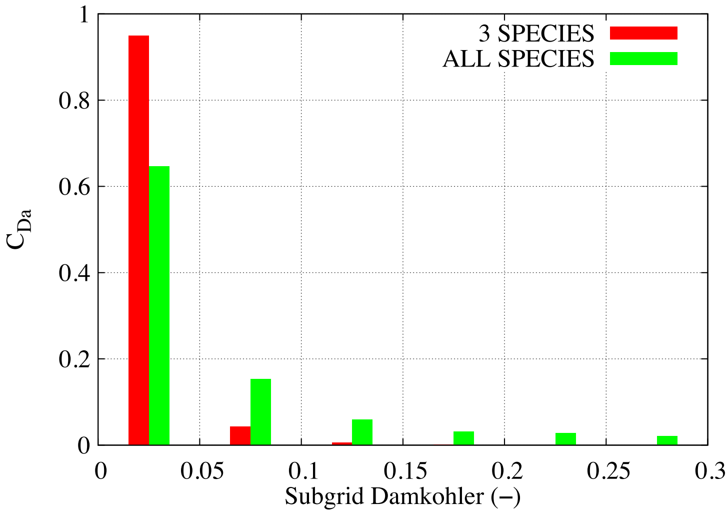

Figure 6.2: Cell ratio in each interval of subgrid Damköhler number of 0.05 for expression 1 with three major combustion products (CO, CO_2 and H_2O) and all combustion products. Fine mesh.

position, for a species to be accounted in the computation of the chemical time scale, its reaction rate must verify:

$$|\dot{\omega}_{k,cell}| \geq 0.01\dot{\omega}_{k,max} \tag{6.1.8}$$

The same criterion is applied for species mass fractions Y_k to prevent the chemical time scale from taking values close to zero:

$$Y_{k,cell} \geq 0.01Y_{k,max} \tag{6.1.9}$$

A comparison between a determination of $Da_{sgs,1}$ taking in account only the three major combustion products (CO, CO_2 and H_2O) and one including all species (22 species) is shown in Fig. 6.2. In the second case, 65% of cells verify $Da_{sgs} < 0.05$ and 83% verify $Da_{sgs} < 0.1$. If the subgrid Damköhler number is computed with only three major combustion products, approximately 95% of cells verify $Da_{sgs} < 0.05$. These discrepancies indicate that minor species are, as expected, less likely to be accurately captured by LES with quasi-laminar model approach.

An in-depth study has been conducted to investigate which species are responsible of the increase in subgrid scale Damköhler numbers. Since the overall chemical time scale $\tau_{c,1}$ is defined as the minimum value of all species chemical time scale $\tau_{c,1}^k$, a species cell ratio C_k has been introduced to understand which species k are controlling most frequently the overall chemical time scale. C_k is defined as the ratio between the number of cells of a species k having the smallest time scale $N_{c,k}$ and the total number of cells N_T such as:

$$C_k = \frac{N_{c,k}}{N_T} \tag{6.1.10}$$

This species cell ratio is displayed in Fig. 6.3 for all species (red histogram) along with the mean mass fraction of each species j (blue square) in the cells where their chemical time scale is the minimum: $\tau_{c,1}^j \leq \tau_{c,1}^k$ for $k = 1, 22$. The mean mass fraction of each species j, M_{Y_j}, is therefore defined as:

$$M_{Y_j} = \frac{\sum_{i=1}^{N_p} \alpha_j Y_j}{N_{c,j}} \tag{6.1.11}$$

where N_p is the number of points verifying the heat release rate criterion (Eq. 6.1.5) and the coefficients $\alpha_j = 1$ if $\tau_{c,1}^j \leq \tau_{c,1}^k$ for $k = 1, 22$ and $\alpha_j = 0$ otherwise. The species cell ratio shows that

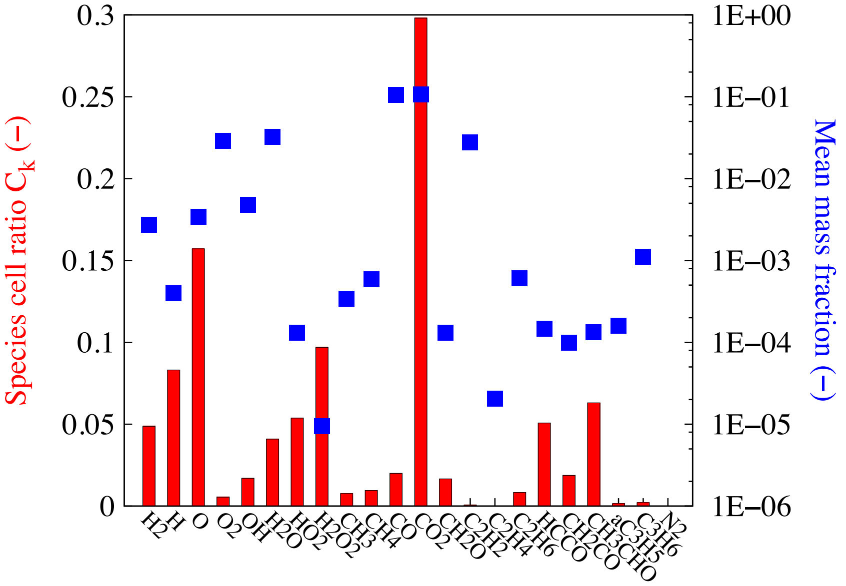

Figure 6.3: Cell ratio (histogram) and mean mass fraction of each species (square). Fine mesh.

the smallest species chemical time scale $\tau_{c,1}^k$ is rarely from hydrocarbons. Species with high mean mass fractions (O_2, H_2O or CO) have low cell ratios, except for CO_2 which ratio is the highest, approximately 0.3. The other species with relatively high ratios are either reaction intermediates (such as O, H) with fast chemistry or species at very low concentrations such as H_2O_2. Another investigation has been completed by taking into account only the cells with large subgrid Damköhler numbers ($Da_{sgs} > 0.05$) which represents 35% of the total number of cells, results are displayed in Fig. 6.4. Note that CO_2 contribution, which was featuring the highest cell ratio when all cells were concerned, vanishes when a condition on significant subgrid Damköhler number is applied. Species responsible of high Da_{sgs} are clearly identified as H, O, HO_2, H_2O_2 and $HCCO$. The hydrogen peroxide (H_2O_2) with very low concentrations, several orders of magnitude smaller than other species, is known to control the first stage of autoignition. Nevertheless, the quantity of cells with large subgrid Damköhler numbers is still low, with less than 17% of cells featuring $Da_{sgs} > 0.1$ and all cells with $Da_{sgs} < 0.3$. Therefore, the investigation of very thorough evaluation on all species shows that the use of quasi-laminar model in these simulations is consistent. The chemical time scale $\tau_{c,1}$ will be based on the three major combustion products CO, CO_2 and H_2O for comparisons with other expressions of subgrid Damköhler number.

Fig. 6.5 shows the comparison between $Da_{sgs,1}$ and $Da_{sgs,2}$ for the fine mesh with an interval of 0.05 for the subgrid Damköhler number. Readers are reminded that $Da_{sgs,1}$ is computed with a chemical time scale based on three major species mass fractions and reaction rates, and $Da_{sgs,2}$ is using chemical time scale from one dimensional laminar premixed flame thickness and speed at stoichiometric conditions. The first expression gives $Da_{sgs,1} < 0.05$ for 95% of the cells and the second expression has all the cells with $Da_{sgs,1} < 0.05$. The condition $Da_{sgs} \ll 1$ is therefore verified for both formulations, which also contributes to justify a posteriori the use of the quasi laminar model. Note that $Da_{sgs,1}$ is greater than $Da_{sgs,2}$ in average leading to the conclusion that $\tau_{c,1}$ is more restrictive than $\tau_{c,2}$, even with only three species (CO, CO_2 and H_2O).

A second comparison is performed with three different formulations of subgrid turbulent time scale, and with the same chemical time scale $\tau_{c,2}$. Results are displayed in Fig. 6.6 with an interval of 0.01 for the subgrid Damköhler number. It is clearly shown that using the second chemical time scale

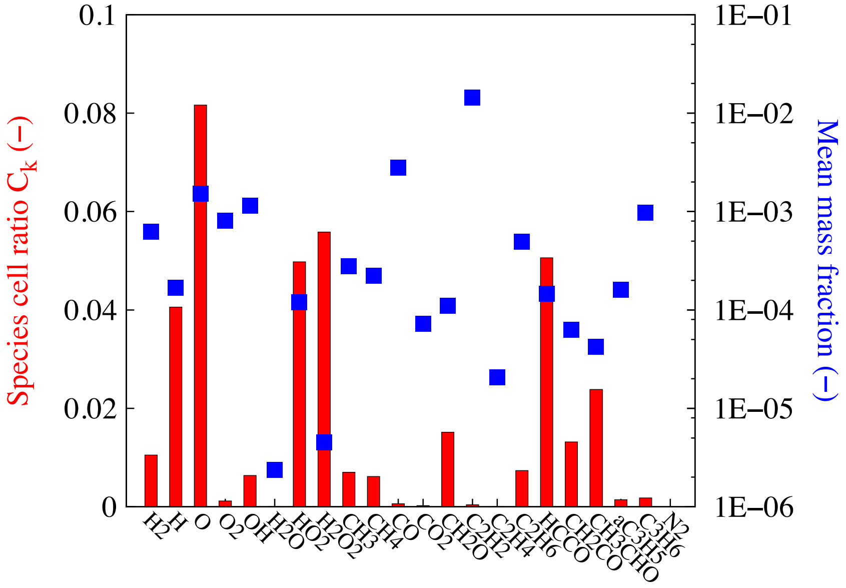

Figure 6.4: Cell ratio of (histogram) and mean mass fraction of each species (square) for cells with $Da_{sgs} > 0.05$. Fine mesh.

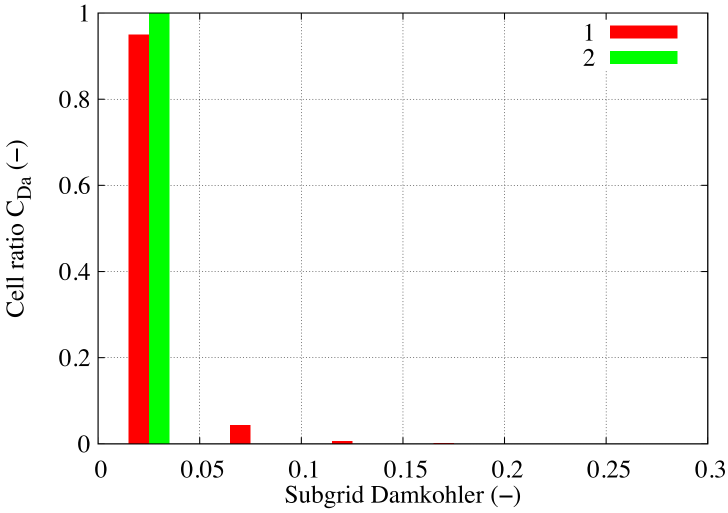

Figure 6.5: Cell ratio in each interval of subgrid Damköhler number of 0.05 for expressions 1 and 2: investigation on chemical time scale. Fine mesh.

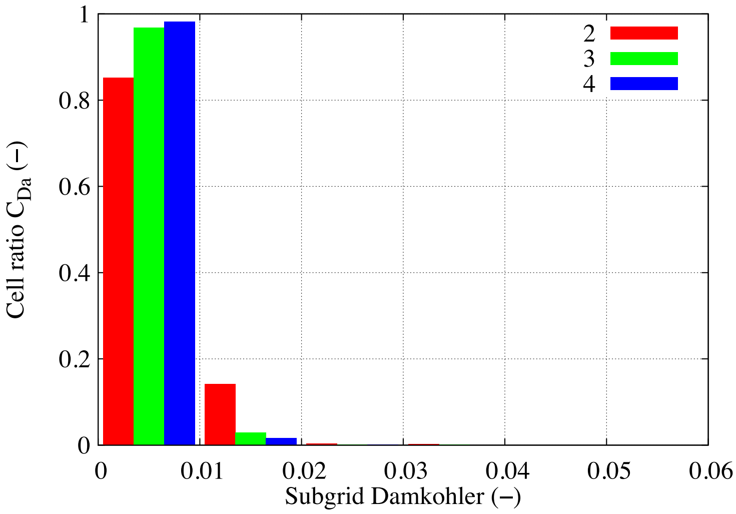

Figure 6.6: Cell ratio in each interval of subgrid Damköhler number of 0.01 for expressions 2, 3 and 4: investigation on subgrid turbulent time scale. Fine mesh.

$\tau_{c,2}$ leads to very small subgrid Damköhler numbers (< 0.02) no matter which subgrid turbulent time scale is chosen. $Da_{sgs,2}$ being the greatest among the three expressions, and coupled with the first comparison (between chemical time scales), the formulation which gives the greatest subgrid Damköhler number in average is $Da_{sgs,1}$. The latter expression is then retained for the comparison with a computation with the coarse mesh (Fig. 6.7). The subgrid Damköhler number is as expected greater in the coarse mesh, but stays relevant with over 85% of cells featuring $Da_{sgs} < 0.05$ and 95% of cells with $Da_{sgs} < 0.1$.

It is also worth mentioning that the expression $Da_{sgs,4}$ uses the same subgrid turbulent and chemical time scales as those used to compute the fine structure volume fraction γ^* in the Partially Stirred Reactor model (see Sec. 3.2.5). We remind that:

$$\gamma^* = \frac{\tau_c}{\tau_c + \tau^*} \tag{6.1.12}$$

and $Da_{sgs,4} = \tau^*/\tau_c$, so the fine structure volume fraction can be rewritten as:

$$\gamma^* = \frac{1}{1 + Da_{sgs,4}} \tag{6.1.13}$$

Fig. 6.8 shows that $Da_{sgs,4} \ll 1$ for coarse and fine meshes, leading to $\gamma^* \approx 1$ for both cases. Therefore, the PaSR model, if implemented, would be in this study no different than the quasi-laminar model approach, neither for the fine mesh nor for the coarse one.

6.2 Velocity of combustion zones

The freestream of the scramjet is supersonic (Mach 2) while the cavity flow is subsonic, the purpose of this section is to investigate whether combustion occurs at subsonic or supersonic speeds. With this aim in mind, a threshold on heat release rate identical to the condition of the section 6.1 is considered, with only cells verifying relation 6.1.5 included in the statistics.

Fig. 6.9 shows a cut in the centerplane between two injectors of heat release rate and Mach number. The isoline Mach = 1 (white line) separates the domain into two region: subsonic below

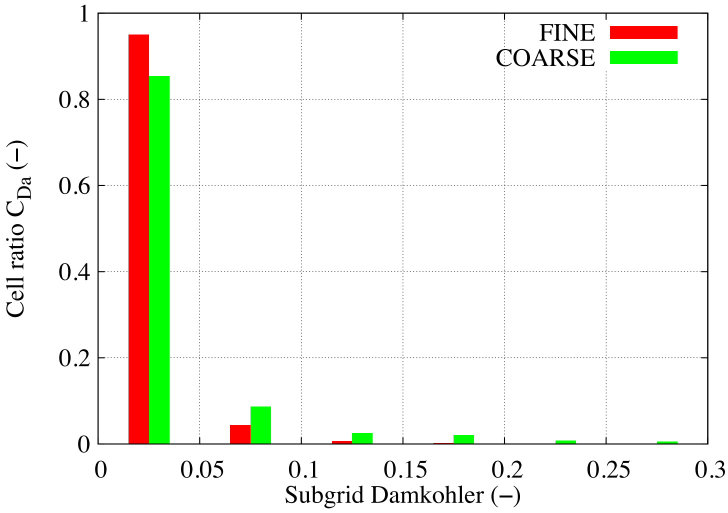

Figure 6.7: Cell ratio in each interval of subgrid Damköhler number of 0.05 for expression 1: comparison between fine and coarse meshes.

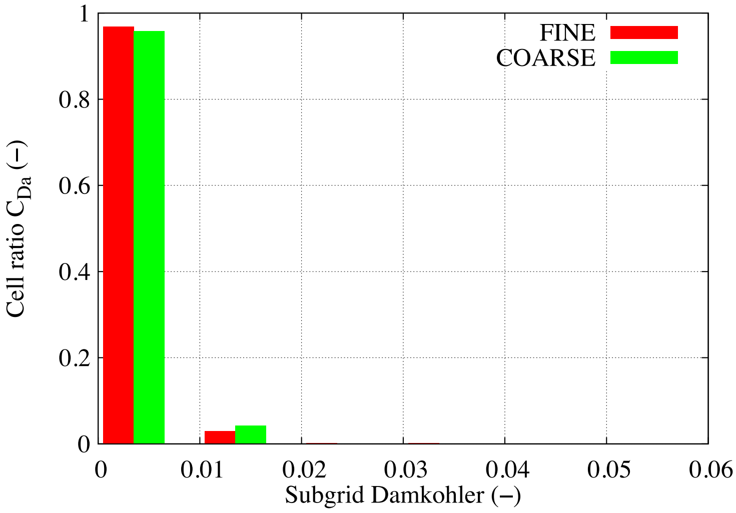

Figure 6.8: Cell ratio in each interval of subgrid Damköhler number of 0.01 for expression 4: comparison between fine and coarse meshes.

and supersonic above. Combustion occurs only inside the cavity and in the mixing layer. There is almost no combustion in supersonic flow and the highest heat release rate is found at the mixing layer, featuring Mach = 0.5. Two quantities are defined to better quantify the observed phenomena. The first quantity indicates the number of cells at each Mach number and is defined as the ratio of number of cells involved in each interval of Mach number on the total number of cells, $C_{Ma,i}$, defined as:

$$C_{Ma,i} = \frac{N_{c,Ma,i}}{N_T} \tag{6.2.1}$$

with $N_{c,Ma,i}$ the number of cells verifying $Ma \in [Ma_i, Ma_i + \epsilon_{Ma}]$, where $\epsilon_{Ma} = 0.1$ is the interval range. And the second is based on the conditional mean of heat release rate on Mach number, $< \dot{\omega}_E \mid Ma >$, to understand which zone has the highest heat release. The conditional mean is adimensionalized by the mean heat release $< \dot{\omega}_E >$:

$$R_{Ma} = \frac{< \dot{\omega}_E \mid Ma >}{< \dot{\omega}_E >} \tag{6.2.2}$$

Fig. 6.10 shows those quantities for the fine (left) and the coarse mesh (right). This plot quantifies what was observed on snapshots of Fig. 6.9 stating that the highest chemical activity appears at Mach = 0.5 and over 95% of combustion occurs at subsonic speeds (Mach < 1). The most reactive region is featuring Mach numbers between 0.1 and 0.3 representing approximately 40% of cells having $\dot{\omega}_{E,cell} \geq 0.01\dot{\omega}_{E,max}$, but with low intensity ($R_{Ma} = 0.8$). This region corresponds to the outer part of the large recirculation zone. The results of the coarse mesh are similar to the fine mesh for the flame distribution (almost no supersonic combustion), but the intensity of combustion given by R_{Ma} is globally lower than the fine mesh by 0.1. This difference is probably due to the flame front being thickened on the coarse mesh which has higher subgrid viscosity.

6.3 Flame regimes

Flame regimes can be characterized by the flame index which was first introduced by Yamashita et al. [178] to distinguish premixed from nonpremixed combustion. This index is based on geometrical considerations depending on fuel (F) and oxidizer (O_2) gradients:

$$F.I. = \nabla Y_F . \nabla Y_{O_2} \tag{6.3.1}$$

If the gradients follow the same direction ($F.I. > 0$), the combustion regime is accounted as premixed, and opposite gradients will lead to nonpremixed flames ($F.I. < 0$). The flame index is here only computed in zones with combustion where the heat release is greater than 1% of maximum heat release rate (see Eq. 6.1.5), so that the gradients of fuel and oxidizer cannot become zero. This formulation is based on one-dimensional flame topology, several improvements have been proposed in the literature [54, 81] to handle more complex flows. Besides, Domingo et al. [39] introduced a normalized flame index expression to analyse the flame regime distribution:

$$F.I. = \frac{1}{2}\left(1 + \frac{\nabla Y_F . \nabla Y_{O_2}}{|\nabla Y_F . \nabla Y_{O_2}|}\right) \tag{6.3.2}$$

The premixed regime occurs when $F.I. = 1$ while $F.I. = 0$ for nonpremixed flames. The previous formulations have limitations and do not fit computations using complex kinetic schemes, since the fuel can decompose before reaching the reaction zone, leading to insignifiant fuel gradients which makes the flame index indeterminate. Felden [52] used a mass fraction based on the fuel and the pyrolysis products of the fuel. In this work, the fuel mass fraction will be built on all the hydrocarbons involved in reactions such that using the 22 species kinetic scheme (S22), Y_F becomes:

$$Y_F = Y_{C_2H_4} + Y_{C_2H_2} + Y_{CH_3} + Y_{CH_4} + Y_{C_2H_6} + Y_{C_3H_6} \tag{6.3.3}$$

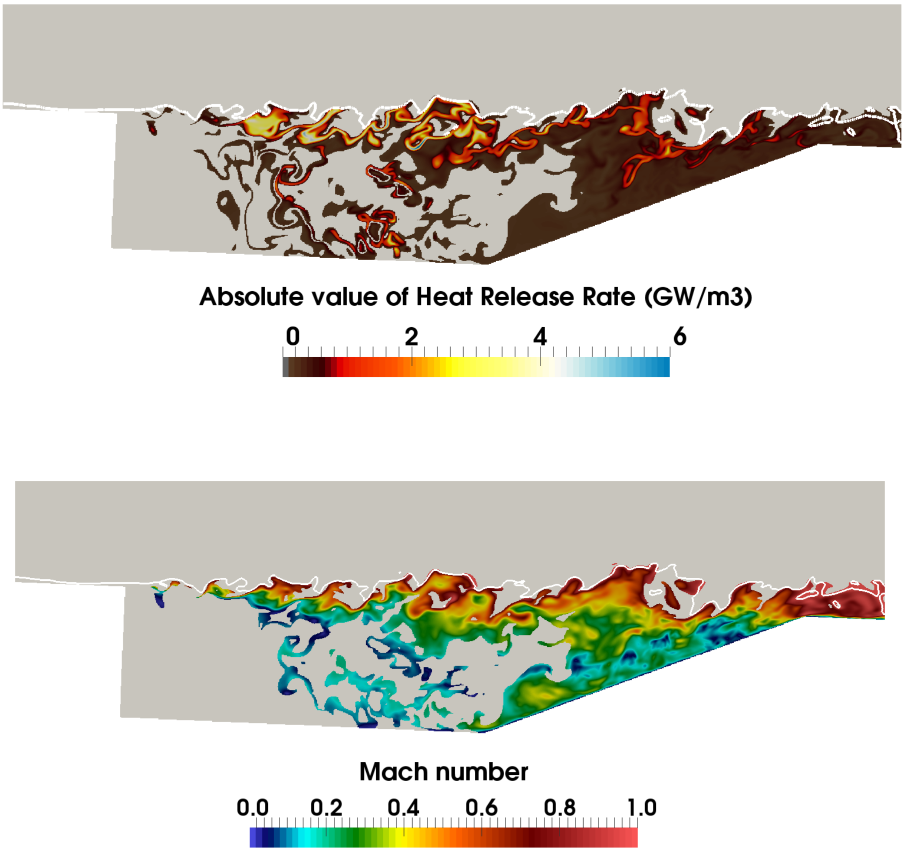

Figure 6.9: Instantaneous fields of (top) Heat release rate and (bottom) Mach number for fine mesh. Cells with heat release rate lower than 1% of maximum heat release are not shown. The white line represents iso-Mach = 1.

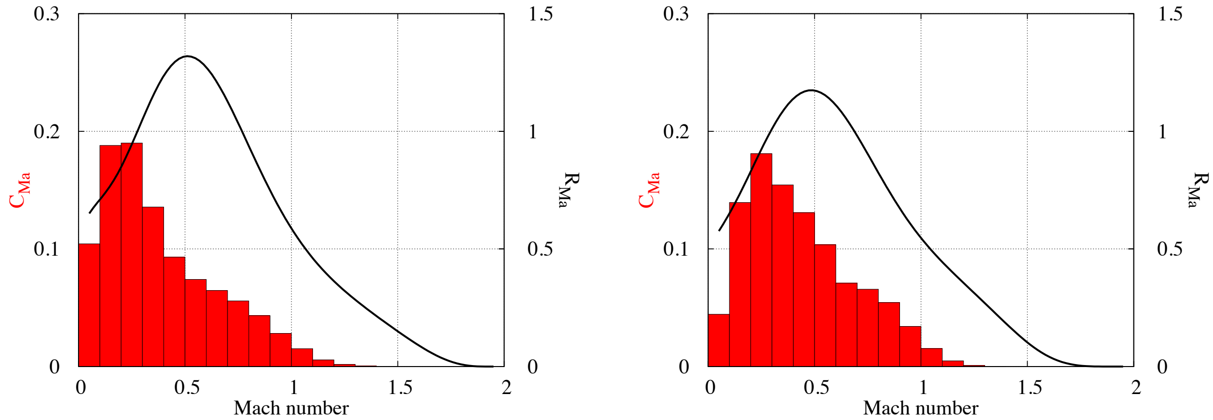

Figure 6.10: Dimensionless conditional mean of the heat release on Mach number R_{Ma} (curve), and percentage of cells contributing to the statistics in each interval (0.1) of Mach number C_{Ma} (histogram): fine mesh (left) and coarse mesh (right).

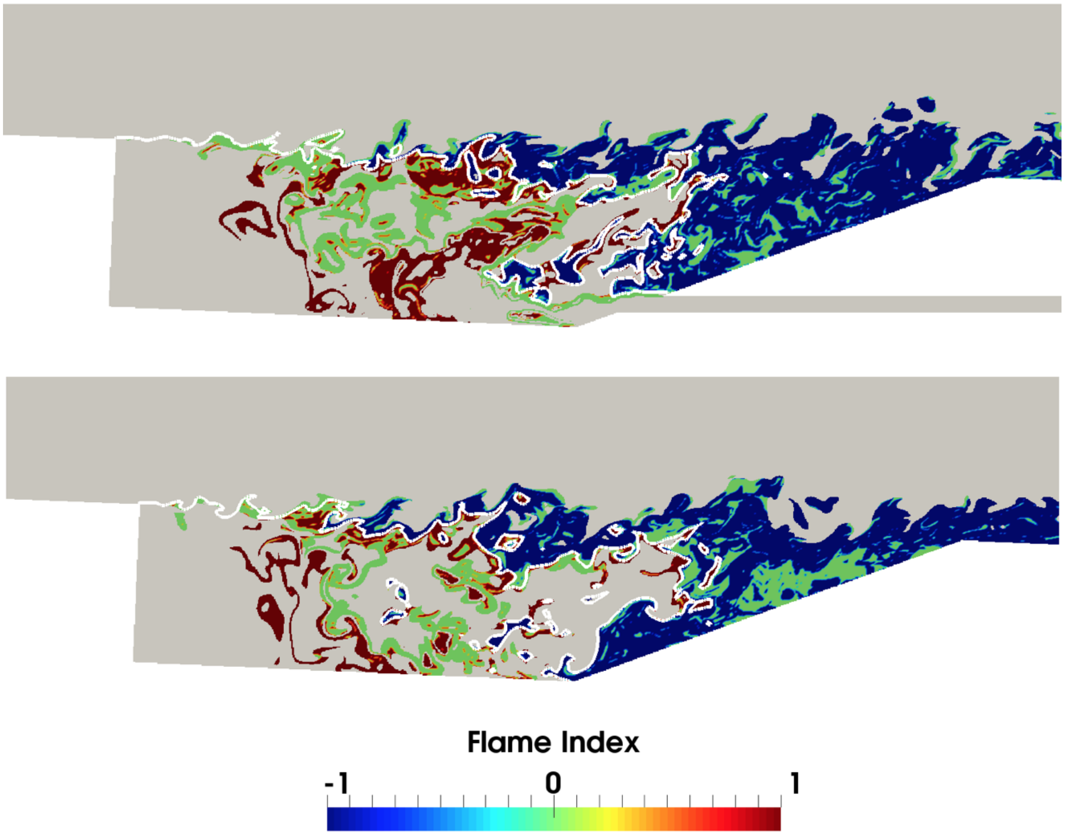

Figure 6.11: Distribution of flame index inside the cavity for injector centerplane (top) and centerplane between two injectors (bottom). -1: lean premixed, 0: nonpremixed, 1: rich premixed. The isoline $Z = Z_{st}$ is displayed with a white line. Case RFA1.

Taking in consideration only cells with $|\dot{\omega}_E| > 0.01\dot{\omega}_{E,max}$, this formulation of Y_F leads to less than 0.14% of points where $\nabla Y_F = 0$ for the fine mesh, which is negligible. Actually, the oxidizer gradient can also become zero, but in very few cells. In order not to deal with this singularity, the flame index is taken equal to 0 when the product $\nabla Y_F.\nabla Y_{O_2} = 0$. The flame index is later modified by Lock et al. [101] to include a ponderation allowing to distinguish between lean and rich combustion:

$$F.I. = \frac{1}{2}\frac{Z - Z_{st}}{|Z - Z_{st}|} \times \left(1 + \frac{\nabla Y_F.\nabla Y_{O_2}}{|\nabla Y_F.\nabla Y_{O_2}|}\right) \tag{6.3.4}$$

where Z is the mixture fraction from the Bilger et al.'s expression (Eq. 2.1.15) and Z_{st} the stoichiometric mixture fraction. This expression of flame index can become indeterminate when $Z = Z_{st}$ which is solved by stating that the factor $(Z - Z_{st})/|Z - Z_{st}| = 1$ if $Z = Z_{st}$. This assumption leaves the flame index to take the values 0 for nonpremixed flames or 1 for stoichiometric premixed flames. As discussed previously, if $\nabla Y_F.\nabla Y_{O_2} = 0$, the ratio $\nabla Y_F.\nabla Y_{O_2}/|\nabla Y_F.\nabla Y_{O_2}|$ is taken equal to zero, the flame index can be either $+0.5$ or -0.5 corresponding to the nonpremixed regions adjacent to the rich premixed and lean premixed areas respectively. The case $\nabla Y_F.\nabla Y_{O_2} = 0$ concerns less than 0.2% of points.

The flame index is displayed in Fig. 6.11 by computing solely in relevant zones where the heat release is greater than 1% of its maximum value. The inner cavity is mostly controlled by nonpremixed combustion while the premixed regime is predominant in the mixing layer and the cavity ramp. The flame index helps to determine the burning regime of the four combustion zones found with heat release rate distribution (see Fig. 5.22 of previous section). The mixing layer above the small recirculation bubble (I) and the interface between the recirculating bubbles (III) are mainly controlled by weak to moderate nonpremixed flames, while the mixing layer above the large recirculation area (II) is provided with vigorous premixed flames, rich in the region close to the middle of the cavity and lean in the area near the cavity ramp. The last combustion zone (IV), located at the exit of the injector, is composed of strong nonpremixed flames. The regions with negative heat release rate (see Fig. 5.18 to compare) located at the interface between the recirculation zones or at the exit of the injector are only featuring rich premixed combustion regime. Neither lean premixed nor nonpremixed flames can be found with negative heat release rate. Furthermore, not all nonpremixed regions are crossed by the stoichiometric line, the cavity is provided with rich nonpremixed combustion near its center and lean nonpremixed combustion at its rear. The combustion regime in the cavity is then very complex and no privileged regime can be easily extracted.

Fig. 6.12 shows the conditional mean of heat release rate by flame index $< \dot{\omega}_E \mid F.I. >$ adimensionalized by the overall mean heat release $< \dot{\omega}_E >$ (blue patterns) and the contribution of each value of flame index to the heat release C_{FI} (red histogram) defined as follow:

$$R_{FI} = \frac{< \dot{\omega}_E \mid F.I. >}{< \dot{\omega}_E >} \tag{6.3.5}$$

$$C_{FI} = R_{FI}\frac{N_{FI}}{N_T} \quad \text{with} \quad \mathrm{N_T} = \sum_{\mathrm{FI}} \mathrm{N_{FI}} \tag{6.3.6}$$

where N_{FI} is the number of points in the interval of considered flame index and N_T the total number of points. The mean heat release rate is similar for each flame index value: from $R_{FI} = 0.8$ in the nonpremixed flames to $R_{FI} = 1.1$ in the premixed flames regardless of the mixture. None of the regimes is only marked by either strong or weak combustion. Fig. 6.12 also shows that most of the contributions to the overall heat release rate come from premixed flames, over 75 %, where the lean premixed regime contribution is approximately 60 %. The contribution to the heat release rate conditionned by the flame index in each plane (y,z), along the axis x $C_{FI}(x)$ is displayed in Fig. 6.13. It shows that the front of the cavity ($x < 0.265$ m) is mainly controlled by nonpremixed combustion where approximately 100% of heat release rate is due to nonpremixed flames. In the middle of the cavity ($0.265 < x < 0.29$), premixed flames start to take place and any combustion regime can be encountered. At the rear of the cavity, the lean premixed regime predominates with over 75% of contribution to heat release rate at almost any position from $x = 0.29$ m. The remaining 25% is principally from nonpremixed flames, almost no rich premixed flames can be observed from the cavity ramp.

The flame index has also been computed and displayed in Fig. 6.14 for the medium fuel loading case (RCA1M) to investigate the combustion regime. The cavity is found to be mainly driven by nonpremixed flames. All the regions with significant heat release rate (see heat release rate snapshots in Fig. 5.35) are featuring flame index values of 0, corresponding to nonpremixed combustion. Rich premixed regime is only observed at the exit of the injector and barely at the mixing layer above the small recirculation area. The mixing layer above the large recirculation area and the cavity ramp are still controlled by premixed combustion, but only lean mixtures can be found in these zones. A lower injection velocity creates less turbulence in the cavity which makes the mixing more difficult. The decrease in fuel loading has a significant impact on the combustion regime.

6.4 Residence time

In addition to the empirical cavity residence time provided by Davis and Bowersox [35, 36] which leads to $\tau_r = 0.9$ ms in the current scramjet configuration, the residence time can be computed

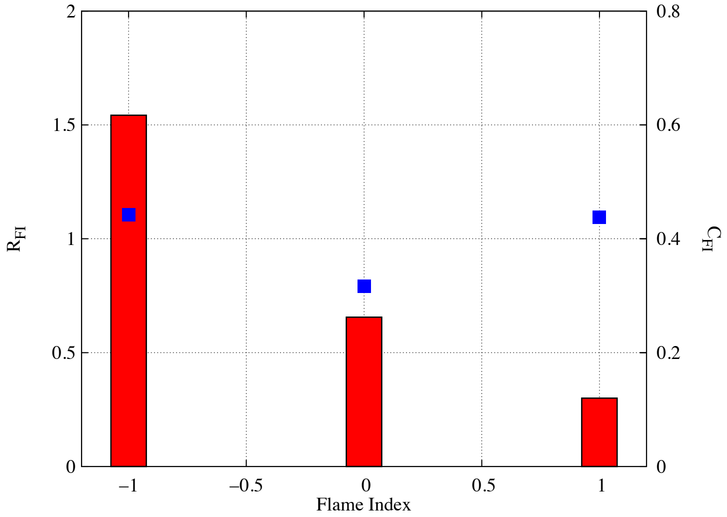

Figure 6.12: Dimensionless conditional mean of heat release by flame index R_{FI} (blue patterns), and contribution of each value of flame index to the heat release C_{FI} (red histogram).

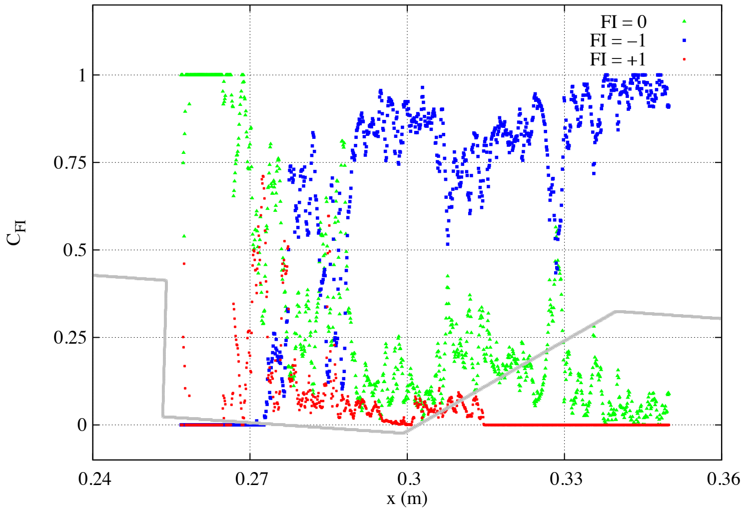

Figure 6.13: Partial contribution to the heat release C_{FI} along x for $FI = -1, 0$ or 1. The gray line represents the cavity geometry.

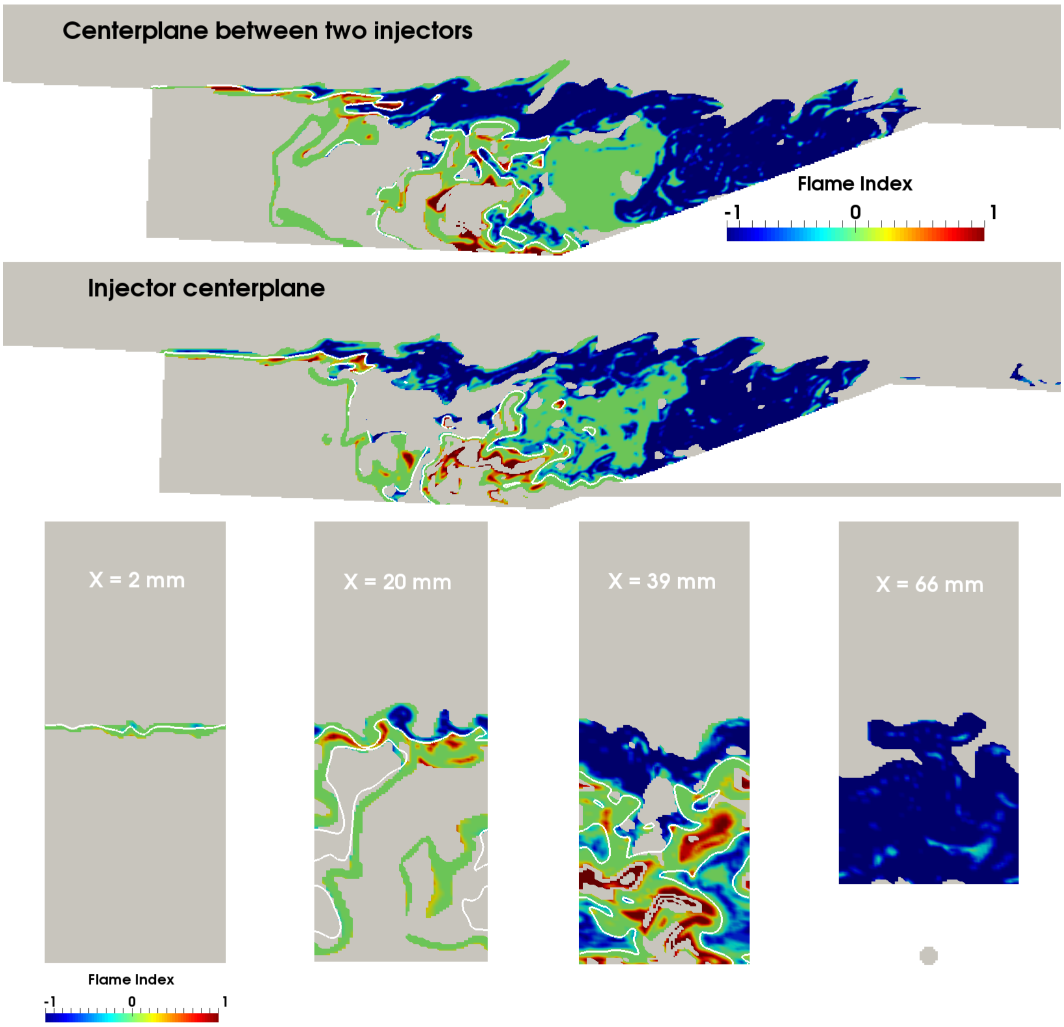

Figure 6.14: Instantaneous flame index in the centerplane between two injectors, in the injector centerplane and in four planes with constant x in the cavity. -1: lean premixed, 0: nonpremixed, 1: rich premixed. The isoline $Z = Z_{st}$ is displayed with a white line. Case RCA1M.

directly in the simulation by adding a transport equation for τ_r [49]:

$$\frac{\partial \overline{\rho}\widetilde{\tau}_r}{\partial t} + \frac{\partial}{\partial x_i}(\overline{\rho}\widetilde{u}_i\widetilde{\tau}_r) = \frac{\partial}{\partial x_i}\left[\overline{\rho}(\nu+\nu_t)\frac{\partial \widetilde{\tau}_r}{\partial x_i}\right] + \overline{\rho} \tag{6.4.1}$$

This transport equation is composed of a convective term, a diffusive term and a source term which increases the residence time by Δt at each timestep. This equation simply gives the time a particle has spent in the computational domain. For reactive systems, the regions of interest, where chemical reactions can occur, can be far from the entry, the residence time should start incrementing once the particle reaches these regions. To account for this constraint, Enjalbert et al. [49] added a factor $S_{\widetilde{Z}}$, which is dependent of the mixture fraction $\widetilde{Z}$, to the source term. The transport equation becomes:

$$\frac{\partial \overline{\rho}\widetilde{\tau}_r}{\partial t} + \frac{\partial}{\partial x_i}(\overline{\rho}\widetilde{u}_i\widetilde{\tau}_r) = \frac{\partial}{\partial x_i}\left[\overline{\rho}(\nu+\nu_t)\frac{\partial \widetilde{\tau}_r}{\partial x_i}\right] + \overline{\rho}S_{\widetilde{Z}} \tag{6.4.2}$$

The factor $S_{\widetilde{Z}}$ is equal to 1 in regions where fuel and oxidizer are mixed ($\widetilde{Z} \in [\epsilon, 1-\epsilon]$ with $\epsilon = 10^{-4}$) and 0 elsewhere. With this implementation, the residence time increments by the timestep Δt only in regions where a mixture between fuel and oxidizer exists. The residence time of the case with one injector, adiabatic walls and coarse mesh (RCA1) is displayed in Fig. 6.16 and Fig. 6.17 for instantaneous fields and in Fig. 6.18 and Fig. 6.19 for averaged fields, for the cuts in the direction z and x respectively. The isoline $\tau_r = 1$ ms is displayed in white. The results are extracted from a 6 ms physical time simulation for the instantaneous residence time, and 3 ms are used to compute statistics. The large recirculation area is featuring low residence times, from 0.8 ms to 1.2 ms, while the residence time in the small recirculation area is higher because of the lower local speed. Besides, the cavity residence time in the theory is determined by the mass exchange in the mixing layer, this time should correspond to the residence time of the lower part of the mixing layer which is around $0.8 - 0.9$ ms in this work. This value of residence time is consistent with the empirical law from Davis and Bowersox [35, 36], but also with the literature where this time is found to be approximately 1 ms in every work about scramjets.

The large recirculation area can be approximated to an ellipse of semi-major axis $a = 20$ mm and semi-minor axis $b = 7.5$ mm (see Fig. 6.15). The circumference of an ellipse C can be approximated to:

$$C \approx \pi\sqrt{2(a^2+b^2)} \approx 95 \text{ mm} \tag{6.4.3}$$

The maximum speed of the large recirculation area being in average $U_m = 250$ m/s, the time required to make a full rotation of the ellipse can be estimated to $t_{rot} = C/U_m = 0.4$ ms. The high residence time in the large recirculation area shows that the burnt gases stay about 2 to 3 full rotations in this area before leaving the cavity.

The scatter plot of residence time versus mixture fraction is displayed in Fig. 6.20 for RCA1. The highest residence time is found at $Z = 0.3$ which is the mixture fraction found in the small recirculation area. As expected, residence time close to 0 is found in regions with quasi-pure oxidizer ($Z \approx 0$) or quasi-pure fuel ($Z \approx 1$). The time required to get a mixture comprise in $Z \in [0.1, 0.5]$ is more than 0.5 ms, reaching a maximum of 0.75 ms at $Z = 0.15$. On the other hand, a stoichiometric mixture ($Z = 0.06366$) requires only 0.3 ms to be obtained, and past $\tau_r = 0.8$ ms, no stoichiometric mixture can be found. It leads to the conclusion that the stoichiometric conditions are obtained very rapidly and does not last long in the cavity (< 0.5 ms) due to intense mixing. The flammable region corresponds to a mixture comprise between $\phi = 0.4$ and $\phi = 5$. The lower flammability limit is featuring low residence times ($\tau_r = 0.15$-0.45 ms). On the other hand, the upper flammability limit can only be reached when the residence time is higher than 0.6 ms, up to 2.9 ms. The mixing

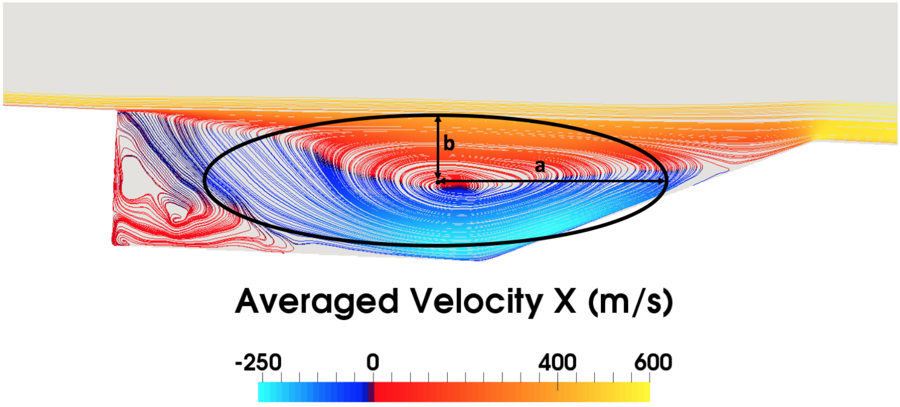

Figure 6.15: Large recirculation area modelized by an ellipse of semi-major axis $a = 20$ mm and semi-minor axis $b = 7.5$ mm.

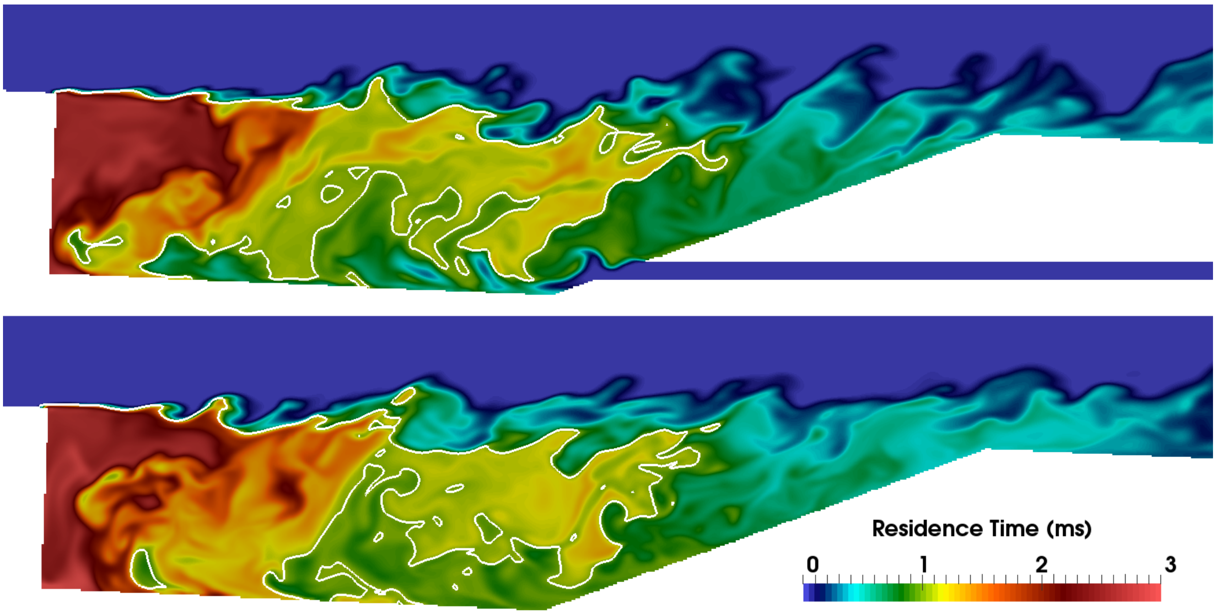

Figure 6.16: Residence time inside the cavity in the injector centerplane (top) and the centerplane between two injectors (bottom) for RCA1. The isoline $\tau_r = 1$ ms is displayed with a white line.

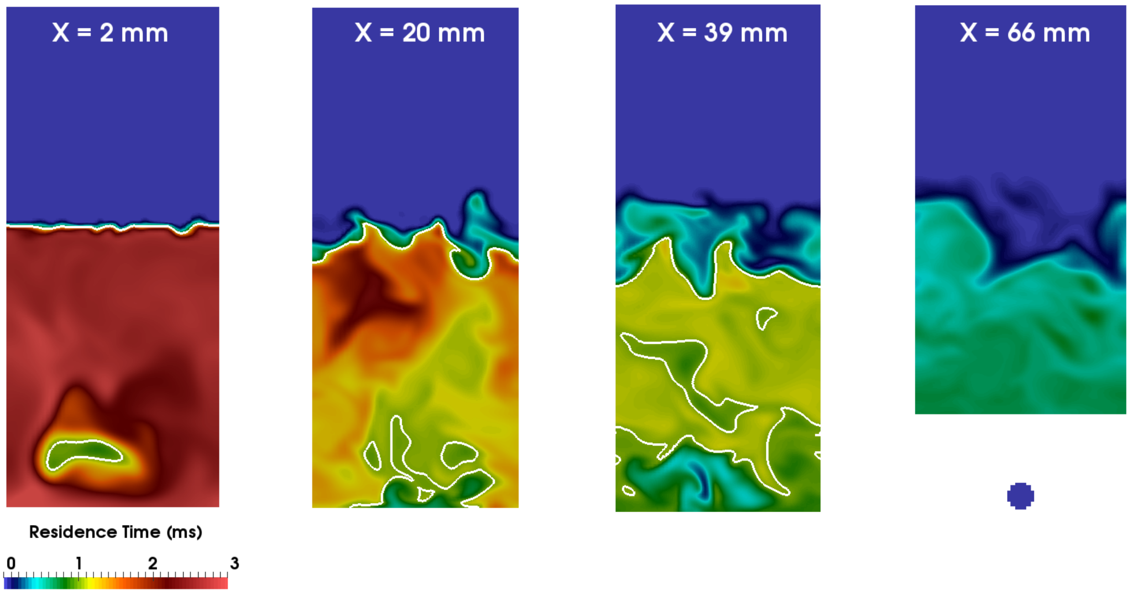

Figure 6.17: Residence time inside the cavity in planes with constant x for RCA1. The isoline $\tau_r = 1$ ms is displayed with a white line.

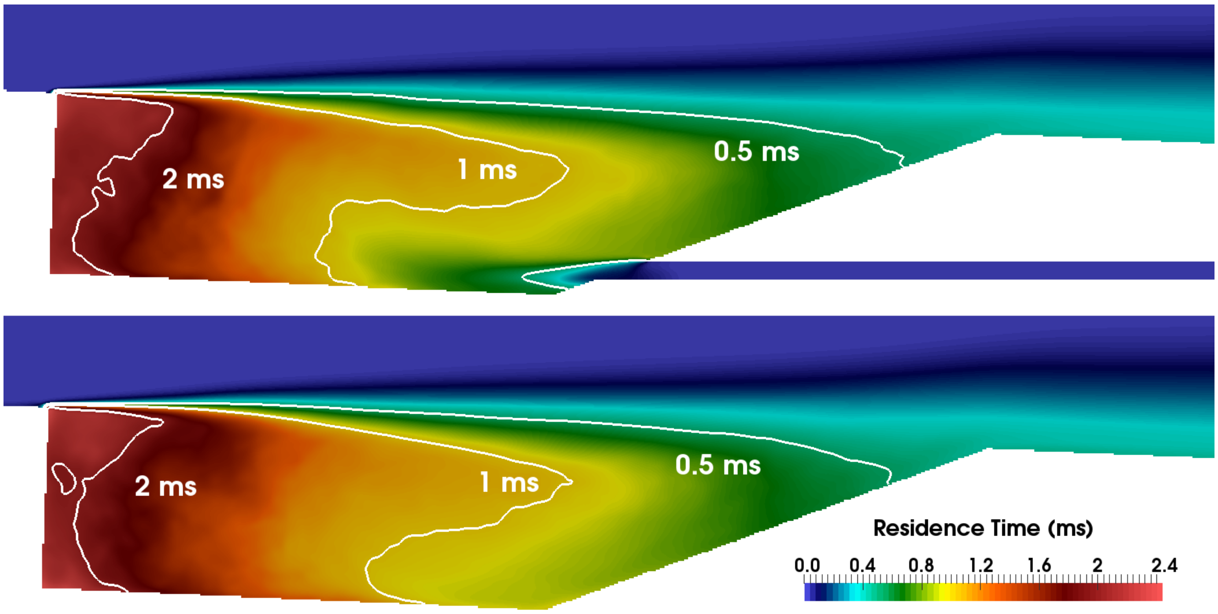

Figure 6.18: Averaged residence time inside the cavity in the injector centerplane (top) and the centerplane between two injectors (bottom) for RCA1. Isolines are displayed with white lines.

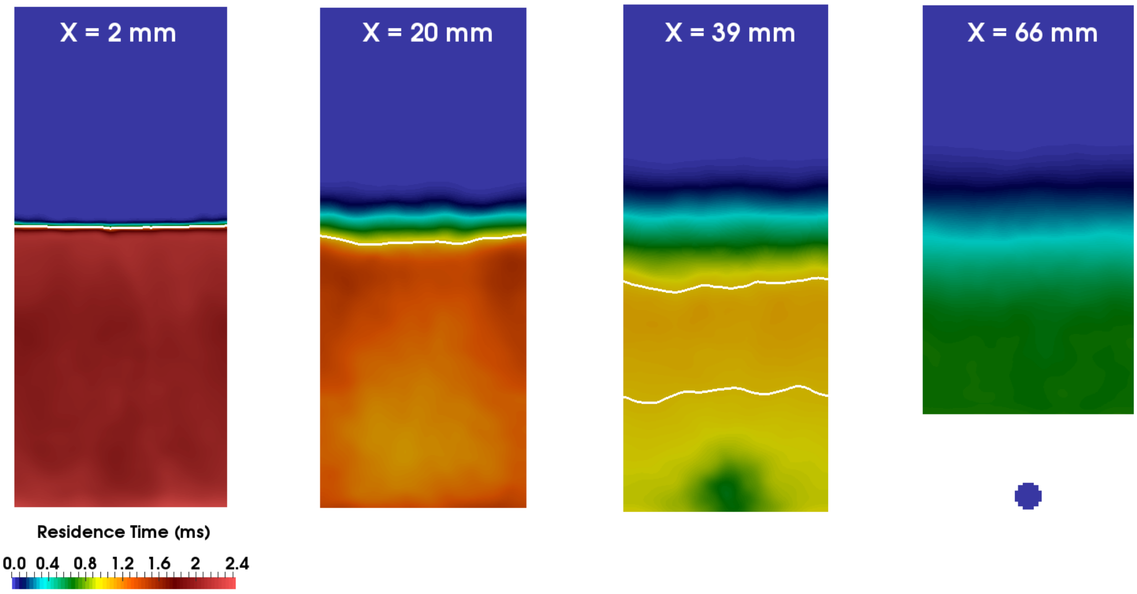

Figure 6.19: Averaged residence time inside the cavity in planes with constant x for RCA1. The isoline $\tau_r = 1$ ms is displayed with a white line.

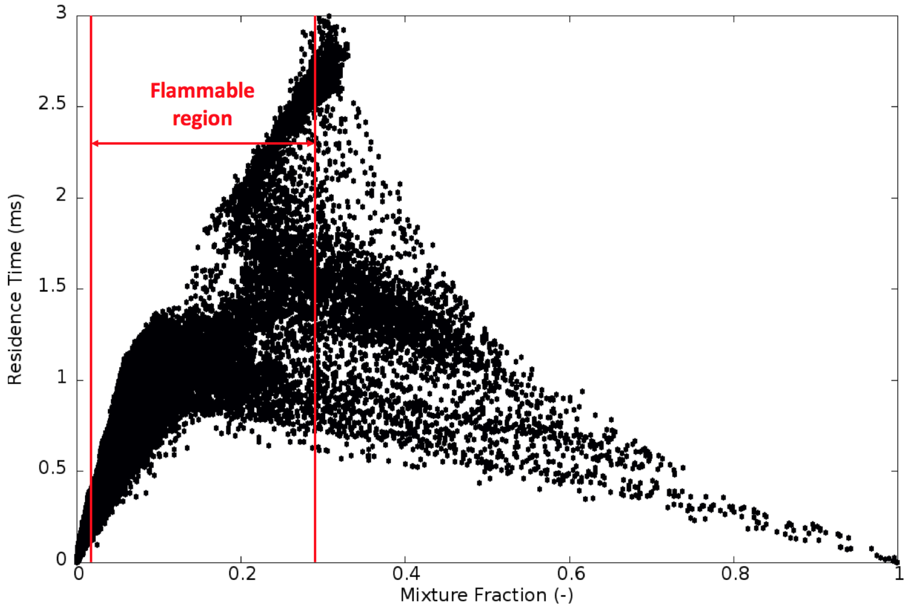

Figure 6.20: Scatter plot of residence time vs. mixture fraction for RCA1. Only 1% of points are shown. The flammability limits of ethylene are shown with red lines.

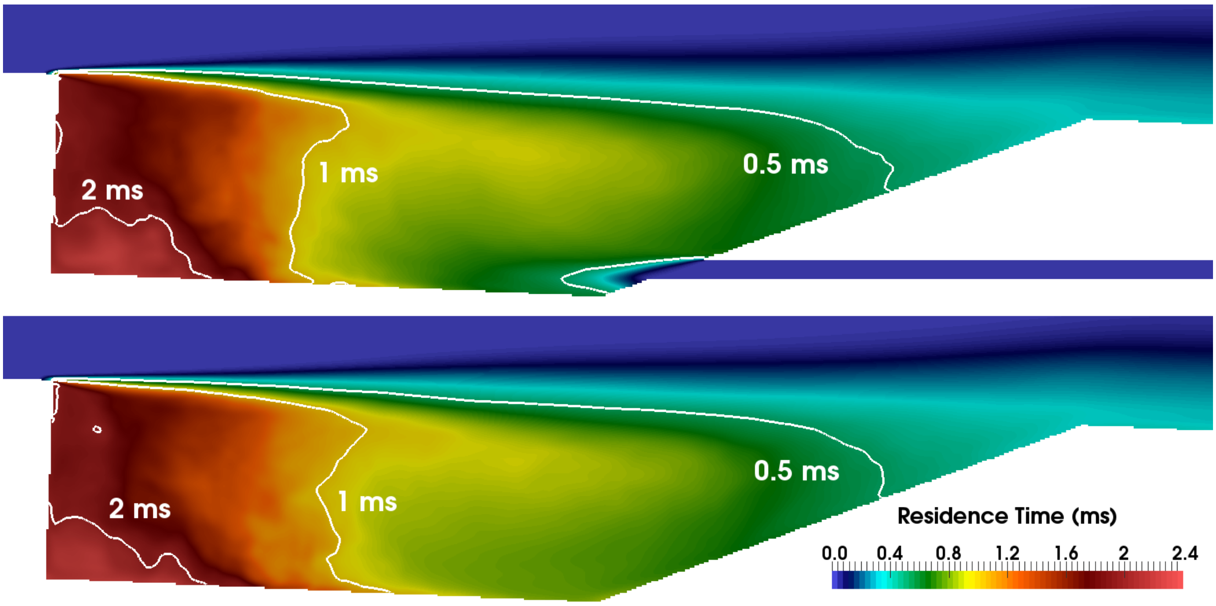

Figure 6.21: Averaged residence time inside the cavity in the injector centerplane (top) and the centerplane between two injectors (bottom) for RCI1. Isolines are displayed with white lines.

time of a mixture with equivalence ratio $\phi = 5$ is therefore reached around 0.6 ms in this cavity.

The averaged residence time of the case with isothermal wall conditions (RCI1) is displayed in Fig. 6.21 in the injector centerplane and in the centerplane between two injectors. As for the adiabatic case, the computation of RCI1 has been performed for 6 ms with the last 3 ms used for statistics. The residence time appears to be lower in the whole cavity for RCI1. The large recirculation area is featuring residence times of $0.6-0.9$ ms for RCI1 compared to $0.8-1.2$ ms for RCA1. To better quantify these differences, averaged residence time profiles inside the cavity at eight different positions are computed for RCA1 and RCI1 and displayed in Fig. 6.22. The difference at the first position ($x = 2$ mm) is only found near the mixing layer. Advancing into the cavity, the difference between RCA1 and RCI1 starts to spread through the entire depth of the cavity, with a maximum difference of 0.3 ms at the interface between the recirculation zones ($x = 20$ mm). This maximum difference decreases to 0.2 ms in the large recirculation zone ($x = 39$ mm) and to 0.1 at the cavity ramp ($x = 66$ mm). As the same cavity is used for RCA1 and RCI1, the smaller residence time of RCI1 is conveyed by larger velocity inside the cavity. Fig. 5.43 (from Sec. 5.6) showed that the streamwise velocity of RCI1 was actually slightly higher than the one of RCA1 in the mixing layer.

The dimensionless conditional mean of the heat release on residence time R_τ, and percentage of cells contributing to the statistics in each interval i of residence time $C_{\tau,i}$ have been computed in cells with heat release rate higher than 1% of maximum heat release rate, to investigate the interaction between combustion and residence time. The expressions of R_τ and $C_{\tau,i}$ are similar to R_{Ma} and $C_{Ma,i}$ of Sec. 6.2:

$$R_\tau = \frac{< \dot{\omega}_E \mid \tau_r >}{< \dot{\omega}_E >} \tag{6.4.4}$$

$$C_{\tau,i} = \frac{N_{c,\tau,i}}{N_T} \tag{6.4.5}$$

where $< \dot{\omega}_E \mid \tau_r >$ is the conditional mean of heat release rate on the residence time and $< \dot{\omega}_E >$ the mean heat release rate over the entire domain. $N_{c,\tau,i}$ is the number of cells verifying $\tau_r \in$

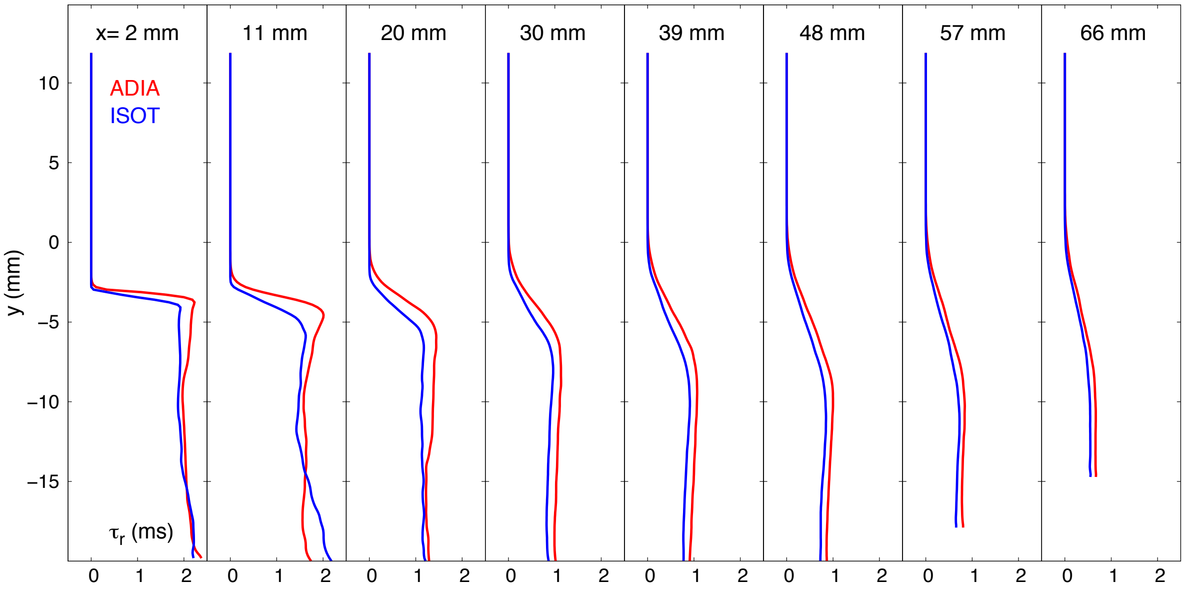

Figure 6.22: Averaged residence time profiles inside the cavity in the centerplane between two injectors: comparison between RCA1 (red) and RCI1 (blue).

$[\tau_{r_i}, \tau_{r_i} + \epsilon_\tau]$, with $\epsilon_\tau = 0.1$ ms the interval range. N_T is the total number of cells. R_τ and $C_{\tau,i}$ are displayed in Fig. 6.23 for RCA1 and RCI1. Significant combustion ($C_{\tau,i} > 0.01$) occurs in a wide range of residence time for both cases, from 0.2 to 1.3 ms for RCA1 and 0.1 to 1.1 ms for RCI1. Almost no combustion can be found in regions where τ_r exceeds 1.5 ms. Looking back at Fig. 6.18, these regions correspond actually to the small recirculation zone. The dimensionless conditional mean of the heat release on residence time R_τ indicates in both cases that the region with the highest chemical activity is featuring residence time of 0.4-0.6 ms. Such strong combustion can be found at the exit of the injector or in the mixing layer above the large recirculation area. Over a residence time of 0.6 ms, the chemical activity starts decreasing while the number of cells contributing to heat release stays relatively the same until $\tau_r = 1.1$ ms for RCA1 and 1 ms for RCI1. The region with residence time between 0.6 and 1 or 1.1 ms corresponds actually to the large recirculation area where both strong and weak combustions coexist. The largest difference between RCA1 and RCI1 lies in the interface between the recirculation areas, where the residence time of RCI1 at this region is shifted to $0.8 - 1.1$ ms instead of $1.1 - 1.3$ ms for RCA1. This difference explains the large contribution to the heat release rate of regions featuring $\tau_r = 0.8 - 0.9$ ms, 22% for RCI1 instead of 11% for RCA1.

6.5 A priori test of a tabulated approach based on 1D laminar premixed flamelets

The purpose of this section is to compare a priori the results of LES on the fine mesh with a premixed flamelet table to know if a simulation with premixed tabulated chemistry could be envisaged.

6.5.1 Chemical equilibrium

The equilibrium computations were performed with EQUIL [107]. This program is an interface between Chemkin [79] which provides species and thermodynamic data and STANJAN [138] which uses these quantities to determine equilibrium based on the minimization of Gibbs free energy. The user can specify initial mixture compositions and choose which state parameters to keep constant.

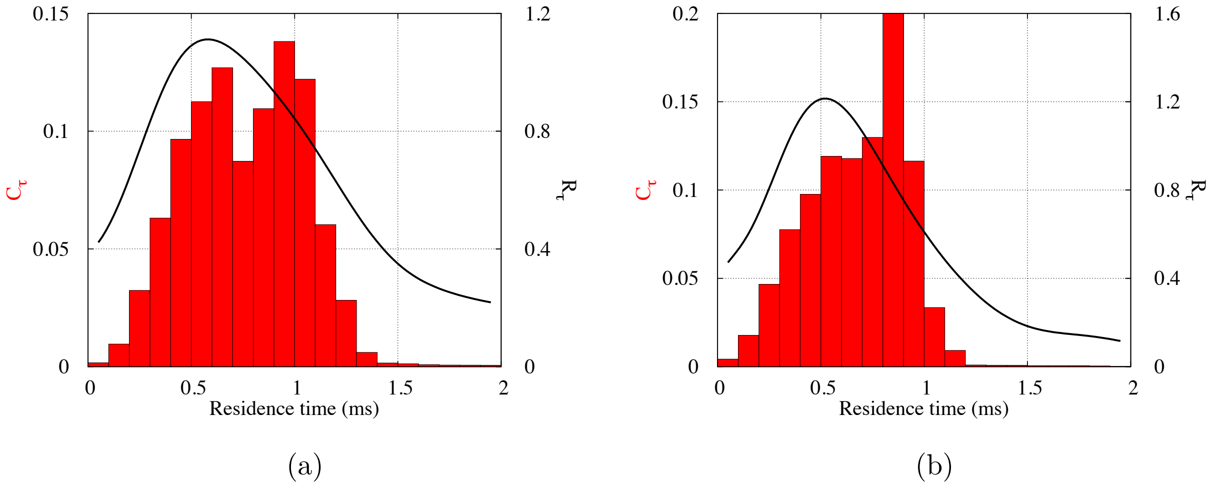

(a) (b)

Figure 6.23: Dimensionless conditional mean of the heat release on residence time R_τ (curve), and percentage of cells contributing to the statistics in each interval (0.1 ms) of residence time C_τ (histogram) for (a) RCA1 and (b) RCI1.

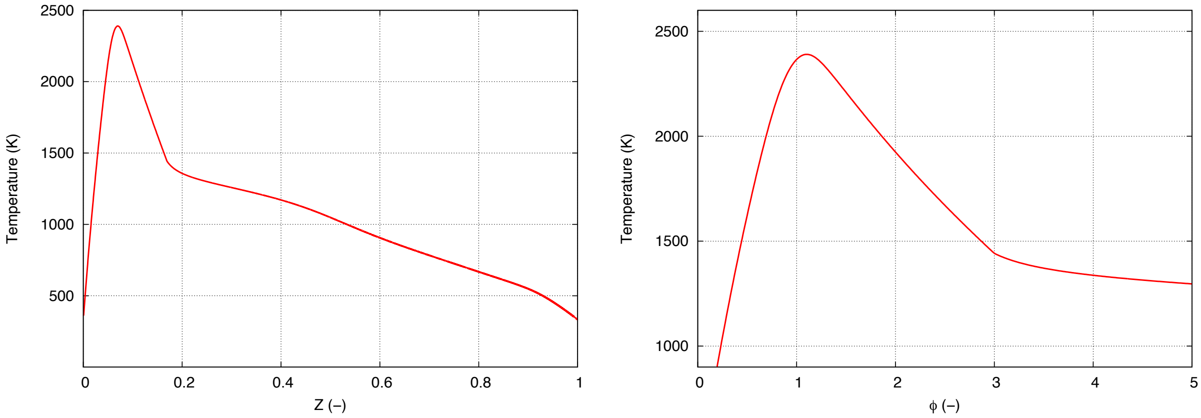

Figure 6.24: Adiabatic equilibrium temperatures: against mixture fraction (left) for $Z \in [0, 1]$, and equivalence ratio (right) for $\phi \in [0, 5]$.

In this work, pressure P and enthalpy h are kept constant for the computations. The initial molar fractions of reactants (ethylene and air) along with temperature and pressure of unburnt gas are specified in the input file of EQUIL. Computations are performed at pressure $P = 66$ kPa and temperature $T = 329$ K and 450 K, with an equivalence ratio ϕ from 0 to 500 (Z from 0 to 0.97). Solely results from the computation with $T = 329$ K are shown in this section.

The adiabatic temperature versus mixture fraction Z or equivalence ratio ϕ is displayed in Fig. 6.24. The function $\phi = f(Z)$ is plotted and shown in Fig. 6.25 to help the conversion from mixture fraction to equivalence ratio. As for the laminar flame speed shown in Sec. 5.2.3.1, the maximum adiabatic temperature, $T_{max} = 2390$ K, is found at an equivalence ratio slightly higher than the stoichiometric mixture, $\phi = 1.1$.

The main products mass fractions at equilibrium vs. the mixture fraction is displayed in Fig. 6.26. The carbon dioxide CO_2 and water H_2O can only be found at low mixture fractions ($Z < 0.17$) while the carbon monoxide CO appears from $Z = 0.07$ and reaches its maximum at $Z = 0.17$ ($\phi = 3$). The progress variable will be constructed from a combination of main products concentrations. Their mass fractions at equilibrium will be used to adimensionalize the progress variable or

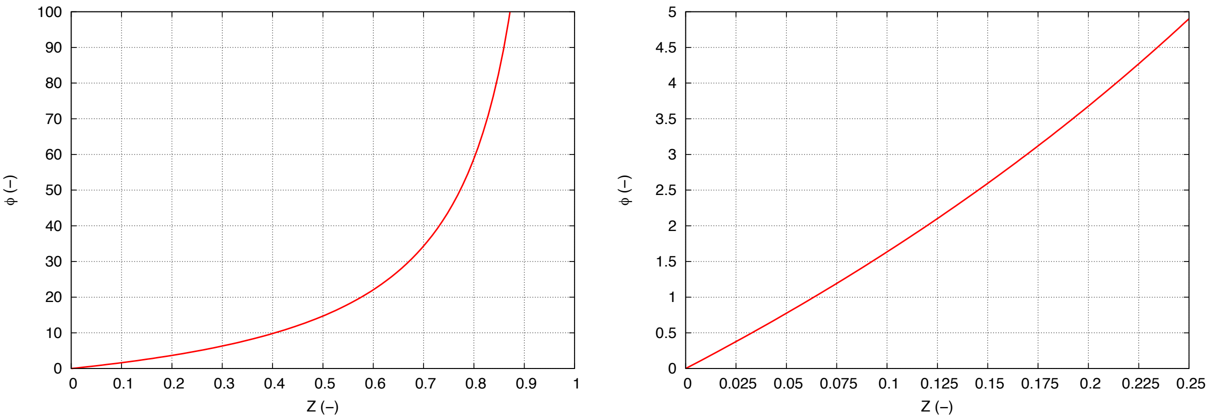

Figure 6.25: Equivalence ratio ϕ vs. mixture fraction Z for $Z \in [0, 1]$ (left) and $Z \in [0, 0.25]$ (right).

to extend the premixed table outside the flammability limits.

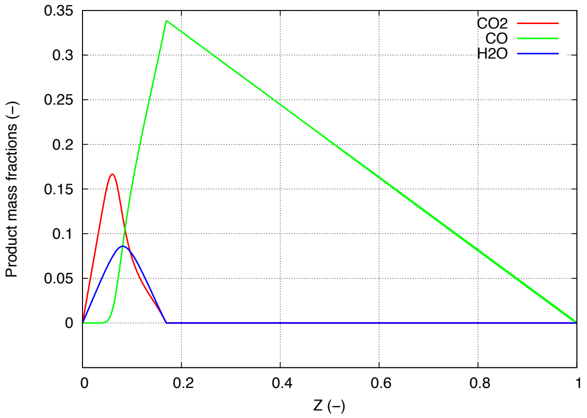

Figure 6.26: Mass fractions at equilibrium for main products of ethylene-air combustion.

6.5.2 One dimensional laminar premixed flames

One dimensional laminar premixed flame propagations were computed with the solver REGATH [19] presented in section 5.2.3.1, at $P = 66$ kPa and $T = 329$ K in the flammability limits range of ethylene, which is $\phi \in [0.4, 5]$, and in a distance of 10 meters. The purpose of this study is not to reach equilibrium with 1D flame propagation which in some cases require a computational domain of hundreds of kilometers, but to build a laminar premixed flame table which contains all the possible solutions of the LES. Therefore, the last point of each flamelet is in general not the equilibrium state.

Fig. 6.27 shows the comparison between the temperature of the last point in REGATH and the adiabatic temperature from EQUIL. The difference between REGATH and EQUIL becomes meaningful at rich mixtures, from $\phi = 2.4$, reaching a peak of $\Delta T = 110$ K at $\phi = 3$, then decreases at very rich mixtures. This gap is due to the size of computational domain of REGATH which is not long enough for the flame to reach equilibrium for rich conditions.

The temperature profiles of laminar premixed flames at different equivalence ratios are displayed in Fig. 6.28. Superadiabatic temperature (SAT) phenomenon can be observed for high equivalence ratios and is identified by a temperature peak in the flame front which is higher than the adiabatic temperature. This phenomenon is only present in hydrocarbon flames at rich mixtures and has been investigated numerically and experimentally by Liu et al. [98] for C1-C3 hydrocarbons and numerically by Meeks et al. [111] for CH_4 and C_2H_2. Aside from the temperature peak, SAT is also

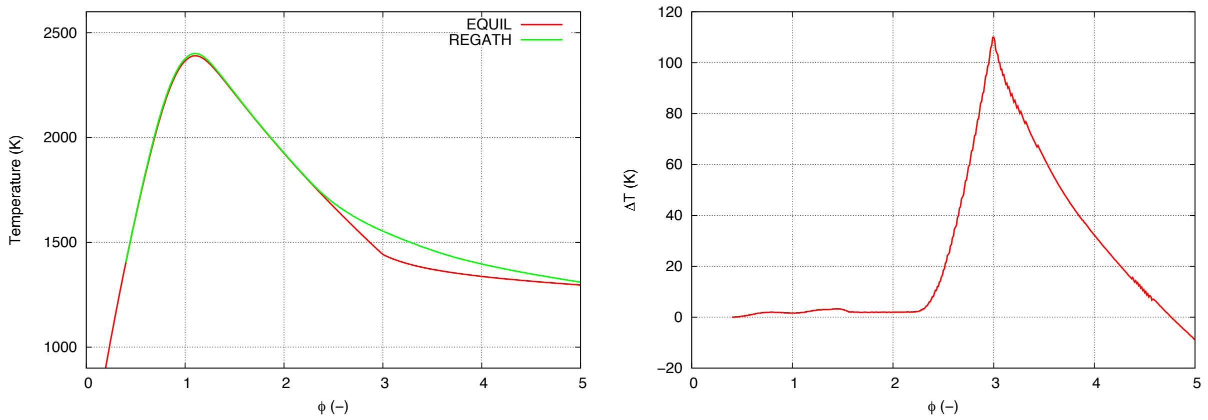

Figure 6.27: Comparison between adiabatic temperature (EQUIL) and one dimensional laminar premixed flame temperature (REGATH) at $x = 10$ m. $\Delta T = T_{REGATH} - T_{EQUIL}$.

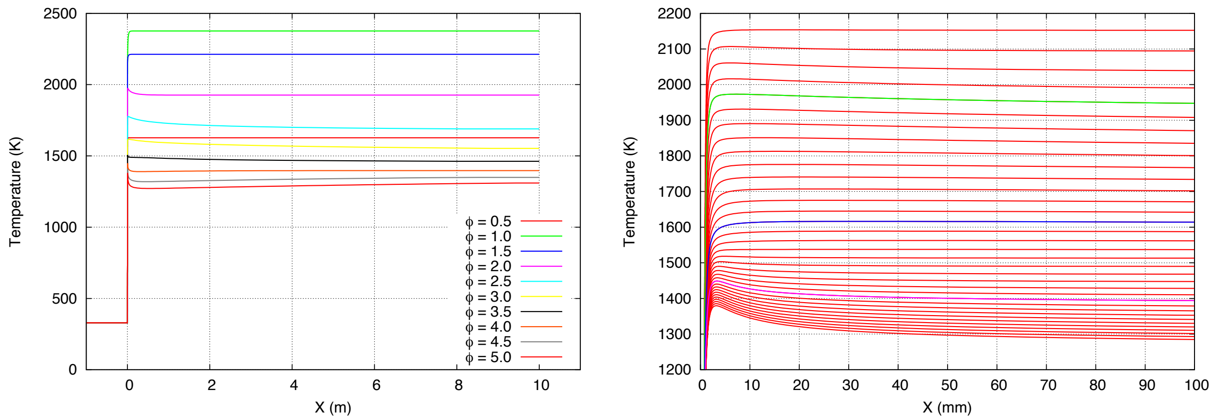

Figure 6.28: Temperature profiles from REGATH at several equivalence ratios: $\phi \in [0.4, 5]$ (left) and at rich compositions: $\phi \in [1.6, 5]$ (right). For sake of clarity, on the right hand side figure, the green line (—) represents $\phi = 2$, blue line (—) for $\phi = 3$ and purple line (—) for $\phi = 4$.

associated with superequilibrium concentrations of some combustion products and with negative heat release rate (endothermic reactions). Meeks et al. [111] believe that SAT phenomenon is due to high gas velocities in the burning region at high equivalence ratios, while Babkin et al. [2] pointed out that SAT generally occurs due to competition between molecular diffusion and heat transfer processes. The right hand side figure of Fig. 6.28 is a close view of the temperature profiles for equivalence ratio ϕ from 1.6 to 5. In the case of ethylene-air combustion, SAT can be observed from $\phi = 1.7$ with a slight temperature peak until $\phi = 3.5$. As the equivalence ratio increases, the peak becomes stronger in the flame region, but as the burnt gas temperature is increasing along x for high equivalence ratios, the difference between the superadiabatique temperature and adiabatic temperature find its maximum at $\phi = 3$ (See. Fig. 6.29).

The difference between the maximum temperature and the temperature at the last point of REGATH solution $\Delta T_1 = T_{max,REGATH} - T_{x=10m,REGATH}$ is compared to the difference to adiabatic temperatures $\Delta T_2 = T_{max,REGATH} - T_{EQUIL}$ and displayed on Fig. 6.29. This figure shows two phenomena identified previously: the change in slope at approximately $\phi = 1.6$ indicates the appearance of superadiabatic temperature; and the disparity between ΔT_1 and ΔT_2 increasing highly above $\phi = 2.4$ reveals that the REGATH solutions are far from equilibrium at these equivalence ratios.

In order to reduce the strong disparity between REGATH and EQUIL at high equivalence ratios, the computational domain of 1D laminar premixed flames has been extended to 5 kilometers for $\phi = 4$.

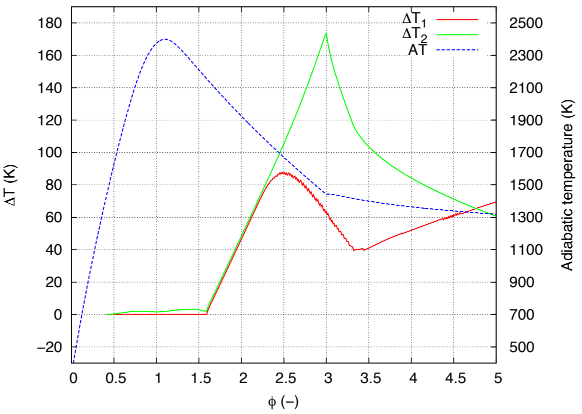

Figure 6.29: Temperature difference between the maximum temperature of the flamelet and respectively the last point of the 1D laminar premixed flame solution: ΔT_1 and the adiabatic temperature: ΔT_2. The adiabatic temperature (AT) of S22 is displayed with dashed line.

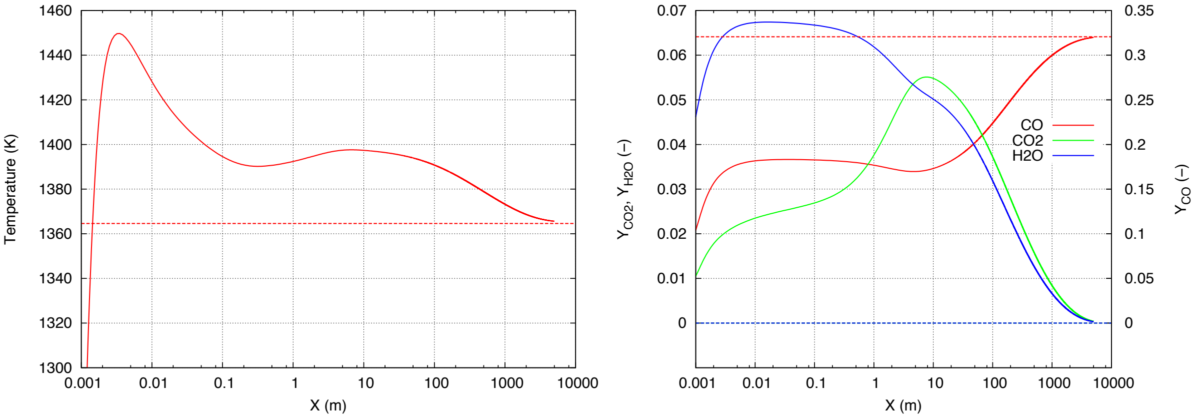

Figure 6.30: Temperature (left) and main product mass fractions (right) along X for $\phi = 4$. The dashed line represents the equilibrium value.

The temperature profile and main product mass fractions are shown on Fig. 6.30. The behaviour of the curves at $X = 10$ m and 5 km is completely different. The evolution of the main products is very slow and requires about 5 km to reach equilibrium at $\phi = 4$ and even more for higher equivalence ratios. As the purpose of this study is not to run tabulated chemistry simulations, but to compare a posteriori the LES results with laminar premixed flame table, we need to know whether the table built with $X_{max} = 10$ m is enough to contain all the LES points, or if further refinements need to be done in some regions.

6.5.3 Expressions of progress variable

The definition of progress variable is a key point in tabulated chemistry and is not straightforward. It is defined as the ratio of local species mass fractions on the same quantity at equilibrium:

$$C = \frac{Y_C}{Y_{C,eq}} \tag{6.5.1}$$

So the progress variable C takes value in $[0, 1]$, with the extrema 0 and 1 corresponding respectively to fresh gases and burnt gases at equilibrium. Y_C can be defined either from the reactants and N_2 or from some major combustion products chosen carefully. In this work, we will be only interested

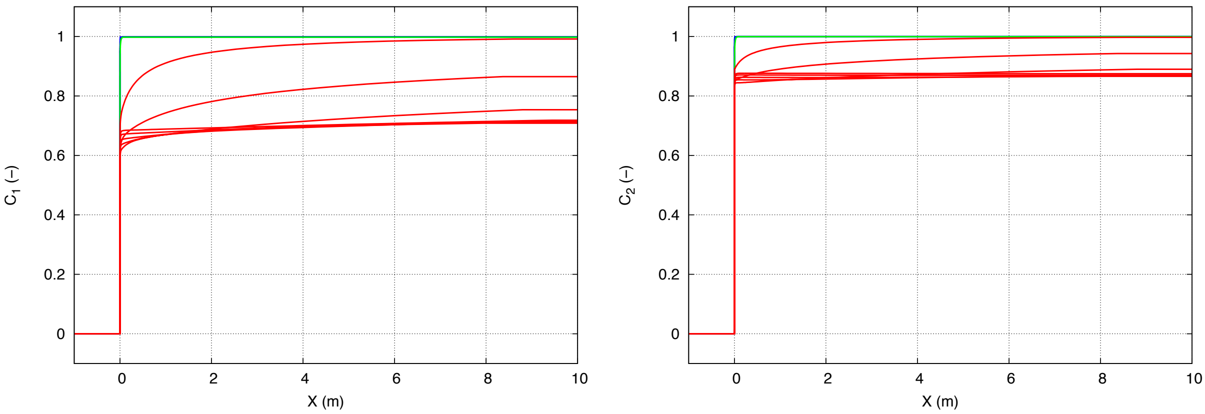

Figure 6.31: Progress variables C_1 (left) and C_2 (right) in physical space at equivalence ratio $\phi \in [0.4, 5]$: blue, green and red colors correspond respectively to lean, stoichiometric and rich mixtures.

in building the progress variable from the main products of ethylene-air combustion. Therefore, Y_C will be constructed with Y_{CO}, Y_{CO_2} and Y_{H_2O}. Two expressions of Y_C are studied and compared:

$$\begin{aligned} Y_{C1} &= Y_{CO} + Y_{CO_2} \\ Y_{C2} &= Y_{CO} + Y_{CO_2} + Y_{H_2O} \end{aligned} \tag{6.5.2}$$

The mass fractions at equilibrium could be taken from the 1D laminar premixed flame results if they are not far from the equilibrium, which is not the case in this study at high equivalence ratios. Thus, mass fractions from EQUIL are used to compute $Y_{C,eq}$, in order to avoid discontinuities when prolongating the flame library outside the flammability limits. The construction of progress variable needs to satisfy two conditions:

(I) the progress variable C must be a monotonically increasing function of the physical coordinate X

(II) all tabulated quantities must be injective functions of the progress variable C

The verification is done for $\phi \in [0.4, 5]$ in Fig. 6.31 for (I) and in Fig. 6.32 for (II).

6.5.4 Construction of laminar premixed tables

Laminar premixed flame tables are generally constructed from 1D flames within the flammability limits and may be extended to all equivalence ratios by interpolation between fresh gases and equilibrium state. The advantage of using REGATH is that the solver can compute flames outside of the flammability limits, thus reducing the prolongation by interpolation which is not always appropriate. This method has already been investigated by Duboc et al. [41, 40] for methane-air combustion by extending the table to $\phi = 5.5$ (the flammability domain of methane-air is $\phi \in [0.6, 1.4]$). The results were found to be more convincing than prolongation with equilibrium values. Here, the 1D flame simulations with REGATH have therefore been extended from $\phi_{max} = 5$ to 50 at $P = 66$ kPa and $T = 329K$ with a computational domain of 10 meters long. The flame speed and the thermal flame thickness are displayed on Fig. 6.33. The highest speed and the lowest thickness are found for $\phi = 1.17$ and worth respectively $s_{L,max} = 88$ cm/s and $\delta_{L,min} = 0.38$ mm at these conditions.

Tables are created at $P = 66$ kPa and $T = 329$ K for both expressions of progress variable with $\Delta C = 0.002$ and for $\phi \in [0.4, 50]$ ($Z \in [0.0265, 0.773]$) with $\Delta\phi = 0.01$ and extended to the whole range of Z by prolongation with equilibrium data of S22. Scatter plot of progress variables (C_1

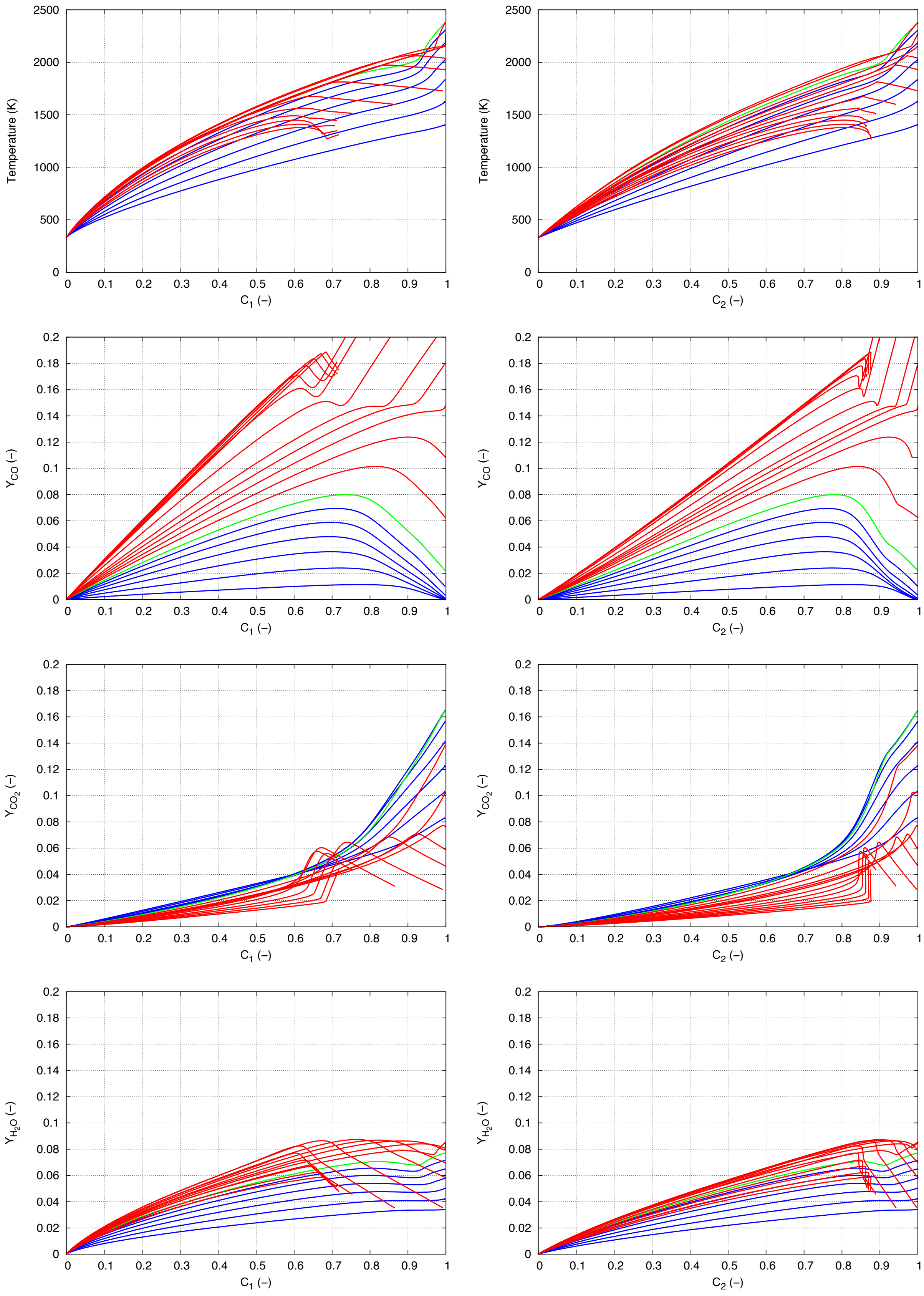

Figure 6.32: Tabulated temperature and major combustion product mass fractions against progress variables C_1 (left) and C_2 (right) at equivalence ratio $\phi \in [0.4, 5]$: blue, green and red colors correspond respectively to lean, stoichiometric and rich mixtures.

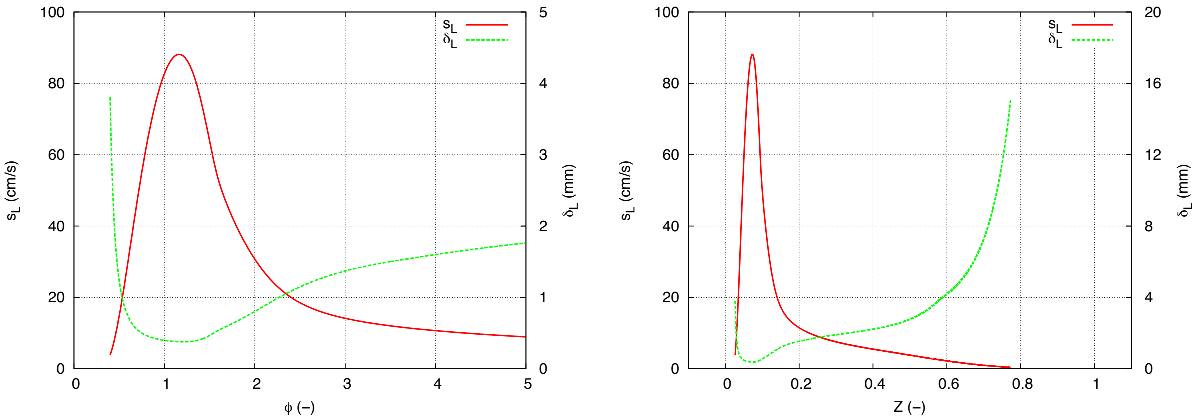

Figure 6.33: Laminar premixed flame speed (——) and thickness (- - - -) within the flammability limits (left) and in the whole computed range of equivalence ratios (right).

and C_2) versus mixture fraction Z of LES results are shown in Fig. 6.34. Each point is displayed with a color representing the intensity of heat release rate: blue for negative values and the shading from purple to yellow for low to high values. The region with negative heat release rate corresponds to the area with SAT (see Sec. 6.5.2), reactions are endothermic in this region in order to tend towards adiabatic temperature. The highest heat release rates are, as expected, found near the stoichiometric mixture ($Z = 0.06366$).

The red curve on Fig. 6.34 represents the last point ($X = 10$ m) of each flamelet, as C is an injective function of X, $C(X = 10 \text{ m}) = \mathrm{C}_{\max}$, which means that all points below this curve are tabulated. There is a small region near $Z = 0.1$ where the progress variable is superior to 1. That phenomenon occurs only when the progress variable is not well defined, since one or several major species are missing to describe correctly this region, or when the number of points is not representative, the phenomenon of $C > 1$ can be due to diffusion. The expression C_1 is therefore not valid in this study since the number of points with $C > 1$ is huge compared to C_2 where less than 0.003% of cells are concerned. The table based on C_1 is consequently discarded, and C_2 is renamed as C in the following.
Besides, the red curve starts to fall down for $Z > 0.57$ ($\phi > 19.5$) and goes under the LES results for $Z > 0.6$, which means that the table does not contain those points. It needs to be extended to include higher progress variables. The prolongation can be done by interpolating between the last point of the flame and the equilibrium data, or by extending the computational domain in that region. The second technique is preferred in this work. The 1D computational domain has been extended to 1 km for $Z > 0.57$ until $Z = 0.835$, because a longer domain is required for higher mixture fraction. The new curve is represented in green color on Fig. 6.34.

At this stage, we would like to know whether the prolongation outside the flammability limits with non-propagating 1D flame (REGATH) gives more consistent results than the one with equilibrium prolongation. Three tables with different prolongations were built and compared to investigate that question. Their characteristics are shown in Tab. 6.2. As the temperature inside the cavity is not constant and is always inferior to 450 K, a fourth table (TAB2b) was constructed at 450 K and 66 kPa to investigate the impact of the fresh gases temperature on the results. The flamelet libraries are displayed on Fig. 6.35.

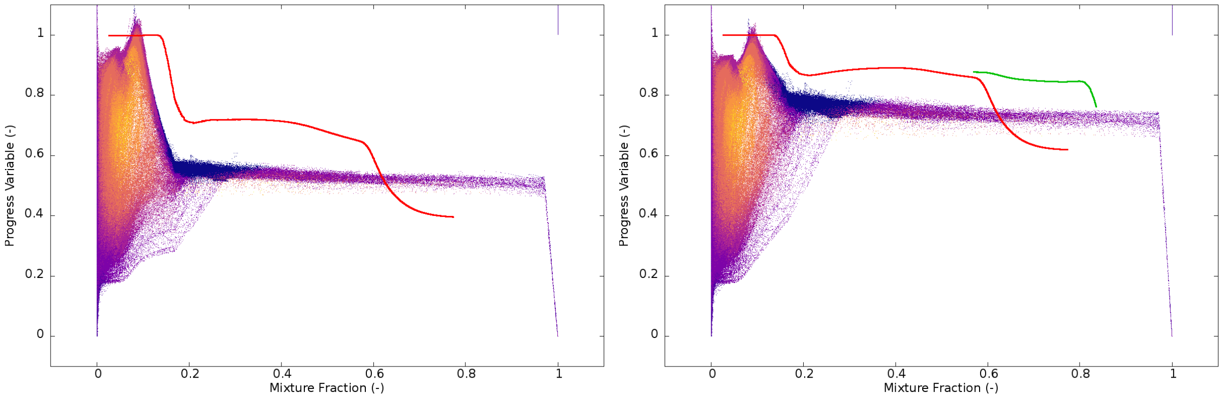

(a) (b)

Figure 6.34: Scatter plot of progress variables C_1 (a) and C_2 (b) vs. mixture fraction: blue color refers to negative heat release rate, the shading from purple to yellow represents cells with low to high heat release rate. The curves show the maximum value of tabulated progress variable for a given composition $C_{max}(Z)$ with a 1D computational domain of 10 m for red color and 1 km for green color.

Table	**1D Flame for ϕ in**	**Prolongation for ϕ in**	**Temperature (K)**
TAB1	$[0.4, 5]$	$[0, 0.4[\cup]5, +\infty[$	329
TAB2	$[0.4, 19.5]$	$[0, 0.4[\cup]19.5, +\infty[$	329
TAB2b	$[0.4, 19.5]$	$[0, 0.4[\cup]19.5, +\infty[$	450
TAB3	$[0.4, 74.5]$	$[0, 0.4[\cup]74.5, +\infty[$	329

Table 6.2: Constructed table features, $P = 66$ kPa.

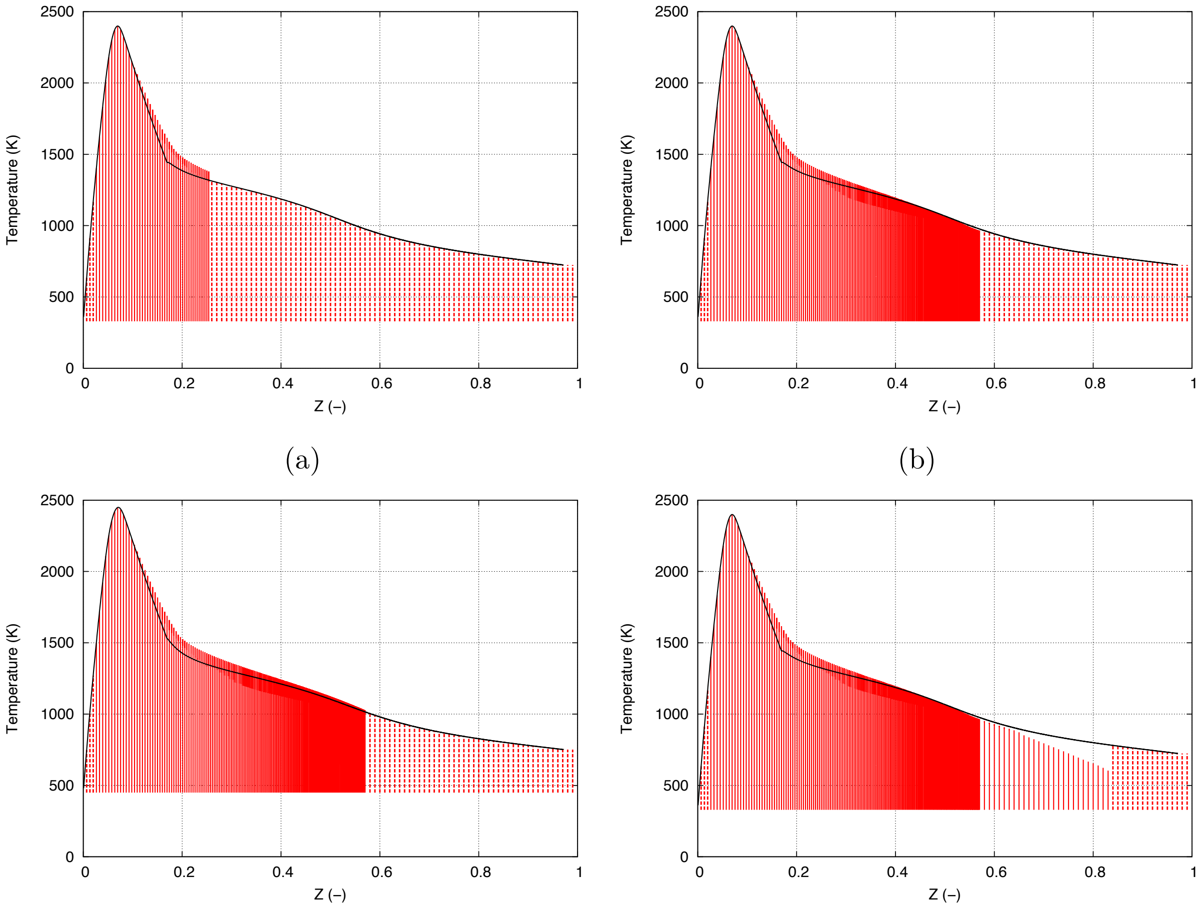

(a)

(b)

(c)

(d)

Figure 6.35: Laminar premixed flamelet libraries: (a) TAB1, (b) TAB2, (c) TAB2b, (d) TAB3. Tabulated (—), interpolated (- - -).

6.5.5 A priori comparison with LES field

The a priori comparison is done on an instantaneous field for an adiabatic computation with one injector (RFA1). The interpolation of the table data into the computational domain has been performed in the following way:

- First, the mixture fraction Z and the progress variable C are computed using the gas composition from the LES Y_k.
- Then, using Z and C computed previously, the corresponding value of each tabulated quantity φ_{tab} is extracted.

In the few locations where $C > 1$ possibly due to diffusion, the values are taken at $C = 1$. Z (resp. C) computed from the LES is generally not equal to a value Z_{tab} (resp. C_{tab}) of the table, Z (resp. C) is therefore bounded by closest upper and lower values of the table $Z_{tab,U}$ and $Z_{tab,L}$ (resp. $C_{tab,U}$ and $C_{tab,L}$). A linear interpolation between values $\varphi_{tab,L}$ and $\varphi_{tab,L}$ at $Z_{tab,U}$ and $Z_{tab,L}$ is performed to find the value φ_{tab} at Z:

$$\varphi_{tab} = (1 - \lambda_Z)\varphi_{tab,L} + \lambda_Z \varphi_{tab,U} \tag{6.5.3}$$

where λ_Z is the distance ratio between Z and $Z_{tab,L}$ defined as:

$$\lambda_Z = \frac{Z - Z_{tab,L}}{Z_{tab,U} - Z_{tab,L}} \tag{6.5.4}$$

The same interpolation is done for C, and finally, we get for any tabulated quantity φ_{tab}:

$$\begin{aligned}\varphi_{tab} =& (1 - \lambda_Z)\left[(1 - \lambda_C)\varphi_{Z_{tab,L},C_{tab,L}} + \lambda_C \varphi_{Z_{tab,L},C_{tab,U}}\right] \\ &+ \lambda_Z \left[(1 - \lambda_C)\varphi_{Z_{tab,U},C_{tab,L}} + \lambda_C \varphi_{Z_{tab,U},C_{tab,U}}\right]\end{aligned} \tag{6.5.5}$$

The comparison has been done for the temperature and the main products mass fractions (Y_{CO}, Y_{CO_2}, Y_{H_2O}). The instantaneous mixture fraction and progress variable for the case RFA1 are displayed in Figs. 6.36 and 6.37 respectively. As we discussed in Sec. 5.3, the mixture is very rich at the front of the cavity ($Z > 0.2$), and lean to moderately rich in the large recirculation area ($Z \in [0.03, 0.1]$), except at the exit of the injector where the mixture fraction is expected to have very high values. On the other hand, the progress variable is globally high in the whole cavity with $C > 0.7$. Values of C higher than 0.9 are found in the large recirculation area, while the small recirculation area is having much smaller values of progress variable $C \approx 0.75$. This result is actually expected, since the time required to reach equilibrium increases strongly with great values of mixture fraction. A very rich mixture would naturally get lower progress variables than a mixture close to the stoichiometric value.

The instantaneous temperature field is displayed in Fig. 6.38 for cuts in the spanwise direction (z) and in Fig. 6.39 for cuts in the streamwise (x) and the transverse (y) directions for LES results and laminar premixed table (TAB2) interpolations. The z-cuts are still taken at the injector centerplane and the centerplane between two injectors. The first y-cut is localized in the mixing layer, while the second corresponds to the middle line of the cavity. The x-cuts are from the interface between the recirculation zones ($x = 20$ mm from the cavity front) and the middle line of the large recirculation area ($x = 39$ mm). At the first glance, temperatures from LES and TAB2 appear very close to each other. The only noticeable difference lies in the small recirculation area where TAB2 underpredicts the temperature.

In order to better quantify the discrepancies detected in the instantaneous temperature fields, values at eight positions inside the cavity with constant x are picked up. These positions are the same as

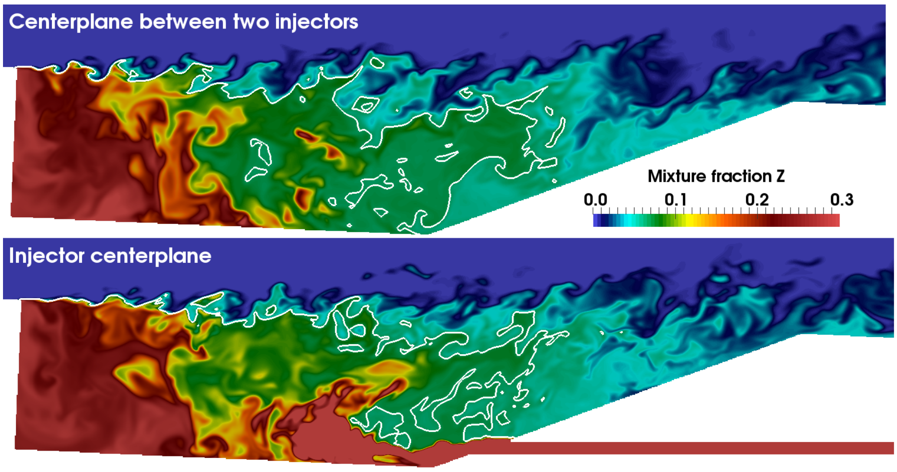

Figure 6.36: Instantaneous field of mixture fraction inside the cavity: centerplane between two injectors (top) and injector centerplane (bottom). The stoichiometric line is displayed in white color.

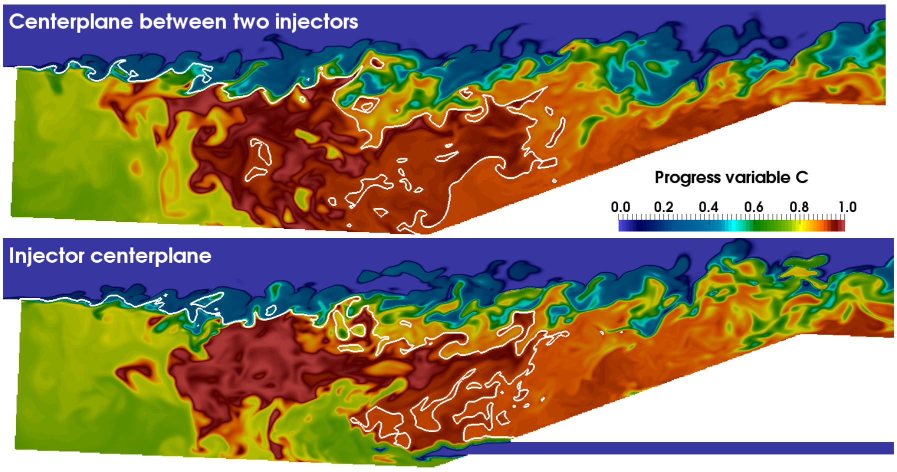

Figure 6.37: Instantaneous field of progress variable inside the cavity: centerplane between two injectors (top) and injector centerplane (bottom). The stoichiometric line is displayed in white color.

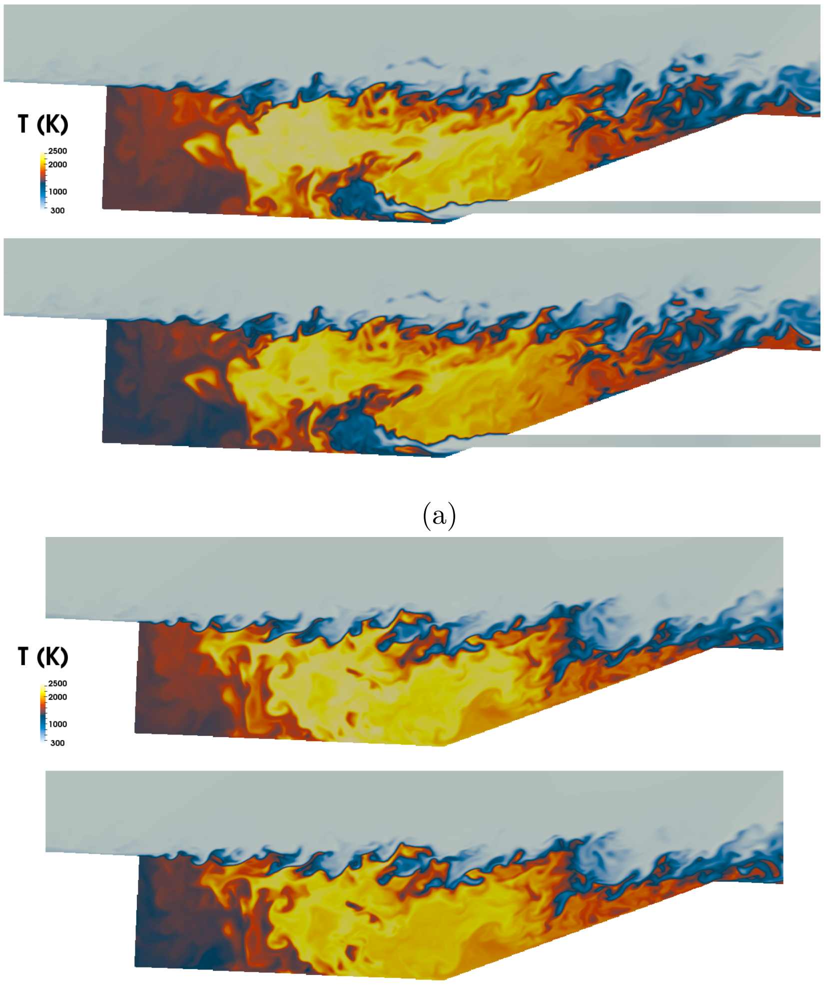

(a)

(b)

Figure 6.38: Temperature comparison with LES results at injector centerplane (a) and centerplane between two injectors (b): LES (top), TAB2 (bottom)

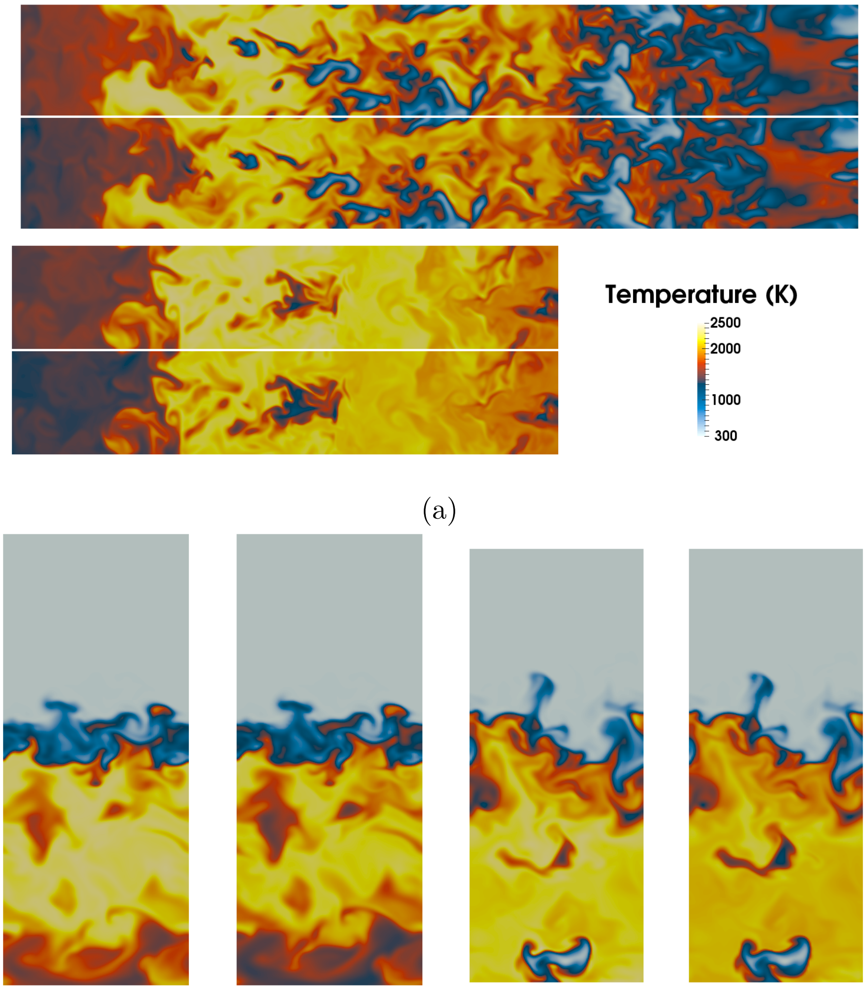

(a)

(b)

Figure 6.39: Temperature comparison with (a) constant y cuts at mixing layer ($y = -7$ mm) and middle line of the cavity ($y = -14$ mm): from top to bottom, LES, TAB2 at $y = -7$ mm, then LES, TAB2 at $y = -14$ mm; and (b) constant x cuts at the interface of the recirculation zones ($x = 20$ mm from the cavity front) and the middle of the large recirculation area ($x = 39$ mm): from left to right LES, TAB2 at $x = 20$ mm, then LES, TAB2 at $x = 39$ mm.

those used for the velocity profiles which are: $x = 2$, 11, 20, 30, 39, 48, 57, 66 mm from the cavity front. The mixture fraction and the progress variable profiles are first displayed in Fig. 6.40. The variation of the mixture fraction is quite small in the cavity, except at the interface between the recirculation areas where Z is found to oscillate a lot. The progress variable is following the same trend as the mixture fraction, except that its variation at the mixing layer is quite important.

The temperature and the H_2O mass fraction profiles for TAB1, TAB2 and TAB3 are displayed in Fig. 6.41 and compared to the LES values in the injector centerplane. Readers are reminded that the only difference between these three tables is the way the prolongation outside the flammability limits was done (see Tab. 6.2 of the previous section). TAB1 has some shortcomings in predicting the temperature or the H_2O mass fraction outside the flammability limits. The two other tables do not have this issue and have very similar results. The only difference between TAB2 and TAB3 lies in a small region at the exit of the injector where TAB3 has more accurate results. This analysis shows that table prolongation with data from equilibrium state is not very consistent in the current simulation and it is preferable to compute (when it is possible) and use 1D laminar premixed flames outside the flammability limits. Compared to the LES, the temperature from the table is weaker at the front of the cavity by about 100 K, and in regions with strong variations of mixture fraction where the discrepancy can reach 200 K. The differences in H_2O mass fraction are linked to the difference in temperature.

A comparison between TAB2 and TAB2b has been performed to investigate the impact of initial temperature of the laminar premixed flame tables. Again, temperature and H_2O mass fraction are displayed in Fig. 6.42 for the injector centerplane. The temperature of the freestream in the case TAB2b is higher because the temperature of the fresh gases is 450 K instead 329 K. TAB2b is having slightly better performance than TAB2 inside the cavity, but the opposite occurs when it comes to the mixing layer. Actually, the average temperature field of the non-reactive case (Fig. 4.16) has shown that only the inner cavity is featuring temperatures around 450 K, the temperature in the mixing layer is lower and approaching the freestream temperature (329 K). An appropriate way would be building more tables with different fresh gas temperatures to improve the results we saw here, but the aim of this work is not the run a simulation using FPI solver, but to estimate if the FPI model could have been consistent. Even with TAB2b where the fresh gas temperature of the premixed table is among the highest of the cavity, the temperature of the LES is still higher in the same areas that were observed previously. The temperature discrepancy in those regions is not only due to the fresh gas temperature of the tables, there is a strong dilution by burnt gases that needs to be accounted for. Besides, there is almost no difference for the mass fraction of H_2O between TAB2 and TAB2b. The initial temperature of the laminar premixed flames has only a slight impact on the results, TAB3 will be used for the next comparisons.

Profiles of mass fractions of CO and CO_2 for LES and TAB3 are displayed in Figs. 6.43 and 6.44 respectively in the injector centerplane and in the centerplane between two injectors. The discrepancies that were observed for the temperature in the injector centerplane are increased for the mass fractions of CO and CO_2. The difference stays relatively low at the large recirculation area for the profiles in the centerplane between two injectors, except at the rear of the cavity ($x = 66$ mm) where it is higher in this centerplane. At the front of the cavity, TAB3 and the LES are totally different regardless of the centerplane. Actually, when Y_{CO} is overpredicted, Y_{CO_2} is underpredicted at the same area. The sum of both mass fractions $Y_{CO} + Y_{CO_2}$ is displayed in Fig. 6.45. The fitting is nearly perfect in the large recirculation area, but still some discrepancies exist in the small recirculation area ($x = 2$, 11 mm) and in the interface between the recirculation zones ($x = 20$ mm). The differencies found between LES and TAB3 are due to several factors that will be discussed in the next section.

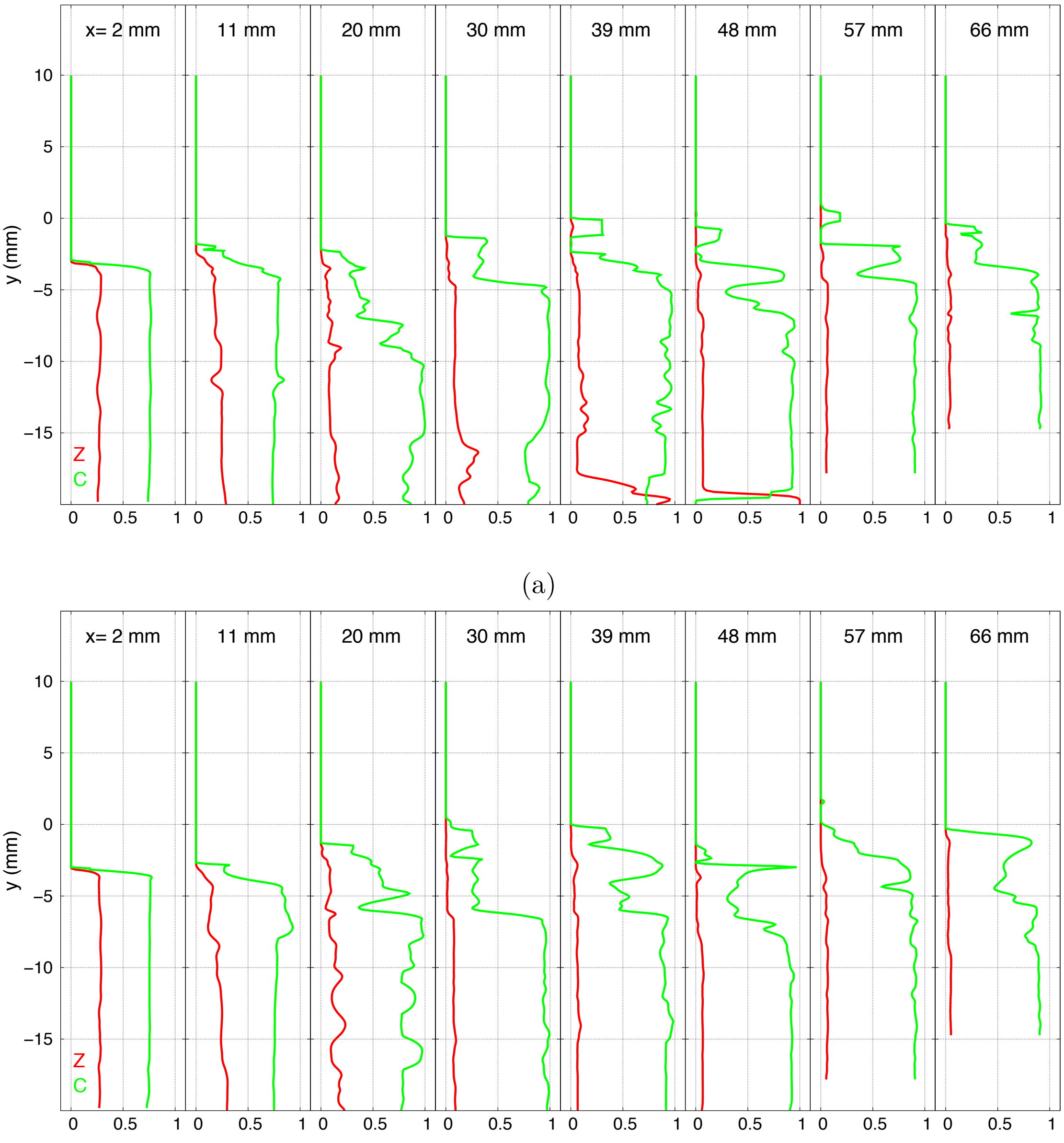

(a)

(b)

Figure 6.40: Instantaneous mixture fraction and progress variable profiles inside the cavity in (a) the injector centerplane, and (b) the centerplane between two injectors.

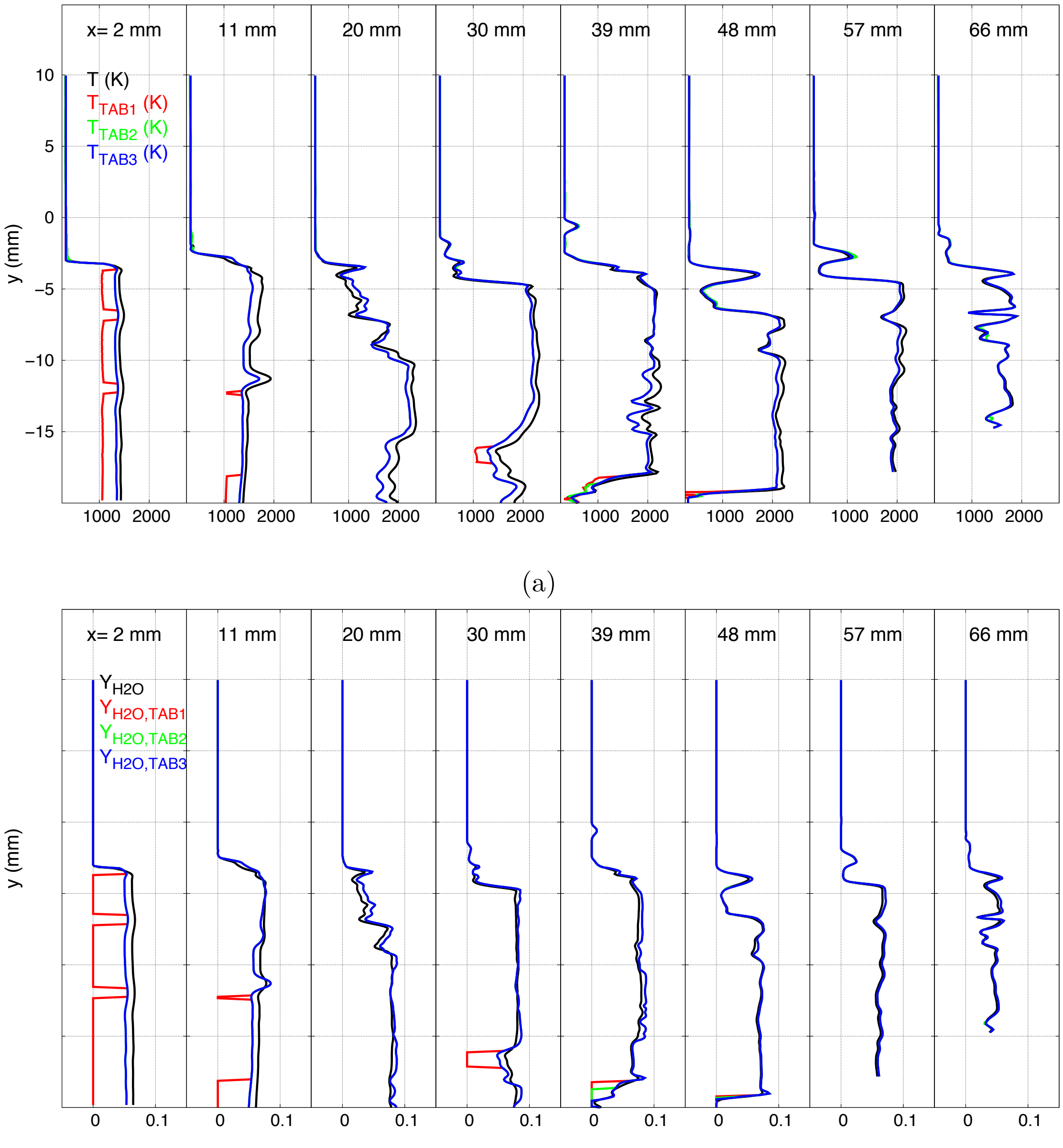

(a)

(b)

Figure 6.41: Instantaneous (a) temperature and (b) mass fraction of H_2O profiles inside the cavity in the injector centerplane: comparison between LES and tables with different prolongation methods outside the flammability limits.

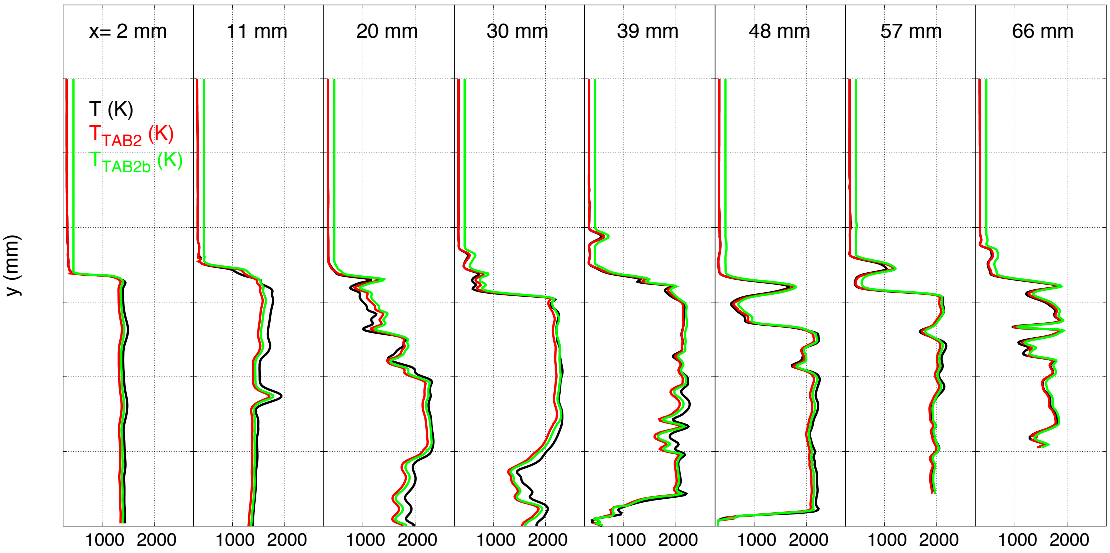

(a)

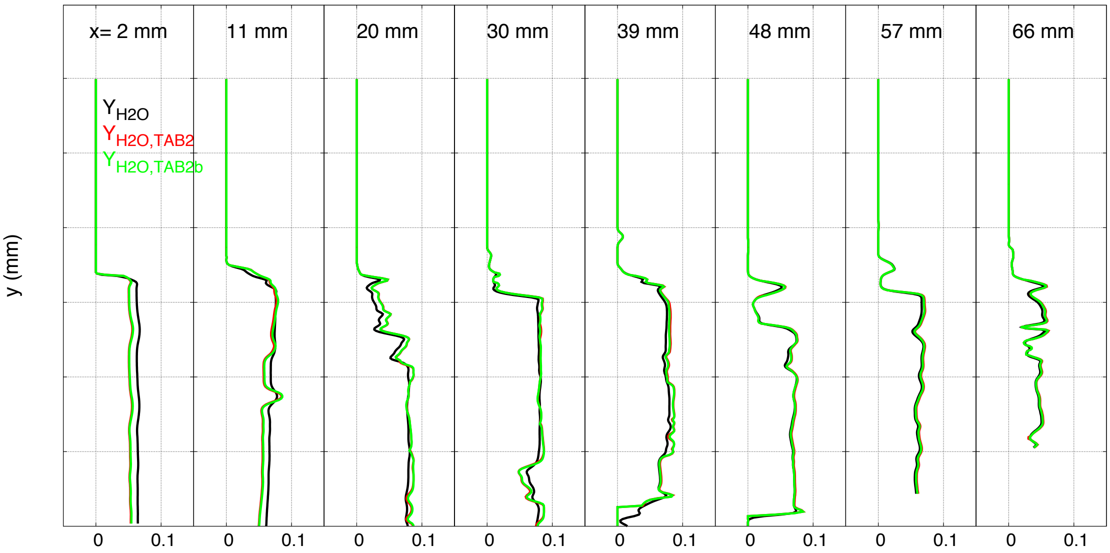

(b)

Figure 6.42: Instantaneous (a) temperature and (b) mass fraction of H_2O profiles inside the cavity in the injector centerplane: comparison between LES and tables with different initial temperatures.

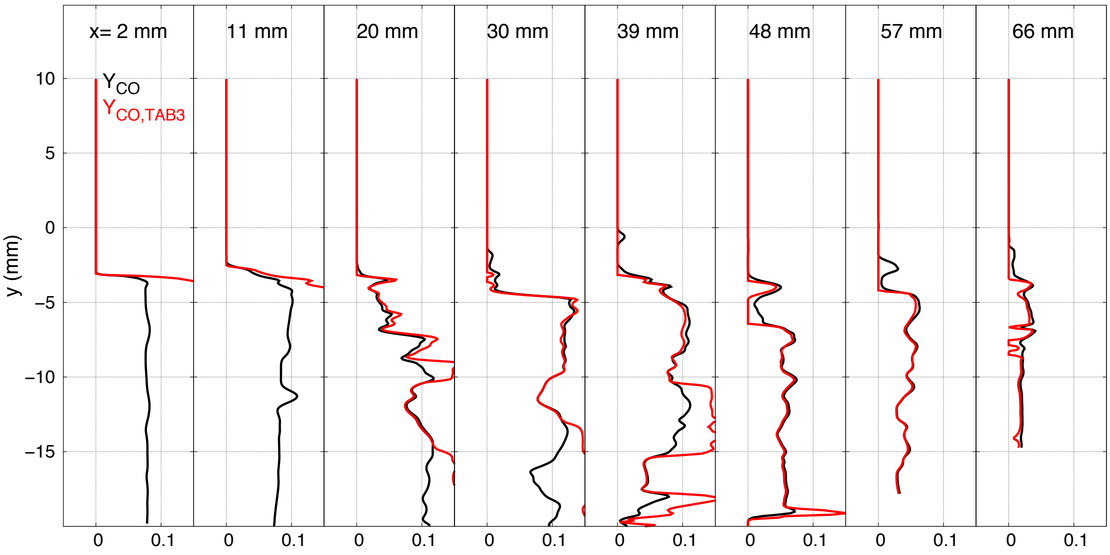

(a)

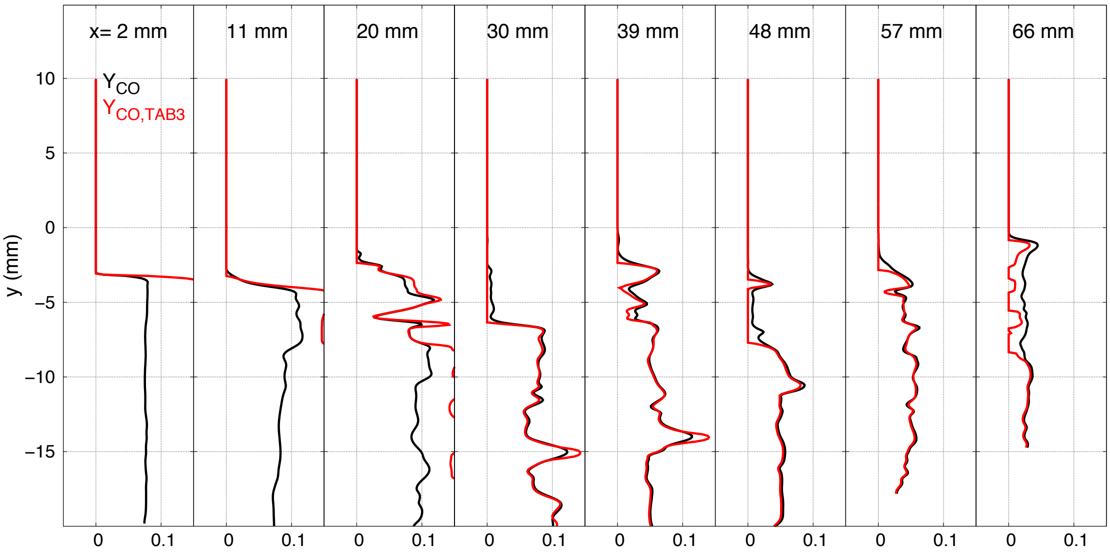

(b)

Figure 6.43: Instantaneous CO mass fraction profiles inside the cavity in (a) the injector centerplane and (b) the centerplane between two injectors: comparison between LES and TAB3.

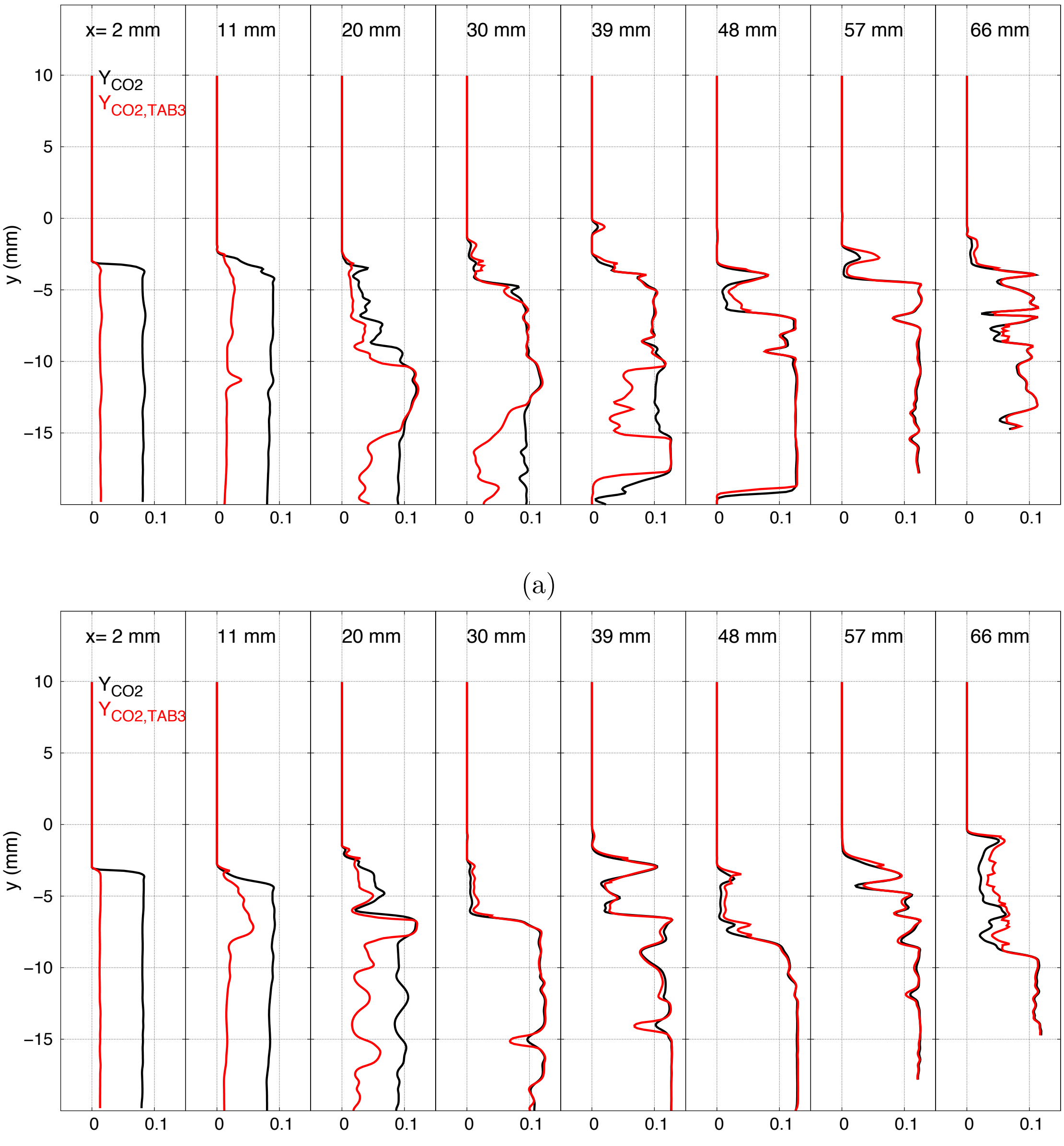

(a)

(b)

Figure 6.44: Instantaneous CO_2 mass fraction profiles inside the cavity in (a) the injector centerplane and (b) the centerplane between two injectors: comparison between LES and TAB3.

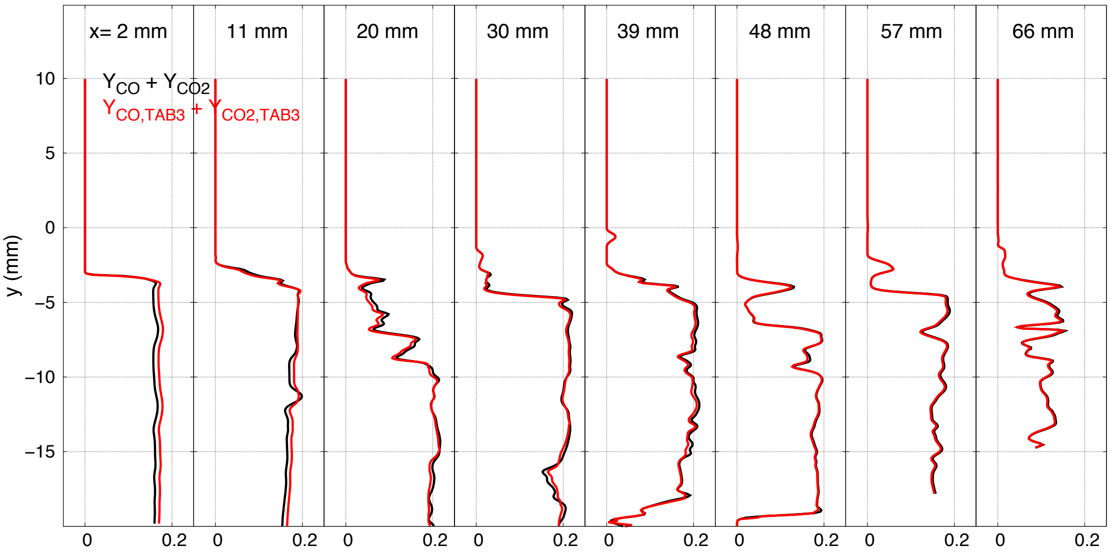

(a)

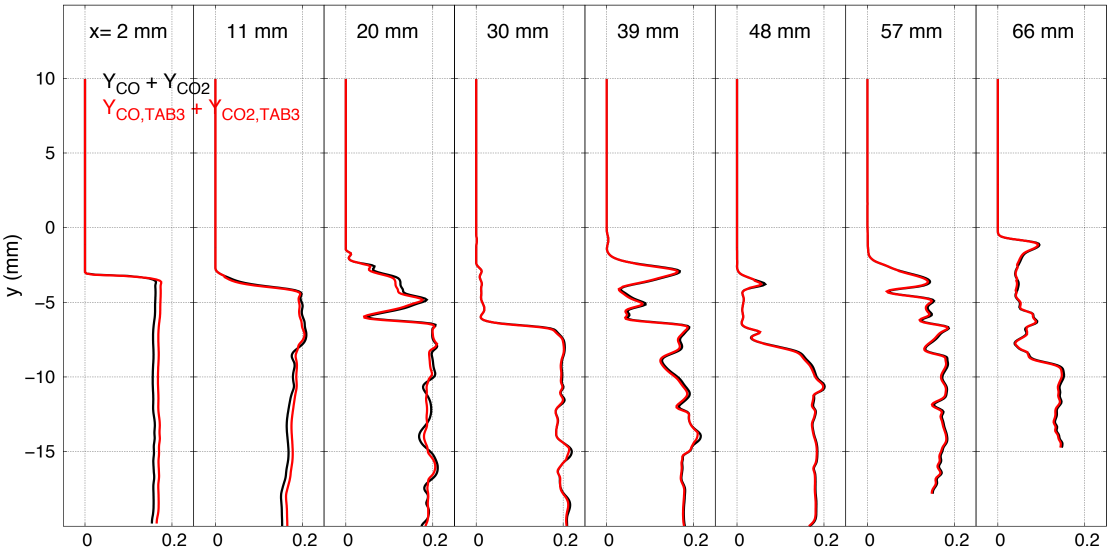

(b)

Figure 6.45: Instantaneous $Y_{CO} + Y_{CO_2}$ profiles inside the cavity in (a) the injector centerplane and (b) the centerplane between two injectors: comparison between LES and TAB3.

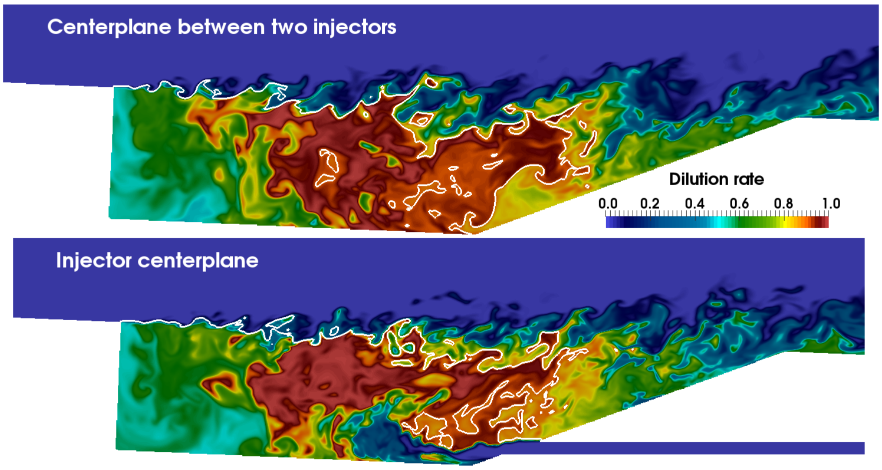

Figure 6.46: Instantaneous field of dilution rate inside the cavity for RFA1: centerplane between two injectors (top) and injector centerplane (bottom). The stoichiometric line is displayed in white color.

6.5.6 Origin of discrepancies between TAB3 and LES

The differences between TAB3 and LES observed previously are caused by several phenomena depending on the area. Dilution by burnt gases, nonpremixed flame regime or strong scalar dissipation can be the origin of these discrepancies.

6.5.6.1 Dilution by burnt gases

The dilution rate is the ratio of the burnt gases in the mixture and is defined as:

$$\mathcal{D}_r = \frac{Y_{BG}}{1 - Y_{N_2}} \tag{6.5.6}$$

where Y_{BG} is the mass fraction of the burnt gases. A species is tagged as burnt gas when it is neither a hydrocarbon (C_nH_m) or a species from air (O_2 or N_2):

$$Y_{BG} = 1 - Y_{C_nH_m} - Y_{O_2} - Y_{N_2} \tag{6.5.7}$$

The instantaneous field of dilution rate is displayed in Fig. 6.46 in the injector centerplane and in the centerplane between two injectors. The whole cavity is strongly diluted by burnt gases with $\mathcal{D}_r > 0.5$. Taking away the nitrogen, the front of the cavity is almost composed of half burnt gases and half fuel ($\mathcal{D}_\nabla \in [0.5, 0.7]$). The dilution rate is the highest in the large recirculation area where only burnt gases are present ($\mathcal{D}_\nabla > 0.9$). Finally, the cavity ramp is featuring dilution rate from 0.4 to 0.7 because of the air entering at this area. Strong dilution is found everywhere inside the cavity, and yet the comparison between LES and TAB3 was satisfying in the most parts of the cavity, therefore, dilution could only be the origin of some minor discrepancies between the LES and the tabulated chemistry. Dilution without heat losses has in fact no impact on premixed flamelet properties.

6.5.6.2 Nonpremixed flame regime

The instantaneous heat release rate and the flame index are displayed in Fig. 6.47 at four cuts in the streamwise direction. The cuts are representing the area of the small recirculation zone ($x = 2$ mm), the interface between the recirculation zones ($x = 20$ mm), the large recirculation zone ($x = 39$ mm) and the rear of the cavity ($x = 66$ mm). No combustion is found in the small recirculation zone,

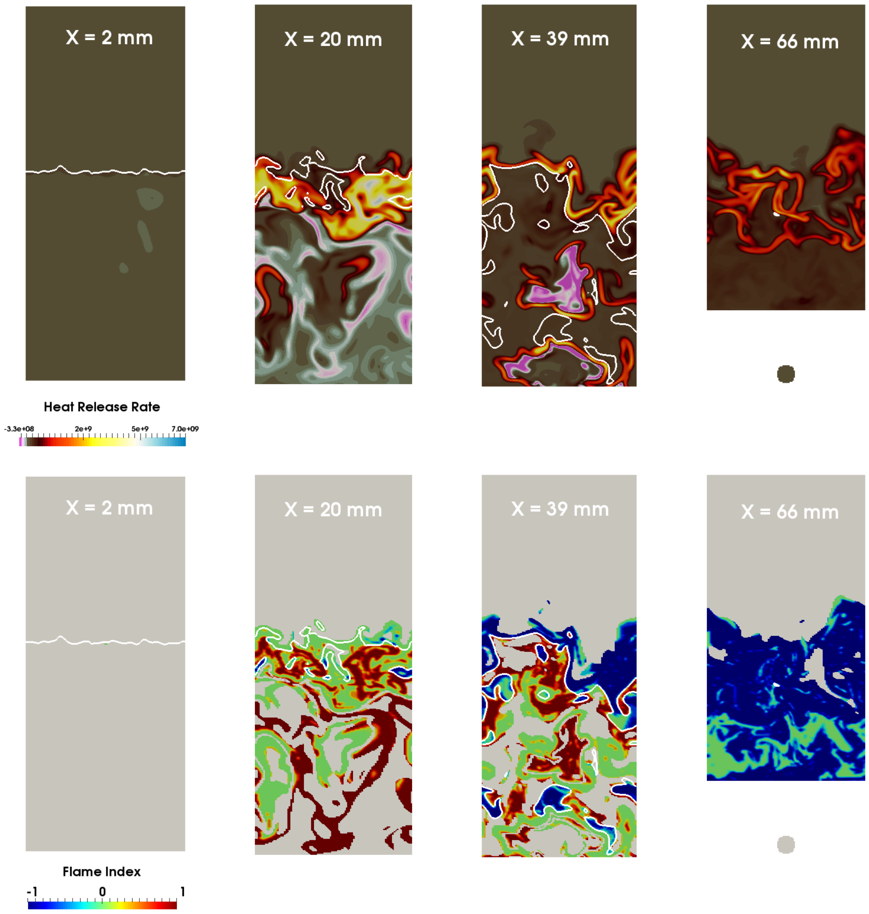

Figure 6.47: Instantaneous heat release rate (top) and flame index (bottom) in the small recirculation zone ($x = 2$ mm), the interface between the recirculation zones ($x = 20$ mm), the large recirculation zone ($x = 39$ mm) and the rear of the cavity ($x = 66$ mm). The stoichiometric line is represented in white color. Case RFA1.

so the burnt gases of this region come from the interface between the recirculation zones where the combustion regime is mostly nonpremixed. Trying to predict a nonpremixed flame with a premixed flame table is expected to be improper. However, nonpremixed combustion is also found in the large recirculation area, and the premixed table is accurate in that region. Fiorina et al. [54] found that a laminar premixed flame tabulation (FPI solver) could be efficient in predicting nonpremixed flames if the mixture fraction is close to the stoichiometric value. Indeed, chemistry near stoichiometry is too fast for any diffusive processes to have an impact on it, and thus becomes independent of the flame configuration. The mixture fraction in the large recirculation area is between 0.05 and 0.10 which is close to the stoichiometric value ($Z_{st} = 0.06366$), chemistry is well predicted by the premixed flame tabulation regardless of the combustion regime. On the other hand, the interface between the recirculation zones is featuring mixture fractions of 0.15 to 0.25, chemistry is slow in that region so diffusive effects can intervene and make this region dependent of the flame configuration.

Another reason would be that the small recirculation area is acting like a perfectly stirred reactor (PSR), and the time required to reach the values given by the premixed flame tabulation is too long to be achieved, since the residence time of this region is only a few milliseconds. The mixture fraction in the small recirculation area is almost constant, therefore a mixture composition at $Z = 0.279$ is extracted from the LES and used as an initial condition for PSR computations with

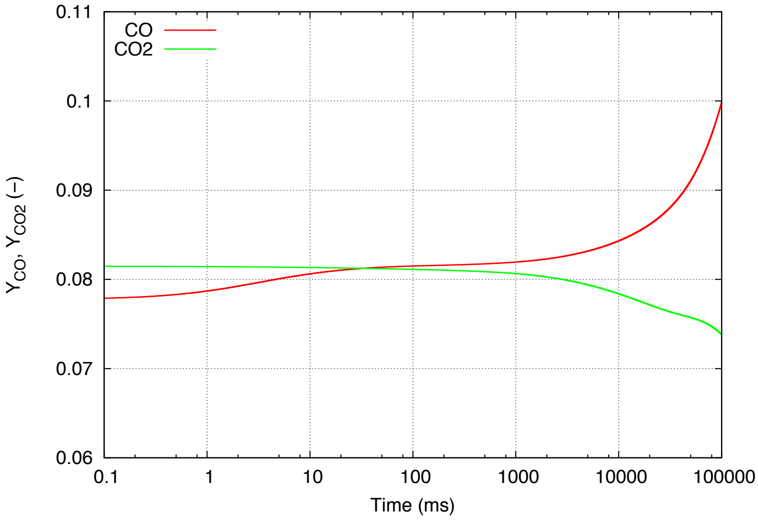

Figure 6.48: Evolution in time of CO and CO_2 mass fractions, computed with SENKIN [106].

SENKIN [106]. The mass fractions of CO and CO_2 are 0.078 and 0.081 respectively for the LES, and 0.158 and 0.013 respectively for TAB3. The mass fractions of CO and CO_2 after 100 s physical time computation are displayed in Fig. 6.48. The mass fraction of CO is increasing while the one of CO_2 is decreasing, then evolving towards the values of TAB3. However, even 100 s is not sufficient for the mass fractions to reach $Y_{CO,TAB3}$ and $Y_{CO_2,TAB3}$. A premixed flame tabulation could never predict the burnt gas composition in this region which is fed by the rich side of a diffusion burning flame structure.

The discrepancies at the front of the cavity being clarified, we are now interested in those in the large recirculation zone, which are probably due to strong scalar dissipations.

6.5.6.3 Scalar dissipations

Three scalar dissipations have been investigated in this section. They are the mixture fraction dissipation χ_Z, the progress variable dissipation χ_{Y_C} and a correlation of both χ_{ZC} and are defined as follow:

$$\begin{cases} \chi_Z = D_Z |\nabla Z|^2 \\ \chi_{Y_C} = D_{Y_C} |\nabla Y_C|^2 \\ \chi_{ZC} = D_{ZC} |\nabla Z| |\nabla Y_C| \end{cases} \tag{6.5.8}$$

where the coefficients D_Z, D_{Y_C} and D_{ZC} are:

$$\begin{cases} D_Z = \dfrac{\lambda}{\rho C_p} \\ D_{Y_C} = \dfrac{D_{CO}|\nabla Y_{CO}| + D_{CO_2}|\nabla Y_{CO_2}| + D_{H_2O}|\nabla Y_{H_2O}|}{|\nabla Y_C|} \\ D_{ZC} = \sqrt{D_Z D_{Y_C}} \end{cases} \tag{6.5.9}$$

Instantaneous fields of these scalar dissipations are displayed in Fig. 6.49 for cuts in the injector centerplane and the centerplane between two injectors, in Fig. 6.50 for cuts in the streamwise direction showing planes at the small recirculation zone ($x = 2$ mm), the interface between the recirculation zones ($x = 20$ mm), the large recirculation zone ($x = 39$ mm) and the rear of the cavity ($x = 66$ mm). Strong dissipation of the mixture fraction is found at the exit of the injector, following the path of the fuel injection. The mixing layer above the small recirculation zone and the interface between the recirculation zones are featuring scalar dissipations of moderate intensity. The difference between χ_Z and χ_{Y_C} is that the dissipation of the progress variable is weak in the interface between the recirculation zones and moderately strong in the whole mixing layer. The scalar dissipations profiles in Fig. 6.51 show that the large discrepancies between LES and TAB3 for Y_{CO} and Y_{CO_2} in the large recirculation zone occur in zones with strong dissipation of mixture fraction. The dissipation of progress variable in the mixing layer only leads to small differences between LES and TAB3.

In order to link the scalar dissipation to the combustion regime, the regions with high values of χ_Z in the injector centerplane at the fourth and fifth cuts ($x = 30$ and 39 mm respectively) have been investigated along with the flame index (Fig. 6.52). In the fourth cut, strong scalar dissipations are located in regions with rich premixed combustion regime ($FI = 1$). While in the fifth cut, the strongest dissipations are found at the exit of the injector ($y \in [-20, -17]$ mm) with nonpremixed combustion regime ($FI = 0$). At the middle of cavity ($y > -15$ mm), rich premixed and nonpremixed combustion regimes are found in zones with moderately strong scalar dissipations. The values of χ_Z are insignificant for areas with lean premixed combustion regime ($FI = -1$) in both cuts. The largest discrepancies between the LES and TAB3 are actually located in regions with moderate scalar dissipations and featuring premixed combustion regime (see temperature profiles in Fig. 6.41). Regions in the large recirculation area with nonpremixed combustion are well predicted for the temperature, even with strong scalar dissipations.

In rich premixed regions with moderate scalar dissipations, solely the concentrations of CO and CO_2 are largely affected, the mass fractions of H_2O between LES and TAB3 were found to be very close to each other. A study on the sensitivity of these species to the gradient of equivalence ratio has been performed for one dimensional laminar premixed flames. The concentrations difference between two mixtures around the stoichiometry ($\phi_1 = 1.1$ and $\phi_2 = 1.15$) and between two rich mixtures ($\phi_1 = 2.1$ and $\phi_2 = 2.15$), $\Delta Y_k = |Y_{k,2} - Y_{k,1}|$ with $k = CO$, CO_2 or H_2O against the progress variable are displayed in Fig. 6.53. ΔY_k is small at low values of progress variable for all the studied species. But for high values of progress variable ($C > 0.9$), the difference becomes large for CO and CO_2 for mixtures around the stoichiometry, and stays small for H_2O. For rich mixtures, only the mass fraction of CO is significantly affected by the change in equivalence ratio. As the mixture fraction in the large recirculation area is around the stoichiometry and the progress variable in this region being higher than 0.9, the large discrepancies found between LES and TAB3 for CO and $CO2$ could be explained by these species being more sensitive to mixture change. In presence of high χ_Z, even for premixed regime, the effect of the local gradient of miture fraction cannot be neglected with a tabulated approach context. New methods including gradient of mixture fraction in the library construction could help [121, 103].

Consequently, the use of a flamelet based model is complicate in this simulation because:

- all possible mixtures can be found in the cavity ($Z \in [0, 1]$),
- the cavity is strongly diluted by burnt gases,
- all combustion regimes occur,
- strong scalar dissipations are present, even in partially premixed regime.

A tabulation with a combined premixed including the effects of Z gradients and nonpremixed tables, taking in account the dilution by burnt gases in the case of a non adiabatic system, could be envisaged to model the combustion. As the pressure in the cavity is relatively uniform and the comparison between LES and TAB3 (built with constant pressure $P = 66$ kPa) led to satisfying results, there is no need to account for the compressibility effect in the tabulation for this scramjet.

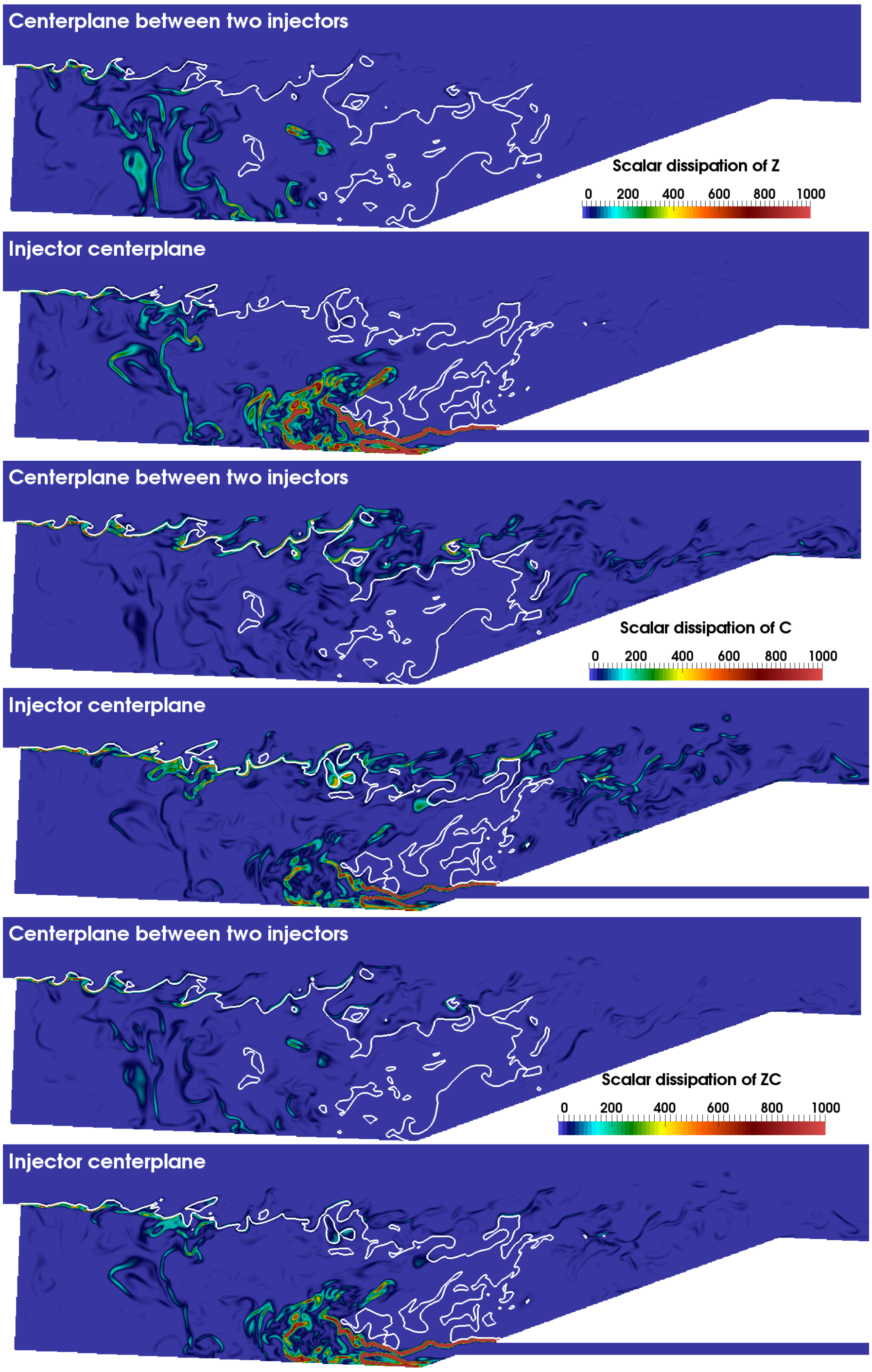

Figure 6.49: Instantaneous scalar dissipations in the centerplane between two injectors and in the injector centerplane. The stoichiometric line is displayed in white color. Case RFA1.

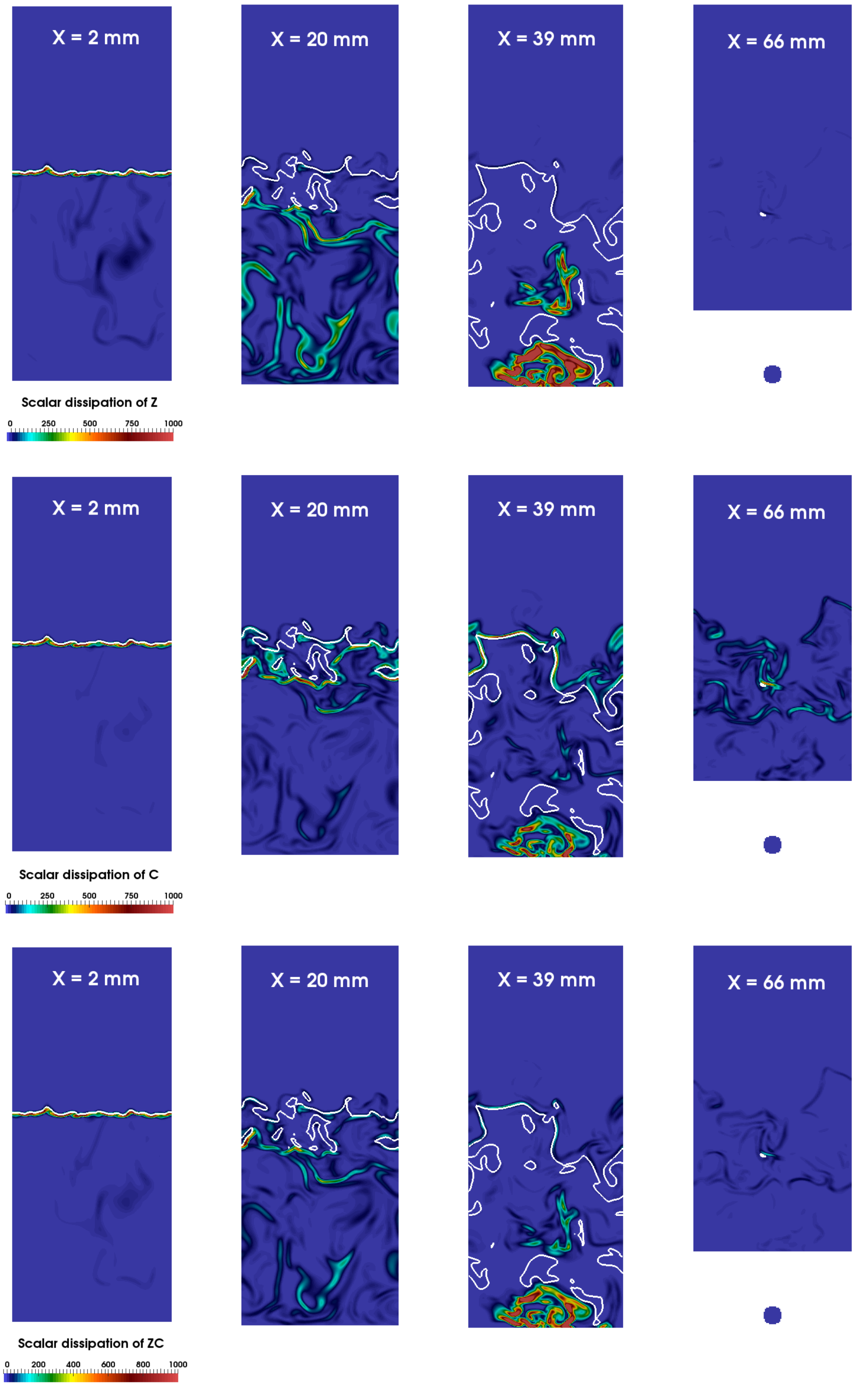

Figure 6.50: Instantaneous scalar dissipations in the small recirculation zone ($x = 2$ mm), the interface between the recirculaton zones ($x = 20$ mm), the large recirculation zone ($x = 39$ mm) and the rear of the cavity ($x = 66$ mm). The stoichiometric line is displayed in white color. Case RFA1.

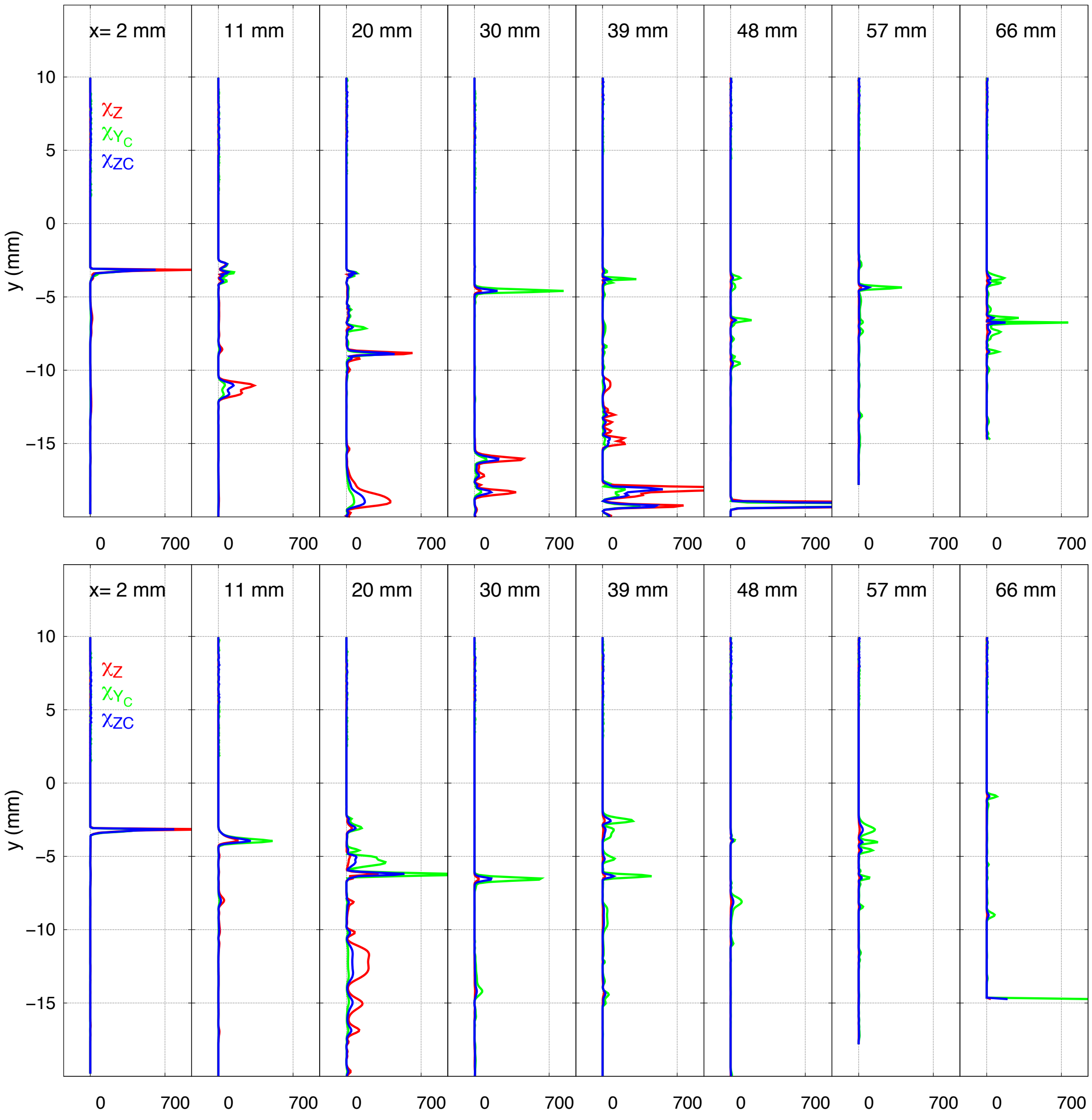

Figure 6.51: Instantaneous scalar dissipations profiles in the injector centerplane (top) and in the centerplane between two injectors (bottom). Case RFA1.

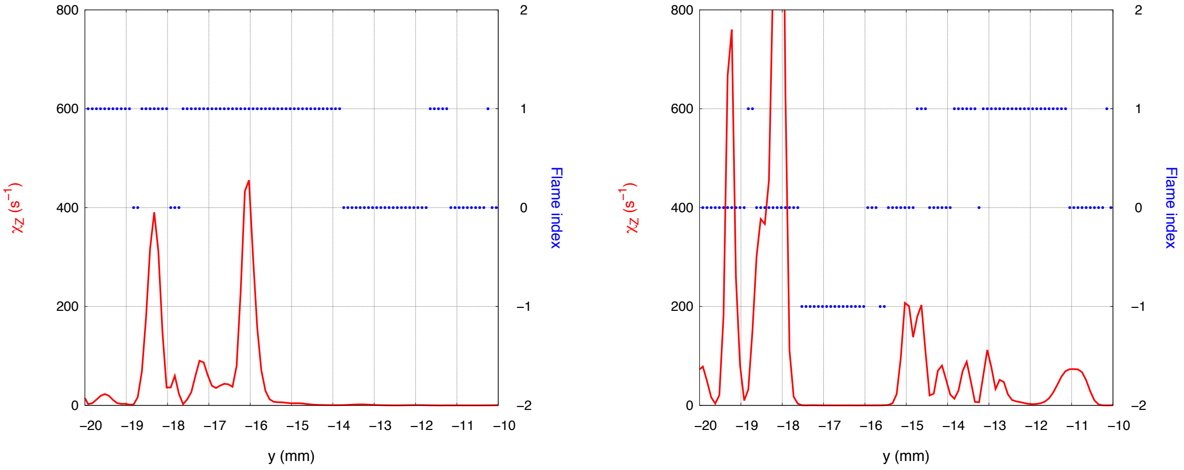

Figure 6.52: Instantaneous fields of scalar dissipation χ_Z and flame index in the injector centerplane at $x = 30$ mm (left) and $x = 39$ mm (right). Case RFA1.

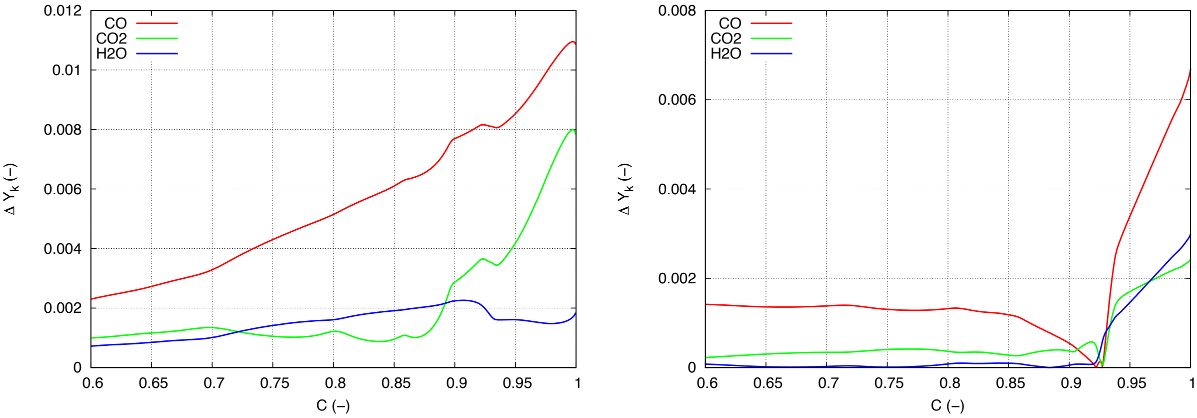

Figure 6.53: Sensitivity of CO, CO_2 and H_2O to the equivalence ratio: ΔY_k vs. progress variable C for mixtures around the stoichiometry (left) and for rich mixtures (right).

Chapter 7

Conclusions and perspectives

Contents

7.1 Conclusions

The purpose of this Ph.D. was to assess to ability of the Large Eddy Simulation framework to predict compressible multi-species reacting flows and to provide some fundamental aspects of cavity-based scramjet physics. These objectives were achieved in this work with several highly refined large eddy simulations and deep analysis of the flow and the chemistry in the cavity.

The fulfilment of this work can be split into three parts:

1. **Coding:** some developments were required to manage numerical simulations and integrated to the solver SiTCom-B:
   - Optimization: the solver has been optimized by limiting the access to the memory which is a very expensive step of the computation. The performance of the code has increased by a factor 2.
   - Immersed Boundary Method (IBM): a well-known issue of a structured code is to deal with complex geometries, since the grid, composed of parallelepipoids, cannot describe any other shape, for example circles. The immersed boundary method was initially implemented in SiTCom-B to overcome this problem, but this initial coding based on STL description has some shortcomings when the geometry is very complex (in presence of corners, or when the ghosts and images points are located in different blocks). An analytical implementation of the IBM was developped during the thesis to deal with the issues encountered with the previous coding. The geometry was better described but this new implementation has the drawback of not being universal, each test case needs to be described mathematically.
   - Artificial ignition spot: the temperature inside the cavity was found around 450 K which made the ignition impossible without any external source. To mimic the sparkling plugs of the experiments, artificial ignition spots (spherical, cylindrical and rectangular) have been implemented to start ignition.
   - Isothermal wall conditions: the solver was initially provided solely with adiabatic wall conditions at the interface between the solid domain modelized with the immersed boundary method and the fluid domain. The isothermal wall conditions were then implemented

  to compare simulations performed with one or another wall conditions. The isothermal wall development has first been validated on test cases, then applied to the cavity-based scramjet configuration.

  - Wall modeling: the dimensionless wall distance y^+ determines the resolution of the mesh near the wall. y^+ was found to be too important in the isolator, so a simple wall modeling based on the expressions of Larsson et al. [89] has been implemented during this thesis and tested on the non-reactive case.
  - Residence time: the cavity residence time is usually estimated with some empirical formulations. In this work, a transport equation for the residence time based on the work of Enjalbert et al. [49] has been implemented in the solver to examine the time spent by the mixture in the cavity.
  - Thickened Flame Model (TFM): the TFM has been implemented in SitCom-B and tested on simple cases during the thesis. As its use for high speed flows might not be relevant, this model was not retained for the simulations performed in this work.

2. **Simulations:** a large number of simulations have been performed to investigate the influence of the grid refinement, of the fuel loadings, of the wall conditions and of the number of injectors:

   - Grid refinement: two meshes were used in this work for the computations, a coarse mesh with $\Delta x \approx 200$ μm and a fine mesh with $\Delta x \approx 100$ μm. The LES are well-resolved for both grids, and almost no difference in the averaged fields (velocity, pressure, temperature...) can be observed.
   - Fuel loadings: four different fuel loadings have been studied in this work, from 0 (non-reactive) to 99 SLPM. As pointed out in the literature, two recirculation zones were found inside the cavity: a small recirculation area at the front of the cavity featuring very low speed and a large recirculation area where the majority of mass transfer between the main stream and the cavity takes place. The reactive cases required an in-depth study on the chemistry of the fuel, ethylene. A reduced chemistry with at least 22 species has been found necessary to be able to reproduce the flame stabilization demonstrating the importance of the kinetics modeling. The LES was found to be capable of reproducing an unstable case (low fuel loading), as well as two stable cases (medium and high fuel loadings). The flame stabilization process is dependent of the amount of fuel injected. In the case of a higher fuel loading (99 SLPM), the flame was stabilized in the mixing layer above the large recirculation area, while a medium fuel loading (56 SLPM) leads to a flame stabilization above the small recirculation area.
   - Wall conditions: a comparison between adiabatic and isothermal wall conditions was performed in this thesis. Both cases show very similar results. The largest difference lies in the temperature at the front of the cavity where it is found to be cooler (about 200 K) in the isothermal case.
   - Number of injectors: a study on the impact of the number of injectors was performed. The geometries were provided with 1, 2 or 11 injectors. The side walls of the 1 and 2 injectors cases were set as periodic while the 11 injectors case had non slipping walls. The periodic conditions of 1 and 2 injectors cases led to similar results for these cases. The flow was symmetric with respect to the injector centerplane (resp. the centerplane between two injectors) for the case with 1 injector (resp. 2 injectors). Because of the “real” walls in the case of 11 injectors, different behaviours were observed at the exit of each injector and the flame location differs from an injector to another.

All these simulations were compared to the experimental data of Tuttle et al. [164]. While the streamwise velocity has been fairly well predicted, there were some discrepancies for the transverse velocity which are also observed in other numerical works [4, 68]. The cavity wall pressure for the reactive cases is very close to the one of the experiment, but not in the non-reactive case where the discrepancy can reach 10 %. However, the experimental results of Tuttle et al. [164] for non-reactive case are not consistent with the experiments performed by Gruber et al. [64].

3. **Analysis of the results:** the second objective of this thesis was to provide fundamental aspects of cavity-based scramjet physics. The last chapter was dedicated to the analysis of the flame structures and to the possible combustion model that could be used to facilitate the simulations.

- Flame structures: the conditional mean of heat release rate on Mach number was computed and revealed that combustion mainly occurs in subsonic regions. Four combustion zones were identified: (I) the mixing layer above the small recirculation area, (II) the mixing layer above the large recirculation area, (III) the interface between the recirculation zones and (IV) the exit of the injector. (I) and (III) were controlled by weak to moderate nonpremixed combustion regime. (II) was provided with strong premixed flames and (IV) with strong nonpremixed flames. The complex combustion regimes in the cavity made the choice of an appropriate combustion model challenging.

- Combustion models: the simulations were performed with the direct evaluation of the source term from the transported quantities (quasi-laminar model). The use of the latter model was justified based on the computation of subgrid Damköhler numbers which indicated that the grids were well refined enough to capture the majority of the combustion phenomenon. The two most used combustion models in supersonic combustor configurations are the Partially Stirred Reactor (PaSR) model and the flamelet model. PaSR was initially considered in this work, but the computation of the fine structure volume fraction γ^* showed that the PaSR would be never activated with the considered grid refinements. The idea was then shifted to an a priori test of a tabulated approach based on one dimensional laminar premixed flamelets. Despite some discrepancies at the front of the cavity, the results were quite convincing, especially for the temperature and the concentration of H_2O. Using a simple premixed flamelet table was not sufficient to predict all the combustion zones of the cavity which are featuring different combustion regimes. A more complex tabulation needs to be considered.

7.2 Perspectives

The underlying physics of a scramjet is very complex and this thesis only dealt with a small part of it. The results of this work can be used as reference points to start studying other phenomena such as the shock structure at the rear of the cavity, the heat exchange with the external environment, or simply improve the current simulations with suitable models.

This thesis was mainly focused on the combustion phenomenon inside the cavity. The strong shock structure at the rear of the cavity was found to oscillate in the cavity ramp. The grids used for the simulations might not be refined enough to capture properly the shock structures. The use of much more refined grids or high order numerical schemes is necessary to start investigating the shock structures.

Baurle [4] compared the isothermal wall conditions to a steady-state one dimensional coupled fluid/solid heat transfer boundary conditions [177] for RANS simulations, and he found that the wall temperature is almost the same at the front and bottom wall of the cavity, but different at the cavity ramp by about 200 K. Using the current simulations as references, the next step would be integrating a coupled fluid/solid solver which should reproduce with more fidelity the real experimental conditions. The radiation could also be envisaged for a future simulation. This phenomenon is often neglected, because the total heat fluxes are mainly due to convective effects [30]. But the radiative effect is actually case-dependent, its contribution can change according to the local equivalence ratio, the wall temperature or the geometry [100]. Therefore, radiation could play a role in this scramjet configuration.

As discussed above, the PaSR model would not be triggered with the grids used in this work. The use of coarser meshes or tabulated chemistry have nevertheless to be considered in order to lower the computational cost if simulations are used for design purpose. First, tabulation including premixed diffusion and dilution as well as the heating by compressibility effect should be attempted. Second, the necessity of subgrid modelling should be accessed for coarser meshes.

Appendices

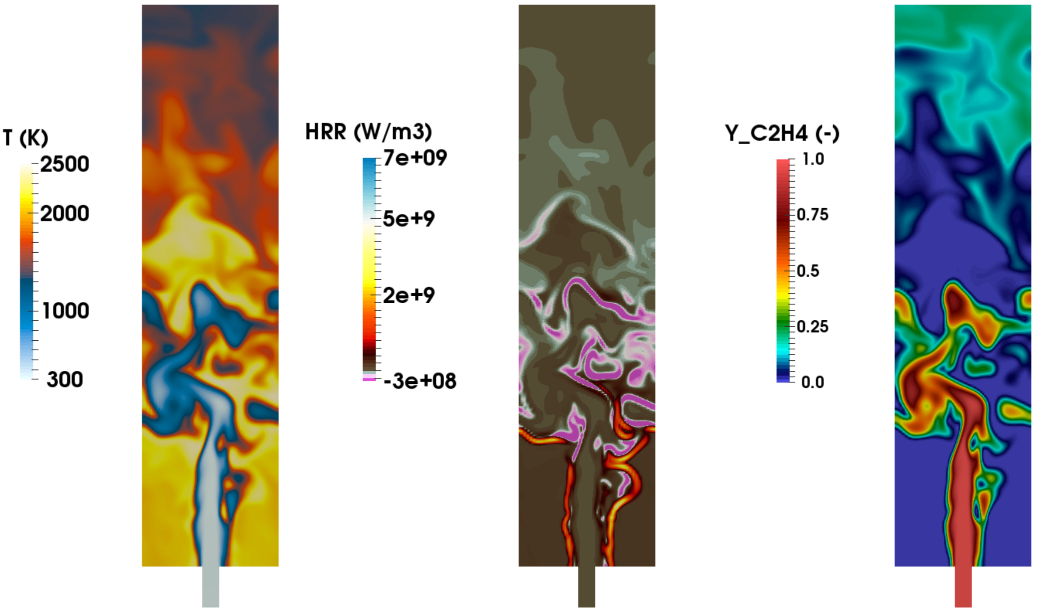

Figure 1: Instantaneous temperature, heat release rate and fuel mass fraction at $y = -19.57$ mm (injector center) for RCA1. Coarse mesh.

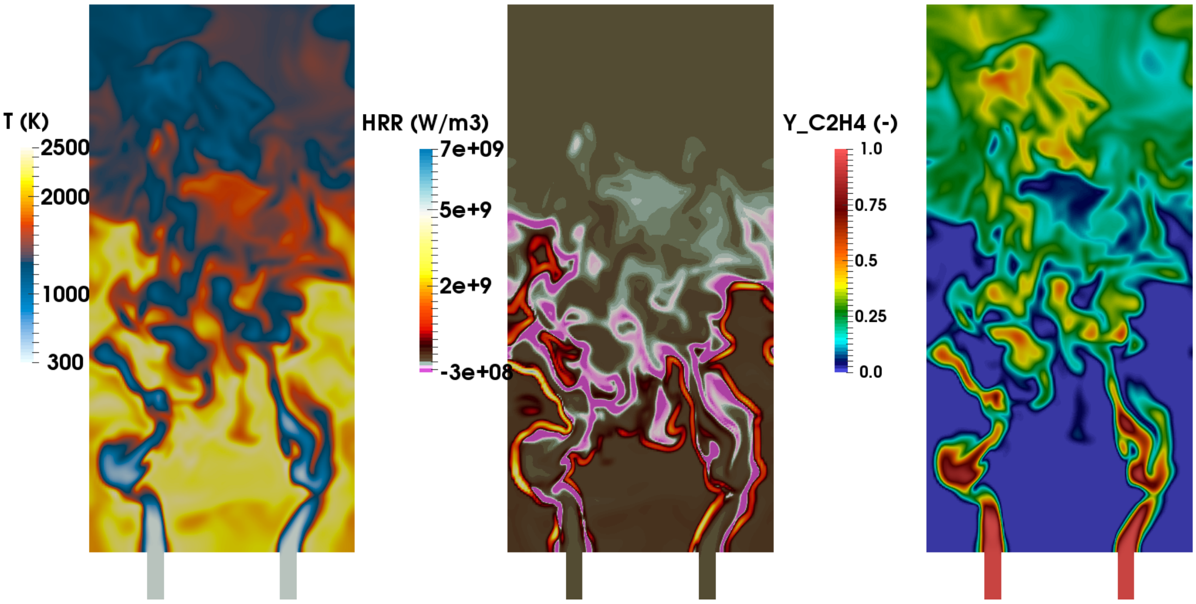

Figure 2: Instantaneous temperature, heat release rate and fuel mass fraction at $y = -19.57$ mm (injector center) for RCA2. Coarse mesh.

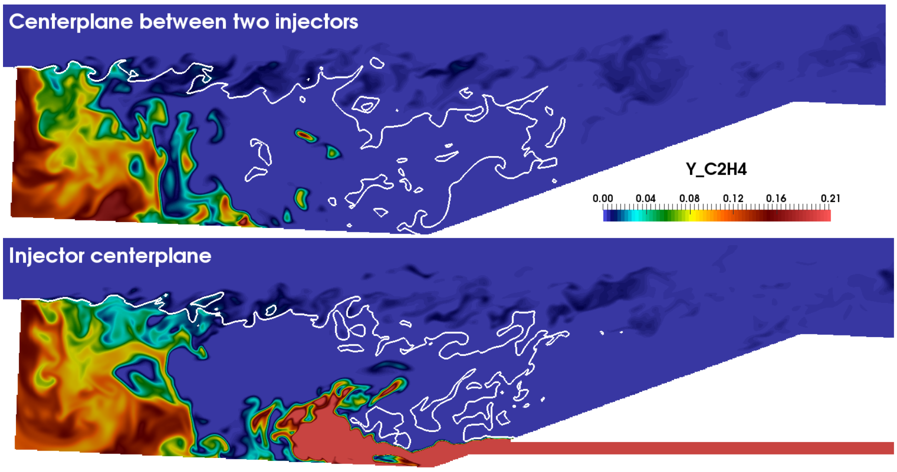

Figure 3: Instantaneous C_2H_4 mass fraction for RFA1.

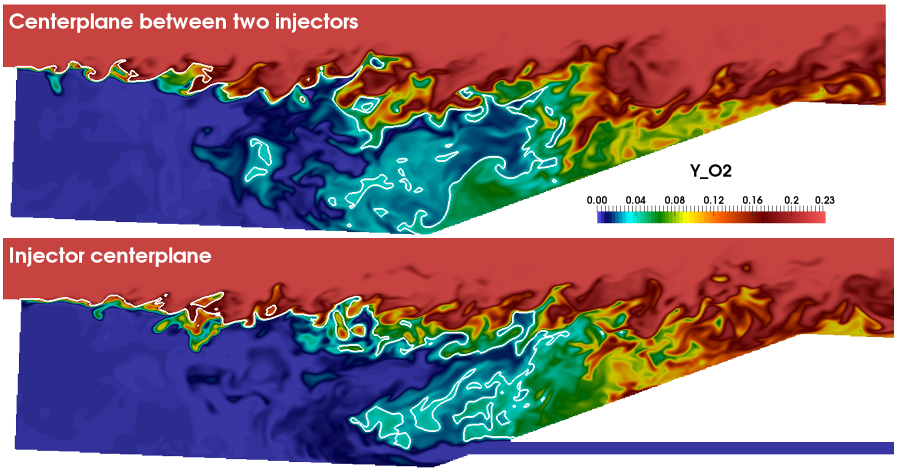

Figure 4: Instantaneous O_2 mass fraction for RFA1.

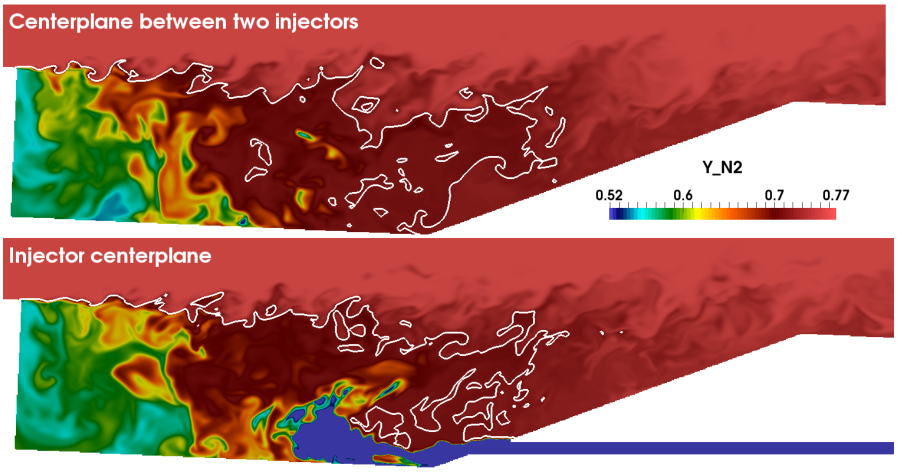

Figure 5: Instantaneous N_2 mass fraction for RFA1.

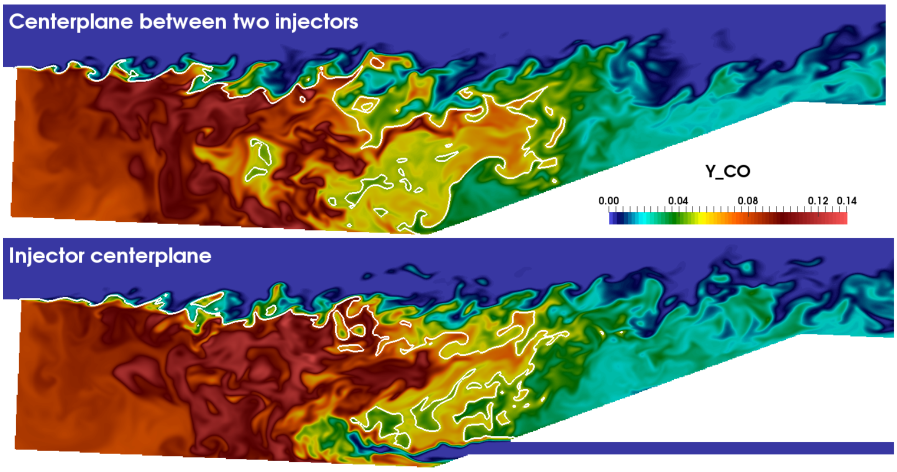

Figure 6: Instantaneous CO mass fraction for RFA1.

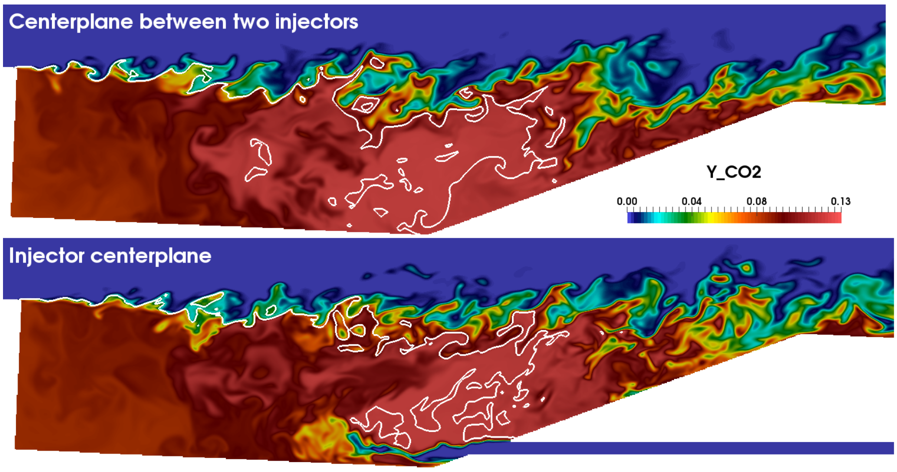

Figure 7: Instantaneous CO_2 mass fraction for RFA1.

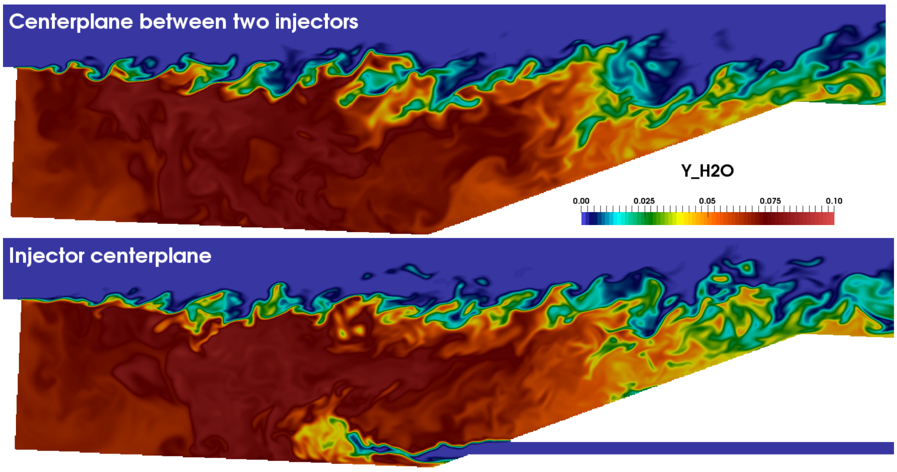

Figure 8: Instantaneous H_2O mass fraction for RFA1.

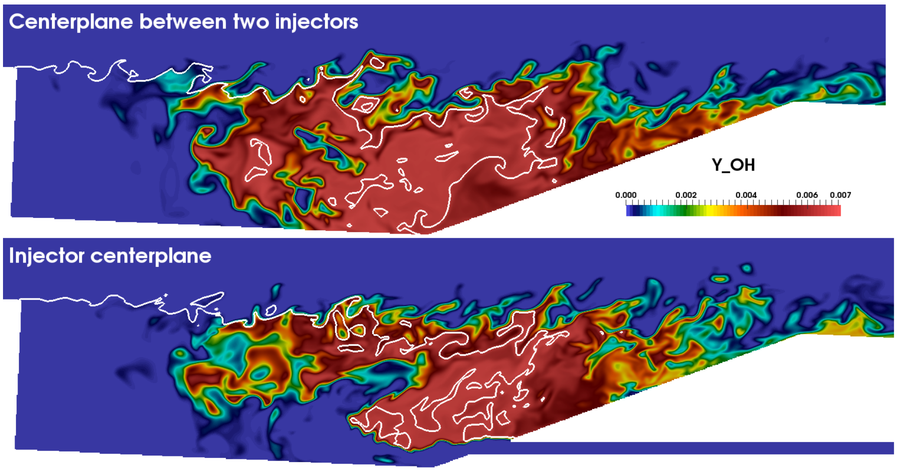

Figure 9: Instantaneous OH mass fraction for RFA1.

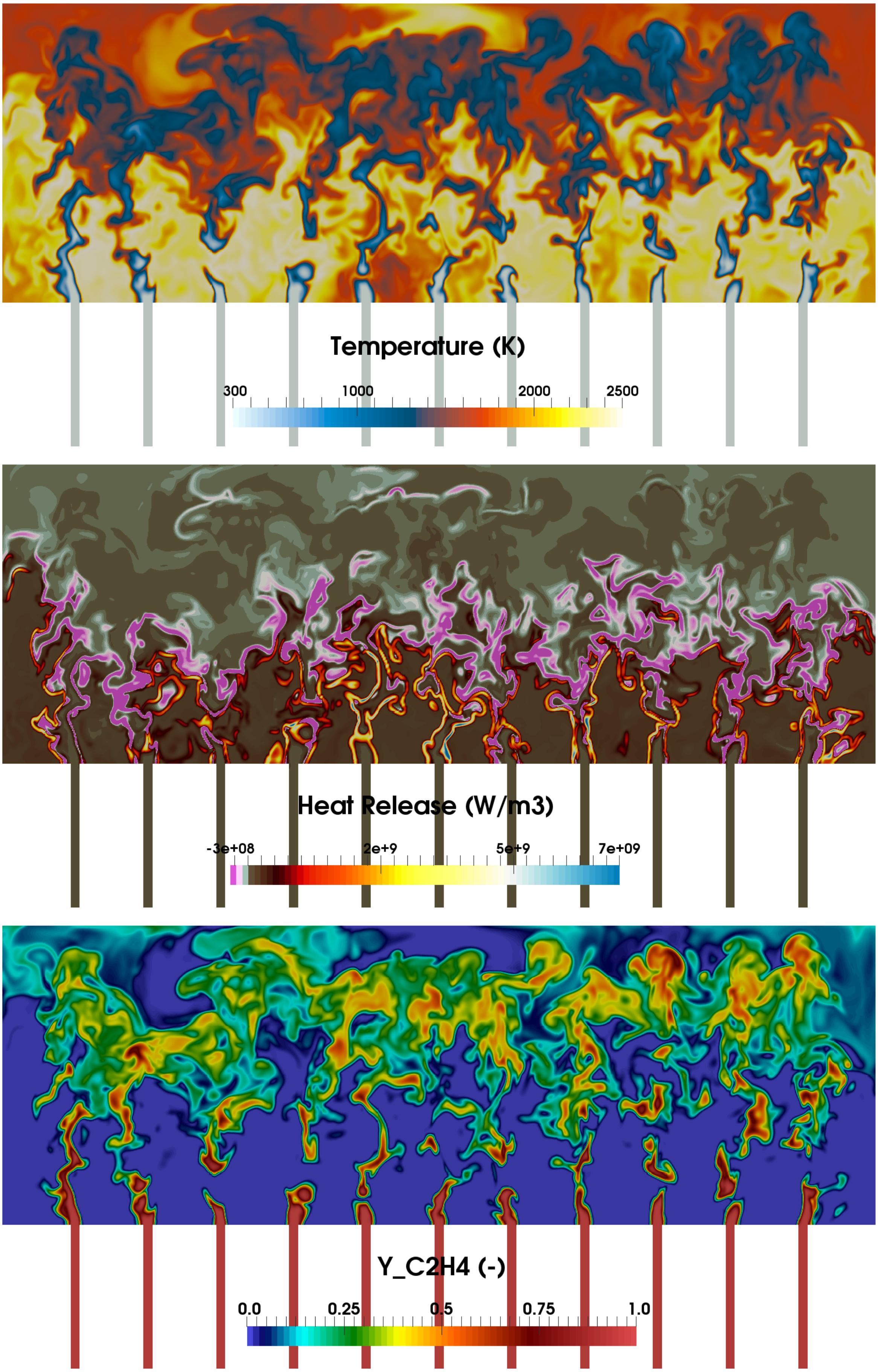

Figure 10: Instantaneous temperature, heat release rate and fuel mass fraction at $y = -19.57$ mm (injector center) for RCA11. Coarse mesh.

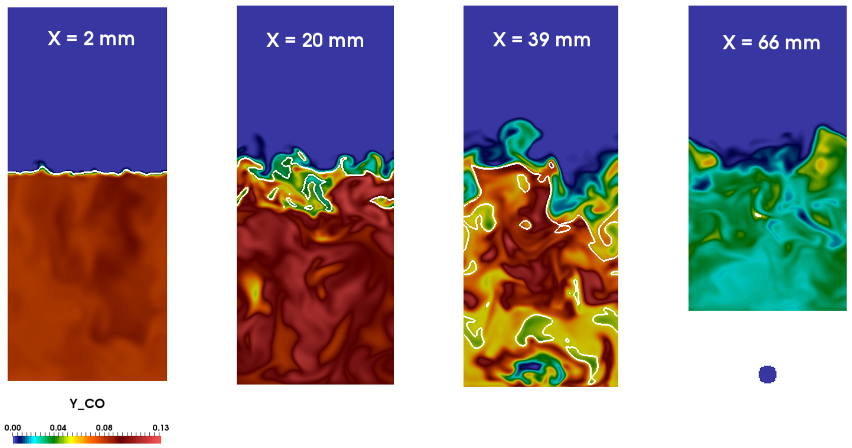
X = 2 mm
X = 20 mm
X = 39 mm
X = 66 mm
Y_CO
0.00
0.04
0.08
0.13

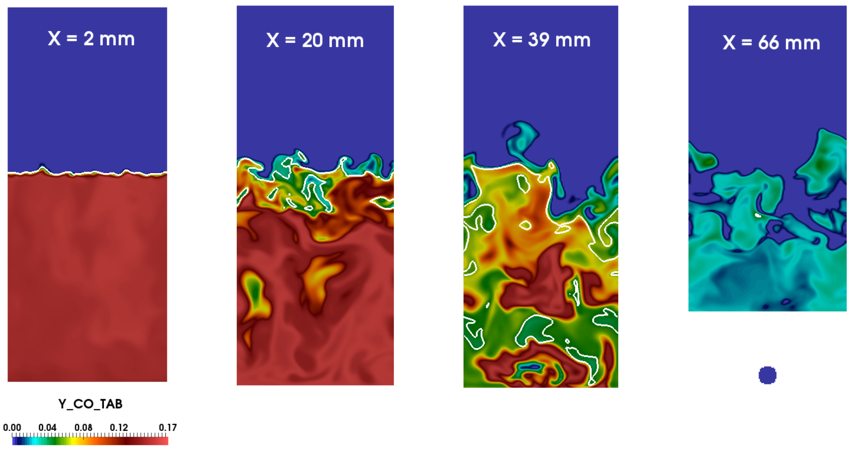
X = 2 mm
X = 20 mm
X = 39 mm
X = 66 mm
Y_CO_TAB
0.00
0.04
0.08
0.12
0.17

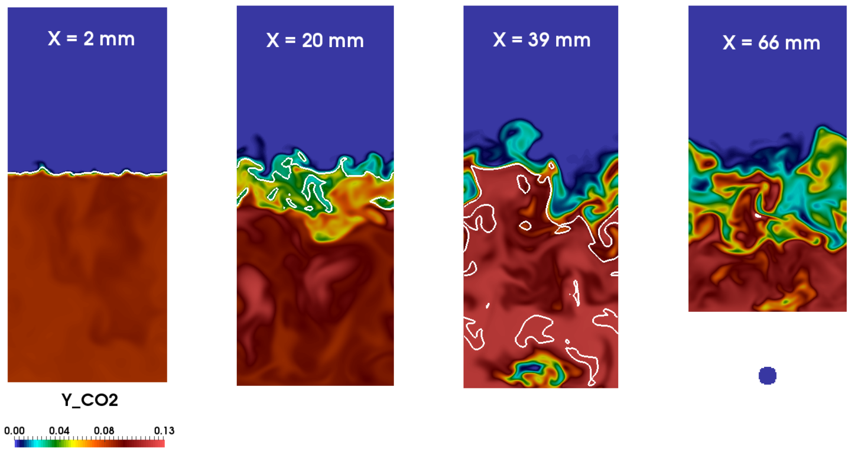
X = 2 mm
X = 20 mm
X = 39 mm
X = 66 mm
Y_CO2
0.00
0.04
0.08
0.13

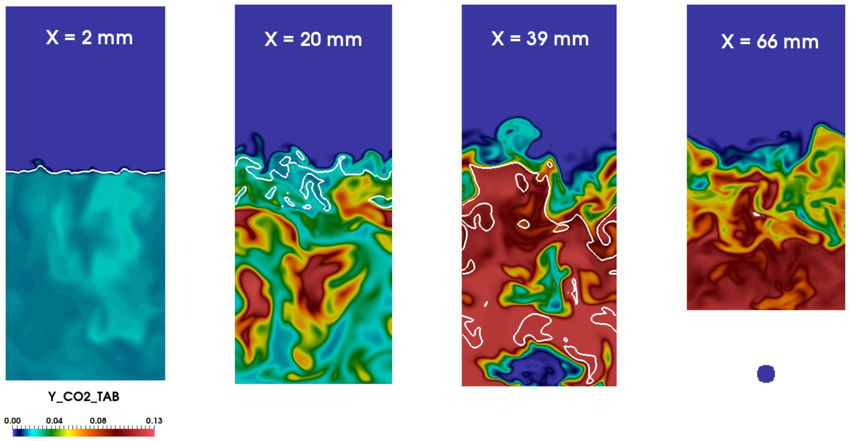
X = 2 mm
X = 20 mm
X = 39 mm
X = 66 mm
Y_CO2_TAB
0.00
0.04
0.08
0.13

Bibliography

[1] Almeida, Y. and Navarro-Martinez, S. (2018). Large eddy simulation of a supersonic lifted flame using the eulerian stochastic fields method. *Proc. Combust. Inst.*

[2] Babkin, V., Bunev, V., and Bolshova, T. (2015). Superadiabatic temperature phenomenon in the combustion process due to a competition between chemical reactions. *Combustion, Explosion, and Shock Waves*, 51(2):151–159.

[3] Baldwin, B. and Lomax, H. (1978). Thin layer approximation and algebraic model for separated turbulent flow. *AIAA Paper*, (78-257).

[4] Baurle, R. A. (2017). Hybrid reynolds-averaged / large eddy simulation of a scramjet cavity flameholder. *AIAA J.*, 55(2):544–560.

[5] Ben-Yakar, A. and Hanson, R. K. (2001). Cavity flame-holders for ignition and flame stabilization in scramjets: An overview. *J. Propul. Power*, 17(4):869–877.

[6] Benard, P. (2015). *Analyse et amélioration d'une chambre de combustion centimétrique par simulations aux grandes échelles*. PhD thesis, INSA de Rouen.

[7] Berglund, M., Fedina, E., Fureby, C., Tegner, J., and Sabel'Nikov, V. (2010). Finite rate chemistry large-eddy simulation of self-ignition in a supersonic combustion ramjet. *AIAA J.*, 48(3).

[8] Bilger, R. W. and Starner, S. H. (1990). On reduced mechanisms for methane-air combustion in nonpremixed flames. *Combust. Flame*, 80:135–149.

[9] Boivin, P., Dauptain, A., Jimenez, C., and Cuenot, B. (2012). Simulation of a supersonic hydrogen-air autoignition-stabilized flame using reduced chemistry. *Combust. Flame*, 159:1779–1790.

[10] Borghi, R. and Destriau, M. (1998). *Combustion and flames, chemical and physical principles*. TECHNIP.

[11] Boughanem, H. and Trouvé, A. (1996). Validation du code de simulation directe NTMIX3D pour le calcul des écoulements turbulents réactifs. Technical Report 42907, Institut Français du Pétrole.

[12] Bouheraoua, L. (2014). *Simulation aux grandes échelles et modélisation de la combustion supersonique*. PhD thesis, INSA Rouen.

[13] Bouheraoua, L., Domingo, P., and Ribert, G. (2017). Large-eddy simulation of a supersonic lifted jet flame: Analysis of the turbulent flame base. *Combust. Flame*, 179:199–218.

[14] Boussinesq, J. (1877). *Essai sur la théorie des eaux courantes*. Imprimerie Nationale.

[15] Burrows, M. and Kurkov, A. (1971). Supersonic combustion of hydrogen in a vitiated air stream using stepped-wall injection. *AIAA Paper*.

[16] Butler, T. and O'Rourke, P. (1977). A numerical method for two dimensional unsteady reacting flows. *Symposium (Int.) on Combustion*, 16(1):1503–1515.

[17] Cabell, K., Hass, N., Storch, A., and Gruber, M. (2011). Hifire direct-connect rig (hdcr) phase i, scramjet test results from the nasa langley arc-heated scramjet test facility. In *17th AIAA Int. Space Planes and Hypersonic Systems and Technologies Conference*.

[18] Cabot, W. (1995). Large-eddy simulations with wall models. In *Center for Turbulence Research*. Annual Research Briefs.

[19] Candel, S., Schmitt, T., and Darabiha, N. (2011). Progress in transcritical combustion: Experimentation, modeling and simulation. In *23rd ICDERS*.

[20] Carati, D., Ghosal, S., and Moin, P. (1995). On the representation of backscatter in dynamic localization models. *Phys. Fluids*, 7(3):606–616.

[21] Chapman, D. (1979). Computational aerodynamics development and outlook. *AIAA J.*, 17(12):1293–1313.

[22] Charlette, F., Meneveau, C., and Veynante, D. (2002a). A power-law flame wrinkling model for les of premixed turbulent combustion part I : non-dynamic formulation and initial tests. *Combust. Flame*, 131:159–180.

[23] Charlette, F., Meneveau, C., and Veynante, D. (2002b). A power-law flame wrinkling model for les of premixed turbulent combustion part II : dynamic formulation. *Combust. Flame*, 131:181–197.

[24] Cheng, T., Wehrmeyer, J., Pitz, R., Jarrett, O., and Northam, G. (1994). Raman measurements of mixing and finite-rate chemistry in a supersonic hydrogen-air diffusion flame. *Combust. Flame*, 99:157–173.

[25] Colin, O., Ducros, F., Veynante, D., and Poinsot, T. (2000). A thickened flame model for large eddy simulations of turbulent premixed combustion. *Phys. Fluids*, 12(7):1843–1863.

[26] Colket, M. B. and Spadaccini, L. J. (2001). Scramjet fuels autoignition study. *J. Propul. Power*, 17(2).

[27] Commons, W.

[28] Correa, S. (1993). Turbulence-chemistry interactions in the intermediate regime of premixed combustion. *Combust. Flame*, 93:41–60.

[29] CRIANN. http://www-tech.criann.fr/calcul/tech/myria-doc/config/.

[30] Crow, A., Boyd, I., and Terrapon, V. (2013). Radiation modeling of a hydrogen fueled scramjet. *Journal of Thermophysics and Heat Transfer*, 27(1).

[31] Curran, E., Heiser, W., and Pratt, D. (1996). Fluid phenomena in scramjet combustion systems. *Annu. Rev. Fluid Mech.*, 28(323-60).

[32] Curtiss, C. F. and Hirschfelder, J. O. (1949). Transport properties of multicomponent gas mixtures. *J. Chem. Phys.*, 17(6).

[33] Davidenko, D., Gökalp, I., Dufour, E., and Magre, P. (2006). Systematic numerical study of the supersonic combustion in an experimental combustion chamber. *AIAA Paper*, (06-7915).

[34] Davis, D. L. (1996). *Numerical Analysis of Two and Three Dimensional Recessed Flameholders for Scramjet Applications*. PhD thesis, Air Force Institute of Technology.

[35] Davis, D. L. and Bowersox, R. D. (1997a). Stirred reactor analysis of cavity flameholders for scramjets. *AIAA Paper*, (97-3274).

[36] Davis, D. L. and Bowersox, R. D. W. (1997b). Computational fluid dynamics analysis of cavity flameholders for scramjets. *AIAA Paper*, (97-3270).

[37] Deardorff, J. (1970). A numerical study of three-dimensional turbulent channel flow at large reynolds numbers. *J. Fluid Mech.*, 41:453–480.

[38] Do, H., Carter, C., Liu, Q., Ombrellow, T., Hammack, S., Lee, T., and Hsu, K.-Y. (2015). Simultaneous gas density and fuel concentration measurements in a supersonic combustor using laser induced breakdown. *Proc. Combust. Inst.*, 35(2):2155–2162.

[39] Domingo, P., Vervisch, L., and Bray, K. (2002). Partially premixed flamelets in les of nonpremixed turbulent combustion. *Combust. Theory Model.*, 6(4):529–551.

[40] Duboc, B., Ribert, G., and Domingo, P. (2019a). Evaluation of chemistry models on methane/air edge flame simulation. *Proc. Combust. Inst.*, 37(2):1691–1698.

[41] Duboc, B., Ribert, G., and Domingo, P. (2019b). Hybrid transported-tabulated chemistry for partially premixed combustion. *Comput. Fluids*, 179:206–227.

[42] Ducros, F., Ferrand, V., Nicoud, F., Weber, C., Darracq, D., Gacherieu, C., and Poinsot, T. (1999). Large-eddy simulation of the shock/turbulence interaction. *J. Comput. Phys.*, 152:517–549.

[43] Ducros, F., Nicoud, F., and Poinsot, T. (1998). Wall-adapting local eddy-viscosity models for simulations in complex geometries. *Numerical Methods for Fluid Dynamics VI*, pages 293–299.

[44] Ducros, F., Sagaut, P., and Quéméré, P. (2000). On the use of relaxation methods for localized dynamic models. *Phys. Fluids*, 12(12):3297–3300.

[45] Duwig, C., Nogenmyr, K.-J., Chan, C.-K., and Dunn, M. J. (2011). Large eddy simulations of a piloted lean premix jet flame using finite-rate chemistry. *Combust. Theory Model.*, 15(4):537–568.

[46] Edwards, J., Boles, J., and Baurle, R. (2012). Large-eddy/reynolds-averaged navier-stokes simulation of a supersonic reacting wall jet. *Combust. Flame*, 159:1127–1138.

[47] Egolfopoulous, F. N., Zhu, D. L., and Law, C. K. (1990). Experimental and numerical determination of laminar flame sppeds: mixtures of c2-hydrocarbons with oxygen and nitrogen. *Proc. Combust. Inst.*, 23:471–478.

[48] Eklund, D., Baurle, R., and Gruber, M. (2001). Computational study of a supersonic combustor fueled by an aerodynamic ramp injector. *AIAA Paper*, (2001-0379).

[49] Enjalbert, N., Domingo, P., and Vervisch, L. (2012). Mixing time-history effects in large eddy simulation of non-premixed turbulent flames: Flow-controlled chemistry tabulation. *Combust. Flame*, 159:336–352.

[50] Evans, J. and Jr., C. S. (1980). Influence of chemical kinetics and unmixedness on burning in supersonic hydrogen flames. *AIAA J.*, 18:188–193.

[51] Fedina, E., Fureby, C., Bulat, G., and Meier, W. (2017). Assessment of finite rate chemistry large eddy simulation combustion models. *Flow Tuburlence Combust.*

[52] Felden, A. (2017). *Development of analytically reduced chemistries (ARC) and applications in large eddy simulations (LES) of turbulent combustion*. PhD thesis, INP Toulouse.

[53] Ferri, A. (1973). Mixing-controlled supersonic combustion. *Annu. Rev. Fluid Mech.*, 5(301-38).

[54] Fiorina, B., Gicquel, O., Vervisch, L., Carpentier, S., and Darabiha, N. (2005). Approximating the chemical structure of partially premixed and diffusion counterflow flames using fpi flamelet tabulation. *Combust. Flame*, 140:147–160.

[55] Franzelli, B. G. (2011). *Impact of the chemical description on direct numerical simulations and large eddy simulations of turbulent combustion in industrial aero-engines*. PhD thesis, INP Toulouse.

[56] Fulton, J., Edwards, J., Hassan, H., McDaniel, J., Goyne, C., Rockwell, R., Cutler, A., Johansen, C., and Danehy, P. (2014). Large-eddy/reynolds-averaged navier-stokes simulation of reactive flow in dual-mode scramjet combustor. *J. Propul. Power*, 30(3).

[57] Fureby, C. (2007). Comparison of flamelet and finite rate chemistry LES for premixed turbulent combustion. *AIAA Paper*, (2007-1413).

[58] Fureby, C. (2009). Large eddy simulation modelling of combustion for propulsion applications. *Phil. Trans. R. Soc. A*, 367:2957–2969.

[59] Fureby, C., Chapuis, M., Fedina, E., and Karl, S. (2011). Cfd analysis of the hyshot ii scramjet combustor. *Proc. Combust. Inst.*, 33:2399–2405.

[60] Germano, M., Piomelli, U., Moin, P., and Cabot, W. H. (1991). A dynamic subgrid-scale eddy viscosity model. *Phys. Fluids*, 3(7):1760–1765.

[61] Ghosal, S., Lund, T., Moin, P., and Akselvoll, K. (1995). A dynamic localization model for large eddy simulation of turbulent flows. *J. Fluid Mech.*, 286:229–255.

[62] Grady, N., Pitz, R., Carter, C., Hsu, K.-Y., Ghodke, C., and Menon, S. (2012). Supersonic flow over a ramped-wall cavity flame holder with an upstream strut. *J. Propul. Power*, 28(5).

[63] Gruber, M., Barhorst, T., Jackson, K., Eklund, D., Hass, N., Storch, A. M., and Liu, J. (2009). Instrumentation and performance analysis plans for the hifire flight 2 experiment. In *45th AIAA Joint Propulsion Conference and Exhibit*.

[64] Gruber, M. R., Baurle, R. A., Mathur, T., and Hsu, K.-Y. (2001). Fundamental studies of cavity-based flame-holder concepts for supersonic combustors. *J. Propul. Power*, 17(1):146–153.

[65] Gruber, M. R., Donbar, J. M., Carter, C. D., and Hsu, K.-Y. (2004). Mixing and combustion studies using cavity-based flameholders in a supersonic flow. *J. Propul. Power*, 20(5).

[66] Gruber, M. R. and Nejad, A. S. (1995). New supersonic combustion research facility. *J. Propul. Power*, 11(5):1080–1083.

[67] Guven, U. and Ribert, G. (2018). Large-eddy simulation of supersonic hydrogen/oxygen combustion: application to rocketlike igniter. *J. Propul. Power*, 34(2):291–307.

[68] Hassan, E., Peterson, D., Walters, D., and Luke, E. (2019). Dynamic hybrid reynolds-averaged navier-stokes/large-eddy simulation of a supersonic cavity: Chemistry effects. *J. Propul. Power.*

[69] Hassan, M. I., Aung, K. T., Kwon, O. C., and Faeth, G. M. (1998). Properties of laminar premixed hydrocarbon/air flames at various pressures. *J. Propul. Power*, 14(4):479–488.

[70] Hirschfelder, J., Curtiss, C., and Bird, R. (1969). *Molecular theory of gases and liquids.* John Wiley & Sons.

[71] Hsu, K.-Y., Carter, C. D., Gruber, M. R., Barhorst, T., and Smith, S. (2010). Experimental study of cavity-strut combustion in supersonic flow. *J. Propul. Power*, 26(6).

[72] Jachimowski, C. (1988). An analytical study of the hydrogen-air reaction mechanism with application to scramjet combustion. *Proceedings of the NASA TP*, (2791).

[73] Jachimowski, C. J. (1977). An experimental and analytical study of acetylene and ethylene oxidation behind shock waves. *Combust. Flame*, 29:55–66.

[74] Jackson, K., Gruber, M., and Buccellato, S. (2013). An overview of the hifire flight 2 project. In *51st AIAA Aerospace Sciences Meeting.*

[75] Jaouen, N., Vervisch, L., Domingo, P., and Ribert, G. (2017). Automatic reduction and optimisation of chemistry for turbulent combustion modeling: impact of the canonical problem. *Combust. Flame*, 175:60–79.

[76] Jaravel, T. (2016). *Prediction of pollutants in gas turbines using large-eddy simulation.* PhD thesis, INP Toulouse.

[77] Jomaas, G., Zheng, X. L., Zhu, D. L., and Law, C. K. (2005). Experimental determination of counterflow ignition temperatures and laminar flame speeds of c2-c3 hydrocarbons at atmospheric and elevated pressures. *Proc. Combust. Inst.*, 30:193–200.

[78] Kalitan, D., Rickard, M., Hall, J., and Petersen, E. (2004). Ignition measurements of ethylene-oxygen-diluent mixtures with and without silane addition. *AIAA Paper*, (2004-1323).

[79] Kee, R., Rupley, F., Coltrin, M., Grcar, J., Meeks, E., Moffat, H., Lutz, A., Dixon-Lewis, G., Smooke, M., Warnatz, J., Evans, G., Larson, R., Mitchell, R., Petzold, L., Reynolds, W., Caracotsios, M., Stewart, W., Glarborg, P., Wang, C., McLellan, C., Adigun, O., Houf, W., Chou, C., Miller, S., Ho, P., Young, P., Young, D., Hodgson, D., Petrova, M., and Puduppakkam, K. (2006). CHEMKIN release 4.1. Technical report, Reaction Design, San Diego, CA.

[80] Kim, K. M., Baek, S. W., and Han, C. Y. (2004). Numerical study on supersonic combustion with cavity-based fuel injection. *Int. J. Heat Mass Transfer*, 47:271–286.

[81] Knudsen, E. and Pitsch, H. (2009). A general flamelet transformation useful for distinguishing between premixed and non-premixed modes of combustion. *Combust. Flame*, 156:678–696.

[82] Kolmogorov, A. N. (1941). The local structure of turbulence in incompressible viscous fluid for very large Reynolds numbers. *Dokl. Akad. Nauk SSSR*, 30:9–13.

[83] Kopp, M., Donato, N., Petersen, E., Metcalfe, W., Burke, S., and Curran, H. (2014). Oxidation of ethylene-air mixtures at elevated pressures, part 1: Experimental results. *J. Propul. Power*, 30(3).

[84] Krauss, R., Mcdaniel, J., Scott, J., Whitehurst, R., and Segal, C. (1988). Unique, clean-air, continuous-flow, high-stagnation-temperature facility for supersonic combustion research. *AIAA Paper*, 88-3059A.

[85] Krol, M. C., Molemaker, M. J., and de Arellano, J. V. G. (2000). Effets of turbulence and heterogeneous emissions on photochemically active species in the convective boundary layer. *J. Geophys. Res.*, 105(D5):6871–6884.

[86] Kuenne, G., Ketelheun, A., and Janicka, J. (2011). Les modeling of premixed combustion using a thickened flame approach coupled with fgm tabulated chemistry. *Combust. Flame*, 158:1750–1767.

[87] Lacaze, G., Vane, Z., and Oefelein, J. (2017). Large eddy simulation of the hifire direct connect rig scramjet combustor. *AIAA Paper*, (2017-0142).

[88] Lamp, A. M. and Chokani, N. (1997). Computation of cavity flows with suppression using jet blowing. *J. Aircraft*, 31(1):545–551.

[89] Larsson, J., Kawai, S., Bodart, J., and Bermejo-Moreno, I. (2016). Large eddy simulation with modeled wall-stress: recent progress and future directions. *Mechanical Engineering Reviews*, 3(1).

[90] Law, C. (2006). *Combustion Physics*. Cambridge University Press.

[91] Legier, J., Poinsot, T., and Veynante, D. (2000). Dynamically thickened flame les model for premixed and non-premixed turbulent combustion. *Proceedings of the Summer Program*, pages 157–168.

[92] Lignell, D. O., Chen, J. H., Smith, P. J., Lu, T. F., and Law, C. K. (2007). The effect of flame structure on soot formation and transport in turbulent nonpremixed flames using direct numerical simulation. *Combust. Flame*, 151(1-2):2–28.

[93] Lilly, D. (1992). A proposed modification of the germano subgrid-scale closure method. *Phys. Fluids*, 4(3):633–635.

[94] Lin, K., Jackson, K., Behdadnia, R., Jackson, T. A., Ma, F., and Yang, V. (2010). Acoustic characterization of an ethylene-fueled scramjet combustor with a cavity flameholder. *J. Propul. Power*, 26(6).

[95] Lin, K., Tam, C., and Jackson, K. (2009). Study on the operability of cavity flameholders inside a scramjet combustor. In *45th AIAA Joint Propulsion Conference and Exhibit*.

[96] Lin, K. C., Tam, C. J., Boxx, I., Carter, C., Jackson, K., and Lindsey, M. (2007). Flame characteristics and fuel entrainment inside a cavity flame holder in a scramjet combustor. In *AIAA Paper*, 2007-5381.

[97] Liu, C. and Liu, Z., editors (1997). *Comments on the feasibility of LES for wings, and on a hybrid RANS/LES approach*. Columbus, Greyden Press.

[98] Liu, F., Guo, H., Smallwood, G., and Gülder, O. (2002). Numerical study of the superadiabatic flame temperature phenomenon in hydrocarbon premixed flames. *Proc. Combust. Inst.*, 29:1543–1550.

[99] Liu, J., Tam, C. J., Lu, T., and Law, C. K. (2006). Simulations of cavity-stabilized flames in supersonic flows using reduced chemical kinetic mechanisms. In *42nd AIAA Joint Propulsion Conference and Exhibit*.

[100] Liu, J. and Tiwari, S. (1996). Radiative heat transfer effects in chemically reacting nozzle flows. *Journal of Thermophysics and Heat Transfer*, 10(3).

[101] Lock, A. J., Briones, A. M., Qin, X., Aggarwal, S. K., Puri, I. K., and Hegde, U. (2005). Liftoff characteristics of partially premixed flames under normal and microgravity conditions. *Combust. Flame*, 143:159–173.

[102] Lodato, G., Domingo, P., and Vervisch, L. (2008). Three-dimensional boundary conditions for direct and large-eddy simulation of compressible viscous flows. *J. Comput. Phys.*, 227:5105–5143.

[103] Lodier, G., Vervisch, L., Moureau, V., and Domingo, P. (2011). Composition-space premixed flamelet solution with differential diffusion for in situ flamelet-generated manifolds. *Combust. Flame*, 158:2009–2016.

[104] Lu, T. F. and Law, C. K. (2005). A directed relation graph method for mechanism reduction. *Proc. Combust. Inst.*, 30(1):1333–1341.

[105] Luo, Z., Yoo, C. S., Richardson, E. S., Chen, J. H., Law, C. K., and Lu, T. F. (2012). Chemical explosive mode analysis for a turbulent lifted ethylene jet flame in highly-heated coflow. *Combust. Flame*, 159(1):265–274.

[106] Lutz, A., Kee, R., and Miller, J. (1990). SENKIN - A Fortran program for predicting homogeneous gas phase chemical kinetics with sensitivity analysis. Technical report, Report No. SAND87-8240 UC-4, Sandia Lab.

[107] Lutz, A., Rupley, F., Kee, R., Reynolds, W., and Meeks, E. (1998). EQUIL : A CHEMKIN implementation of STANJAN for computing chemical equilibria.

[108] Magnussen, B. (1981). On the structure of turbulence and a generalized eddy dissipation concept for chemical reaction in turbulent flow. *AIAA Paper*.

[109] Martinez-Ferrer, P., Buttay, R., Lehnasch, G., and Mura, A. (2014). A detailed verification procedure for compressible reactive multicomponent navier-stokes solvers. *Comput. Fluids*, 89:88–110.

[110] Mathur, T., Gruber, M. R., Jackson, K., Donbar, J. M., Donaldson, W., Jackson, T. A., and Billig, F. (2001). Supersonic combustion experiments with a cavity-based fuel injector. *J. Propul. Power*, 17(6).

[111] Meeks, E., Kee, R., Dandy, D., and Coltrin, M. (1993). Computational simulation of diamond chemical vapor deposition in premixed c2h2/o2/h2 and ch4/o2 strained flames. *Combust. Flame*, 92:144–160.

[112] Meneveau, C. and Poinsot, T. (1991). Stretching and quenching of flamelets in premixed turbulent combustion. *Combust. Flame*, 86(4):311–332.

[113] Merlin, C. (2011). *Simulation numérique de la combustion turbulente : Méthode de frontières immergées pour les écoulements compressibles, application à la combustion en aval d'une cavité.* PhD thesis, INSA Rouen.

[114] Metcalfe, W., Burke, S., Ahmed, S., and Curran, H. (2013). A hierarchical and comparative kinetic modeling study of c1-c2 hydrocarbon and oxygenated fuels. *Int. J. Chem. Kinet.*, 45(10):638–675.

[115] Micka, D. and Driscoll, J. (2009). Combustion characteristics of a dual-mode scramjet combustor with cavity flameholder. *Proc. Combust. Inst.*, 32(2):2397–2404.

[116] Moin, P. and Kim, J. (1982). Numerical investigation of turbulent channel flow. *J. Fluid Mech.*, 118:341–377.

[117] Moin, P., Squires, K., Cabot, W., and Lee, S. (1991). A dynamic subgrid-scale model for compressible turbulence and scalar transport. *Phys. Fluids*, 3(11):2746–2757.

[118] Moule, Y. and abd A. Mura, V. S. (2014). Highly resolved numerical simulation of combustion in supersonic hydrogen-air coflowing jets. *Combust. Flame*, 161:2647–2668.

[119] Nakaya, S., Hikichi, Y., Nakazawa, Y., Sakaki, K., Choi, M., Tsue, M., Kono, M., and Tomioka, S. (2015). Ignition and supersonic combustion behavior of liquid ethanol in a scramjet model combustor with cavity flame holder. *Proc. Combust. Inst.*, 35:2091–2099.

[120] Neely, A. J., Riley, C., Boyce, R. R., Mudford, N. R., Houwing, A. F. P., and Gruber, M. R. (2003). Hydrocarbon and hydrogen-fuelled scramjet cavity flameholder performance at high flight mach numbers. In *12th AIAA Int. Space Planes and Hypersonic Systems and Technologies.*

[121] Nguyen, P.-D., Vervisch, L., Subramanian, V., and Domingo, P. (2010). Multidimensional flamelet-generated manifolds for partially premixed combustion. *Combust. Flame*, 157:43–61.

[122] O'Conaire, M., Curran, H., Simmie, J., Pitz, W., and Westbrook, C. (2004). A comprehensive modeling study of hydrogen oxidation. *Int. J. Chem. Kinet.*, 36(11):603–622.

[123] Oefelein, J. (2006). Large eddy simulation of turbulent combustion processes in propulsion and power systems. *Prog. Aerospace Sci.*, 42(1):2–37.

[124] O'Rourke, P. and Bracco, F. (1979). Two scaling transformations for the numerical computation of multidimensional unsteady laminar flames. *J. Comput. Phys.*, 33(2):185–203.

[125] Perng, S. W. and Dolling, D. S. (1996). Passive control of pressure oscillations in hypersonic cavity flow. In *34th Aerospace Sci. Meeting.*

[126] Peskin, C. (1972). Flow patterns around heat valves: a numerical method. *J. Comput. Phys.*, 10:252–271.

[127] Peters, N. (1986). Laminar flamelet concepts in turbulent combustion. In Institute, T. C., editor, *21st Symp. on Combustion*, pages 1231–1250.

[128] Petit, X., Ribert, G., Domingo, P., and Lartigue, G. (2013). Large-eddy simulation of supercritical fluid injection. *J. Supercrit. Fluids*, 84:61–73.

[129] Pierce, C. and Moin, P. (2004). Progress-variable approach for large-eddy simulation of non-premixed turbulent combustion. *J. Fluid Mech.*, 504:73–97.

[130] Piomelli, U. (1993). High Reynolds number calculations using the dynamic subgrid-scale stress model. *Phys. Fluids*, 5:1484–1490.

[131] Piomelli, U. (2008). Wall-layer models for large-eddy simulations. *Prog. Aerospace Sci.*, 44:437–446.

[132] Piomelli, U. and Balaras, E. (2002). Wall-layer models for large-eddy simulations. *Annu. Rev. Fluid Mech.*, 34:349–374.

[133] Piomelli, U. and Liu, J. (1995). Large-eddy simulation of rotating channel flows using a localized dynamic model. *Phys. Fluids*, 7(4):839–848.

[134] Poinsot, T. and Lele, S. (1992). Boundary conditions for direct simulations of compressible viscous flows. *J. Comput. Phys.*, 101(1):104–129.

[135] Poinsot, T. and Veynante, D. (2005). *Theoretical and numerical combustion.* Edwards.

[136] Qin, Z., Lissianski, V. V., Yang, H., Gardiner, W. C., Davis, S. G., and Wang, H. (2000). Combustion chemistry of propane: a case study of detailed reaction mechanism optimization. *Proc. Combust. Inst.*, 28:1663–1669.

[137] Rasmussen, C. C., Driscoll, J. F., Hsu, K.-Y., Donbar, J. M., Gruber, M. R., and Carter, C. D. (2005). Stability limits of cavity-stabilized flames in supersonic flow. *Proc. Combust. Inst.*, 30:2825–2833.

[138] Reynolds, W. (1986). The element potential method for chemical equilibrium analysis: Implementation in the interactive program STANJAN, version 3. Technical report, dept. of mechanial engineering, Stanford Univ.

[139] Ribeiro, F., Boukharfane, R., Robin, V., and Mura, A. (2018). Numerical study of combustion stabilization in a scramjet engine model with cavity flameholder. *Tenth International Conference on Computational Fluid Dynamics (ICCFD10).*

[140] Richardson, L. F. (1922). *Weather prediction by numerical process.*

[141] Sabel'Nikov, V. and Fureby, C. (2013). LES combustion modeling for high Re flames using a multi-phase analogy. *Combust. Flame*, 160:83–96.

[142] Sabel'Nikov, V. and Silva, L. F. D. (2002). Partially stirred reactor : Study of the sensitivity of the monte-carlo simulation to the number of stochastic particles with the use of a semi-analytic, steady-state solution to the PDF equation. *Combust. Flame*, 129:164–178.

[143] Sagaut, P. (2000). *Large Eddy Simulation for Incompressible Flow: An Introduction.* Springer.

[144] Saghafian, A., Shunn, L., Philips, D. A., and Ham, F. (2015a). Large eddy simulations of the hifire scramjet using a compressible flamelet/progress variable approach. *Proc. Combust. Inst.*, 35:2163–2172.

[145] Saghafian, A., Terrapon, V., and Pitsch, H. (2015b). An efficient flamelet-based combustion model for compressible flows. *Combust. Flame*, 162:652–667.

[146] Sarno, R. L. and Franke, M. E. (1994). Suppression of flow-induced pressure oscillations in cavities. *J. Aircraft*, 31(1):90–96.

[147] Schmisseur, J. D. (2015). Hypersonics into the 21st century: A perspective on afosr-sponsored research in aerothermodynamics. *Prog. Aerospace Sci.*, 72:3–16.

[148] Schmitt, T., Boileau, M., and Veynante, D. (2015). Flame wrinkling factor dynamic modeling for large eddy simulations of turbulent premixed combustion. *Flow Tuburlence Combust*, 94:199–217.

[149] Shan, R. and Lu, T. (2012). Ignition and extinction in perfectly stirred reactors with detailed chemistry. *Combust. Flame*, 159:2069–2076.

[150] Shu, C. and Osher, S. (1988). Efficient implementation of essentially non-oscillatory shock-capturing schemes. *J. Comput. Phys.*, 77:439–471.

[151] Shur, M., Spalart, P., Strelets, M., and Travin, A. (2008). A hybrid rans-les approach with delayed-des and wall modelled les capabilities. *Int. J. Heat Fluid Flow*, 29(6):1638–1649.

[152] Singh, D. J. and Jachimowski, C. J. (1993). Quasiglobal reaction model for ethylene combustion. *AIAA J.*, 32:213–216.

[153] SiTCom-B. https://www.coria-cfd.fr/index.php/sitcom-b.

[154] Smagorinsky, J. (1963). General circulation experiments with the primitive equations. *Monthly Weather Review*, 91(3):99–164.

[155] Smith, G., Golden, D., Frenklach, M., Moriarty, N., Eiteneer, B., Goldenberg, M., Bowman, C., Hanson, R., Song, S., Gardiner, W., Lissianski, V., and Qin, Z. (1999). GRI-mech 3.0.

[156] solver, V. https://vulcan-cfd.larc.nasa.gov.

[157] Spalart, P. (2000). Strategies for turbulence modelling and simulations. *Int. J. Heat Fluid Flow*, 21:252–263.

[158] Spalart, P. and Allmaras, S. (1992). A one-equation turbulence model for aerodynamic flows. *AIAA Paper*, (92-0439).

[159] Sunami, T., Magre, P., Bresson, A., Grisch, F., Orain, M., and Kodera, M. (2005). Experimental study of strut injectors in a supersonic combustor using oh-plif. *AIAA Paper*, (2005-3304).

[160] Swanson, R., Radespiel, R., and Turkel, E. (1998). On some numerical dissipation schemes. *J. Comput. Phys.*, 147:518–544.

[161] Swanson, R. and Turkel, E. (1992). On central-difference and upwind schemes. *J. Comput. Phys.*, 101:292–306.

[162] Tatsumi, S., Martinelli, L., and Jameson, A. (1995). Flux-limited schemes for the compressible navier-stokes equations. *AIAA J.*, 33:252–261.

[163] Terrapon, V., Ham, F., Pecnik, R., and Pitsch, H. (Annual Research Briefs 2009). A flamelet-based model for supersonic combustion. *Center for Turbulence Research.*

[164] Tuttle, S. G., Carter, C. D., and Hsu, K.-Y. (2014). Particle image velocimetry in a nonreacting and reacting high-speed cavity. *J. Propul. Power*, 30(13):576–591.

[165] Urzay, J. (2018). Supersonic combustion in air-breathing propulsion systems for hypersonic flight. *Annu. Rev. Fluid Mech.*, 50(593-627).

[166] Vakili, A. D. and Gauthier, C. (1994). Control of cavity flow by upstream mass injection. *J. Aircraft*, 31(1):169–174.

[167] Varatharajan, B. and Williams, F. (2002). Ethylene ignition and detonation chemistry, part 1: detailed modeling and experimental comparison. *J. Propul. Power*, 18(2).

[168] Veynante, D. and Vervisch, L. (2002). Turbulent combustion modeling. *Progress in Energy and Combustion Science*, 28(3):193–266.

[169] Vinuesa, J. F., Porte-Agel, F., Basu, S., and Stoll, R. (2006). Subgrid-scale modeling of reacting scalar fluxes in large-eddy simulations of atmostpheric boundary layers. *Environ. Fluid Mech.*, 6(2):115–131.

[170] Volpiani, P. S. (2017). *Modèle de plissement dynamique pour la simulation aux grandes échelles de la combustion turbulente prémélangée.* PhD thesis, Université Paris-Saclay.

[171] Vreman, A. (2004). An eddy-viscosity subgrid-scale model for turbulent shear flow: algebraic theory and applications. *Phys. Fluids*, 16(10).

[172] Wang, G., Boileau, M., and Veynante, D. (2011a). Implementation of a dynamic thickened flame model for large eddy simulations of turbulent premixed combustion. *Combust. Flame*, 158:2199–2213.

[173] Wang, H. and Laskin, A. (2007). A comprehensive kinetic model of ethylene and acetylene combustion.

[174] Wang, H., Qin, N., Sun, M., Wu, H., and Wang, Z. (2011b). A hybrid les(large eddy simulation)/assumed sub-grid pdf (probability density function) model for supersonic turbulent combustion. *Sci. China Technol. Sci.*, 10:2694–2707.

[175] Wang, H., Wang, Z., and Sun, M. (2013). Experimental study of oscillations in a scramjet combustor with cavity flameholders. *Exp. Thermal and Fluid Sci.*, 45:259–263.

[176] Wang, H., Wang, Z., Sun, M., and Qin, N. (2015). Large eddy simulation of a hydrogen-fueled scramjet combustor with dual cavity. *Acta Astronautica*, 108:119–128.

[177] White, J. (2002). A modified wall matching treatment to account for local solid to fluid thermal coupling. *Proceedings of the JANNAF CS/APS/PSHS/MSS Joint Meeting.*

[178] Yamashita, H., Shimada, M., and Takeno, T. (1996). A numerical study on flame stability at the transition point of jet diffusion flames. In *Symposium on Combustion*, volume 26, pages 27–34.

[179] Yaws, C. L. (2001). *Matheson gas data book*, volume Seventh Edition.

[180] Yoshizawa, A. (1986). Statistical theory for compressible turbulent shear flows, with the application to subgrid modeling. *Phys. Fluids*, 29(2152).

[181] Zhang, X. and Edwards, J. A. (1990). An investigation of supersonic oscillatory cavity flows driven by thick shear layers. *Aeronaut. J.*, 94(940):355–364.

[182] Zhang, X., Rona, A., and Edwards, J. A. (1998). The effect of trailing edge geometry on cavity flow oscillation driven by a supersonic shear layer. *Aeronaut. J.*, pages 129–136.